Catalysis^{cubed}

Cyclopropanations inside a porphyrin-based supramolecular M_8L_6 aggregate

Dissertation

zur

Erlangung des Doktorgrades (Dr. rer. nat.)

der

Mathematisch-Naturwissenschaftlichen Fakultät

der

Rheinischen Friedrich-Wilhelms-Universität Bonn

vorgelegt von

Theresa Lena Harings

aus

Bonn

Bonn, 2025

Angefertigt mit Genehmigung der Mathematisch-Naturwissenschaftlichen

Fakultät der Rheinischen Friedrich-Wilhelms-Universität Bonn

Gutachter/Betreuer: Professor Arne Lützen

Gutachter: Professor Andreas Gansäuer

Tag der Promotion: 26.02.2026

Erscheinungsjahr: 2026

Table of contents

1. Introduction

Everything that exists in our cosmos – from the smallest particle to the largest structure – can be ultimately tracked back to chemical reactions. Over billions of years, nature has served as the greatest chemist, continuously optimising processes through evolution. These natural mechanisms provide not only a great variety of possible reactions, but often also unrivalled efficiency. Therefore, it is not surprising that natural processes, even in modern research, are still of major interest and inspire scientists all over the world across disciplines. In fact, the observation and study of nature's processes established, among others, the groundwork for a field of scientific innovation known as biomimetics.[1]

Biomimetics, also referred to as biomimicry, is an interdisciplinary field of research, dealing with the understanding and replication of strategies employed by nature. Thereby, researchers take an advantage of evolutionary optimised processes, analysing and adapting them for technical, medical and industrial applications. The idea behind this is rather simple: Nature has already developed solutions that are sustainable, energy-efficient and effective. By mimicking these, scientists aim to create new technologies, aligning closer with these principles of nature in order to reach similar levels of efficiency.[2]

The term biomimetics was established by *Otto Schmitt* in the 1950s, an American biophysicist, while studying the technical adaptation of the electronical action transmission of a nerve. *Schmitt* developed a device that mimicked the function of neural signal conduction, an early example of translating biological processes into engineering. His work thereby marked the beginning of a systematic approach to copy nature's designs. In the following decades, this concept evolved and several subtopics emerged, including bionics, which refers more specifically to the adaptation of biological principles into technical designs.[3]

One of the most prominent examples in this field is the so-called lotus effect, a phenomenon first observed in the self-cleaning of lotus leaves. Despite growing in swampy environments, lotus plants remain remarkably clean which originates from a rough surface, shown in figure 1. Thereby, small air pockets form between water droplets and the nanostructures on the surface of the lotus leaves. This reduces the wettability of the plant and creates a superhydrophobic surface. Additionally the leaves are coated with small wax crystals, leading to water droplets which do not attach to the leaf but stay structurally intact.[4] By this, water droplets which land on the leaves roll of quickly, collecting dirt and other debris along their way.[5]

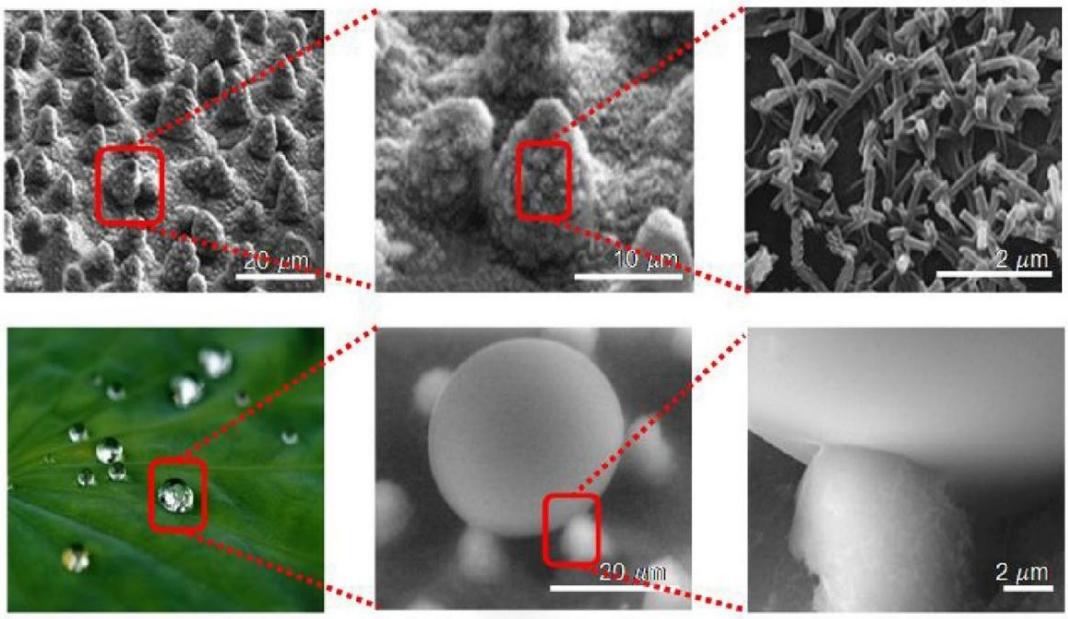

Figure 1: Water repelling surface of lotus leaves with scanning electron micrographs of the surface structures.[5] Figure reprinted with permission from *Elsevier*.

This discovery led to the development of new materials with similar properties. Today, this effect is transferred to a range of commercial products such as water repellent paints, self-cleaning glass and protective coatings for roof tiles or boat hulls in order to enhance their durability and reducing maintenance.[6]

However, the relevance of biomimetics is not limited to surface structures. The investigation of natural phenomena on a molecular level has become a vibrant area of scientific research. Living organisms, especially plants, synthesise a variety of different substances for diverse functions ranging from photosynthesis and pigmentations[7] to defence strategies[8] or inter-species communication[9]. These compounds, are often formed under mild conditions, even utilising the by-products of other naturals syntheses, making them remarkably efficient and economic.

2. Porphyrins

One notable class of compounds, showcasing nature's complexity, are the porphyrins. These highly conjugated macrocycles were recognised early by scientists due to their frequent occurrence in nature, but also their intense colour. Because of their unique chemical properties, porphyrins are frequently studied in fundamental science, as well as in applied technology. Their potential application ranges from solar energy conversion,[10] photodynamic therapy for cancer treatment[11] to catalysis and even molecular electronics.[12]

Biomimetic approaches for the application of porphyrins are especially promising due to the possibility to form tailored compounds, mimicking the efficiency of natural processes, yet combining this with high stability, which is necessary under industrial conditions. Synthetic porphyrin derivatives have been employed to imitate the catalytic activity of enzymes[13] or the absorbance of light across a wide spectrum in order to develop new dye-sensitised solar cells.[10]

Scientific interest in the chemical nature of porphyrins dates back to the late 19th century, mainly concerning the structures found in blood, urine and bile of the human body. These porphyrins and their derivates were a substantial element of the research on certain diseases, in which for example specific porphyrins are excreted in the urine. These investigations contributed significantly to early stages of biomedical research especially regarding diseases characterised by abnormal porphyrin metabolism.[14]

2.1 Porphyrins in nature

The porphyrin ring consists of four pyrrole units, linked *via* methine bridges, forming a fully conjugated π-system. This extended delocalisation is responsible for their characteristic purple or red colour, though depending on the substitution pattern or metal-coordination, some porphyrins can even appear green or blue. Additionally, porphyrins exhibit strong fluorescence in organic solvents and in exceptional cases also in solid state. Such optical behaviour is a direct consequence of the electronic structure, where the energy difference of the HOMO-LUMO corresponds to a wavelength of light within the visible light range. The ease of functionalisation at the *meso*- or *β*-positions provide further means of tuning their spectroscopic properties resulting in attractive compounds for photonic and optoelectronic applications.[15]

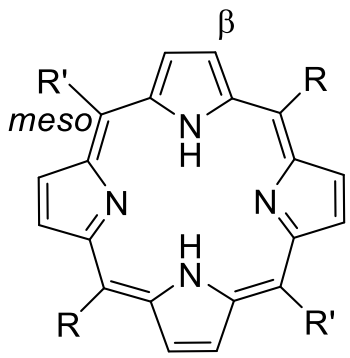

Figure 2: Structure of the porphyrin core.

Not only their spectroscopic but also their structural properties allow for diverse applications. Their ability to coordinate metal-ions, along with the possible fine tuning of electronical and steric properties make them highly versatile class of substances.[15]

Metal coordination can either occur centrally within the cavity of the porphyrin ring where four nitrogen atoms provide a preorganised ligand environment, or at specific substituent positions on the outside of the ring. The coordination on the inside is thereby much more favoured due to the prearranged tetradentate nature of the porphyrin core. Depending on the radius of the metal, the coordinated metal can either be in the plane of the macrocycle

or adopt an out-of-plane position.[16] These metals alter the properties of porphyrins drastically, enabling a broad range of applications. Nature provides some of the most striking examples of porphyrin-based functionality in the form of chlorophyll and haemoglobin.

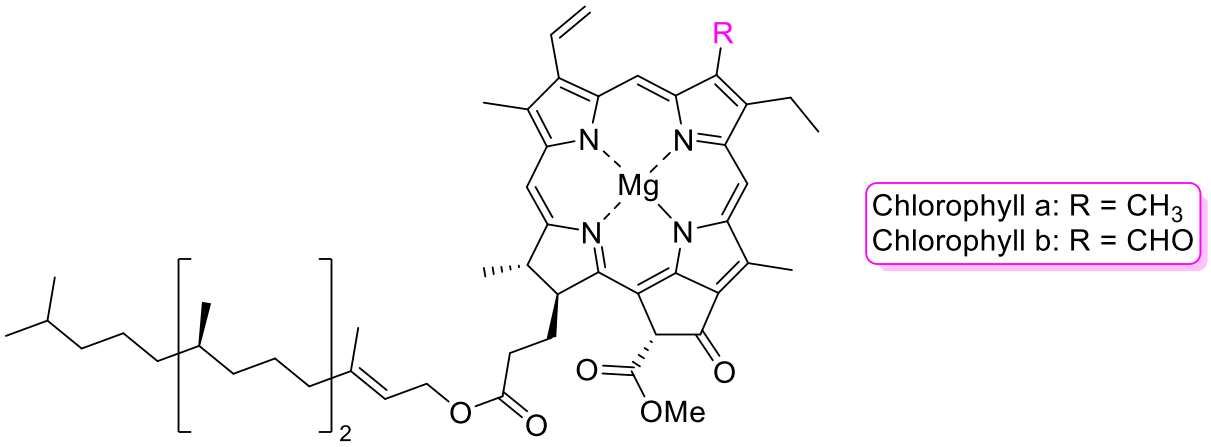

Figure 3: Porphyrin unit of chlorophyll a and b.

As shown in figure 3, chlorophylls are based on reduced porphyrin unit known as a chlorin, equipped with a central magnesium(II)-ion. This class of compounds is indispensable to life on earth, serving as the key photocatalyst in photosynthesis.[17]

Photosynthesis is one of the most crucial biochemical reaction on the planet, guaranteeing the survival of almost all living organisms. It enables the formation of oxygen and glucose out of carbon dioxide, catalysed by sunlight. Hereby, the absorption of solar energy occurs in antenna pigments, containing multiple chlorophyll units. As it is shown, in a simplified style, in figure 4 photons excite electrons of the accessory pigments (chlorophyll, green in figure 4). The excitation promotes electrons to energetically higher excited states. Due to the specific arrangement and proximity of the chlorophyll molecules, the excitation energy is efficiently transferred *via Förster* resonance energy transfer (FRET) to a central reaction centre.[18] This rapid energy transfer between exited states of different light harvesting and energy transmitting molecules prevents excited electrons form relaxing to the ground state, enabling efficient channelling of energy towards the reaction centre (blue in figure 4). There, the energy of multiple light harvesting pathways is combined and utilised to drive electron transfer processes that ultimately power the conversion of carbon dioxide and the formation of elemental oxygen.[19,20]

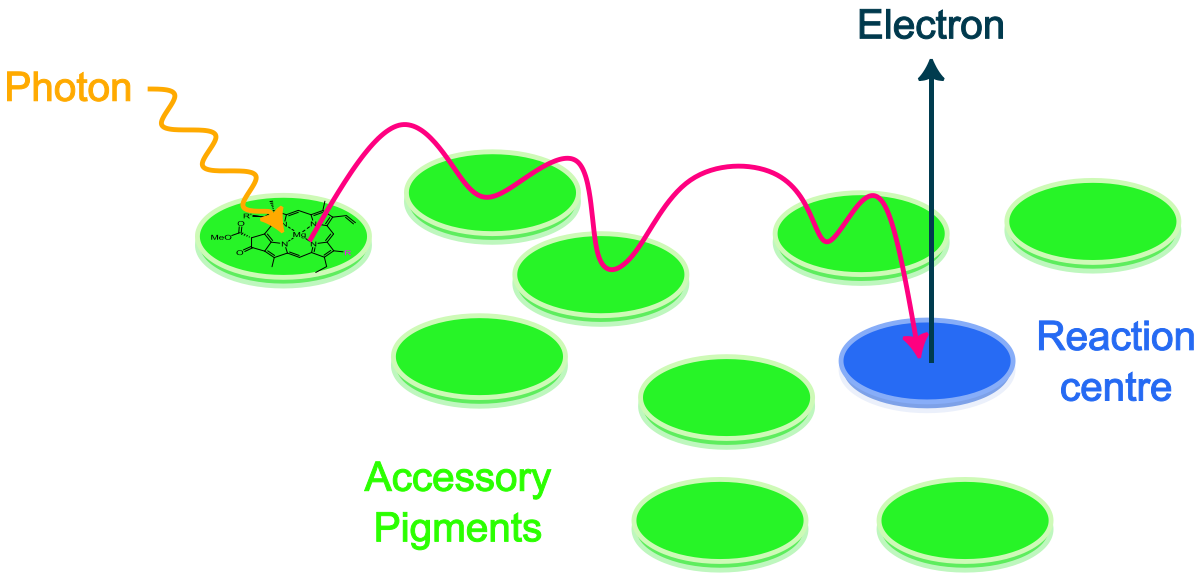

Figure 4: Schematic illustration of light-harvesting and energy transfer process.[18,21]

Another biologically vital porphyrin-based class of compounds are haemoglobins, the oxygen transport protein in red blood cells. The haemoglobins in the blood also contain a porphyrin ring, known as heme, which coordinates an iron(II) ion at its centre.[22]

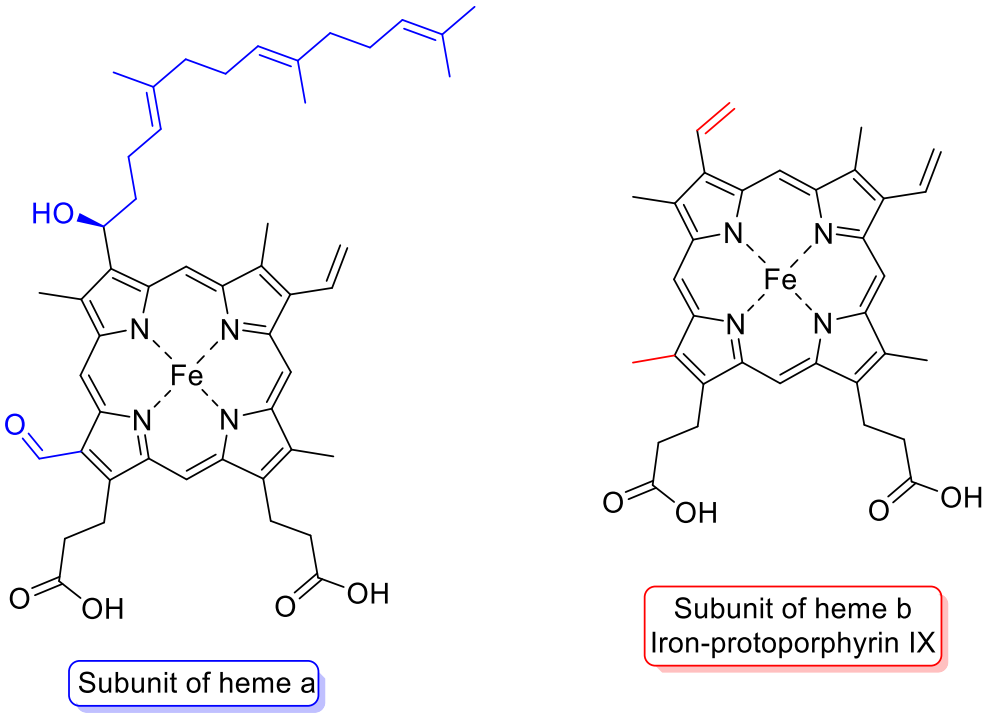

Figure 5: Porphyrin units of heme a (left) and heme b (right).[22]

Herein, the heme group is the prosthetic group, the active centre, of the enzyme. This is enclosed in the enzymatic pocket, evoked by folding of four polypeptide chains around the

heme group, forming a hydrophobic surrounding. In this shielded environment, oxygen can interact reversibly with the iron centre, allowing the heme groups to switch between oxygenated and deoxygenated species. The rate of oxygenated heme is thereby depending on the oxygen pressure in the surrounding tissue. In the lungs a relatively high oxygen pressure prevails, leading to all four of the heme groups in one unit of haemoglobin being present in the oxygenated state. It then travels through the blood and releases oxygen in tissue where less oxygen is present, as for example muscles.[23]

Another prominent example of proteins containing heme groups are the cytochrome P450s (CYPs). This group of monooxygenases is a common representative with over 1000 different members in biological compounds. Even in humans, more than 40 different types of cytochromes P450 are present acting as catalysts for several processes as the oxidation of drugs, steroids and fatty acids. By this, they have a major impact on drug efficiency and detoxification.[24]

The active centre of these proteins is the iron-protoporphyrin IX, shown in figure 5 on the right. The main difference between cytochrome P450s and other heme proteins is the presence of an additional cysteine group, acting as a ligand at the iron centre. This provides an altered electron density of the surrounding porphyrin ring, allowing the activation of molecular oxygen.[24]

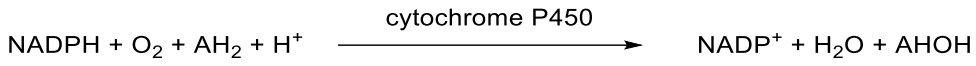

Figure 6: P450-dependant oxygenation reaction of nicotinamide adenine dinucleotide phosphate (NADPH) and an organic compound (A) in the presence of elemental oxygen.[24]

However, not only the affinity of iron towards oxygen plays a crucial role in the applications of cytochrome P450s, but also the stable oxidation states iron can adapt. In the initial form of a cytochrome P450 the iron-ion has an oxidation state of +III but during the catalytic cycle it is reduced to +II and subsequently oxidised stepwise to +IV. Each of these intermediates provides additional applications in different processes. This leads to a range of catalytic cycles, all intertwined with each other, forming a catalytical globe.[24,25]

Due to this high presence in natural compounds, easy detectability and huge variety of adaptations, porphyrins gained early the interest of researchers in many fields. Due to their easily tuneable nature, they became rather prominent in multiple different topics as catalysis, medicine or supramolecular assemblies.

2.2 Porphyrins in industry

In many industrial processes bio-inspired catalysts, often based on porphyrin derivates, are employed. Especially prominent are porphyrin-catalysts in the field of oxidations and CH-bond activations, in which different metalloporpyhrins can catalyse different reactions. Cobalt-porphyrins, for example, are very effective catalysts for C-O bond formation when combined with elemental oxygen.[26] This reactivity stems from their ability to activate elemental oxygen through metal-oxygen intermediates, thereby enabling selective oxidation processes under relatively mild conditions.

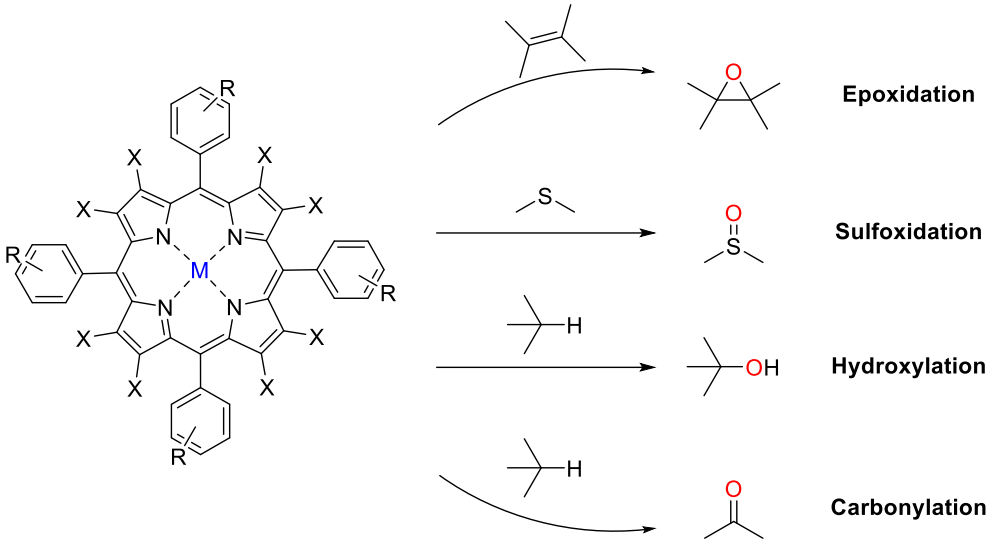

Figure 7: Overview of porphyrin based industrial catalysis.[27]

By manganese- or iron-porphyrin catalysed oxidations of olefins, in which the porphyrin serves as a biomimetic analogue of natural oxygenases, epoxides can be formed. These are of great interest due to their variable applications as intermediates in the formation of polymers, as well as their potential application in drugs.[27] Such transformations are highly valued, because they can proceed with remarkable regio- and stereoselectivity, often avoiding harsh reagents. By selective tailoring of the steric bulk and the electronic nature of the substituents not only the reactions outcome but also turnover frequency and catalyst lifetime are influenced.[28]

However, porphyrins are not only crucial as catalysts but also are applied in dye-sensitised solar cells (DSSCs), where their photophysical properties play a central role in the performance and efficiency of the device. The general properties of porphyrins as their efficient absorption of sunlight and participation in energy transfer processes, renders them ideal candidates for light-harvesting by mimicking nature's own photosynthetic pathways.[29] In DSSCs, porphyrins serve as sensitiser dyes, that capture solar radiation and convert it into chemical excitation

energy. Upon absorption of a photon, an electron of the porphyrin enters an excited energy state and is subsequently injected into the conduction band of a semiconductor. This leads to charge separation and thereby to the formation of an electric current that can be used for power generation. By modifications, either changing substitution or introducing metals, the electronic and steric properties of the porphyrin can be finely tuned to match the requirements of the respective system, leading to more efficient photon-harvesting and electron-transfer. This finetuning also allow precise control over the absorption spectrum, redox potential and excited state lifetime, enabling the design of sensitiser molecules that are optimally matched to the semiconductor and electrolyte system employed.[30]

Beyond their application in solar energy conversion and industrial catalysis, porphyrin have also attracted attention as functional dyes and pigments. As introduced in previous chapters, porphyrins exhibit a variety of strong colourful appearances, wherefore they are often found in pigments and dyes. These are not only applied in medicine but also as natural, non-toxic dyes for fabrics and plastics. Porphyrin dyes are also applied in industrial pigments,[31] benefitting from high thermal stability, biodegradability and high resistance against chemical degradation and environmental conditions, as for instance UV-light, but also inspire researchers to develop new environmentally friendly dyes.[32] The ability to fine-tune absorption maxima enables the design of dyes with specific colour profiles, spanning from deep reds to purples, blues and greens, enabling customised coloration for different functional or aesthetic applications. Moreover, the inherent stability of the porphyrins helps retain colour intensity and optical performance even under prolonged UV exposure, resulting in attractive compounds for outdoor applications. In emerging research, functionalised porphyrins are also being investigated as “smart” pigments that change colour or fluorescence in response to environmental stimuli, such as pH-values or temperature, enabling their utilising in innovative sensing technologies. For example, porphyrins containing protonatable substituents undergo distinct spectral shifts upon acid-base interactions, producing visible pH-dependent colour transitions. Similarly, metalloporpyhrins integrated into thermoresponsive polymer matrices display temperature-dependent absorption or fluorescence changes, acting as visual thermochromic indicators. Such functionalised are porphyrins therefore considerable promising for innovative sensing technologies, where colour variation serves as an easily detectable signal of environmental change.[33]

2.3 Porphyrin synthesis

The biosynthetical formation of porphyrins is a remarkable process, requiring the action of numerous specialised enzymes, each catalysing a specific step along the pathway to

assemble the highly ordered macrocyclic structure. As an example, the biosynthesis of protoporphyrin is shown in figure 8.[34]

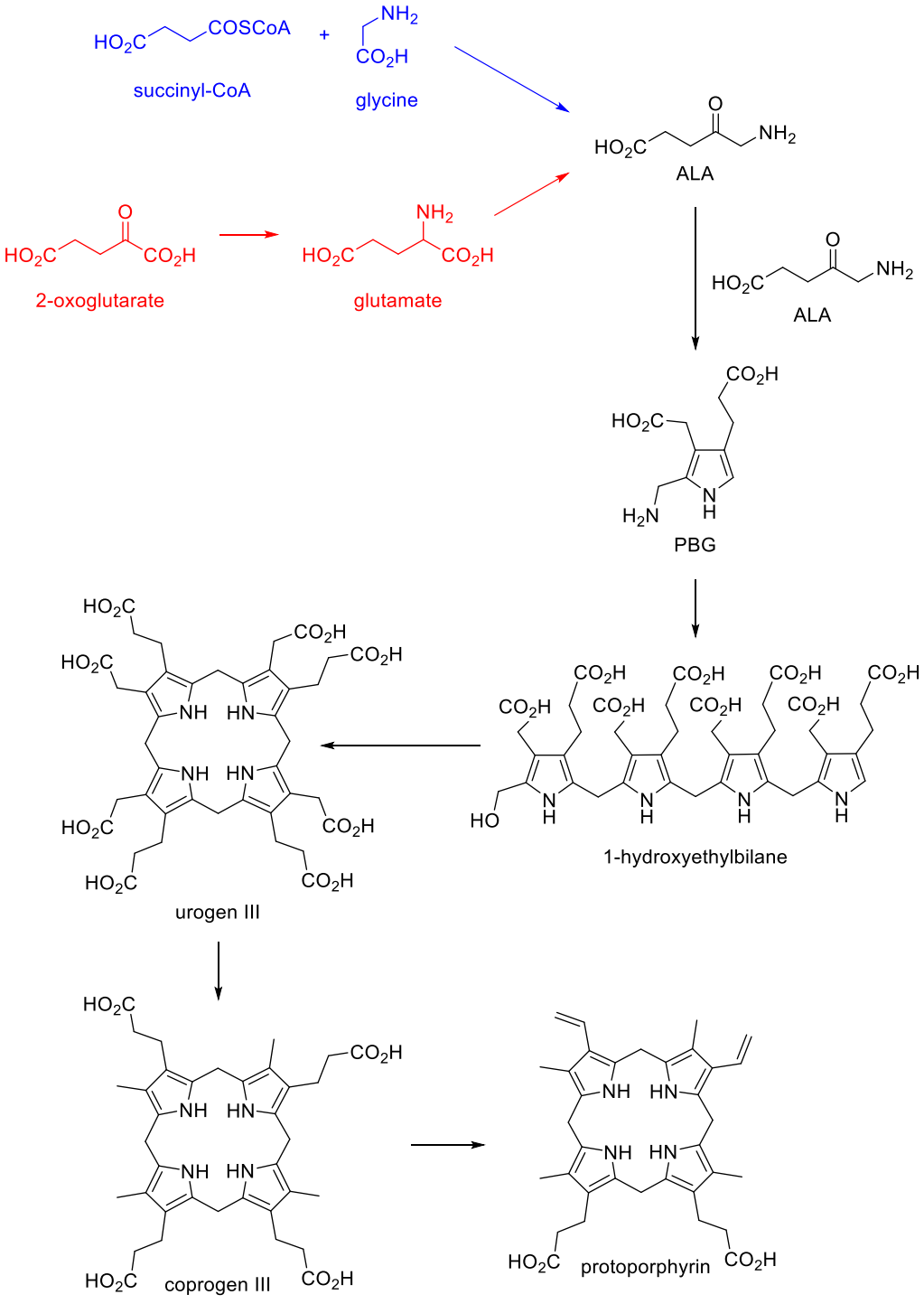

Figure 8: Biosynthesis of protoporphyrin.[34]

The formation of 5-aminolaevulinic acid (ALA) is achieved in two different pathways as shown in figure 8 in blue and red. The condensation of glycine and succinyl-CoA, displayed in blue,

was discovered first and takes place in animals. The synthesis of ALA from glutamate (red) is mainly found in algae and plants. From this point on, animals, plants and algae follow the same steps in order to form the protoporphyrin, which acts as a precursor for the formation of heme groups as well as chlorophylls.[34] Due to the large variety of different enzymes and their excellent control of reactivities, nature can form rather unsymmetrical porphyrins. These provide substituents, which are exactly matching the demand on size, electronical properties and functional groups for their respective application in biological processes. The synthetical formation of porphyrins on the other hand, gets progressively challenging with decreasing symmetry.[34]

Artificial porphyrin synthesis has been a challenging research topic in the last century. Highly symmetrical porphyrins can be formed *via* a fourfold condensation of pyrrole with the respective aldehydes followed by subsequent oxidation in order to create an aromatic system. Thereby, polymerisation and other side reactions, as well as fragmentation are frequently observed problems. As a result, the yield is most common between 10–20%.[35] The synthesis of less symmetrical structures is even more challenging. From the simple approach of mixing the starting materials and attempting a fourfold condensation many different products form. In order to prevent that, different stepwise approaches are utilised like the synthesis of an open stranded molecule followed by cyclisation, formation of a precursor containing two pyrrole moieties and one *meso*-substituent or even functionalisation of a “preformed” porphyrin.[35]

An additional issue is the poor solubility of porphyrins, due to interactions between the individual molecules, leading to strongly interconnected stacks. This not only hampers possible scale up but also the purification of porphyrins after their successful formation.[35]

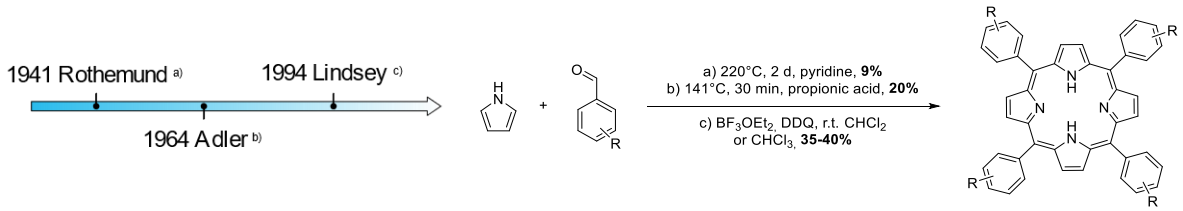

Figure 9: Timeline of modifications on porphyrin synthesis.[36–38]

In order to overcome these issues, the synthetic procedure has been modified multiple times since the first approach, published by *Rothemund* in 1941.[36] Here, pyrrole and the respective aldehyde are reacted in a sealed tube at 220°C for two days. These harsh conditions yielded tetraphenylporphyrin (TPP) in just 9% yield, without functional group tolerance.[36]

Slightly milder conditions were established by *Adler* in 1964, whereby the same substrates as in *Rothemunds* approach are employed. Here, the substrates are heated at 141°C in propionic

acid for only 30 minutes. Also, an open beaker is used instead of a sealed tube.[37] This method yields approximately 20% of TPP and provides a synthetically less challenging setup, while enabling a broad substrate scope.

In 1994, *Lindsey* published another synthetic pathway, in which pyrrole and the respective aldehyde first react in a self-assembly process to a porphyrinogen. This acid catalysed step is supported by BF_3-ethanol as a cocatalyst and is performed in chloroform or dichloromethane. After one hour the formation stops and the porphyrinogen can be converted into the porphyrin using DDQ as an oxidant. This method yields the porphyrins in 0 to 50%, depending on the employed aldehyde.[38]

Later, these methods were even further modified by, for example, performing the synthesis under exclusion of air,[39] usage of transition metal catalysts[40,41] or even microwave conditions.[42]

3. Concepts of host-guest chemistry

Porphyrins, beyond their well-established role as homogeneous and heterogeneous catalysts are often found in supramolecular complexes due to remarkable geometrical features. Their rigid, planar macrocyclic framework and the ease with which their electronic and steric properties can be functionalised, make them suitable for a variety of different purposes. By choosing an adequate substitution pattern, they can self-assemble into larger, cage- or belt-like aggregates, presenting a discrete internal cavity.[43] These so-called host-molecules are able to encapsulate smaller molecules, the guests. This interaction can dramatically alter guest reactivity due to the preorganisation of substrates in geometrically favoured positions in relation to each other or potential catalysts. Also, the local polarity inside the cavity of supramolecular hosts can be quite different in comparison to the surrounding. The host itself can interact with substrates inside its cavity, which is summarised under the term of second-coordination sphere effects and will be discussed in detail in later chapters.[44]

Then again, porphyrins can act as guest molecules if the respective host provides a suitable cavity. This dual role highlights the great significance of porphyrins in many different applications. In order to frame host guest chemistry, three fundamental concepts must be introduced. First, supramolecular interactions, discussing the significance of the interplay of non-covalent interactions. Second, self-assembly, describing thermodynamic and kinetic pathways by which building blocks organise into architectures with higher order. Finally, molecular recognition, describing the principles by which a host interacts with suitable guests, relying on geometrical, i.e. shape and size, and interactional complementarity.[44]

3.1 Supramolecular interactions

Supramolecular chemistry, unlike covalent chemistry, is based on non-covalent interactions like hydrogen bonds or *van der Waals* interactions. These usually provide lesser bond strengths than covalent bonds but the interplay of many non-covalent interactions can be used to form large, distinct assemblies. *J. D. van der Waals*, after whom the previously mentioned *van der Waals* interactions were named, first recognised the impact of non-covalent interactions during his Ph. D. studies in the late 19th century.[45] This force is an example for one of the weaker non-covalent interactions, occurring between all atoms and only depending on the distance of these atoms.[46]

Another example of non-covalent interactions are electrostatic interactions, describing the repulsion or attraction of charged or polar molecules, as metal-coordination. Thereby, they behave like magnets, molecules of the same polarity repulse each other, leading to a higher distance between those parts, as molecules of different polarity attract each other, bringing them into closer proximity.[44] These forces tend to have a rather large magnitude reaching up to 350 kJ/mol for charged species, in comparison to other non-covalent interactions.[47] The power of these effects depends not only on the kind of polar particles but also on the surrounding media, for example electrostatic interactions are weaker in hydrophilic media. Due to the solvation shell hydrophilic solvents form around charged particles, caused by their own dipole, parts of the electrostatic field are absorbed, and thereby, the overall strength is lowered.[44]

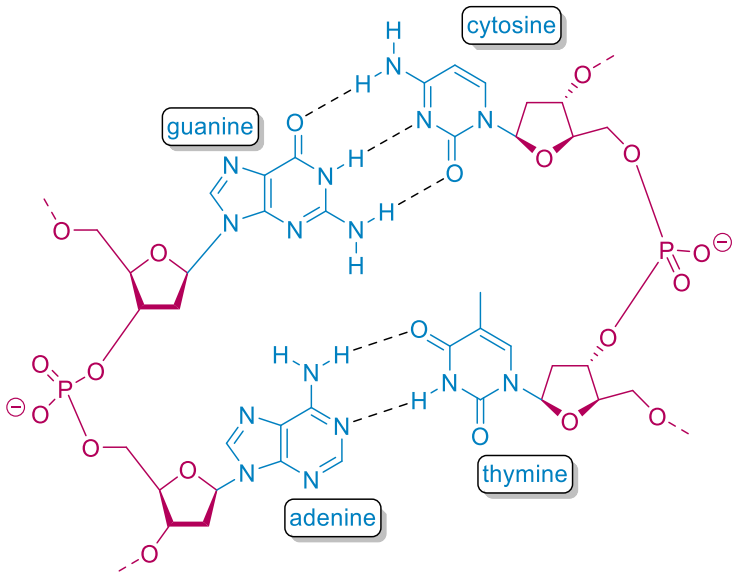

Figure 10: Hydrogen bond (black) formation between nucleobases in DNA.[48]

Prominent examples for non-covalent interactions can again be found in nature, for example in the hydrogen bonds responsible for the pairing of nucleobases in the DNA strands. This pairing occurs not only due to the contrary electron density at the electron pairs of oxygen/nitrogen, acting as the negative charge, and hydrogen atoms, which provide a more positive partial charge, but also on the shape complementarity of the building blocks. As shown in figure 10, the guanine can mainly bind to cytosine and adenine to thymine, mismatched pairs are thereby also possible, but they are significantly less stable and lead to a distortion of the DNA strand. On one hand this selective coupling is based on the complimentary binding sites, as the guanine-cytosine pair form three hydrogen bonds per pair, however adenine and thymine only form two.[48] On the other hand, these base-pairs show a shape complementarity as a result of which they can come into closer proximity to each other, enabling stronger interactions between the coordination sites. Additionally, π-stacks are present between different π-systems of the DNA, forming the twisted double strand. This principle of shape complementarity is also a fundamental component of molecular recognition and self-assembly.

3.2 Self-Assembly and molecular recognition

Self-assembly is a process in which individual molecular or supramolecular building blocks spontaneously combine into larger, often well-defined aggregates. This process leads to the formation of the thermodynamically most favoured species, relying only on the chemical information encoded in the shape, functionality and interaction preferences of the components. *Whiteside* and co-workers described this method in 2005 as a bottom-up approach, in contrast to the traditional top-down approach, commonly used in micro- and nanofabrication, where bulk materials are systematically divided into smaller functional parts to achieve the desired structure.[49,50]

However, in the bottom-up approach, the desired product is formed by piecing together small fragments, which already have the required information, determining the products features, encoded in their structures. This information then control the formation of one dominant product species by combining structural features of the participating building blocks. The formed aggregate is thereby, in most cases, in the thermodynamic minimum of all potential outcomes of the reaction. Thus, the reversible manner of non-covalent interactions benefits to the formation of the desired product, since partially assembled aggregates can break again into their building blocks, repeating the assembly process until the thermodynamically most stable product forms. As a result of this highly dynamic process, supramolecular complexes provide an error correction during their formation, leading to a great control of the reactions outcome.[49,44]

The design ideas of supramolecular complexes can be described with the molecular-library- and the symmetry-interaction-approach. In both principles electron donor- and acceptor-components are combined and by their favoured coordination-geometry, as well as the respective stoichiometry, the final structure can be predicted.[49,44]

This process was described by *Fujita et. al*. in 2001 by combining 2,4,6-tri(pyridin-4-yl)-1,3,5-triazine with a *cis*-protected palladium group, as shown in figure 11. The donors (pyridine moieties) exhibit, in this example, coordination angles of 120° and the acceptor (Pd(II)-ions) can coordinate in 90° angles due to their favoured square planar coordination geometry and the presence of *cis*-protection groups.[51]

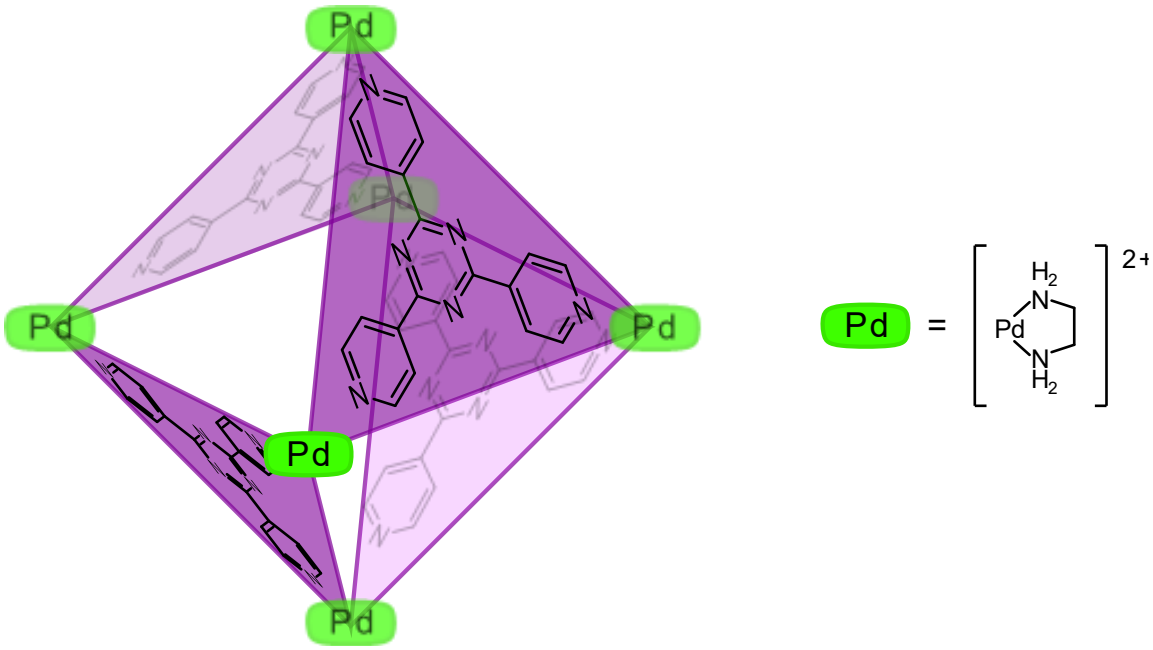

Figure 11: Pd_6L_4 octahedron published by *Fujita et. al*.[51]

The combination of these distinct angular preferences dictates the spatial arrangement of the resulting assembly. In a stoichiometric ratio of six metal centres to four organic ligands, the self-assembly is driven towards the formation of a well-defined, discrete octahedral structure, shown in figure 11. In this configuration, each ligand bridges between three metal centres, resulting in a highly symmetrical architecture.[51]

In their studies *Fujita* and his group investigated the influence of a small change in the coordination geometry of the ligand by changing the previously used one to 2,4,6-tri(pyridine-3-yl)-1,3,5-triazine, which provides an altered coordination geometry due to its capability to rotate around the single bond connecting the pyridine units with the central triazine.

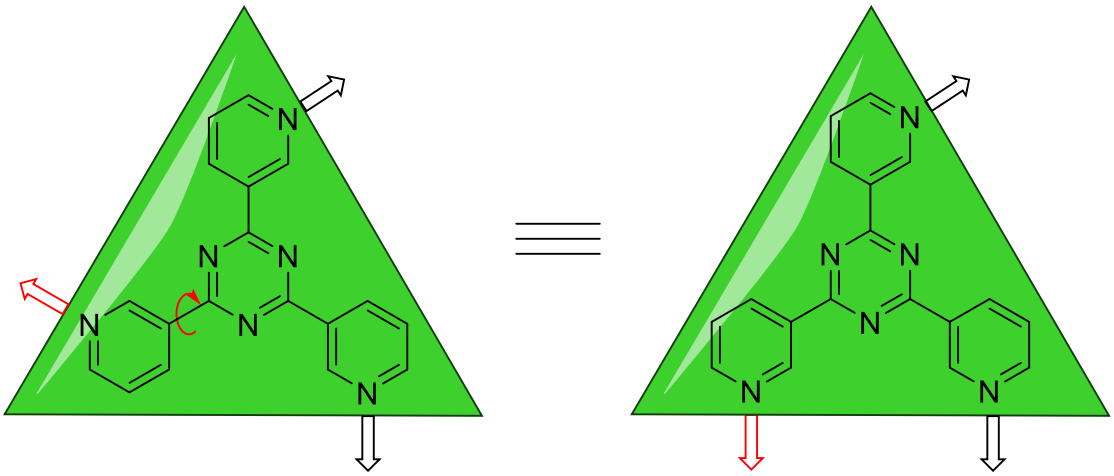

Figure 12: Rotation isomers of new ligand.[51]

Hence, the pyridine group, marked with a red arrow in figure 12, can either point into another (left) or the same directions (right) as the neighbouring group, and thereby, different assemblies can be formed. With this altered ligand the same *cis*-protected palladium unit as well as consistent stoichiometry of metal and ligand, *Fujita* and his group managed to form a cone shaped aggregate, shown below in figure 13.[51]

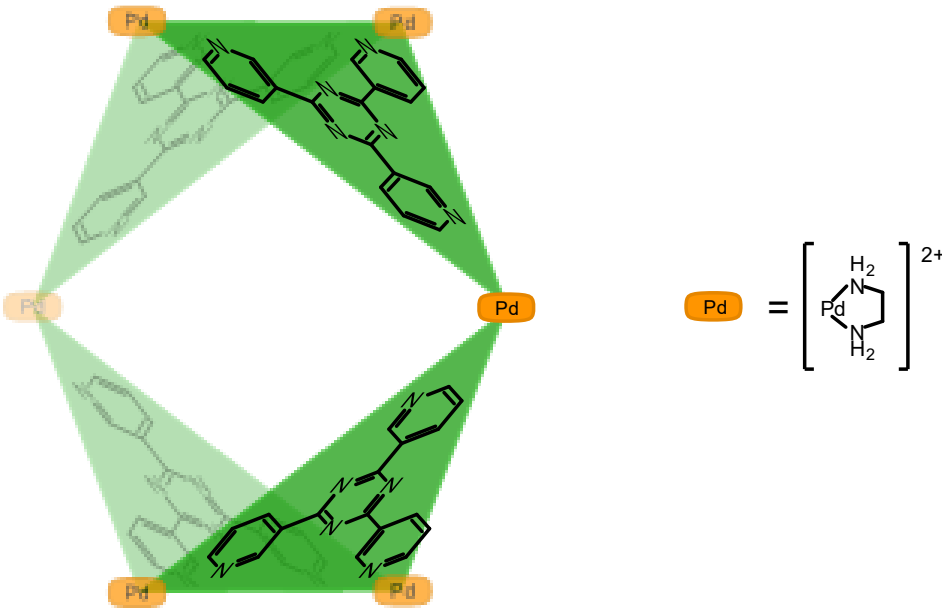

Figure 13: Square-pyramidal cone.[51]

This drastic change in the structure of the supramolecular aggregate, with just small adjustments in the ligand, illustrates the impact of coordination angles in the fields of supramolecular chemistry and molecular recognition.

Molecular recognition is a concept, already known since the end of the 19th century, when *Emil Fischer* introduced the lock and key principle. Again, this principle was found in natural processes, as in this case, the interaction of substrates with enzymes. He observed different behaviours of the stereoisomers of hexoses when combined with yeast. Afterwards, he discovered the presence of invertin and emulsin, both glucoside-cleaving enzymes, but their effect highly depends on the configuration of the glucoside.[52] *Fischer's* theory states that, due to complementarity in shape and interaction sites, only certain enzymes can process specific substrates similar to the specificity of only certain keys being able to open one lock. This metaphor, although pioneering for the state of scientific understanding at this time, suggests a rather stiff interaction motive but in reality, enzymes consist of a somewhat flexible structure, changing upon interaction with substrates. This modification to the original theorem was published by *Koshland* in 1958[53], highlighting the explicit adjustment of enzymes to the respective substrate. *Koshland* extended this modified version of *Fischer's* lock and key principle in 1994 by introducing the induced fit model.[54]

This modification also explains aspects, the lock and key principle lacked. For instance, *Fischer* describes the addition of substrates to the enzyme but it remained unclear why no smaller substrates could interact in similar manner. Also, the differences in the selectivity of enzymes could not be clarified with the enzyme as a rigid template for catalysing biological processes.[55]

In the time of *Fischer's* studies, the composition of enzymes remained unclear but in the first half of the 20th century their structure was investigated further and with this *Koshland* was able to notice the structural changes of enzymes upon the addition of a fitting substrate.[55]

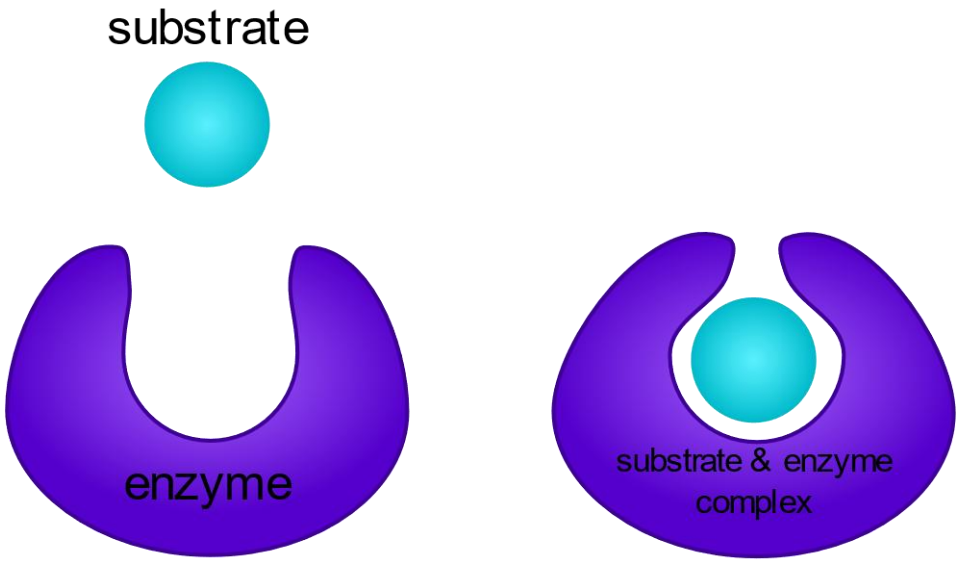

Figure 14: Induced fit model, shown in a simplified manner.[54,55]

These structural changes are shown in figure 14, in which the protein strands of the enzyme (shown in purple) adapt an altered conformation upon the substrate-binding (blue), forming the enzymatic pocket. The effects of this will be discussed in later chapters.

3.3 Supramolecular host-guest chemistry

The previously introduced models can not only be used to design supramolecular assemblies by definition of stoichiometry, bonding angles, shape, size and functionality, but also the interaction of host and guest molecules can be described by the models of self-assembly and molecular recognition.

The field of host-guest chemistry can be traced back to the discovery of crown ethers by *Pedersen* in 1967.[56] Since then a variety of hosts, possessing different shapes and cavity-compositions, and therefore, different possible applications, were introduced. Many of these are applied in the fields of supramolecular polymers, supramolecular frameworks, drug delivery, artificial light harvesting systems and many more.[57] In the design of host structures, it has to be distinguished between covalent hosts, which interact *via* non-covalent bonds with their respective guests, or supramolecular hosts, already consisting of non-covalently assembled architectures themselves.

Covalent hosts can be found in many different sizes and shapes, with crown ethers as one of the most prominent examples. They are widely known for their coordination to ions inside their cavity. Thereby, different types of recognition can take place, depending on the molecular structure of host and guest. Most macrocycles provide a two-dimensional hole-type cavity, in which the guest is located. The interaction of host and guest, thereby depends on the size complementarity as well as their electronical properties. Macrobicycles on the other hand, provide three dimensional spheroidal cavities, enabling coordination of larger molecules from different sites and angles.[44]

Non-covalent hosts include a broad range of supramolecular architectures that rely on weak, reversible interactions rather than covalent bonds to form themselves or bind their guests. Among, the most prominent examples are supramolecular capsules of resorcinarenes, which are widely recognised for their ability to encapsulate ions or neutral molecules within their cavities. The type and strength of molecular recognition depend strongly on the complementarity between host and guest in terms of size, shape and electronic properties. While many macrocyclic hosts feature a two-dimensional, ring-like cavity that accommodates smaller guests, others form more complex three-dimensional binding pockets. Such architecture, shown exemplarily in figure 11 and 13, allow for multiple non-covalent

interactions, enabling the selective and reversible encapsulation of a wide variety of molecular species.[44,47] The encapsulation of one or more guests proceeds according to a similar principle than the host-formation, in which the host itself is located on a higher energy level than the host-guest complex, as shown in figure 15.[58]

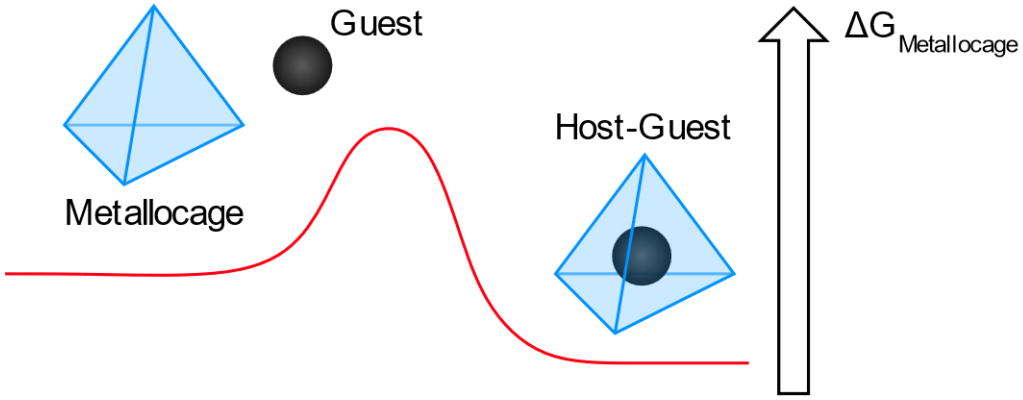

Figure 15: Energy-diagram of guest encapsulation.[58]

However, the dynamic behaviour, used during the formation process to generate the thermodynamically most stable structure, enables the opening of already formed assemblies in solution, whereby guests can enter hosts either by diffusion through the pores or the opening. This is an essential process in the application of supramolecular hosts towards the usage of their inner cavity in the concept of molecular flasks, in which the inner volume of hollow structures is used as a reaction environment on a molecular level, for example in supramolecular catalysis.[59]

4. Supramolecular catalysis – general concepts

Supramolecular catalysis is, as well as supramolecular chemistry itself, a rather young field of chemical research. Especially since the 1990s many new insights and revolutionary developments were achieved. In that time catalysis on its own became increasingly important due to the need of “greener” alternatives for many processes, able to reduce waste formation and to protect the vulnerable environment. The usage of catalysts is particularly suitable for green chemistry, since they enable reaction pathways which would not be possible without their use, while being employed in substoichiometric amounts, which makes them resource-saving. Additionally, catalysts are not consumed during the catalysis, making them reusable, so that they are able to perform multiple reaction cycles. This “lifetime” of the catalyst is noted as the turnover number (**TON**), stating the number of cycles the catalyst can perform before the reaction stops, usually calculated by dividing the reached yield by the applied catalyst loading. This end of what seems like a never-ending cascade of subsequent catalytic

cycles can have several reasons like the completed conversion of substrates, the occurrence of side reactions or degradation of the catalyst.[60]

Supramolecular catalysis, unlike conventional catalysis, is based on the idea of enzyme mimicking in order to utilise the advantages which enzymatic catalysis has reached in its evolutionary process. However, this promising goal has some obstacles lying in its way to the finished supramolecular catalyst that need to be overcome. The design of the host system itself has to be perfectly balanced between the number and orientation of the weak non-covalent interactions, already discussed in chapter 3.1, and steric repulsion of each group or building block.[60] Since the catalytic reaction takes place inside the cavity of the supramolecular host, as in the enzymatic pocket in nature, this space has to specifically match the requirements of this certain reaction. Thereby, the size is a key factor, limiting potential substrates and strongly influencing shape and conformation of transition states and the formed products. These needs must be taken into account in the design of a supramolecular catalyst, making it a highly tailored assembly respective to a specific type of applications.

4.1 Fundamentals of supramolecular catalysis

The first examples of supramolecular catalysts were published in the 1970s, strongly correlated with enzymatic catalysis and natural compounds. Therefore, it is no surprise that several of these first representatives are based on cyclodextrins. Cyclodextrins are not only readily available but they also provide an excellent coordination of hydrophobic substrates inside their cavity when surrounded by an aqueous medium.[60,61]

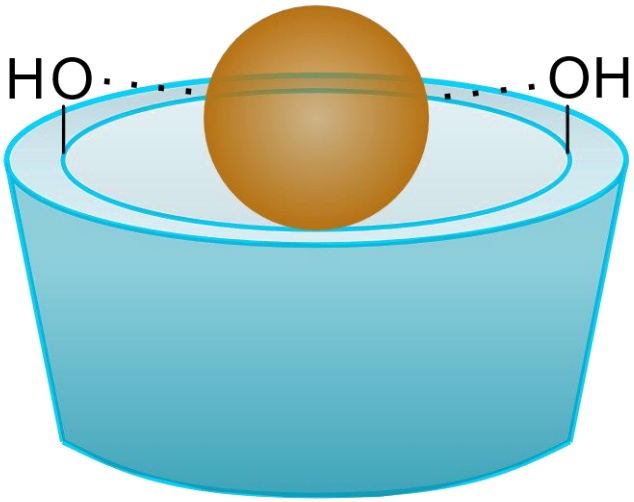

Figure 16: Schematic guest (brown) complexation in cyclodextrin (blue).[61]

The hydrophobic internal cavity of cyclodextrins, shown in blue, can benefit the encapsulation of hydrophobic guest-molecules, depicted in brown, while increasing solubility of the host-guest complex in aqueous media, as shown in figure 16. Moreover, the hydroxy-groups on the exterior can also, stabilise the guest in certain conformations upon interactions as hydrogen bonds or can directly interact with it in catalytical processes.[61]

One of the first examples of supramolecular catalysis using cyclodextrins was published by *Breslow* and *Overman* in 1970.[62] They introduced the nickel-catalysed hydrolysis of *para*-nitrophenylacetat, which is coordinated to the hydrophobic cavity of cyclohexaamylose, shown in a simplified manner in figure 17.

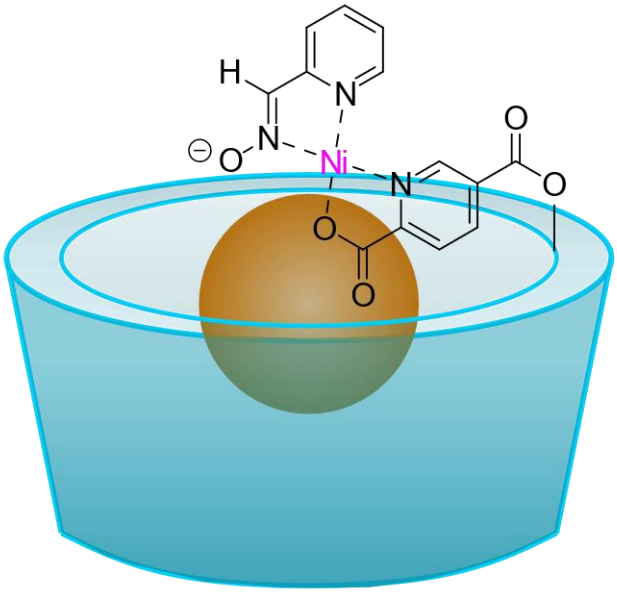

Figure 17: Nickel-based catalytic cyclodextrin introduces by *Breslow* and *Overman*.[62]

This specially designed catalyst enabled the reaction to proceed 1000 times faster than in the uncatalysed case. In their work *Breslow* and *Overman* noticed that the acceleration of chemical reactions by metal catalysts can be rather drastic, but is also limited to substrates which can bind strongly to the catalytical active metal. The conversion of other substrate remained challenging so they copied natural enzyme catalysis, which uses non-covalent interactions to bring substrates into close proximity with the active centre, even when the substrate itself does not provide suitable binding sites for the catalyst.[62]

This effect, amongst numerous others, can be summarised under the topics of nanoconfinement and second coordination sphere effects. These are typical aspects of enzymatic catalysis, which are mimicked in supramolecular catalysis. Enzymes usually consist of a catalytically active metal centre, shown in red in figure 18, with directly surrounding ligands,

e.g. the natural porphyrins. Hereby, the reactive centre, e.g. a metal ion, is responsible to define the catalytic process, while the surrounding ligands, the first coordination sphere, shown in purple, influence sterical and electronical properties, altering mechanistic pathways of the catalysis.

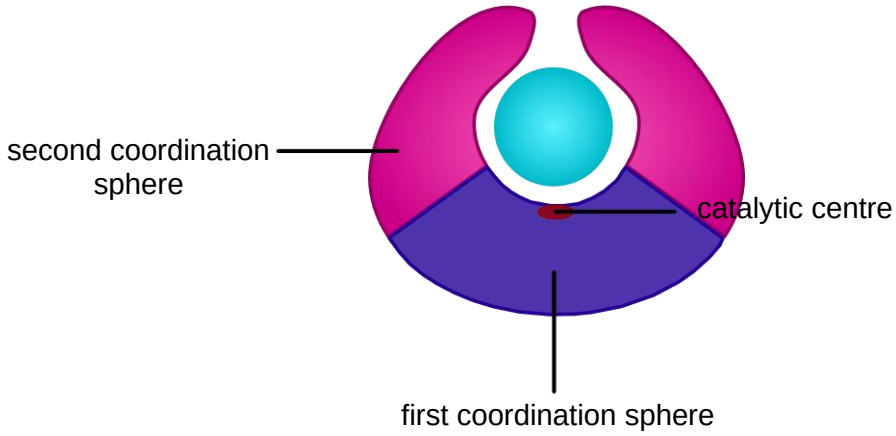

Figure 18: First (purple) and second coordination sphere (pink) with catalytic centre (red) of enzymes and a substrate (light blue).

Additionally, residues which are not directly bound to the metal, the second coordination sphere, shown in pink, can still have a major impact on the reaction's outcome. In enzymes these residues are usually consisting of several amino acid chains, moving freely in the surrounding media without the presence of a suitable substrate. Upon interaction with the substrate, they are able to orient in a certain manner in order to form enzymatic pockets, building up a microenvironment around the catalytically active centre.

4.2 Confinement effects and microenvironments

Over the years, a variety of different capsules has been designed to mimic the structure of enzymatic pockets over the years in order to provide a controlled environment around the active centre and shield the catalyst from the outside. These examples can be supramolecular assemblies as well as covalent capsules, whereby the first ones provide several benefits already introduced in chapter 3.

Regardless of their structure, these molecular flasks provide a void in their cavity in which the respective reactions can take place. This volume is significantly smaller than the surrounding bulk, which leads to confinement effects, influencing several aspects of the catalysis. Confinement effects consist of three subtopics: the physical constraint effects, electronic effects and the molecular enrichment effect.[63]

The physical constrain effect has widely been studied in tubes, but also in other host structures. Typical examples to show the importance of this effect can be found in polymer chemistry, in which the topology can be drastically altered by constraining the polymerisation inside carbon nanotubes (CNTs).[64]

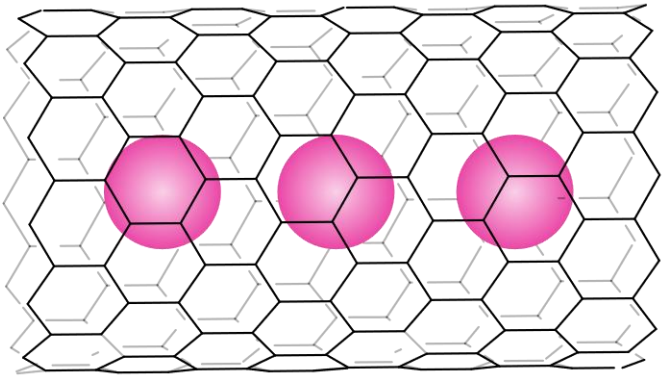

Figure 19: Monomer (pink) orientation inside a carbon nanotube.[64]

By applying the constrain, shown in figure 19, the synthesis of a new topology of polymeric fullerene oxide can be generated, which would not be possible in the bulk. The narrow diameter of these carbon nanotubes, prevent the formation of a branched three-dimensional polymer, which is favoured in bulk, but benefits the formation of only linear nonbranched polymer strands. This principle allows, thereby, a controlled alteration of reaction pathways and the resulting products.[64]

Electronic effects can be attributed to the confinement effects, as well as second coordination sphere effects. As explained in previous chapters, the second coordination sphere is not directly bound to the catalytically active centre, so it influences the reaction in a less active manner than the first coordination sphere. One of the most important aspects of the second coordination sphere is the stabilisation of transition states, leading to them being energetically more favoured, which decreases the activation energy barrier of the respective reaction. This can either be the same transition state as in the bulk reaction, or a different transition state that might be favoured due to the confined room in which the reaction takes. This can have various physical causes, the most obvious one is the size and spatial orientation of the respective transition states. Thereby, smaller transition states which fit better into the confined space can now be more favoured than they would be in the bulk, just due to their size. Additionally, the second coordination sphere can interact with the transitions states themselves in an electronic way, by which certain groups can be stabilised in a particular position or the electronic properties can stabilise some transition states better than others.[65]

The latter case is described by *Pan et al*.,[66] who also used carbon nanotubes as a confinement catalyst, as shown in figure 18. This studies, however, dealt with the tuning of redox properties inside these carbon nanotubes by utilising their unique electronic properties. Thereby, iron oxide was implemented into CNTs with varying diameters. They observed that the auto-reduction, which these iron particles can undergo, benefited by encapsulation. This was explained by the better electronical stabilisation of iron in its metallic state in comparison to the iron oxide. In the redox-cycle of iron-oxide to metallic iron, with subsequent reoxidation to iron oxide, the reduction is more favoured than without the carbon nanotubes due to the additional product-stabilisation, but the reoxidation is less favoured, since the substrate is now more stable than in the bulk.[66]

The molecular enrichment effect is the last subtopic of confined spaces benefitting reactions inside them. Thereby, the local concentration of substrates inside the host-complex, shown in grey in figure 20, is significantly increased than in comparison with the reaction in the bulk. As a result of this, the substrates, shown in green and purple in figure 20, can interact faster, once they are both encapsulated in the host-complex, leading to a major increase in the reaction speed.

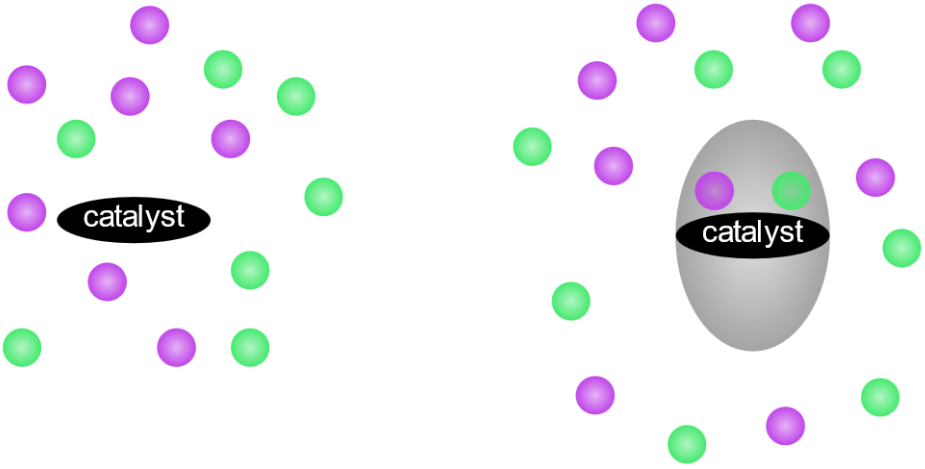

Figure 20: Local concentration with (right) and without confinement (left) of substrates (green and purple) inside a supramolecular cavity (grey).

But not only the local concentration of substrates is higher, they are also in a certain orientation, benefiting the formation of specific transition state geometries enabling the controlled formation of a specific product.[63]

The second major aspect, which alters reactions inside molecular flasks, is the formed microenvironment around the active centre. This not only separates the guests from non-encapsulated compounds, but also provides a changed polarity due to the mostly hydrophobic host-walls. Additionally, the inside of the supramolecular host can only be accessed *via* pores in the outer shell, limiting not only the size of possible guests but also their three-dimensional orientation due to different bulkiness. This substrate selectivity is of major importance in enzyme catalysis, since biological system provide a significantly more versatile set of compounds which can undergo the respective conversion. But as the catalysis should only proceed with particular substrates, it is necessary to restrict the amount of substrates which can be converted by the catalytic system. In synthetical chemistry this substrate selectivity can also be used in cascade reactions which will be discussed in chapter 4.4. The pore size not only limits potential substrates but also contributes to the shielding effect of the host shell. Except the pore size and orientation, the encapsulation can also be limited by the size and shape of the 'free' volume inside the host. This can not only limit size and shape of substrates but also their orientation to each other, introducing the topic of preorganisation.[67]

4.3 Preorganisation and shape complementarity

The concept of preorganisation can be divided into two distinct types, both of which find analogies in enzymatic catalysis. Enzymes have evolved preorganisation to an extraordinary degree, using it to increase the efficiency, selectivity and speed of biochemical reactions significantly. However, as introduced with the induced fit model in previous chapters, the design of a supramolecular host remains despite the versatile models challenging.[68]

The first type of preorganisation involves the structural formation of the catalytic environment, more specifically, the active centre and its immediate surrounding, the enzymatic pocket. In enzymes, this well-defined microenvironment provides a space that orientates functional groups, shields the reactive centre from external interference and promotes reaction specificity, as discussed in previous chapters. In synthetic systems, this concept is replicated through the design of supramolecular host complexes. These offer confined cavities with a defined shape and size that mimic enzymatic pockets and serve as a molecular flask, providing distinct local reaction sites. Their structural rigidity and spatial precision allow an effective substrate recognition and transition state stabilisation.[68]

The second type of preorganisation relates to the orientation of substrates within the catalytic cavity. When a substrate binds to a preorganised active site, its spatial orientation is constrained, allowing a special alignment of reactive groups. This not only lowers the activation energy of enzymatic catalysis but also drastically influences the selectivity of the formed

intermediate and thereby the product. By guiding substrates in distinct geometries enzymes as well as supramolecular catalysts can selectively form isomers which are otherwise inaccessible or just in minor amounts under conventional, bulk-phase conditions. This selectivity is especially important in many fields. For example, in drug development, in which enantiomeric purity can have profound consequences. Enantiomers of certain compounds can thereby exhibit vastly different biological activities, pharmacokinetics or toxicological profiles, making precise control over stereoselectivity essential.[69]

An example of this dual-level preorganisation can be found in the work of *Sanders* and co-workers, employing a zinc(II)porphyrin-based host to catalyse the *Diels-Alder* reaction. In this system, both dienophile and diene are equipped with pyridine-groups, able to coordinate to the zinc ions of the host-complex.

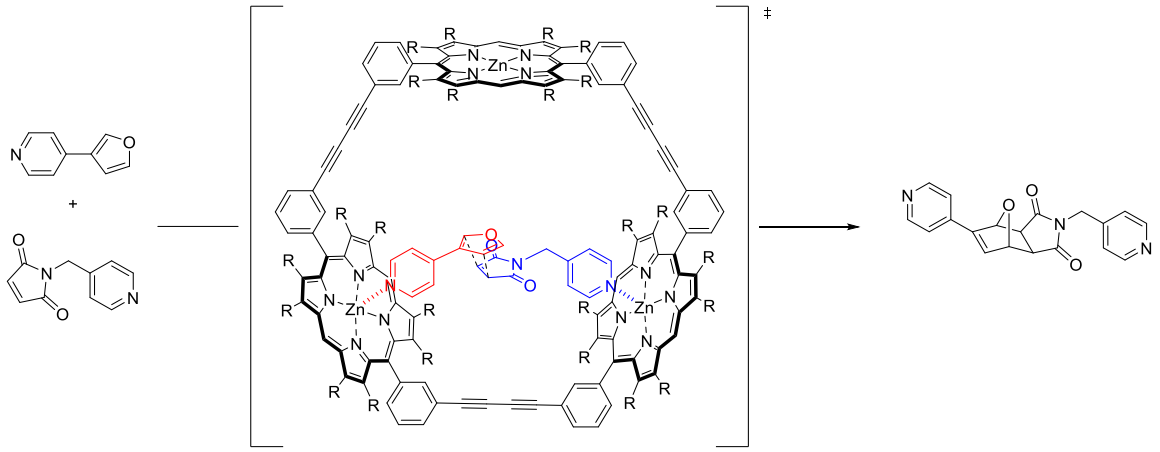

Figure 21: Substrate preorganisation in a zinc(II)-porphyrin based tricyclic nanoreactor.[68,70]

This coordination fixes the substrates in a specific orientation and distance within the cavity, enforcing a spatial arrangement that favours one particular reaction pathway. The result is the highly selective formation of the exo-product, shown in figure 21 on the right, whereas the uncatalysed reaction typically yields a mixture of the endo- and exo-products. Without the supramolecular catalyst, such selectivity could only be achieved under harsher conditions such as significantly increased temperatures.[68]

This illustrates how precise spatial control of guest molecules within a host can not only stabilise the transition state but also predefine its entire geometry. This transition state-like preorganisation offers an additional rate enhancement that surpasses the acceleration due to close proximity of the reaction partners as described in previous chapters.[70]

In 2016 *Rebek* and co-workers published the vase-shaped molecular capsule shown in figure 22. This is able to support the cyclisation of different substrates while enabling distinct control of the formed product due to two factors which determine the structure of the transition state.[71]

First, the polar imidazolidin-2-one moieties on the rim of the capsule ensure not only a good solubility in aqueous media, but also can coordinate polar groups of the guest molecules as shown in figure 22. In this example a flexible alkane-chain with amine-groups at both ends is encapsulated. Thereby, the polar amines coordinate to the polar rim and the non-polar chain orientates itself along the walls and bottom of the capsule. This fixed position of the guest inside the cavity allows only certain reaction pathways since the movement, and thereby, the interaction sites, are rather limited.[71]

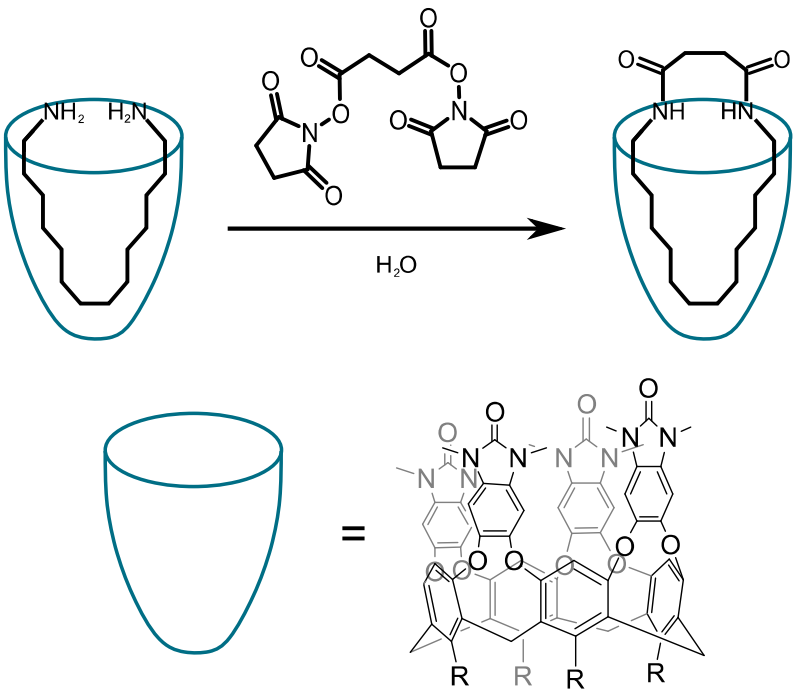

Figure 22: Preorganisation in an U-shaped molecular flask with R = 3-methyl-1-propyl-imidazole.[71]

The second factor is the complementarity in shape and functionalities which can benefit encapsulation and subsequent conversion even further. The importance of shape complementarity was already highlighted, by showcasing the impact on supramolecular assemblies. The relevance of shape and size complementarity is displayed by performing the cyclisation experiment shown above with different chain-lengths. In the respective publication *Rebek et al*. tested C_{11}-, C_{12}-, C_{14}- and C_{16}-chain lengths with and without the presence of the cavitand, for what the results are summarised in the following table.[71]

Table 1: Amino acid syntheses from diamines and succinic anhydride.[71]

yields [%]			
diamine	**without cavitand**	**with cavitand**	**improvement factor**
C_{11}	26	64	2.4
C_{12}	27	71	2.6
C_{14}	34	61	1.8
C_{16}	34	64	1.9

These experiments show on the one hand an increased yield without cavitand for longer alkyl-chains. *Rebek et al.* explained this with the improved solubility of the shorter amines C_{11} and C_{12} in water, enabling background reactions in bulk without the presence of the cavitand which are limited for longer chain lengths.

On the other hand, in the presence of cavitand not only a significant increase of the yield can be observed but also the maximum improvement at a chain length of C_{12}. This allows the assumption that from this length on the chains are too long to adapt a good fit inside the cavity, forcing the substrate to adopt a strained coiled conformation which makes the formation of the host-guest complex less favourable.[71]

4.4 Dynamic and adaptive catalytic systems

The previously introduced insights in the formation and application of supramolecular host-guest systems can be further used to design even more complex systems as adaptive systems responding to certain stimuli.

Light is one of the most prominent types of stimuli used in chemistry. Once again, nature can be seen as the inspiration behind photochemistry, given that light is a widely utilised energy source in several different natural processes. The most obvious example is the photocatalytic conversions performed by chlorophyll molecules. In supramolecular chemistry, light energy can either benefit the cage formation itself or alter the cages' structure once it formed.[72] This stimulus induced alteration can occur in three different types. First, the building blocks of the assembly can undergo a geometry change, leading to a distortion of the overall structure. This method is the most common one for supramolecular frameworks which are applied further on as for example in catalysis. Thereby, upon irradiation with light, the cavity inside the complex can be changed in its size, form and polarity, enabling easy changes in the reactions surrounding provided by the molecular flask.[72] This can even lead to a switching behaviour in which the supramolecular aggregate can only act as a host after irradiation with light of a certain wavelength and can be switched off upon irradiation with a different wavelength,

terminating its function as a host molecule thus, allowing spatial-temporal control of the catalysis.

Mandolini et al. introduced a similar case, in which a bis-barium complex of an azobis-(benzo-18-crown-6) ether is applied as a photo-switchable supramolecular catalyst. With light of either 370 nm or 480 nm the diazo-bridge connecting both crown-ethers can be switched between its *trans* and *cis*-state as shown in figure 23.[73]

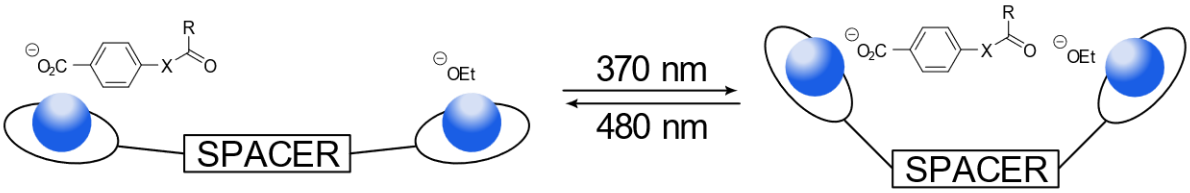

Figure 23: Photo switching between trans and *cis*-state of supramolecular complex with X = N(Me)/O.[73]

As depicted above, only the *cis*-state (right) is catalytically active in the basic ethanolysis of esters and anilides since both reactants are brought into close proximity, as in the *trans*-state they remain separated. This allows the controlled on- and off-switching of catalytic activity.[73]

The second type of stimuli response is the disassembly of a supramolecular architecture into the respective building blocks. This process describes the counterpart of how light of a certain wavelength benefits the formation of supramolecular complexes since light of another wavelength often leads to the inversion of this route. Thus, complex formation can be controlled even better allowing the purposeful assembly or disassembly. Especially in terms of product inhibition this allows a potential solution to the high binding affinity some products may show inside the complex.[72]

Severin et al. published an example for this method in 2018 in which a metastable-state photoacid, which is able to transfer a proton upon irradiation, is added to metallosupramolecular assemblies, combining photo- and pH-sensitivity. Upon irradiation with violet light a proton is transferred from the acid to the ligand and since the protonated ligand cannot participate in the complex anymore the aggregate disassembles, as shown in figure 24. This enables controlled guest release from the cavity and because the complex reassembles in the dark the process can be repeated multiple times Since product inhibition is a severe drawback of supramolecular catalysis and is mainly prevented by strictly chosen reaction pathways and a restricted substrate scope, limiting potential applications drastically, the application of supramolecular aggregates, as the one presented by *Severin et al.*, can be a potential solution to this problem.[74]

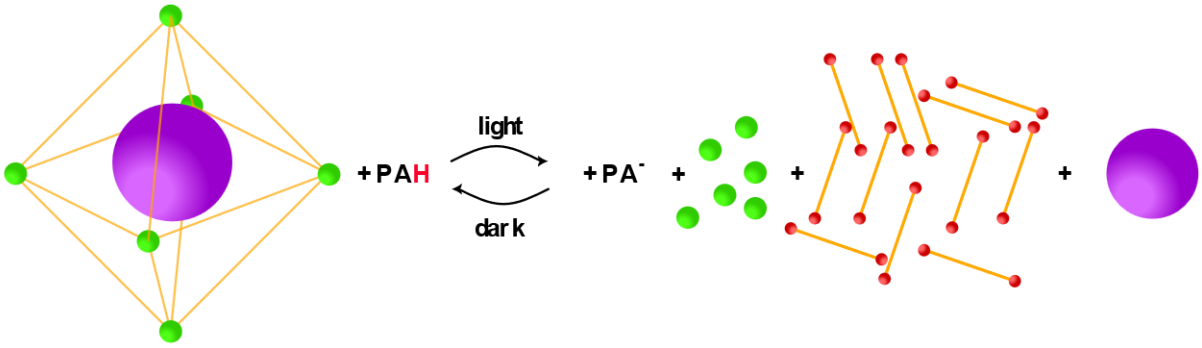

Figure 24: Supramolecular photoacid octahedron with pyridyl ligands (orange), Pd^{2+} corners (green) and a guest (purple).[74]

The last type of stimuli response is a combination of the previous two kinds in which, upon irradiation with light of a certain wavelength, the existing aggregate disassembles and is reassembled in a different structure. This often takes place in assemblies consisting of different ligands providing the same or similar binding motifs in varying sizes.[72]

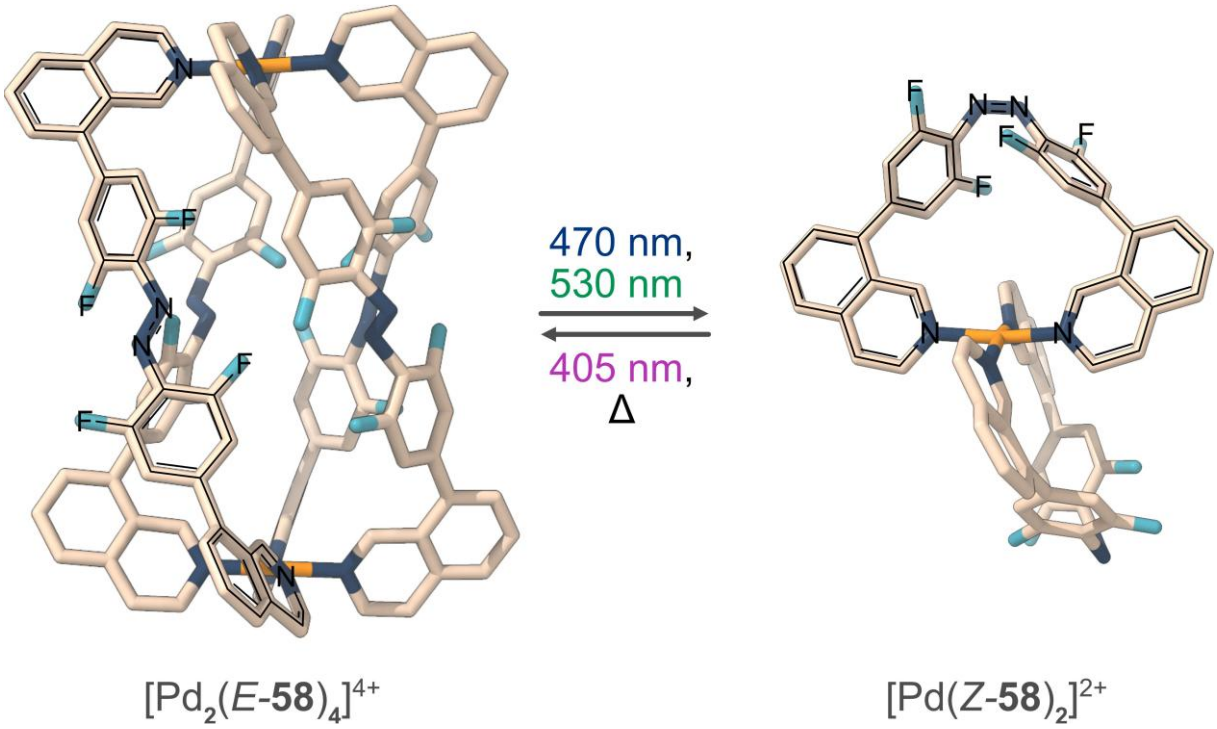

Figure 25: Palladium complex published by *Sessler et al.* which changes composition upon irradiation with light of different wavelengths.[72]

The ultimate goal of adaptive supramolecular catalysis, additional to gain precise control over reactivity and the outcome of the catalysis by stimuli responsive systems, are cascade reactions in which multiple catalysts are combined with one single substrate, performing multiple catalytic steps after each other without the necessity of purification in-between.

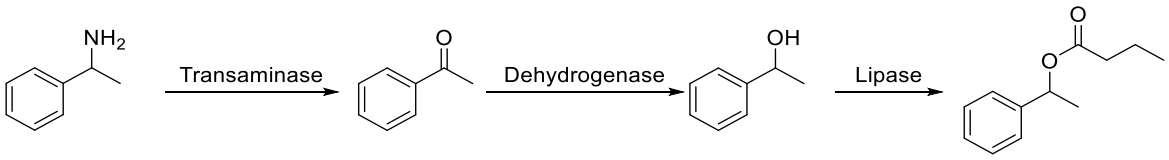

Figure 26: Enzyme catalysed cascade reaction.[75]

Once again, the inspiration originates in natural processes where enzymes are already performing these types of catalytic processes, as shown exemplarily in figure 26.[75]

Fujita et al. established a supramolecular approach to this type of catalytical cascade. They synthesised two $Pd_{12}L_{24}$-supramolecular catalysts, with incompatible functional groups, a TEMPO residue to perform an oxidation of a terminal alcohol function to the respective aldehyde and a *McMillan* organocatalyst which subsequently transforms the intermediate aldehyde. This is only possible because the supramolecular spheres prevent the two catalytic centres to directly interact with each other.[76]

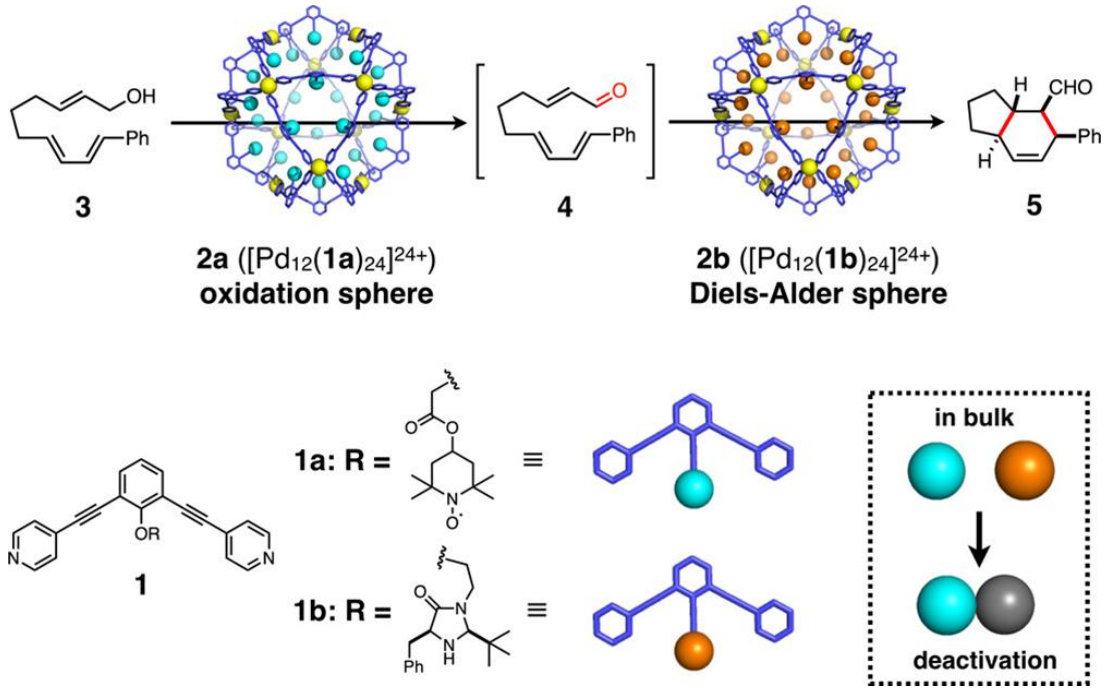

Figure 27: Supramolecular cascade catalysis with two $Pd_{12}L_{24}$ spheres.[76] Reprinted with permission from the *American Chemical Society*.

Systems like this are extremely hard to design since an enormous amount of detailed planning is necessary as each substrate has to be encapsulated only in the respective catalyst with proper release of the formed product. The potential of cross reactions is drastically increased compared to a supramolecular catalysis with only one catalytic system but also is this kind of catalysis highly desirable due to its drastic increase in efficiency.[76]

5. Porphyrin-based catalytic structures

Porphyrin-based spatially controlled catalysis represents a powerful combination of the well-defined, tunable properties of porphyrins, introduced in chapter 2, and the efficiency and selectivity of distinct assemblies as host-guest architectures, metal-organic frameworks (MOFs), and covalent picket-fence porphyrins. Researchers have developed catalysts mimicking enzymatic behaviour achieving drastically increased selectivity and control, while benefiting from cooperative effects and environmental responsiveness. The ability to coordinate a wide variety of metals, combined with the possibility of fine-tuning their properties by substitution or integrating secondary binding motifs, enables the creation of multifunctional catalytic systems. These systems have been applied in, among other topics, oxidation, photo-redox and small-molecule activation reactions offering a modular approach designing catalysts that benefit from both molecular precision and supramolecular adaptability.[77]

5.1 Metalated porphyrins in non-supramolecular catalysis

Porphyrins are utilised in a variety of catalytic applications in numerous forms. They can either be employed as catalysts on their own, already discussed in chapter 2.2, as picket fence porphyrins, in metal-organic frameworks or as supramolecular catalysts.

The term of picket fence porphyrins was first introduced by *Collman et al.* in 1975 during their studies on the oxygen transport mechanism of heme-porphyrins. Their work emphasised that not only the catalytically active porphyrin-core but also the surrounding protein environment plays a crucial role by physically shielding the active metal centre. They observed that the reactivity of the metal ion in natural systems, like haemoglobin, are tightly regulated by amino acid residues forming a protective “fence” around the active site.[78] Following, picket-fence porphyrins have been developed with a wide range of substituents to tailor steric and electronic properties. These modifications can either introduce steric bulk that hinders stacking of porphyrins, which enhances solubility or the selectivity towards smaller substrates in the respective catalysis. Furthermore, many picket-fence derivatives incorporate functional groups capable of additional coordination motifs, facilitating secondary coordination sphere effects, as discussed in chapter 4. In catalysis, picket-fence porphyrins have proven especially useful in mimicking enzymatic oxidation reactions, as for example the iron porphyrin, shown in figure 28,

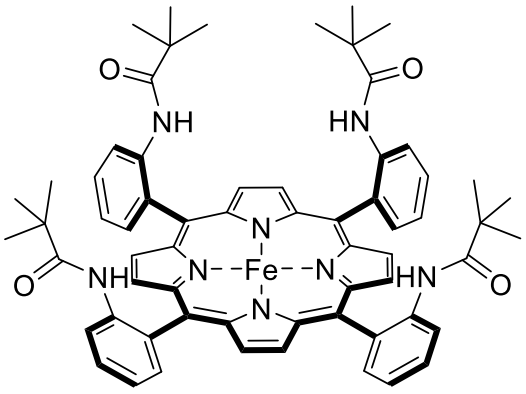

Figure 28: Exemplary structure of a picket fence porphyrin

which has been employed in oxidation reactions, mimicking cytochrome P450s. These structures exhibit controlled binding and activation of elemental oxygen allowing effective oxidations under mild conditions.[79]

Porphyrin based metal-organic frameworks (MOFs) are a distinct class of porous crystalline materials, combining the well-defined coordination chemistry of porphyrins with the structural tunability of MOFs. Thereby, the rigid, planar macrocycles of porphyrins are excellent to build up MOFs with strong metal-chelating affinities. The porphyrins not only contribute to the framework's stability but also to catalytic, photochemical and electronic properties.

Suslick et al. published such a porphyrin-based MOF in 2005 aiming to form exceptionally robust frameworks which can be applied as catalysts. Due to the high thermal stability of metalloporpyhrins and their ability to remain in their distinct coordination even after loss of surrounding solvents, they are highly suitable building blocks for such projects.

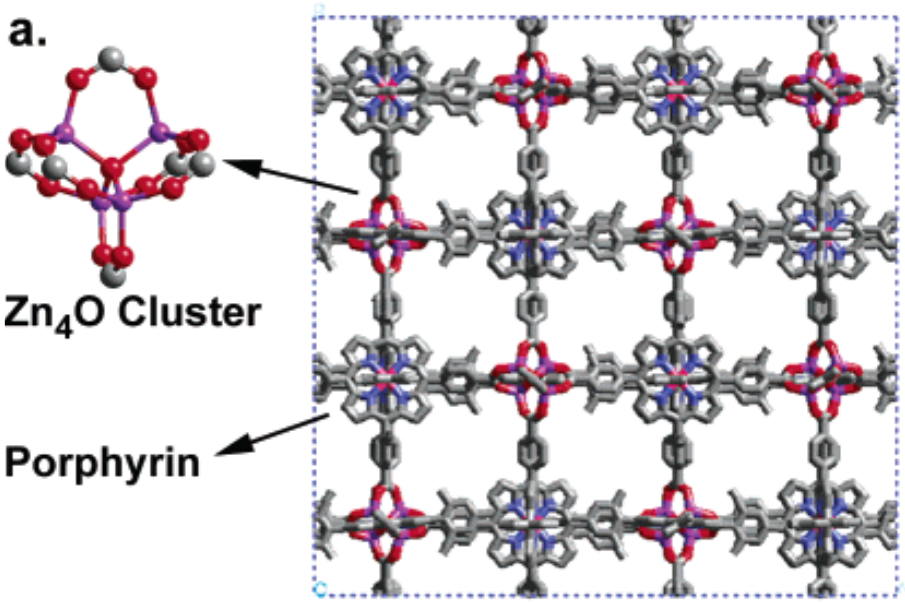

Figure 29: MOF from zinc porphyrins with ZnO_4 clusters by *Suslick et al*.[80] *Reprinted with permission from the American Chemical Society.*

In the respective work they highlighted the selecetivity towards the shape and size of guest induced by pores of different dimensions. Additionally, the presented MOF was applied in hydrocarbon oxidations in which the framework acted as a robust heterogeneous catalyst.[80]

5.2 Porphyrin-based supramolecular catalysts

Porphyrins are also often found in supramolecular catalysts analogous to their use as building blocks in MOFs. Because of their flat structure they are often employed in cubic assemblies, as e. g., published by *de Bruin et al.* in 2013, shown in figure 30.[81]

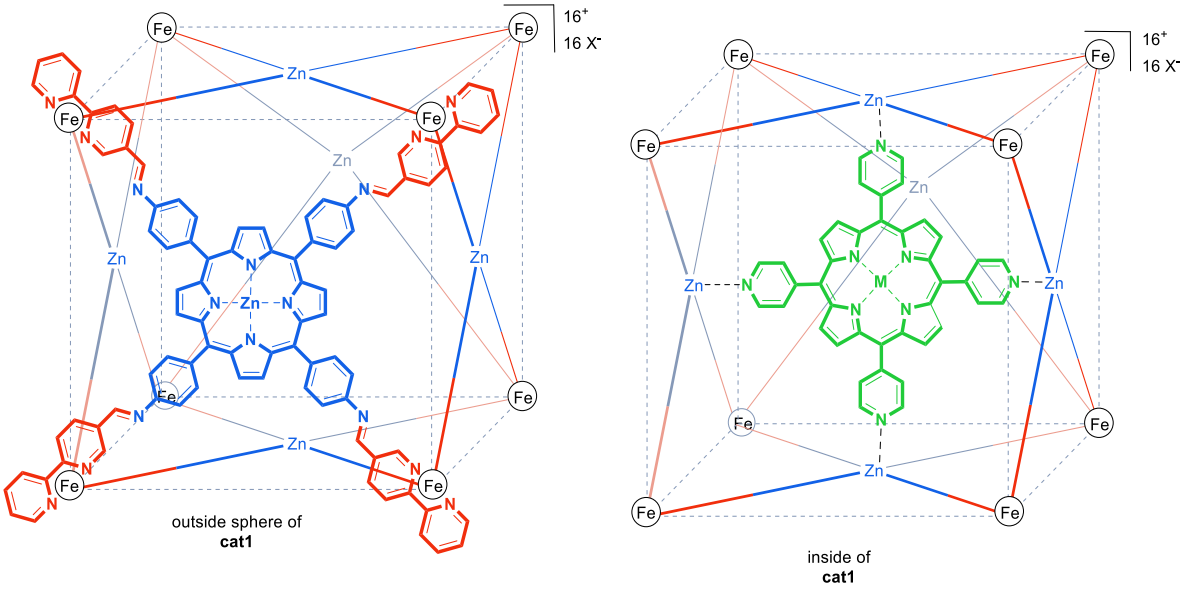

Figure 30: The outer sphere of the supramolecular cube **cat1** (left) with catalytical active metalloporphyrin inside (right).[81]

In this structure two different porphyrins are utilised, one to form the faces of the cubic host and the second one as the actual catalyst coordinated to the inside of the cube. In the respective work, *de Bruin et al*. introduced the synthesis *via* subcomponent self-assembly, whereby either the cube with the catalytically active porphyrin inside can be formed directly, using the benefiting template effect or without the inner porphyrin to form the "empty" **cube1** which can be modified afterwards. This catalyst was employed in the cobalt-catalysed cyclopropanation of styrene, whereby the yield was increased from 7% with the cobalt-tetrapyridineporphyrin (**Co-TPyP**) without the cubic host to 50% using the supramolecular catalyst even with low catalyst loadings as 0.8 mol%.[81]

In following studies, the counterion was exchanged from triflate to triflimide leading to a drastically enhanced solubility, allowing different solvents in the respective catalysis. Moreover, size selectivity studies were performed, showing that even larger substrates like 2-vinylnaphtalene and ((4-vinylphenyl)methylene)dibenzene can be converted by the supramolecular catalyst shown in figure 30. Furthermore, the already low catalyst loading of 0.8 mol% could further be decreased to 0.25 mol% still yielding up to 88% product, corresponding to a turnover number (**TON**) of 351. These results will be discussed further in later chapters, comparing them to the content of this work.[82]

6. Motivation and objective

Based on the work on porphyrin-based supramolecular catalysts by *de Bruin et al.*, the present study aims to investigate the limits of supramolecular catalysts, particularly in terms of functional group tolerance and the conversion of non-terminal alkenes. Since supramolecular catalysis in confined, well-defined spaces has proven to be a promising method to achieve enzyme-like selectivity and rate enhancement. However, the limits of such systems, especially when introduced to sterically challenging or electronically diverse substrates, remain rather unexplored. Understanding these limitations is crucial for translating supramolecular concepts into a broader application in synthetic chemistry.

In this work, the porphyrin-based supramolecular catalysts shown in figure 30 and also a structurally modified analogue, previously introduced by *de Bruin* an co-workers in 2021, shown in figure 31, are synthesised.[83]

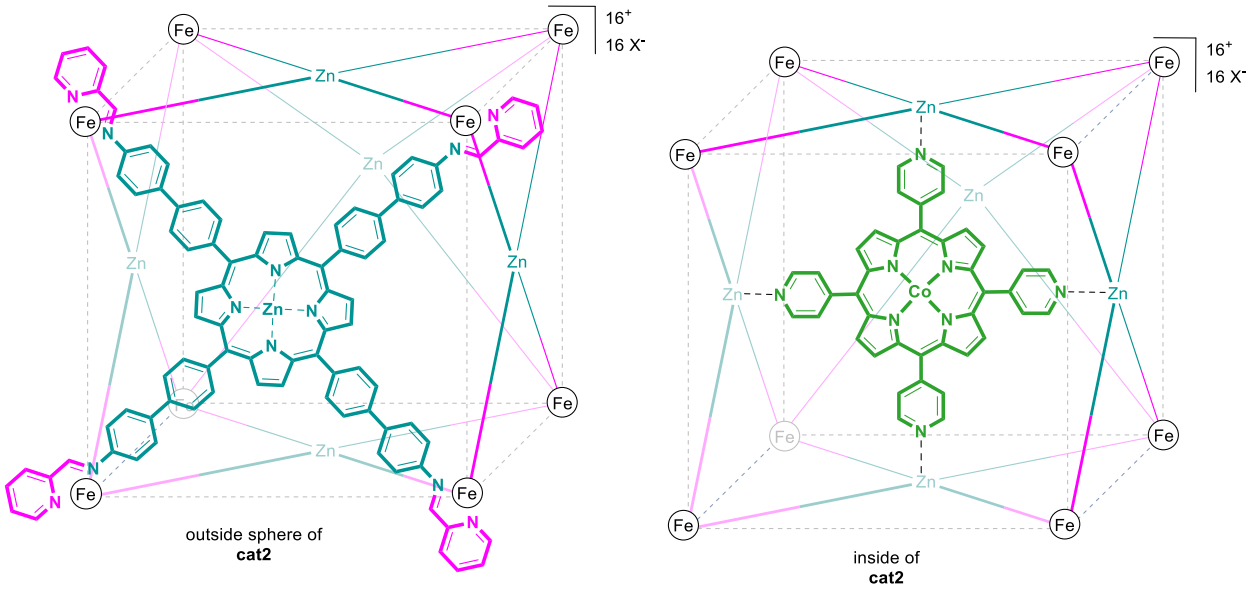

Figure 31: Porphyrin-based supramolecular catalyst utilised in this work.

Both catalysts are assembled from their respective molecular building blocks *via* subcomponent self-assembly, affording a well-defined architecture capable of hosting catalytic conversion inside their confined cavities. The cobalt porphyrin core thereby acts as a catalyst for cyclopropanation reactions, while the surrounding supramolecular framework introduces spatial control, restricted substrate access and a distinct microenvironment around the active site. Such confinement effects are known to strongly influence the reaction pathway, stabilise reaction states, by e.g., preventing the dimerisation of active intermediates in the

cyclopropanation of styrene derivatives and enable selective transformations that may not occur under bulk-phase conditions. These effects shall be investigated further in this study.

Following successful complexation and characterisation of the supramolecular systems, cyclopropanation reactions are chosen to evaluate their catalytic performance. They represent a sensitive test reaction because they require precise control of both substrate orientation and carbene transfer reactivity. Reaction parameters such as solvent, temperature and the concentration of each substrate are systematically optimised to identify conditions that maximise conversion and selectivity.

Once suitable reaction conditions are found, the cyclopropanation of various styrene derivatives is carried out to test the influence of electronic effects of different substituents and substitution patterns on catalytic efficiency and selectivity. Therefore, electron-donating and electron-withdrawing groups at different positions of the aromatic system were used to gain further insights on how the supramolecular pocket interacts with the reaction.

To further investigate the versatility of the system, non-terminal alkenes are added to the substrate scope. The cyclopropanation of such internal double bonds presents a more significant steric challenge and thereby displays spatial restrictions of the supramolecular system. Observing, whether more complex substrates can enter the cavity and are transformed efficiently provides valuable information about the adaptability of these systems.

Finally, a series of control experiments is performed to determine the origin of the observed catalytic activity. These include reactions with the individual building blocks, employed as catalyst, and partially assembled supramolecular systems. Comparing these results allows the distinguishing between true supramolecular catalysis, where the host-guest architecture actively benefits the reaction and non-specific background catalysis. Through these systematic investigations, this work aims to provide a more detailed understanding of how the confinement within porphyrin-based supramolecular catalysts influence activity, selectivity and the substrate scope, ultimately contributing to the rational design of next-generation enzyme mimics.

7. Retrosynthetic pathways

The synthesis of the supramolecular catalyst published by *de Bruin et al.* in 2013 consists of three convergent syntheses.[81] In this work the synthesis was modified slightly, as shown in the following retrosynthesis.

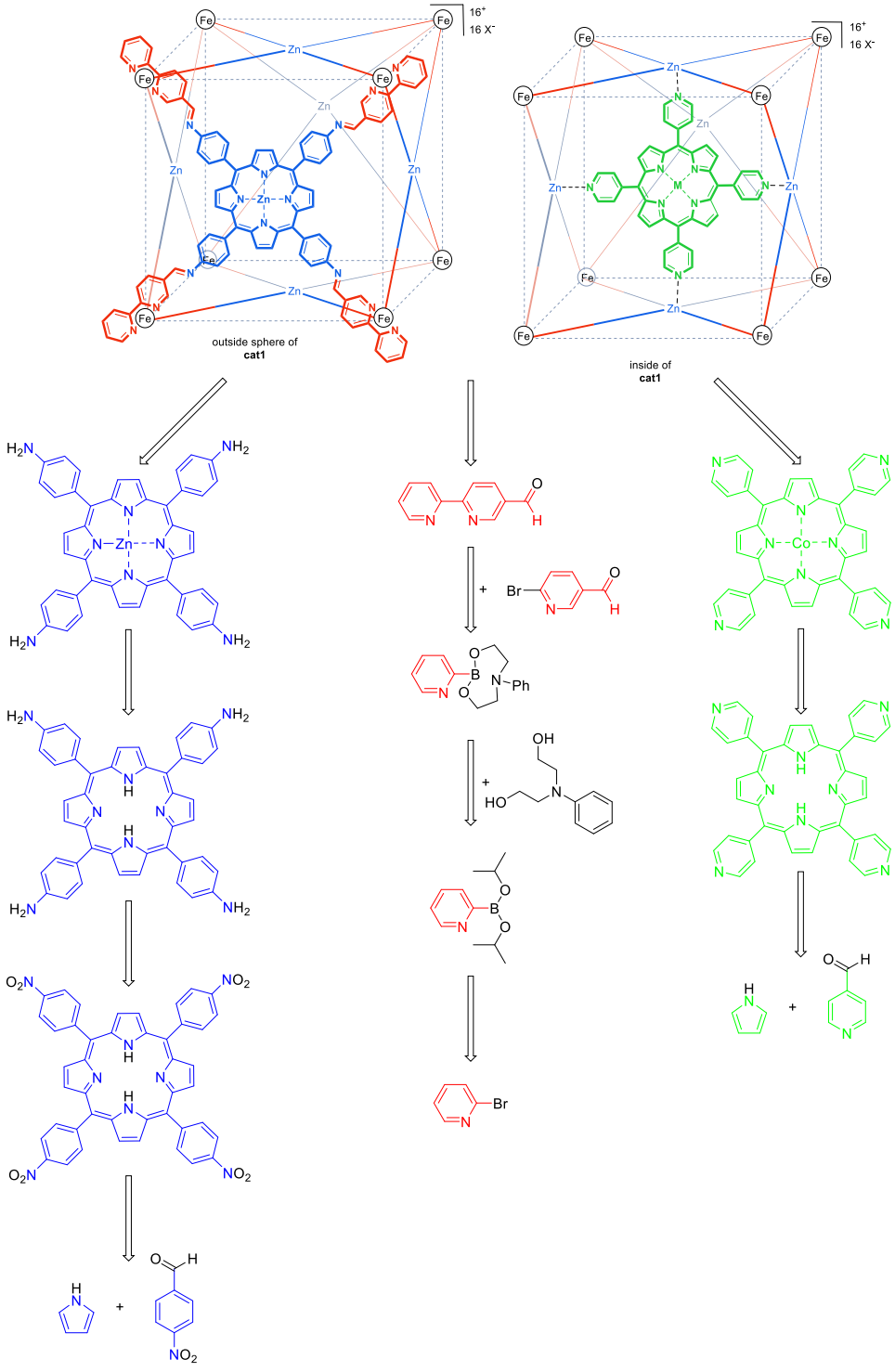

Figure 32: Retrosynthesis of the M_8L_6 supramolecular catalyst **cat1**.

The supramolecular host **cat1** consists of two building blocks, shown in blue and red in figure 32, which are combined with an iron(II)-salt in a subcomponent self-assembly process. Hereby, each aldehyde (red) is combined with one of the amine functions of the zinc-porphyrin (blue) in an imine-condensation, where the generally low stability of imins has to be considered.[84] The formation of the supramolecular host is thermodynamically favoured and the cubic geometry is predetermined by the coordination angle of each building block as well as their stoichiometry. In this system, eight metal-ions (black), six zinc-porphyrins (blue) and 24 aldehydes (red) are combined to form the host. *De Bruin et al.* observed the formation of the host without the catalytically active guest-porphyrin (green), as well as the direct synthesis of the filled cubic system in a one-pot synthesis.[81] The second approach is more promising, since the catalytically active cobalt-porphyrin acts as a template for the assembly, since it provides additional coordination sites, directing the zinc-porphyrins into the right position and distance respective to each other.

The zinc-porphyrin (blue) itself can be synthesised in three consecutive steps, first the nitro-porphyrin has to be formed with subsequent reduction to amine functionalities. The direct formation of the amine-porphyrin is not possible, because of potential interference of the amines during the porphyrin condensation. The last step is the metalation with zinc(II) acetate to provide the coordination sites at which the pyridine-porphyrin (green) will be attached in the assembly.

The bipyridine-aldehyde (red) was originally formed in a *Stille*-cross coupling but since tin-organic compounds are used, which are highly toxic, an alternative route was chosen.[81] The shown *Suzuki*-coupling is an alternative reaction, but also contains obstacles that must be overcome. Boronic acid esters of electron poor systems, as pyridines, are prone towards protodeboration. Especially, the *ortho*-position is disfavoured to bear boronic acid ester, which is necessary for this system. This problem was already addressed by the our group in 2010[85] by the formation of a stabilised boronic acid ester.

Here, the electron poor boronic acid ester is stabilised by the nitrogen atom, which can form an intramolecular dative bond to the boron atom. Advantageous is not only the comparably high stability of these boronic acid ester, making them bench stable for several months, but also their simple preparation in only two steps. Additionally, since the diisopropyl-pyridin-2-ylboronate is generated and transformed *in situ* to the respective boronic acid ester, no purification is required in between both steps.

The last compound is the catalytically active cobalt-tetrapyridineporphyrin (green) whose synthesis is similar to the first porphyrin, but since pyridines do not interfere with the porphyrin-formation, it can be synthesised in one step with following metalation.

An alternative supramolecular catalyst **cat2** has also been introduced by *de Bruin* and his group in 2021, which consists of similar components as **cat1**, shown in figure 33.[83,83]

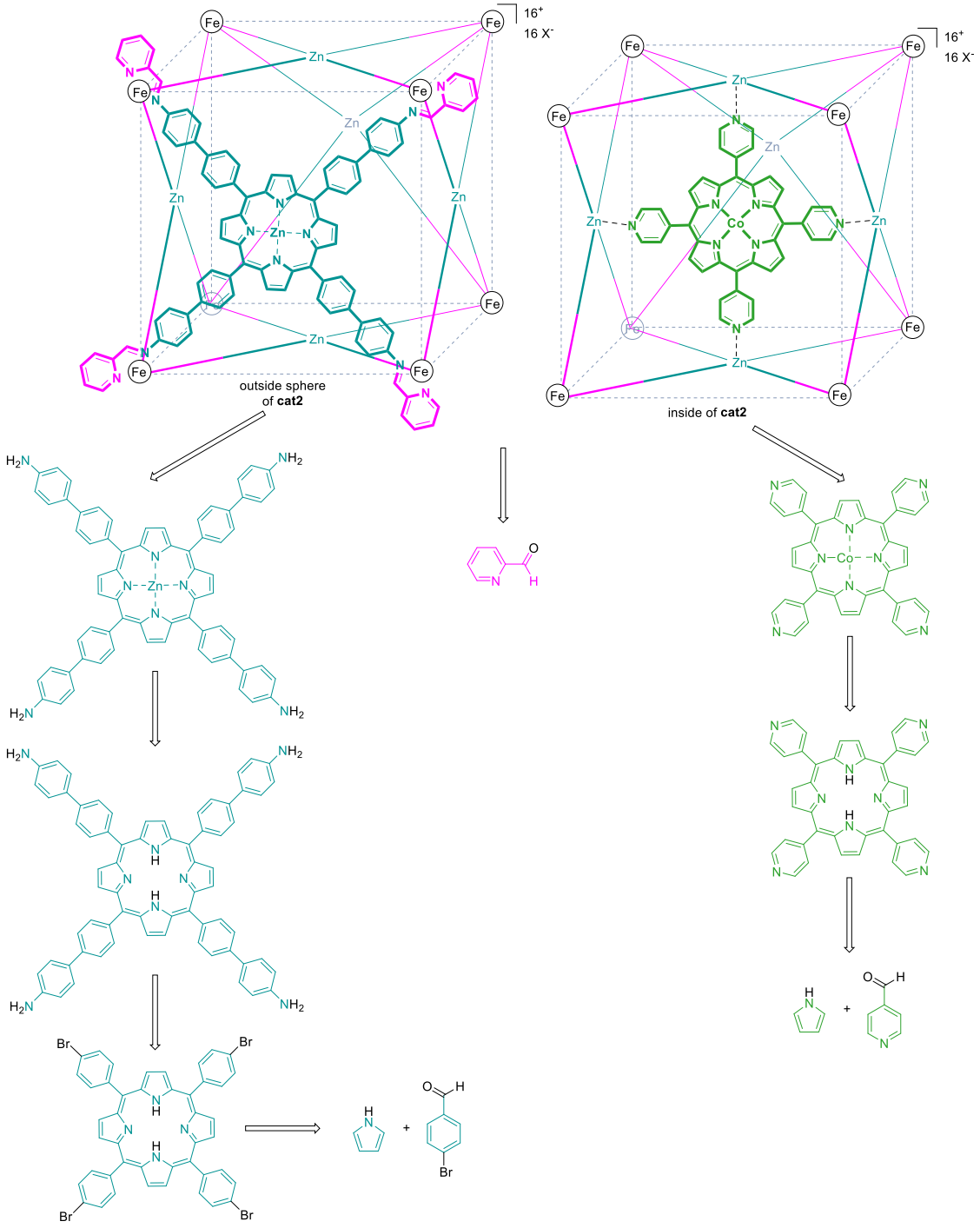

Figure 33: Retrosynthesis of supramolecular catalyst **cat2**.

However, in this new catalyst **cat2**, shown in figure 33, the imine, which is formed during the subcomponent self-assembly, coordinates to the iron-ions on the corners of the cubic host. Thereby, the rather labile imine-group is additionally stabilised and the formed complex should be more robust. Not only is the imine in this supramolecular aggregate better stabilised, but also the 2-pyridinealdehyde (pink) is significantly cheaper than the bipyridine aldehyde used in the previous cube. Hence, only two fragments have to be synthesised making this catalyst way more efficient when it comes to synthetic effort and more economic. The cobalt-porphyrin (green) is formed as already described in the previous retrosynthesis. The zinc-porphyrin, used to build the faces of the cube, can be formed in three consecutive steps, starting with the porphyrin-formation of the shown bromoporphyrin, followed by a *Suzuki*-cross coupling and lastly the metalation of the porphyrin with zinc(II)-ions.

In these systems a variety of different porphyrins are applied, which is why the synthesis of this substance class was investigated deeply. As already introduced in previous chapters, porphyrin-synthesis usually suffers not only from low yields (20%) but also from their poor solubility, resulting in a rather challenging purification. Hence, porphyrin-synthesis remained a developing field in the last century in order to find a synthesis and purification method providing porphyrins in higher yields, while still ensuring high purity. This issue was commonly addressed by application of transition-metal catalysts[40] which are often pricey. In order to keep the reaction as economic as possible, alternative pathways were approached.

8. Porphyrin synthesis and purification

One of the most commonly employed methods for porphyrin syntheses, was first reported by *Rothemund et al.*[36] in 1941, providing porphyrins in yields around 10%. This pioneering procedure was modified further by *Adler et al.*[37] and *Lindsey et al*.[38] *Adler's* adaptation, published in 1967, has become one of the most frequently cited in modern protocols.[86] This stems from the fact, that it is comparatively short, experimentally straightforward and generally produces porphyrins of high quality without requiring complex equipment.

The synthesis described in the following chapter is derived from *Adler's* procedure but with further modifications, aiming for an increased product yield while preserving high purity. In *Adler's* original method, equimolar amounts of pyrrole and the chosen aldehyde were dissolved in propionic acid and heated to reflux for 30 minutes, exemplarily shown in figure 34. The reaction mixture was then cooled to room temperature to allow the product to precipitate. The solid was then collected by filtration and subsequent washing with methanol and hot water.[86]

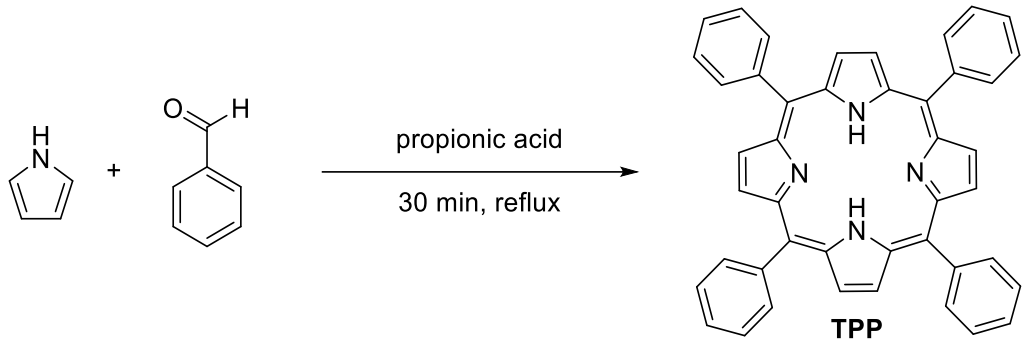

Figure 34: Synthesis of *meso*-tetraphenylporphyrin according to *Adler*'s protocol.[86]

In the present work, this classic method served as the starting point for further investigations and optimisation. During initial trials, it was observed that, although the filtrate appeared clear immediately after filtration, a secondary precipitate formed after resting for approximately 16 hours at room temperature. This indicated incomplete precipitation, which lowers the yield significantly. To address this, the reaction mixture was added to an excess of water upon reaching room temperature. The dilution of propionic acid under these conditions prevents it from protonating the porphyrin, a key factor, since potential peripheral substituents and the "inner" nitrogen atoms can be protonated. Such protonated porphyrins are water-soluble salts, which remain in solution and thereby escape precipitation.

Following the dilution, the mixture was stored overnight in a refrigerator. The lower temperature further reduces porphyrin solubility, while the extended resting time allows for thorough

precipitation before filtration. Depending on the particle size of the formed precipitate, some porphyrins may require multiple filtrations to completely recover the product due to the formation of very fine particles, which are not collected in the first filtration. In these cases, it can be advantageous to return the filtrate to cold storage for an additional night to check for further particle formation.

The washing stage must also be adjusted for each porphyrin, as solubility varies with the nature of the substituents. While *Adler's* protocol describes methanol washing for the tetraphenylporphyrin **TPP**, some other porphyrins are partially soluble in methanol, leading to reduced yields if this solvent is used to wash the sample.

Finally, it should be noted that porphyrins possess characteristic fluorescence and frequent monitoring of this property throughout the work-up is an especially useful strategy to ensure maximal product recovery. This not only aids in yield optimisation but also provides a quick, non-substance-consuming indication of product presence in various fractions.[19]

In the present work three porphyrins were used for the supramolecular assemblies shown in figure 32 and 33, summarised below.

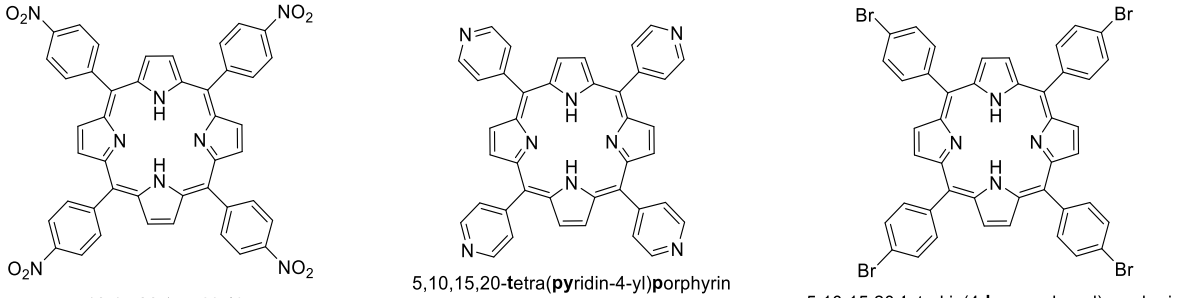

Figure 35: Summary of porphyrins used in supramolecular assemblies.

Except for the previously described modifications each porphyrin synthesis was tailored even further to the properties of the respective porphyrin.

5,10,15,20-tetrakis(4-nitrophenyl)porphyrin (TNPP)

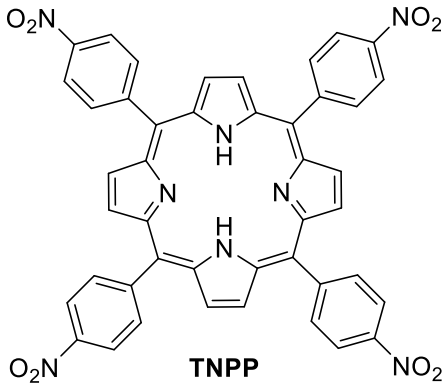

Figure 36: Structure of **TNPP**.

The synthesis of tetra-nitrophenyl porphyrin (**TNPP**) was initiated according to *Alder's* procedure, with the previously described modifications in the precipitation process. In addition to the standard washing steps with water and methanol, an extra washing stage with ethyl acetate was introduced, each solvent being used until the filtrate appeared colourless. Given that side-products from porphyrin syntheses, as well as the porphyrins themselves, are frequently intensely coloured, their presence is easily detectable with the naked eye. After these washing steps, ^{1}H-NMR analysis showed additional signals, not related to the product. Therefore, the solid was recrystallised from pyridine with subsequent storage in the refrigerator overnight. Afterwards, the formed precipitate was filtered and washed another time with water, methanol and ethyl acetate. This decreased the amount of by-products but, in order to generate a higher purity, the solid was mixed with acetone and refluxed for 30 minutes. After cooling to room temperature, the mixture was poured into an excess of water and stored again in the fridge overnight. Afterwards, the formed solid was collected by filtration and washed with water, methanol and ethyl acetate. Finally, the product was dried under reduced pressure. By these modifications to the standard procedure the yield was increased from 23%[87] to 70% with a high purity proven by NMR and elemental analysis.

5,10,15,20-tetrakis(4-pyridin-4-yl)porphyrin (TPyP)

The tetrapyridylporphyrin **TPyP** was also synthesised according to the modified procedure introduced beforehand. Here, longer reaction times than the previously applied 30 minutes proved beneficial, leading to an optimum yield after 2 hours, as shown in table 2. This is in contrast to *Adlers*' statement in his publication from 1967 that longer reaction times generally decrease the yield of porphyrins.[37]

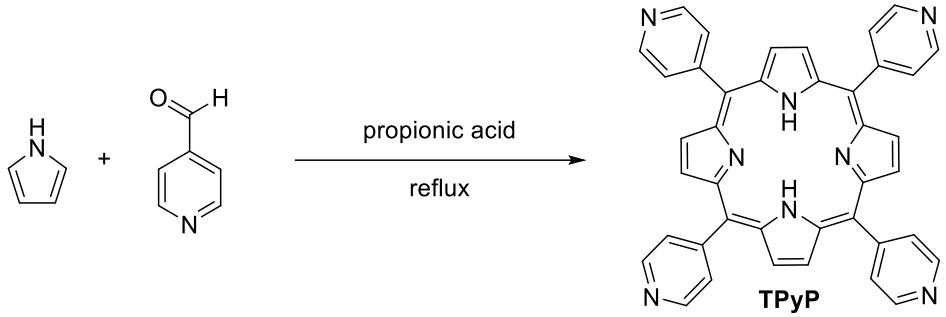

Table 2: Screening of reaction times at 0.2 M concentration for **TPyP**.

time	concentration	yield
30 minutes	0.2 M	32%
2 hours	0.2 M	51%
3 hours	0.2 M	49%

In the experiments summarised in table 2, a concentration of 0.2 M, respective to both substrates, is employed, consistent with the original method described by *Adler*. The results show, that the formation of this porphyrin is not complete after 30 minutes, as the yield increases significantly when the reaction time is extended to two hours. However, extending the reaction further to three hours aligns with *Adler's* observations, showing that while the yield does not improve, the NMR analysis indicates a decrease in the purity of **TPyP**.

Following this, the effect of substrate concentration on the synthesis was investigated more systematically. Given the limited solubility of porphyrins, it was hypothesised that higher dilution could facilitate their formation. Consequently, the reactions were repeated at lower concentrations of 0.07 M and 0.0002 M to explore this possibility and optimise the reaction conditions.

Table 3: Screening of reaction times at 0.07 M and 0.002 M concentration for **TPyP**.

time	concentration	yield
1 hour	0.07 M	3%
2 hours	0.07 M	10%
3 hours	0.07 M	21%
1 hour	0.002 M	-
2 hours	0.002 M	5%
3 hours	0.002 M	17%

Higher dilution is thereby lower yielding, with progressively decreasing yields from 51% (2 hours with 0.2 M) to 10% (2 hours with 0.07 M) and 5% (2 hours with 0.002 M). However, the reaction proceeds longer at lower concentration, shown by the increasing yield even after 2 hours. At a concentration of 0.2 M the reaction reaches completion after 2 hours, while at a concentration of 0.07 M a significant increase from 10% yield after two hours to 21% after three hours can be observed. This trend becomes even more clear at the most diluted concentration of 0.002 M, at which the yield increases from 5% after two hours to 17% after three hours. This discussed the constant movement speed of molecules at a certain temperature. With higher dilution which corresponds to fewer particle in the solution, the molecules need longer reaction times to meet each other and thereby, to interact.[88] Hence, the elongation from two to three hours is still increasing the yield, even though it is still considerably lower than the corresponding synthesis using the higher concentration of 0.2 M. Hence, one should generally consider this option for the synthesis of individual porphyrins as the difference might be significant. Further dilution to 0.002 M leads to an even greater reduction in yield, with no detectable traces of the desired porphyrin in the NMR after one hour. After two hours, 5% yield is observed, increasing to 17% after three hours. This again demonstrates that, at higher dilution, the reaction requires a longer time to proceed and the optimal outcome might not be reached in the content of this study.

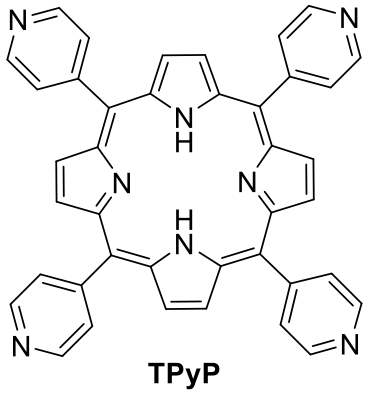

TPyP

Figure 37: Structure of **TPyP**.

To optimise the formation of **TPyP**, slight modifications are required. During porphyrin formation, the pyridine substituents are readily protonated by propionic acid, which hampers complete precipitation, and thereby, reduces the overall yield. To address this, the reaction mixture, after refluxing for the respective reaction time, is allowed to cool to room temperature and subsequently added to a saturated sodium bicarbonate solution rather than water. This step, neutralises the propionic acid and deprotonates the pyridine groups, enabling proper precipitation when the solution is rested in

the fridge overnight. This modification was applied in all previously discussed experiments as well as for every other porphyrin containing pyridine moieties.

The washing step is again another critical stage, as the choice of solvent must be tailored to the specific porphyrin. Using an unsuitable solvent bears the risk of dissolving the product, and thereby, drastically lowering the yield. For **TPyP**, small amounts dissolve in methanol, which is evident from the characteristic red fluorescence of the methanol extract typical of porphyrins. Consequently, **TPyP** was washed exclusively with water. However, subsequent NMR analysis indicated that the product's purity was insufficient. This can be overcome by applying a novel purification-method for porphyrins, which will be described in a later chapter.

5,10,15,20-tetrakis(4-bromophenyl)porphyrin (TBrPP)

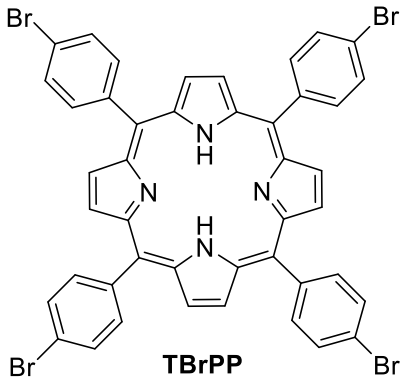

Figure 38: Structure of **TBrPP**.

The synthesis of **TBrPP** was once again carried out using the modified procedure described in the previous sections. As before, the concentration of the reaction mixture was maintained at 0.2 M, ensuring consistency across experiments and allowing to focus primarily on monitoring the influence of different reaction times. To systematically evaluate this, the mixture was allowed to react for one, two and three hours, respectively. The outcomes of these experiments are summarised in table 4.

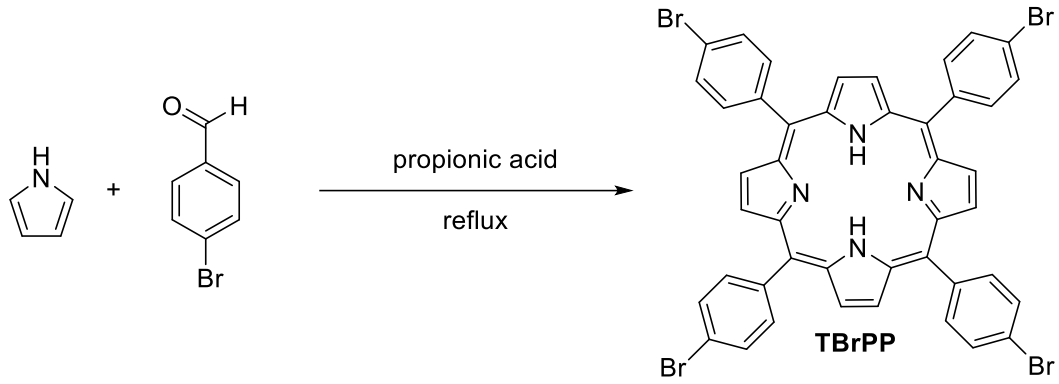

Table 4: Screening of reaction times at 0.2 M concentration for **TBrPP**.

time	concentration	yield
1 hour	0.2 M	11%
2 hours	0.2 M	26%
3 hours	0.2 M	45%

Similar to the synthesis of **TPyP**, the reaction proceeds, with the yield gradually increasing from 11% after one hour to 26% after two hours and 45% after three hours. According to the modified procedure, the reaction mixture was refluxed, then allowed to cool to room temperature before being poured into an excess of water to enhance precipitation. Since the bromophenyl groups are not protonated during the porphyrin formation, addition to a basic solution, as required for **TPyP**, is unnecessary. After resting in the refrigerator overnight, the formed precipitate was collected by filtration and washed with water and methanol. However, the ^{1}H-NMR spectrum exhibited additional signals, than the ones of the expected porphyrin structure, indicating that further purification was required. Although longer reaction times might have led to an even higher yield, the yield of 45% after 3 hours was considered as sufficient to proceed.

Commonly used purification methods for porphyrins

One of the most common and versatile purification methods in organic synthesis is column chromatography. For decades it has been regarded as a reliable and effective approach for separating complex mixtures, isolating target compounds and ensuring the purity required for subsequent applications. Despite these advantages, column chromatography is increasingly critically examined when viewed through an ecological and environmental lens. In the era of sustainable chemistry, where the guiding principles of “green chemistry” demand a minimisation of resource consumption, waste generation and overall energy use, this well-established technique reveals significant drawbacks. However, it still represents one of the most efficient, and therefore, still commonly used purification tools in synthetic chemistry.[89]

A key ecological concern lies in the excessive solvent consumption required for standard column chromatography. Depending on the scale of the synthesis and the polarity of the respective compounds, liters of organic solvents such as hexane, dichloromethane or ethyl acetate are consumed in the purification of only a few grams of product. This disproportionate ratio, between solvent use and product yield, highlights a fundamental inefficiency of the technique. The employed solvents are often volatile, toxic and derived from non-renewable petrochemical sources, which increases the environmental burden. Their widespread use not only accelerates the depletion of limited resources but also results in the release of harmful vapours and greenhouse gases if not carefully managed.[90]

Another major ecological limitation arises from the formation of hazardous waste. After elution of the column chromatography, the majority of solvents become chemically contaminated and cannot be reused without complex and costly recovery procedures. As a result, large quantities of mixed solvent waste must be collected and disposed as hazardous chemical waste. From

an economic perspective, the costs associated with both purchasing fresh solvents and managing waste disposal, represent a substantial portion of a laboratory's operating budget, making column chromatography not only environmentally unsustainable but also financially demanding.[90,91]

Furthermore, the ecological footprint of column chromatography is not limited to solvents alone. The use of stationary phases, most commonly silica gel or alumina, contributes to additional waste streams. These materials are typically single-use and after a purification run, they are discarded along with the residual adsorbed compounds, adding to solid laboratory waste.[91]

Considering these issues, column chromatography exemplifies the growing tension between traditional laboratory practices and the modern mandate for sustainable, green chemistry. While its utility as a purification method is undeniable, its ecological disadvantages demand serious attention. Strategies such as solvent minimisation, replacement of toxic solvents with greener alternatives, adoption of high-efficiency stationary phases and exploration of solvent-free purification approaches are possible improvements.[92]

Although column chromatography remains one of the most frequently employed purification methods in synthetic organic chemistry, its application to porphyrins is particularly challenging. This technique suffers from limitations when used with nitrogen-rich compounds. The difficulty is primarily based on the strong interactions formed between porphyrins and the stationary phase, typically silica gel. The surface of silica is decorated with acidic silanol groups, which can interact in hydrogen bonding and coordination with the basic nitrogen atoms of porphyrins. As a consequence, instead of eluting smoothly under gradient conditions, porphyrins frequently suffer from anomalous retention behaviour, broad peak tailing and poor product recovery.[93]

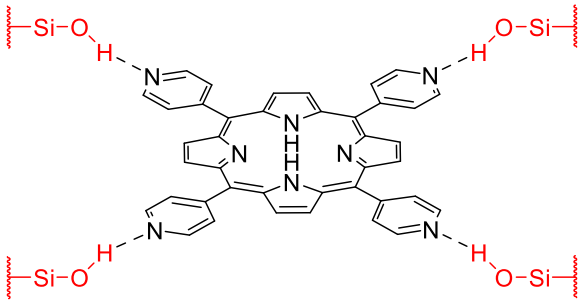

Figure 39: Coordination of **TPyP** to silica *via* hydrogen bonds.

This problem becomes especially pronounced in porphyrins bearing substituents such as pyridines or anilines. These functional groups contain highly exposed nitrogen atoms that can interact with the silanol moieties, leading to strong and sometimes even irreversible interactions, as shown in figure 39. Even porphyrins lacking additional hydrogen-bearing substituents are no exception: the four inner core nitrogen atoms of the macrocycle itself can participate in coordination with the silica

surface. One typical consequence is peak tailing, where analyte bands elongate and overlap, compromising selectivity and purity of the separated compounds.[94]

Beyond issues of selectivity, the strength of these porphyrin-silanol interactions can result in irreversible adsorption of a significant amount of the compound on the stationary phase. In practical terms, this means the column's runs often suffer from poor recovery, with a substantial fraction of the sample irretrievably lost within the column material. Such losses are not only wasteful when it comes to synthetic efficiency but also particularly problematic in porphyrin chemistry, where multistep syntheses frequently yield products in only modest amounts. The need for consecutive columns, consume large volumes of organic solvents and tolerate low recovery makes column chromatography an even more costly and environmentally burdensome purification choice for porphyrins than for most other substance classes.[94]

Given these challenges, alternative purification strategies are highly desirable. Recrystallisation is one of the most straightforward and effective alternatives for porphyrins. Unlike chromatography, recrystallisation takes advantage of the intrinsic ability of porphyrins to form crystalline lattices under appropriate solvent conditions. By careful selecting a solvent, or solvent mixture, in which the porphyrin exhibits moderate solubility at high temperatures and low solubility upon cooling, impurities can often be excluded from the growing crystals. This method offers several advantages like avoiding strong adsorbing interactions with silica which reduces the released product drastically. Additionally, recrystallisation typically consumes significantly less solvent overall and provides material of high purity in a single step. Hence, it is inherently more sustainable, generating minimal hazardous waste and moreover does not require a single-use stationary phase.[95]

However, recrystallisation is not universally applicable. The method relies on favourable solubility differences between the product and its impurities and some porphyrins may resist crystallisation due to steric hindrance or solubility profiles. Nevertheless, recrystallisation can generally deliver both, higher yields and better ecological performance than chromatography. In addition, combining crystallisation with preliminary purification, can further enhance efficiency. Thus, while column chromatography remains a rather default technique in synthetic organic synthesis, in the context of porphyrin chemistry, recrystallisation should be strongly considered as a greener, more cost-effective and often more reliable alternative.

A significant drawback of recrystallisation, despite its many advantages, lies in the often time-consuming process of identifying suitable solvents or solvent mixtures. Unlike standardised purification techniques, recrystallisation requires a tailored approach for each

individual compound. Porphyrins in particular present a considerable challenge in this respect, as they are often poorly soluble and their solubility can vary dramatically depending on even subtle structural changes. Factors as the type and position of substituents, the presence or absence of a central metal ion and the polarity or coordination behaviour of peripheral functional groups all influence how readily a porphyrin will dissolve in a given solvent system. As a result, there is no single “universal” protocol that can be applied across the entire class or porphyrins.

Consequently, the purification of each new porphyrin derivative often necessitates a fresh cycle of trial and error in order to identify the most effective recrystallisation conditions. Therefore, a variety of solvents and mixtures, balancing sufficient solubility at elevated temperature with poor solubility upon cooling has to be tested systematically. While this process can ultimately yield highly pure materials, it also introduces an element of unpredictability and additional experimental effort. Thus, the search for the “perfect” solvent system begins all over for nearly every porphyrin, representing a practical limitation to the otherwise sustainable and elegant method of recrystallisation.

Novel purification for porphyrins by acid-base recrystallisation

Both purification methods introduced previously still exhibit significant shortcomings when applied to porphyrin chemistry, making the development of an alternative method not only desirable but necessary. In this work, such an alternative has been elaborated. This newly established procedure based on acid-base recrystallisation can be applied to nearly all porphyrins and circumvents the well-known disadvantages of column chromatography or recrystallisation.

The chemical functionalities that are typically problematic in column chromatography, in particular the strongly basic nitrogen atoms, become advantageous in this new method. While these basic groups tend to interfere with smooth elution and separation during column chromatography, here they provide the foundation for a more efficient purification strategy. A key principle underlying this method is the reversible protonation of porphyrins. When dissolved porphyrins are treated with acids such as hydrochloric acid, protonated species are formed, shown exemplarily in figure 40.

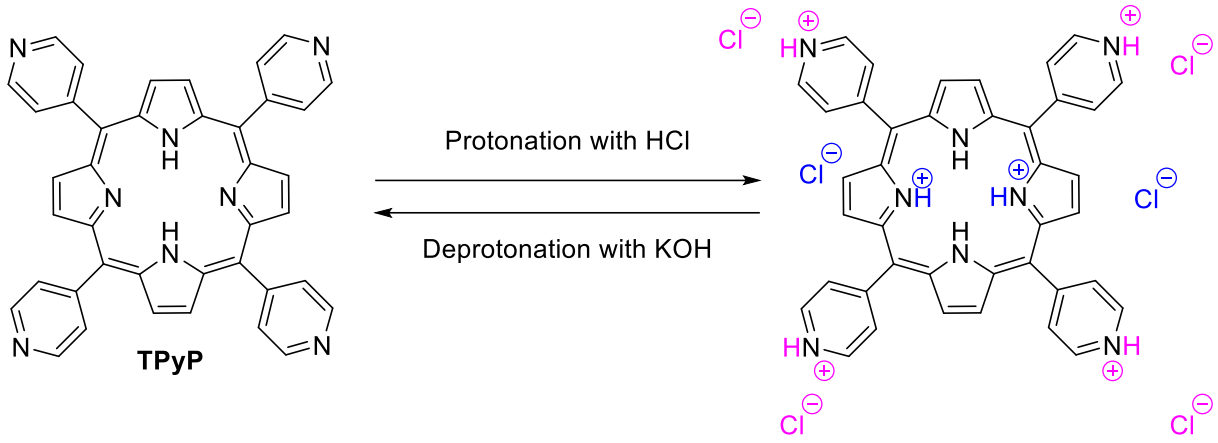

Figure 40: Reversible protonation of porphyrin substituents (pink) and the porphyrin core (blue).

These cationic species exhibit a salt-character, which alters both their colour as well as solubility. Whereas porphyrins typically appear red in organic solvents, protonation shifts their colour to green or blue. More importantly, the resulting porphyrin salts are insoluble in organic solvents, and therefore, precipitate from solution.

Thereby, it is essential to choose an appropriate organic solvent in the first step, that both dissolves the porphyrin efficiently and mixes homogeneously with hydrochloric acid, such as acetone of dimethylformamide (DMF). Immiscible solvents lead to the formation of hydrochloric acid droplets within the organic phase and protonated porphyrin accumulates within these droplets rather than precipitating efficiently.

For successful purification, complete protonation must be ensured without excess acid addition. The further addition of hydrochloric acid after complete protonation can lead to re-dissolution of the salt in concentrated hydrochloric acid, reducing the yield. To avoid this, hydrochloric acid is added in small amounts, followed by resting periods at low temperatures. This promotes the formation of larger flakes of porphyrins salt, which simplifies and accelerates the subsequent filtration.

The protonated porphyrin is isolated by filtration and this process is repeated until the filtrate contains no further traces of precipitate. A coloured filtrate, particularly with a reddish fluorescence, indicates incomplete protonation. In such cases, small portions of acid are added and the cycle is repeated until the filtrate becomes pale yellow and does not fluoresce anymore. At this stage, the porphyrin is effectively separated from impurities that cannot be protonated, and therefore, remain dissolved.

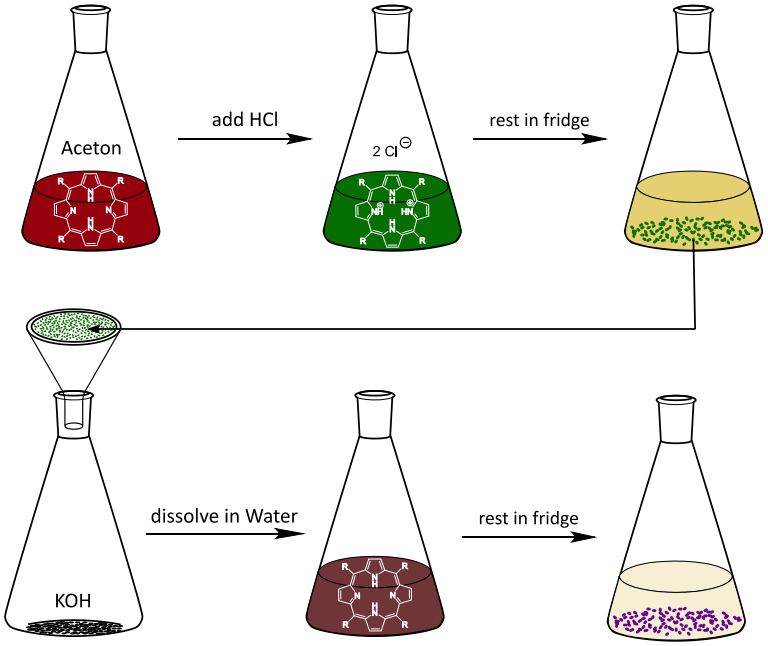

Figure 41: Schematic overview of the acid base recrystallisation.

The isolated protonated porphyrin salt is water-soluble, which allows a second purification step: when dissolved in water, insoluble impurities remain on the filter, while the porphyrin salt passes into the aqueous phase. To regenerate the neutral porphyrin, the aqueous solution is treated with potassium hydroxide pellets. Deprotonation restores the porphyrin in its original, uncharged state, which is again insoluble in water and precipitates from the solution as a purple solid. This step not only regenerates the original porphyrin but also provides an additional purification cycle.

The precipitated porphyrin is collected by filtration, washed thoroughly and finally dissolved in a suitable organic solvent. Evaporation of the solvent under reduced pressure, followed by drying *in vacuo*, gives the pure porphyrin. Compared to conventional methods, this approach is less environmentally harmful, avoids drawbacks of chromatographic separation and results in high purity and yields.

An additional advantage of this method, in comparison to recrystallisation, is its universal applicability. Hereby, it is important to notice that the applicability of the newly introduced purification strategy is not limited to porphyrins bearing basic substituents such as pyridyl or aniline groups. As illustrated in figure 40 in blue, even the inner nitrogen atoms of the porphyrin macrocycle itself can be protonated under acidic conditions.

This broadens the scope of the method drastically, as it enables its use for nearly all porphyrin derivatives, regardless of the substituents attached to the periphery of the ring. In principle, the

only limitation arises in the case of porphyrins that are already water-soluble in their nonprotonated form. For such compounds, the key principle of this purification method, namely the solubility difference between the neutral and protonated species, holds no longer true.

An example of this exception was observed with the tetra-phenol substituted porphyrin **TOHPP**. In this case, the neutral species already dissolves in aqueous solution. Upon protonation, the solubility of the compound does not change significantly, which prevents the selective precipitation and phase separation required for efficient purification. Thus, for porphyrins of this type, the method cannot be applied successfully. However, **TOHPP** was successfully synthesised by deprotection of **TOMePP** with BBr_3.

Additional exceptions to this method are metalated porphyrin species, since the protonation takes place on the inner nitrogen atoms of the porphyrin macrocycle. By this, the metal dissociates from the porphyrin core, regaining the unmetalated porphyrin species. Nonetheless, these cases remain relatively rare and for the majority of porphyrins the acid-base recrystallisation provides a straightforward and highly effective route to isolate the target compound in high purity.

Scope for porphyrin synthesis and purification

To further investigate the applicability of both the synthetic route and the purification strategy, a series of porphyrins with varying substitution patterns was synthesised following this approach together with *Justen*.[96] The modified synthetic procedure was systematically applied to these compounds in order to examine whether reliable, reproducible and high-yielding syntheses could be achieved across a broad structural range. After the novel purification method was employed, three of the five compounds synthesised by *Justen*, were synthesised an additional time with applying the acid-base recrystallisation method. In doing so, not only the efficiency of the synthetic modification, but also the versatility of the purification concept was validated.

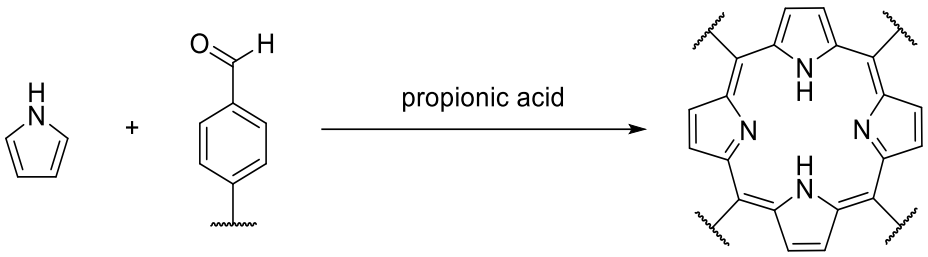

Figure 42: General equation of porphyrin synthesis.

In addition to the three porphyrins that were described in the previous sections (**TNPP**, **TPyP** and **TBrPP**), a further set of four porphyrins bearing distinct substituents and substitution patterns were successfully synthesised by *Justen* by employing the modified synthetic procedure.[96] This extension of the synthetic scope was designed not only to verify the generality of the methodology but also to explore how different electronic and steric effects influence porphyrin formation, stability and purification. Each of these four derivatives displayed unique behaviours during synthesis, offering valuable insights into the reactivity and handling of functionalised porphyrins.

The first compound, 5,10,15,20-tetrakis(4-iodophenyl) porphyrin (**TIPP**), was synthesised by *Justen* on multiple occasions in order to optimise conditions for the photo-labile iodo-substituents. During this process, it became evident that light plays a crucial role in the outcome of the reaction. When light was not carefully excluded, the 4-iodobenzaldehyde precursor gradually degraded over time, which in turn suppressed the formation of the desired porphyrin. In contrast, performing the synthesis under dark conditions consistently produced the targeted product. Apart from light sensitivity, this system demonstrated an additional vulnerability towards elevated temperatures. When heated to 150°C, ^{1}H-NMR spectroscopy revealed the appearance of a second porphyrin species, suggesting thermal instability and partial degradation. At room temperature, the condensation failed even after extending the reaction time up to 18 hours. However, at a moderate temperature of 100°C, the reaction proceeded smoothly and selectively, forming only a single porphyrin species giving **TIPP** in a yield of 24%.[96] This synthesis was repeated with the acid-base recrystallisation method instead of excessive washing. Thereby, an increase in yield to 30% could be observed, proving the newly applied method to be less product consuming, yielding similar results as reported in literature with 32%.[97]

In a subsequent experiment, 5,10,15,20-tetrakis(4-(tert-butoxy)phenyl)porphyrin **TO*t*BuPP** was prepared by *Justen* to investigate whether the modified synthetic method was also applicable to sterically demanding substituents. The introduction of bulky *tert*-butoxy groups was expected to pose a challenge due to increase steric hindrance. Indeed, under the standard conditions of 150°C, the reaction did not proceed efficiently. By lowering the temperature to 100°C the formation of the porphyrin was achieved successfully. After isolation, the crude product was washed with water and cold methanol, which was sufficient to remove impurities. No further purification was necessary and the compound was obtained in a yield of 23%. The results highlight the adaptability of the synthetic method to different steric environments, with minor modifications to the reaction conditions.

The *para*-methoxy-substituted porphyrin **TOMePP** was formed according to the modified reaction procedure by *Justen*. Therefore, the temperature of 150°C was applied for 2 hours yielding 28%.[96] Again, the synthesis was repeated with the novel purification procedure under otherwise identical conditions, yielding the product in 37%.

Table 5: Scope of synthesised porphyrins, with [a] performed by *Justen* and [b] initially performed by *Justen*, but repeated with the novel purification method.[96]

substitution	time	temperature	additional comments	purification method	yield
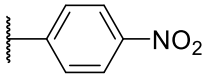 **TNPP**	30 minutes	150°C	-	recrystallisation in pyridine and acetone	70%
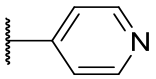 **TPyP**	2 hours	140°C	precipitation in saturated KOH solution	acid-base recrystallisation	51%
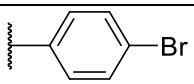 **TBrPP**	2 hours	150°C	-	acid-base recrystallisation	45%
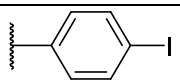 **TIPP**	30 minutes	100°C	exclusion of light	acid-base recrystallisation	30%[b]
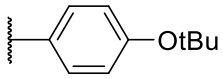 **TO*t*BuPP**	2 hours	100°C	-	washing	23%[a]
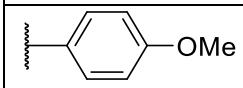 **TOMePP**	2 hours	150°C	-	acid-base recrystallisation	37%[b]
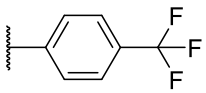 **TCF_3PP**	2 hours	150°C	-	washing	30%[a]
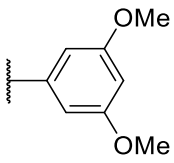 **$T(OMe)_2PP$**	30 minutes	150°C	-	acid-base recrystallisation	52%[b]

The fourth target, a trifluoromethyl-substituted porphyrin **TCF_3PP**, was synthesised by *Justen* according to the modified procedure without the need for further alterations. In this case, the standard conditions of 150°C with a reaction time of two hours were effective. Following the reaction, the product was filtered and subsequently washed with water and methanol. Interestingly product solubility was visibly indicated during purification: the fluorescence of the

methanol filtrate gradually shifted from blue to red, indicating the stepwise dissolution of the porphyrin over time. At this stage, the washing was stopped and the product was collected. The compound was obtained in high purity without the need for any additional purification steps and it was isolated in a yield of 30%. This example illustrates the practicality of the modified synthesis for electron-withdrawing substituents such as trifluoromethyl groups, which appear to tolerate the reaction conditions well.

Finally, the synthesis of the dimethoxyphenyl-porphyrin **T(OMe)$_2$PP** was performed by *Justen* to evaluate whether alternative substitution patterns could also be tolerated. The reaction was carried out under modified conditions, with a reduced reaction time of 30 minutes at 150°C. This shortened reaction time proved sufficient for porphyrin formation, yielding 13%.[96] The reaction was performed an additional time, but this time the crude product contained minor impurities detectable in the ^{1}H-NMR spectrum. To achieve the desired level of purity, the newly developed purification method was applied once again. This approach effectively removed the residual impurities and yielded the porphyrin in high purity. Notably, this compound was isolated in the highest yield among the four additional derivatives and the second highest overall, reaching 52%, which is a drastic increase compared to the 13%, reached with excessive washing of the product.

Summarised, the results demonstrate that the modified synthetic procedure and purification for porphyrin formation is highly versatile, tolerates a variety of substituents with differing steric and electronic properties. Nevertheless, the studies also emphasise the importance of carefully optimising reaction conditions, particularly with respect to temperature, reaction time and special requirements due to specific starting materials in order to achieve the desired outcome. Through these systematic investigations, valuable insight into the synthetic behaviour of porphyrins with challenging substituents were gained, providing a solid foundation for further expansion of porphyrin chemistry. Additionally, to ensure high purity of these compounds, the combination of NMR analysis with elemental CHNS analysis was established as a new standard for extraordinary purity.

Less symmetrical porphyrins

The scope of the previously described synthetic strategy has been limited to porphyrins bearing four identical substituents in a symmetrical arrangement. While this class of compounds is highly relevant for a variety of applications and gives further synthetic insights, its structural uniformity limits the compounds in terms of chemical diversity. To broaden the scope and to test the universal applicability of the synthetic procedure, less symmetrical porphyrins were therefore synthesised together with *Schmidt*.[98] These molecules incorporate two different

types of substituents at the *meso*-positions, thereby reducing their overall symmetry and increasing structural complexity. In addition, they were deliberately constructed in a manner that preserves functional coordination sites for supramolecular interactions. Specifically, each of these less-symmetrically substituted porphyrins carries pyridine moieties at two opposite *meso*-positions, ensuring that coordination to metal centres and non-covalent assembly processes can still occur.

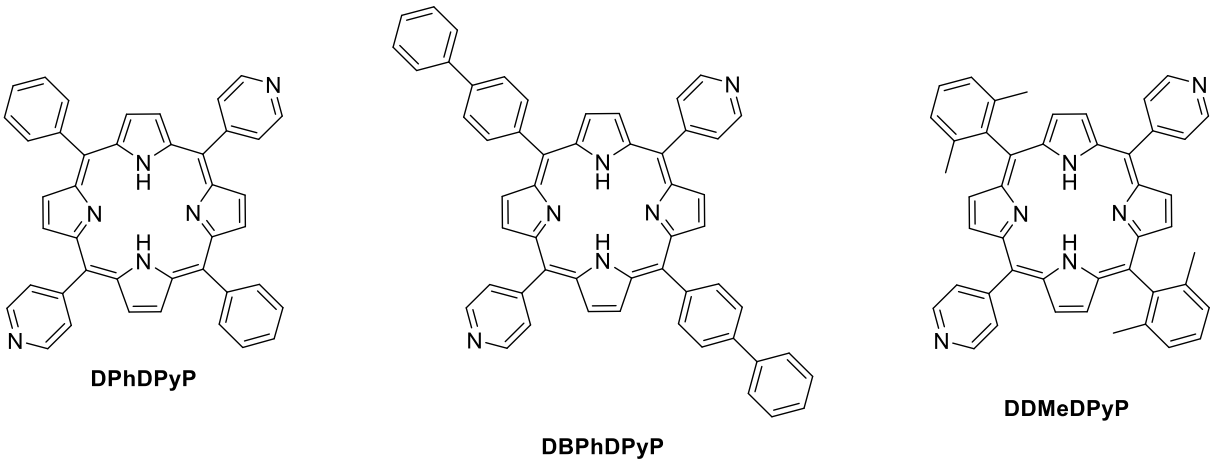

Figure 43: Summary of the investigated less symmetrical porphyrin derivatives.

The first representative, 5,15-diphenyl-10,20-di(pyridin-4-yl)porphyrin (**DPhDPyP**), is the most straightforward example. In this compound, two phenyl groups are introduced at the *meso*-positions. The incorporation of these substituents can preserve conjugation and maintain the planar geometry of the porphyrin core while the phenyl rings adopt a twisted orientation, which should enhance the solubility of the system by preventing the formation of π-stacks. As is well documented, that porphyrins often suffer from solubility issues due to their strong tendency to form highly ordered π-π stacks.[99] The extended aromatic surface of neighbouring porphyrins can align in a parallel fashion, giving rise to aggregates stabilised by π-stacking interactions. Although these assemblies are structurally robust, they significantly reduce the solubility of the respective compound in common organic solvents and thereby limits their processability.

To address this problem even further, a second derivative was designed by *Schmidt*, 5,15-di([1,1'-biphenyl]-4-yl)-10,20-di(pyridine-4-yl)porphyrin (**DBPhDPyP**). In this structure, the simple phenyl substituents are replaced with biphenyl groups. The biphenyl moieties introduce an even stronger rotational flexibility between the two aromatic rings, which prevents the substituents from adopting a fully coplanar orientation with respect to the porphyrin macrocycle. As a result, the overall molecular shape becomes more twisted and less flat

compared to **DPhDPyP**. This geometric modification influences the solubility significantly. Because the peripheral arms are no longer aligned in a single plane, neighbouring porphyrins cannot approach each other as closely as before, thereby reducing the formation of tightly packed π-stacks. Consequently, **DBPhDPyP** is expected to exhibit improved solubility, compared to its simpler analogue, while still retaining the coordination ability of the pyridyl substituents.[98]

A third derivative was designed by *Schmidt* to further disrupt intermolecular stacking interactions. In 5,15-bis(2,6-dimethylphenyl)-10,20-di(pyridin-4-yl)porphyrin (**DDMeDPyP**), additional steric hindrance is introduced directly at the *ortho*-positions of the phenyl substituents through the addition of methyl groups, pointing in orthogonal direction in comparison to the porphyrin core. These stick out of the molecular plane and physically hinder the close approach of neighbouring porphyrin cores. By shielding the aromatic surface of the macrocycle, these groups act as a steric barrier that prevents π-stackings. As a result, **DDMeDPyP** is expected to display significantly enhanced solubility in comparison to both **DPhDPyP** and **DBPhDPyP**.[98]

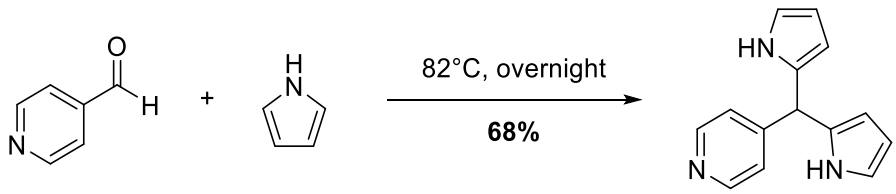

Figure 44: Precursor for less symmetrical porphyrins.

All three of these porphyrins were formed according to the introduced procedure but since they do not bear the same substituent on every *meso*-position they cannot be formed directly from pyrrole and the respective aldehydes. Therefore, the formation of a precursor was necessary which was synthesis according to a general procedure introduced by *Laha et al.* in 2016.[100] By synthesis of the pyridine equipped precursor, shown in figure 44, each of the three described porphyrins can be formed by combination of the precursor with the respective aldehyde.

Each of these less symmetrically substituted porphyrins was synthesised following the modified procedure, in which the condensation reactions were carried out under reflux at 150°C in propionic acid. In contrast to some of the previously studied porphyrins, a reaction time of 1 hour was sufficient to form the desired products. As pyridine groups are readily protonated under the acidic conditions employed during the porphyrin formation, the precipitation was nor carried out in water, but rather in a saturated aqueous solution of

potassium hydroxide. This deprotonates the pyridine moieties, reducing solubility, and thereby, leads to efficient and complete precipitation of the porphyrins from the reaction mixture.

The first compound investigated in this series, **DPhDPyP**, required an additional purification step following the synthesis. The crude product was initially isolated as expected, however, the ^{1}H-NMR spectrum revealed minor impurities. To address this, the newly developed purification method based on acid-base recrystallisation of the porphyrins was applied. This process provided the product in high purity in a yield of 35%.

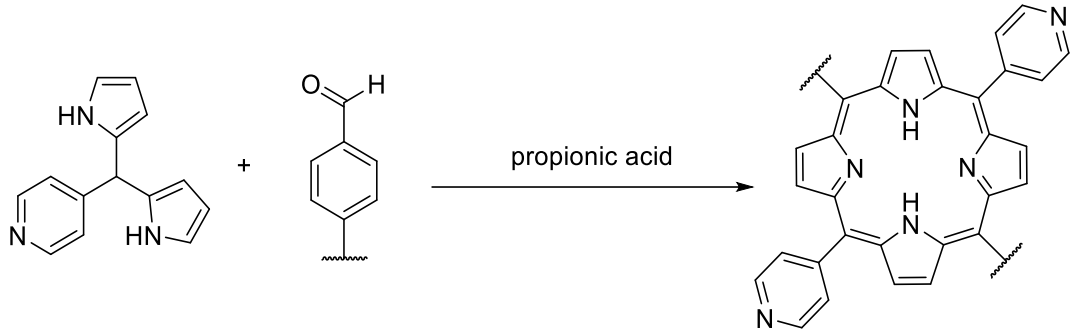

Table 6: Scope of less symmetrical porphyrins with reaction conditions, with [a] performed by *Schmidt*[98].

substitution	time	temperature	additional comments	purification method	yield
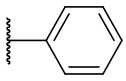 **DPhDPyP**	1 hour	150°C	precipitation in saturated KOH solution	acid-base recrystallisation	35%
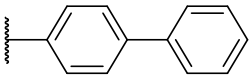 **DBPhDPyP**	1 hour	150°C	precipitation in saturated KOH solution	washing	59%[a]
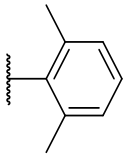 **DDMeDPyP**	1 hour	150°C	precipitation in saturated KOH solution	washing	-[a]

The second derivative, **DBPhDPyP**, was synthesised under the same modified conditions. Here, the biphenyl substituents did not interfere with the formation of the porphyrin macrocycle and the desired product could be isolated by washing the crude product with water and ethyl acetate. Additional purification steps were not required, since the product was already obtained in high purity with a significantly increased yield of 59%. This improved yield may be attributed

to the steric influence of the biphenyl substituents, which could hinder undesired side reactions and benefit the solubility which facilitates the purification.

The final example, **DDMeDPyP**, presented a considerably greater challenge. In this case, the sterically demanding 2,6-dimethylphenyl substituents, positioned close to the reactive aldehyde functionality, appear to hinder the condensation reaction. As a consequence, the intended porphyrin was not obtained under the applied conditions. Instead, analysis of the reaction mixture, *via* ^{1}H-NMR, revealed the formation of **TPyP**, accompanied by unreacted aldehyde and residual pyrrole, as shown in figure 45.

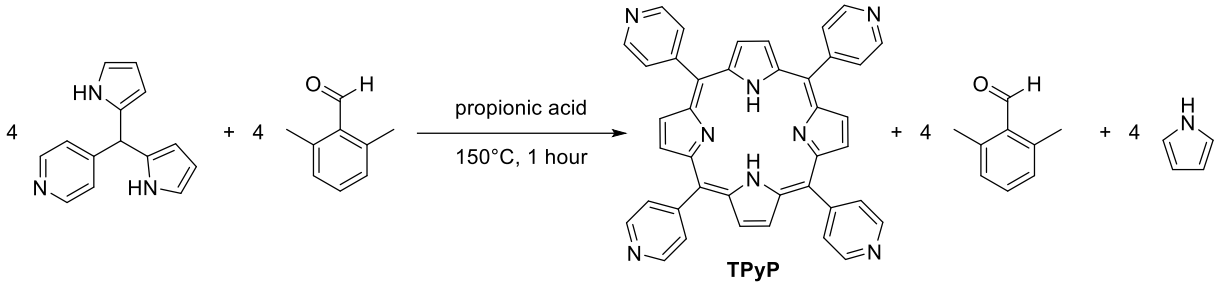

Figure 45: Formation of **TPyP** instead of **DDMeDPyP**.

This unexpected outcome suggests that fragmentation of the precursor occurred under the reaction conditions, shown in figure 45, favouring the exclusive formation of **TPyP**. This highlights an important limitation of the method when applied to porphyrins bearing sterically bulky substituents near the aldehyde. While the modified procedure proved adaptable for highly symmetrical systems bearing the same substituent on every *meso*-position and also less symmetrical porphyrins including phenyl and biphenyl substituents, the additional steric hindrance introduced by the *ortho*-methyl groups suppressed the desired condensation pathway.

In summary, the synthetic series demonstrated both the applicability and limitation of the modified porphyrin synthesis, as well as the newly introduced purification method. These findings provide valuable insights into the scope of porphyrins with accessing a variety of different functionalities and substitution patterns with overall high yields and outstanding purity. Limitations for the synthetic procedure were found to be sterically hindering groups in case of the less symmetrical porphyrins and in the purification method for water soluble and metalated porphyrins. Since these only occur rarely in the substance class of porphyrins, the synthetic route, as well as the purification method remains highly universal in potential applications.

Elemental analysis

The porphyrins described in the previous sections were not only obtained in comparably high yields but also isolated in high purity, an achievement that is noteworthy given the difficulties associated with assessing the purity of porphyrin derivatives. One of the central challenges arises from their poor solubility in common organic solvents. Even though NMR spectroscopy is typically considered the method of choice for verifying the structural integrity and purity of organic compounds, porphyrins often only partially dissolve in the employed solvents. As a result, NMR spectra can draw an incomplete or misleading picture. For example, it is possible to record spectra that only display product signals, indicating high purity, while in reality, insoluble fractions of the sample remain undetected. These could have the same composition as the dissolved portions, but they may just as well consist of residual starting materials, by-products or decomposition products that remain invisible to the NMR. Consequently, counting solely on NMR analysis does not provide a fully reliable assessment of the purity of porphyrin compounds.

Mass spectrometry provide insights in the composition of assemblies and their fragments but cannot give reliable informations on the purity of these compounds. Additionally, the detection of supramolecular architectures is highly challenging due to their low stability under the respective conditions. Therefore, electron-spray ionisation is used as a very mild technique, but since the compound has to be dissolved for its analysis, this technique poses obstacles for compounds, which suffer from poor solubility.

To overcome this limitation and to obtain more trustworthy informations, additional methods must be applied. One particularly powerful technique is elemental analysis, which enables deeper insights into a sample’s composition. In elemental analysis the experimentally measured weight percentage of specific elements are compared directly with the theoretical values calculated for the proposed molecular formula.[101]

In the context of organic chemistry, elemental CHNS analysis has established itself as a widely applied technique for this purpose. This method quantitatively determines the amounts of carbon, hydrogen, nitrogen and sulphur present in a given sample. It is not only found in organic synthesis but also in pharmacy to confirm a compound’s identity and evaluate its purity to ensure that they meet the purity standards required for medical applications.[101]

The technique itself is based on a highly automated process involving combustion, gas chromatography and quantitative detection. During measurements, the sample is first subjected to complete combustion at elevated temperatures in the presence of a catalyst. This

ensures that all elements within the sample undergo full oxidation, thereby transforming them into their respective oxides. Specifically, carbon is converted to carbon dioxide, hydrogen into water, nitrogen into molecular nitrogen and sulphur into sulphur dioxide. These gaseous products are subsequently carried through the system, where they undergo chromatographic separation. Following, sensitive detectors quantify the amount of each gas present, from which the relative weight percentages of the corresponding elements can be calculated. Thereby, a deviation of ±0.4% between experimental and theoretical values is widely regarded as acceptable. In some cases, higher deviations for carbon values are also accepted, since these are typically higher in organic molecules than the weight percentage of hydrogen or nitrogen. Thereby, the relative difference is more balanced. Larger deviations may point to the presence of impurities, incomplete removal of solvents or other experimental shortcomings. Thus, when combined with additional techniques such as NMR spectroscopy, elemental CHNS analysis provides a highly reliable basis for confirming both the identity and purity of porphyrin compounds, even in cases where solubility limitation complicate spectroscopic evaluation.[101,102] The results for experimental CHNS analytics, compared to the calculated values with the respective deviations are summarised in table 7.

Table 7: Summary of the results of CHNS analysis of the porphyrins, presented in this work, in collaboration with *Justen*[a]. * The ^{1}H-NMR spectrum of **TPyP** shows traces of propionic acid. Taken this into account, the expected values were recalculated with **TPyP** * 1/7 propionic acid to be 77.16% (C), 4.30% (H) and 17.81 (N). This reduces the deviation to 0.01% (C), 0.32% (H) and 0.03% (N). ** The ^{1}H-NMR spectrum of **TBrPP** shows traces of water. Taken this into account, the expected values were recalculated with **TBrPP** * ½ H_2O to be 56.26% (C), 2.90% (H) and 5.96% (N). This reduces the deviation to 0.14% (C), 0.18% (H) and 0.16% (N).

	calculated			experimental			deviation		
substitution	**C [%]**	**H [%]**	**N [%]**	**C [%]**	**H [%]**	**N [%]**	**C [%]**	**H [%]**	**N [%]**
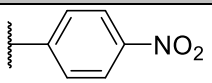 **TNPP**	66.50	3.30	14.10	67.11	3.87	13.97	0.61	0.57	0.13
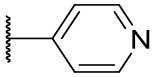 **TPyP**	77.65	4.24	18.11	77.17	4.62	17.84	0.48*	0.38*	0.27*
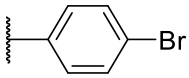 **TBrPP**	56.81	2.82	6.02	56.12	2.72	5.80	0.69**	0.10**	0.22**
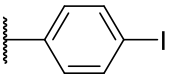 **TIPP**	47.17	2.52	5.00	47.33	2.31	5.27	0.16	0.21	0.27
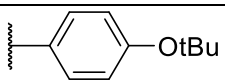 **TO*t*BuPP**[a]	79.79	6.92	6.20	78.90	6.93	5.97	0.11	0.01	0.23

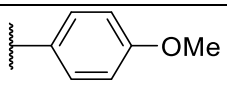 **TOMePP**	78.45	5.12	7.62	78.62	5.07	7.44	0.17	0.05	0.18
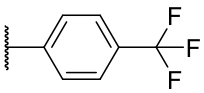 **TCF_3PP**[a]	due to the fluorine content, no CHNS analysis could be performed.								
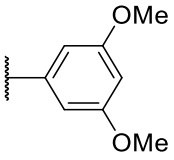 **$T(OMe)_2PP$**	73.05	5.42	6.55	72.78	5.42	6.23	0.27	0.00	0.32
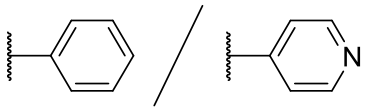 **DPhDPyP**	81.80	4.58	13.63	81.55	4.42	13.70	0.25	0.16	0.07

9. Synthesis of catalyst building blocks

With a reliable method for the formation and purification of porphyrins the assembly of porphyrin based supramolecular architectures was investigated. The supramolecular cubic host shown in figure 46, introduced by *de Bruin* and co-workers in 2013[81], is formed *via* subcomponent self-assembly of three components. The iron(II) salt, here either iron-triflate or -triflimide, is commercially available and can be exchanged respective to the requirements for the counterion. This influences the system's solubility significantly while also having a major impact on the crystallisation behaviour of the complex.

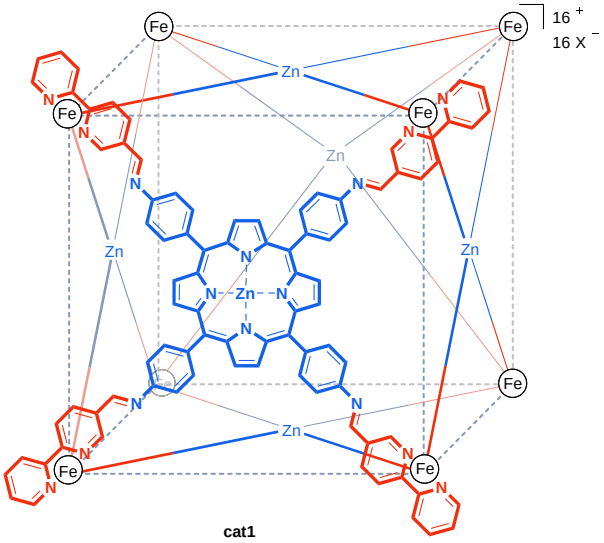

Figure 46: Simplified structure of **cat1**.

[2,2'-bipyridine]-5-carbaldehyde (red)

The aldehyde (red) can either be synthesised in a twostep synthesis or can be purchased commercially. However, due to its high price, a synthetic approach was chosen to provide a more cost-effective and scalable route. In literature, this compound has previously obtained *via* a *Stille* cross-coupling.[81] While effective and well-established, this reaction involves tin-organic intermediates, which are known to be highly toxic and environmentally harmful and thereby, should be avoided whenever possible.[103]

As an alternative, other palladium-catalysed cross-coupling reactions were considered, with the *Suzuki* cross-coupling as the most promising example. This method, which employs boronic acids or boronic acid esters as coupling partners, offers several advantages in comparison to the *Stille*-coupling. Boronic acids are generally less toxic, more stable and thereby easier to handle compared to tin-organic compounds.[104] Furthermore, the *Suzuki* reaction is highly versatile, compatible with a wide range of functional groups and often provides good to excellent yields under relatively mild conditions. These features make it particularly suitable for sensitive substrates such as the targeted aldehyde. From an economic perspective, boronic acid derivatives are often more accessible and less expensive than the corresponding tin reagents, further increasing the attractiveness of this route.

However, the *Suzuki* cross-coupling of this compound is rather challenging. Boronic acids can sometimes undergo side reactions such as protodeboronation, especially under harsh

conditions or when electron-deficient heteroaryl boronic acids are used. In this case, the coupling of two pyridine rings at the position directly adjacent to the nitrogen atoms is complicated since these positions are especially electronically deactivated. Careful optimisation of the catalyst system, ligands, bases and solvents is therefore essential to achieve efficient coupling.

In order to suppress the undesired protodeboronation of electron-deficient heteroaryl boronic acid derivatives the protocol of *Gütz* developed in 2010 in our group was applied.[85] According to this, optimal results were achieved when employing 10 mol% $Pd(PPh_3)_4$ as catalyst, in combination with bromine as the leaving group instead of chlorine.

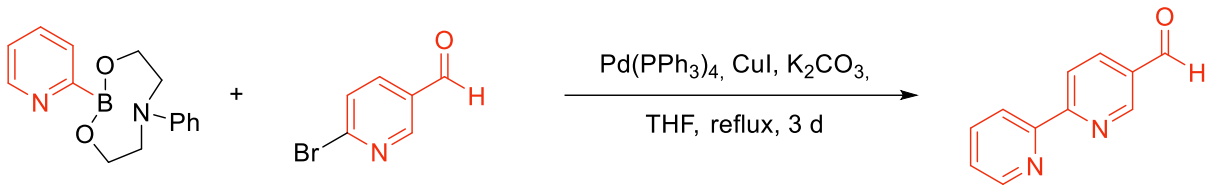

Figure 47: *Suzuki-Miyaura* cross-coupling to [2,2'-bipyridine]-5-carbaldehyde.

The choice, of the halide was shown to have a significant impact on the coupling efficiency, with the more reactive bromine providing the desired product in 90% yield and the chlorine under the same conditions didn't yield the product at all. The coupling partners, consisting of 2-bromopyridine and the boronic acid ester, shown in figure 47, were used in a ratio of 1.7 equivalents of the boronic acid ester to 1.0 equivalent of the bromopyridine. This excess of boronic acid ester was required to counteract the side processes such as protodeboronation. In the optimisation of the reaction conditions, two bases were evaluated, potassium carbonate and caesium fluoride. While the use of CsF did not afford any product, potassium carbonate under otherwise identical conditions produced the desired compound in 90% yield. This highlights the crucial role of the base in *Suzuki-Miyaura* couplings, particularly for electron-deficient systems, where subtle changes in solubility, nucleophilicity or metal-base interactions can drastically alter the outcome of the reaction.[85]

To prevent deboronation of the boronic acid ester, before it is able to perform the desired reaction, a specially stabilised boronic acid can be used, shown in figure 48. The boronic ester, introduced by *Hodgson* provides a dative bond between the electron pair of the nitrogen towards the boron, pushing electron density in this labile group. Thereby, the effect of the electron-deficient pyridine is weakened and the compound becomes bench stable for several months instead of degrading in a few hours.[105]

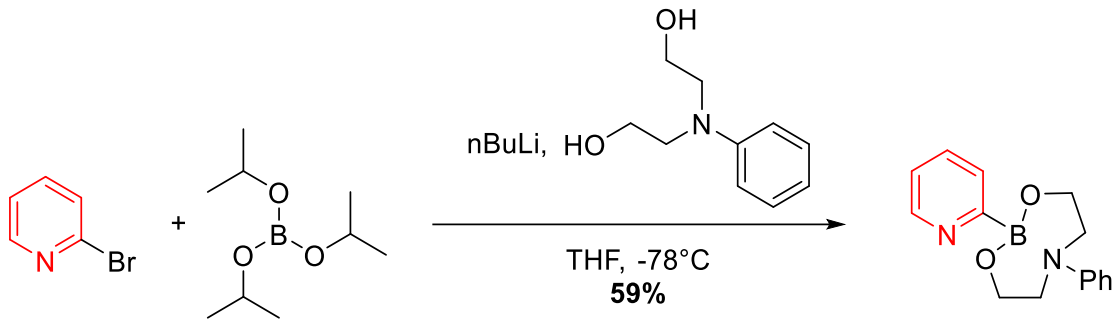

Figure 48: *In situ* generation of stabilised boronic acid ester.

This compound is generated *in situ* through transformation of the diisopropyl boronic acid ester, shown in figure 48. This method allows the desired compound to be formed directly within the reaction environment, thereby minimising the degradation efficiently.

Zinc-5,10,15,20-Tetrakis(4-aminophenyl)porphyrin (Zn-TAPP, blue)

With the porphyrins in hand described in chapter 8, their transformation into the final building blocks, necessary for the self-assembly of the cubic host was targeted. The zinc-porphyrin (blue) was formed by reduction of the previously formed **TNPP** and subsequent metalation with zinc(II)-ions.

The reduction of **TNPP** to 5,10,15,20-Tetrakis(4-aminophenyl)porphyrin (**TAPP**) was carried out in accordance with the procedure described by *Struch* in 2013, who reported a yield of 35%.[106] In the context of efficiently reducing the nitro-groups, tin(II)chloride in hydrochloric acid was identified as the most suitable reagent. To gain deeper understanding of the reaction and to improve its efficiency, systematic investigations were performed with respect to three key parameters: concentration, reaction time and temperature. The outcomes of these experiments are summarised in table 9.

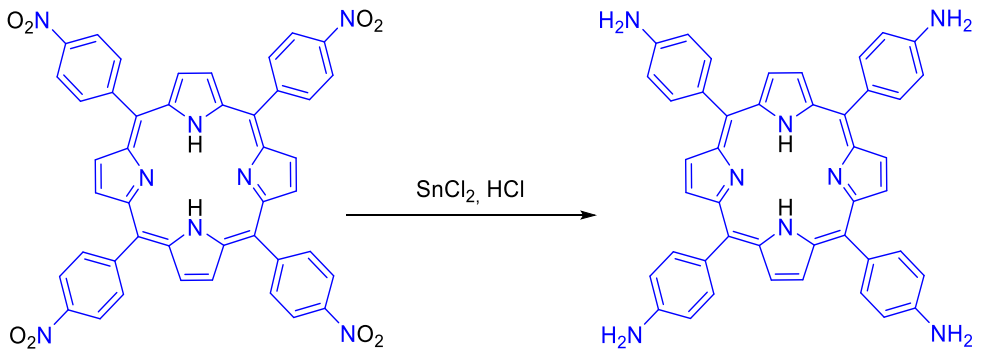

TNPP **TAPP**

Table 8: Screening of reaction conditions for reduction of **TNPP** to **TAPP**.

time	temperature	concentration	yield
1 hour	70°C	0.004 M	55%
1 hour	70°C	0.005 M	50%
1 hour	70°C	0.008 M	22%
1 hour	70°C	0.004 M	55%
2 hours	70°C	0.004 M	26%
1 hour	110°C	0.004 M	32%
2 hours	110°C	0.004 M	42%

From this data, several trends become clear. In the first set of experiments, the influence of concentration was examined by performing the reduction at 0.004 M, 0.005 M and 0.008 M. A clear relationship emerged; higher diluted conditions gave higher yields of the desired product. In contrast, increasing the concentration to 0.008 M led to a decrease from 55 % at 0.004 M to 22% yield. These concentrations were chosen, since the concentration used in literature was rather diluted and higher concentration might benefit faster conversion. Since this theory has been disproved, the second set of experiments was targeted, focusing on the effect of reaction time at a constant temperature of 70°C. Thereby, a shorter reaction duration of one hour proved more advantageous yielding 55%. Extending the reaction time to two hours, however, resulted in a significantly lower yield of 26%. Finally, the role of the reaction temperature was investigated by performing the reduction at an elevated temperature of 110°C. Under these conditions, yields were consistently lower than at 70°C, regardless of the time. This finding indicates that higher temperatures are not beneficial for short reaction times, but yield better results after 2 hours than the lower temperature of 70°C. However, the yield of 42% could be improved further by elongating the reaction time but since the initial condition yielded 55% at a lower temperature and shorter reaction time, these conditions were considered the most promising. In conclusion, these observations highlight the importance of carefully balancing the reaction parameters to achieve an optimal outcome. The best results for this reduction were obtained at a concentration of 0.004 M, a temperature of 70°C and a reaction time of one hour.

The final step in the formation of zinc-**TAPP** (blue fragment) is the metalation of **TAPP** with zinc(II)-ions. For this purpose, zinc(II) acetate was employed as the metal source and both the stoichiometry of the reagent and the duration of the reaction were systematically optimised. The results of these experiments are listed in table 10.

In the first set of experiments, the effect of the solvent system on the reactions' outcome was investigated. Initially, a mixture of dimethylformamide (DMF), chloroform ($CHCl_3$) and methanol

(MeOH) in a ratio of 1:3:0.7 was employed, as reported in literature.[107] While this mixture did lead to successful metalation, the subsequent work-up proved problematic. Precipitation of the metalated porphyrin is typically facilitated by the addition of the reaction mixture to water, however, in this case, the biphasic nature of the system caused significant difficulties. Both DMF and methanol are miscible with water, whereas chloroform forms droplets at the bottom of the vial. Thereby, a considerable fraction of the product remained dissolved in the chloroform, preventing efficient precipitation and reducing the overall product recovery. To address this issue, the solvent system was simplified by using pure DMF. This adjustment increased the yield from 12% to 17%.

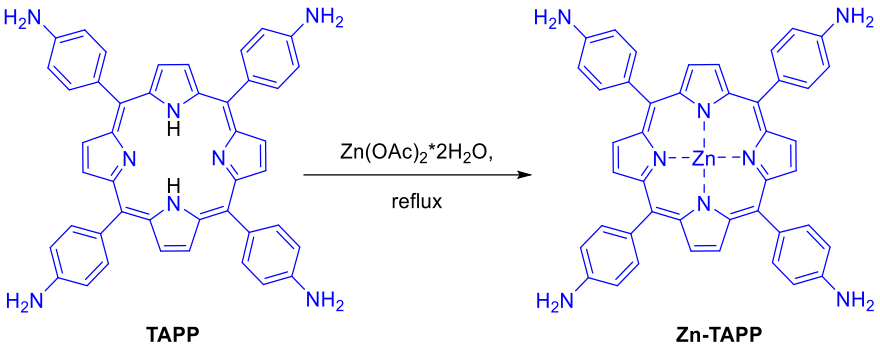

Table 9: Condition screening for the metalation of **TAPP** with zinc(II) acetate.

zinc(II) acetate	time	solvent	yield
4 equivalents	1 day	DMF/$CHCl_3$/MeOH	12%
4 equivalents	1 day	DMF	17%
12 equivalents	1 day	DMF	86%
12 equivalents	2 days	DMF	94%
12 equivalents	3 days	DMF	94%

The second series of experiments focused on the effect of the stoichiometry of zinc(II) acetate. When the reaction was carried out with four equivalents the yield was rather unsatisfying at 17% in pure DMF. Increasing the stoichiometry to 12 equivalents, while keeping all other conditions constant, led to a significant improvement with the yield increasing to 86%. Finally, the influence of the reaction time was investigated. Extending the duration from one to two days resulted in an increase in yield from 86% to 94%. However, further elongation to three days provided no additional benefit, with the yield plateauing at 94%. This suggests that the metalation reaction reaches completion within two days under the chosen conditions.

In summary, these optimisation experiments show that the most effective protocol for the metalation reaction is the use of 12 equivalent of zinc(II) acetate in DMF with a reaction time of two days. The excess of zinc(II) acetate can be easily removed during the work-up due to

its water soluble character. This procedure provides high yields of the metalated porphyrin while avoiding the complications associated with mixed solvent systems.

Cobalt-5,10,15,20-tetrakis(4-pyridin-4-yl)porphyrin (Co-TPyP, green)

The final compound of the supramolecular assembly **cat1** is the catalytically active cobalt porphyrin. This can be formed by metalation of the previously synthesised **TPyP** with cobalt(II) acetate according to literature.[108]

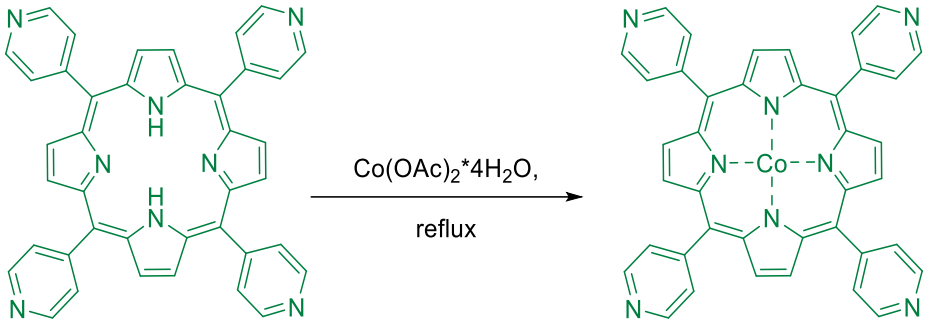

TPyP **Co-TPyP**

Table 10: Condition screening for cobalt-metalation of **TPyP**.

cobalt(II) acetate	time	yield
4 equivalents	5 hours	90%
4 equivalents	3 days	92%

The reaction was initially attempted as described by *Sakai et al*. by mixing **TPyP** with four equivalents of cobalt(II) acetate in DMF, followed by heating to reflux for five hours. This provided the product in 90% yield, however, the purification of this compound caused some difficulties. Porphyrins not only tend to form π-stacks, due to their large and flat conjugated system, but also are metalated pyridine-porphyrins forming coordinating bonds between the positively charged metal and the free electron pair of the pyridyl-groups nitrogen atoms.

Additionally, the employed excess of cobalt(II) acetate can be incorporated in these stacks, hindering its' proper removal. This leads to an enormously stable network of porphyrins shown in figure 49, whereby this compound exhibits very poor solubility in most organic solvents. This hinders purification significantly, since impurities are nearly impossible to remove once they are incorporated in the stacks. Only by gradually breaking up the stacks the impurities can be removed. In order to loosen up the tightly packed system recrystallisation in methanol was attempted to remove excess metal salts. Thereby, the solid was not dissolved completely at reflux temperature, as it would usually be the case in recrystallisation. However, the dark colour

and red fluorescence of the suspension indicated at least partial solubility of the product, which allowed to remove impurities step by step. Afterwards, this step was repeated in chloroform in order to remove remaining starting material. **TPyP** is indeed able to form π-stacks, as many other porphyrins, but is due to the lack of cobalt-nitrogen coordination significantly better soluble. Thereby, unmetalated starting material is soluble in chloroform and can be removed rather easily.

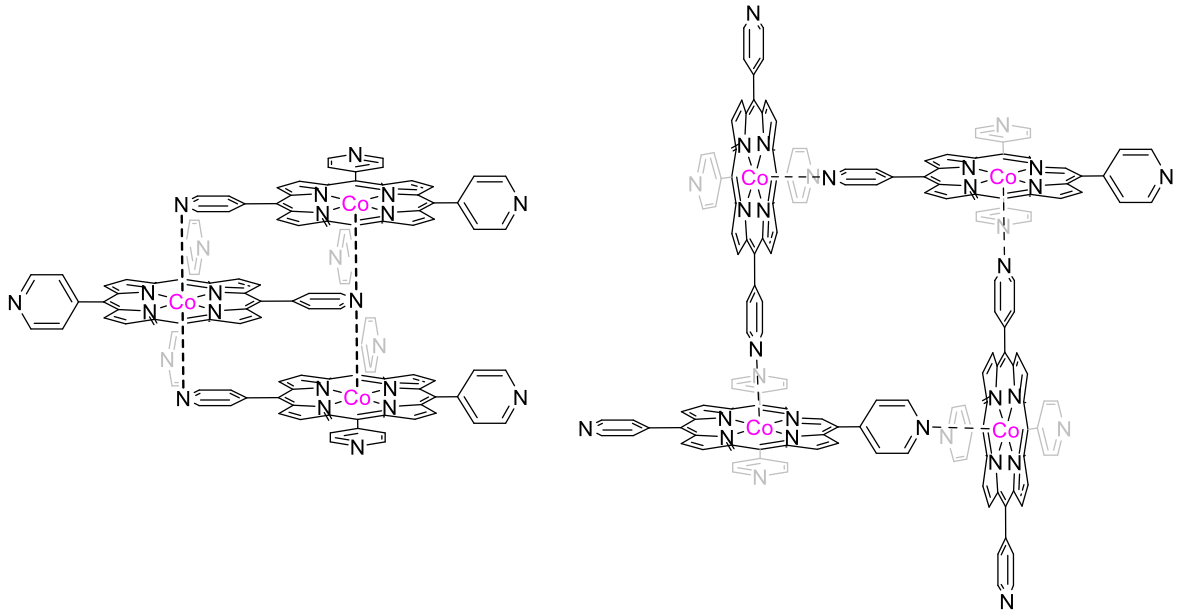

Figure 49: Potential networks of stable porphyrin stacks of **Co-TPyP**.

After modifying the purification method, the reaction time was elongated from the initial five hours to three days. However, this only increased the yield from 90% to 92% giving no significant benefit of the longer reaction time. Due to the modifications of the synthesis, this building block could be formed in a good overall yield of 47% (51% in the porphyrin synthesis, 92% for the metalation).

Alternative supramolecular catalyst

An alternative catalyst design can prevent the issue of the rather low yielding synthesis of the bipyridine fragment (red) and **TAPP** (blue) of the previously introduced supramolecular host **cat1**. In this design, shown in figure 50, the porphyrin is enlarged by one phenyl-ring on each strand (turquois), whereby the bipyridine aldehyde can be shortened to just one pyridine moiety (pink). The 2-pyridinecarbaldehyde is significantly cheaper than the bipyridine aldehyde employed in **cat1** and consequently must not be synthesised but can be acquired commercially.

An additional advantage of **cat2** compared to **cat1** is the better stabilisation of the labile imine bond. Both systems are formed by subcomponent self-assembly, building the metal coordination between nitrogen and iron at the same time as the imine condensation. However, in **cat1** the imine is not involved in the metal coordination, since only both nitrogen atoms of the bipyridine bind to the iron-atoms, forming the corners of the cubic system. In **cat2** however, the imine is involved in the metal coordination, stabilising it better than in **cat1**.

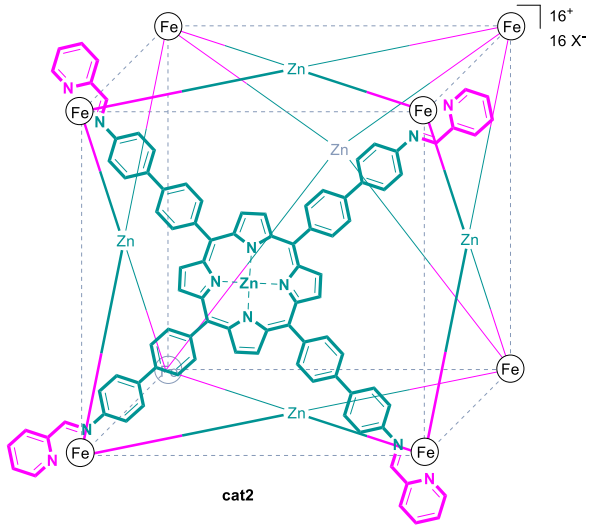

Figure 50: Simplified structure of **cat2**.

Lastly, although the zinc-porphyrin used in **cat2** is larger than the **Zn-TAPP** of **cat1** both are formed in a three-step synthesis. The synthesis of **Zn-TAPP** additionally suffered from low yields in the reduction of **TNPP** to **TAPP**, which is prevented with **cat2**. Since both supramolecular hosts provide similar cavity volumes, the catalytically active **Co-TPyP** moiety is suitable for both systems.

Zinc-(porphyrin-5,10,15,20-tetrayl)tetrakis(([1,1'-biphenyl]-4-amine)) (Zn-TAbPP)

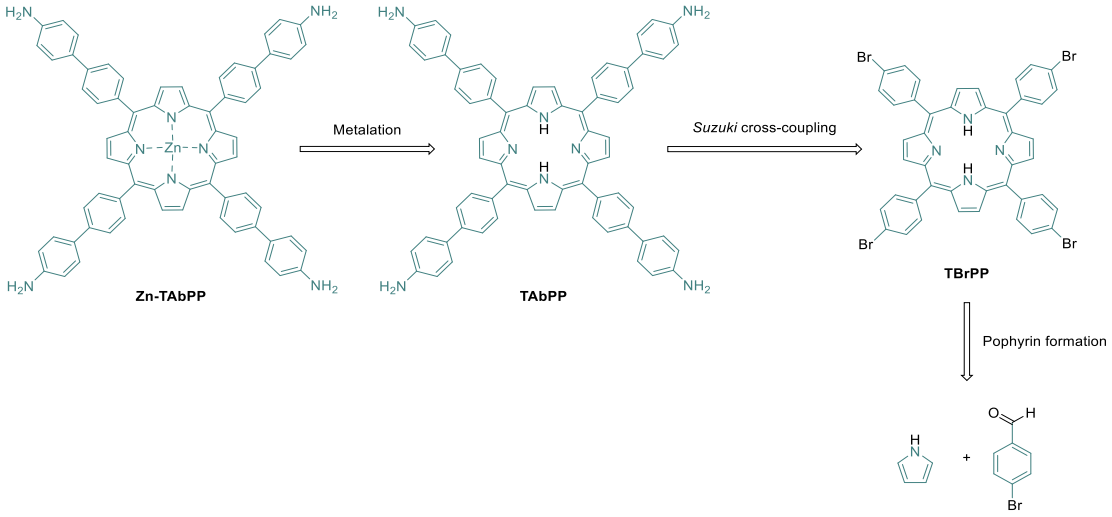

Figure 51: Retrosynthesis of **Zn-TAbPP**.

The first step in the synthesis of the metalated tetraaniline-biphenyl-porphyrin (**Zn-TAbPP**), shown in figure 51, is the formation of a halogen decorated tetraphenylporphyrin. In the studies towards a more efficient porphyrin synthesis, described in chapter 8, *para*-iodophenyl-porphyrin (**TIPP**) and *para*-bromophenyl-porphyrin (**TBrPP**) were

synthesised. For the following *Suzuki* cross-coupling reaction **TIPP** would in general be the better substrate due to the lower stability of C-I bonds in comparison to C-Br bonds. However, not only the synthesis but also the handling of **TIPP** is significantly more challenging than for **TBrPP** due to the light sensitivity of most iodine-containing compounds. Additionally, **TBrPP** was obtained in 45% yield in comparison to **TIPP** which only yielded 30%.

Hence, the synthesis of the desired **Zn-TAbPP** was performed starting with a *Suzuki* cross-coupling of **TBrPP** with the *para*-aniline-pinacolester. The synthesis was carried out according to literature, however, here the more stable pinacol-ester derivative was used instead of the boronic acid as described by *Reek et al*.[83] This substitution of the boronic acid with the pinacol-ester was motivated by its higher stability under the applied conditions, which in turn facilitated handling and storage significantly. In literature, the *Suzuki* cross-coupling involving tetrabromophenylporphyrin **TBrPP** is typically performed at a very low concentration of 0.003 M with respect to the porphyrin substrate. Such rather diluted concentration is most likely chosen in order to address the well-known issue of poor solubility of porphyrin derivatives in many organic solvents. Nevertheless, DMF was chosen as the solvent, which has proven in this work to be the most efficient organic solvent for dissolving porphyrins. Due to this solvent compatibility, such an extensive dilution might not be necessary. This assumption was confirmed by the results in table 12.

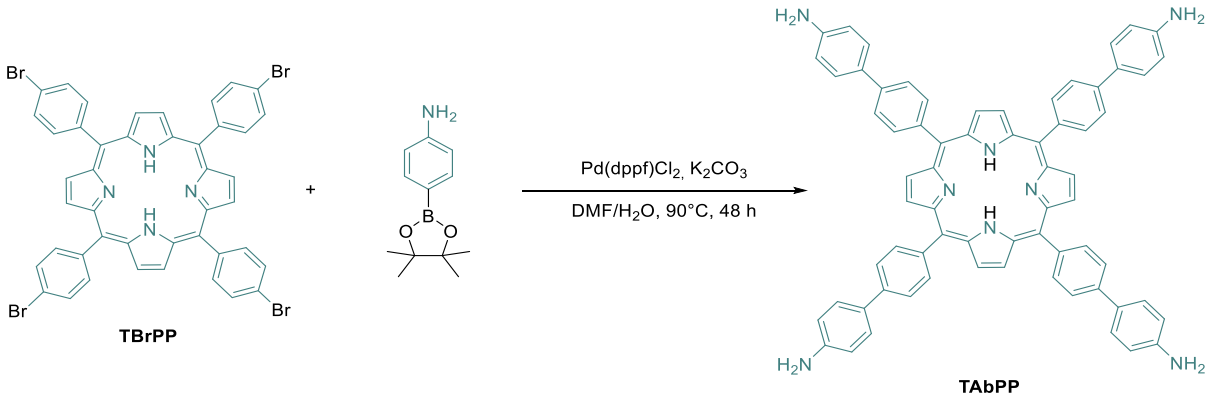

Table 11: Screening of reaction conditions for the *Suzuki* cross-coupling of **TBrPP**.

time	concentration	yield
2 days	0.003 M	38%
3 days	0.003 M	64%
2 days	0.006 M	81%
3 days	0.006 M	83%

First, the concentration of 0.003 M with a reaction time of 48 hours, as stated in literature, was applied, yielding disappointing 38% in comparison to the 90% yield reached by *Reek et al.* which might be explained by the higher stability of the employed boronic acid ester which can result in a reduced activity. To investigate whether the yield could be improved by extending the reaction duration, the same conditions were maintained, but the reaction time was increased to three days. This indeed led to an improved yield of 64%. Although this increase showed that the reaction benefits from longer duration, the obtained yield still fell short compared to the 90% reported by literature. Consequently, the reaction time alone was not sufficient to overcome this issue.

Given the improvable performance at 0.003 M, attention was shifted towards increasing the substrate concentration. By doubling it to 0.006 M, the outcome improved significantly. Even with a shorter reaction time of only two days, the yield increased to 81%. To test whether the yield could be increased even further, the same concentration was employed for an extended duration of three days. However, this adjustment only produced a small increase in yield, rising from 81% to 83%. This indicates that at this concentration the reaction is finished within the first 48 hours. The overall yield of 81% corresponds thereby to a yield of 95% for each coupling, which explains why with this yield the threshold of the efficiency is reached. In both experiments, the longer reaction time provides higher yields, which indicates that the optimum might not be reached but the small increase from 81% to 83% implies the presence of a plateau for the efficiency of this reaction.

Following the successful coupling, the next step was the metalation of **TAbPP** to yield the corresponding zinc-complex **Zn-TAbPP**, shown in figure 52.

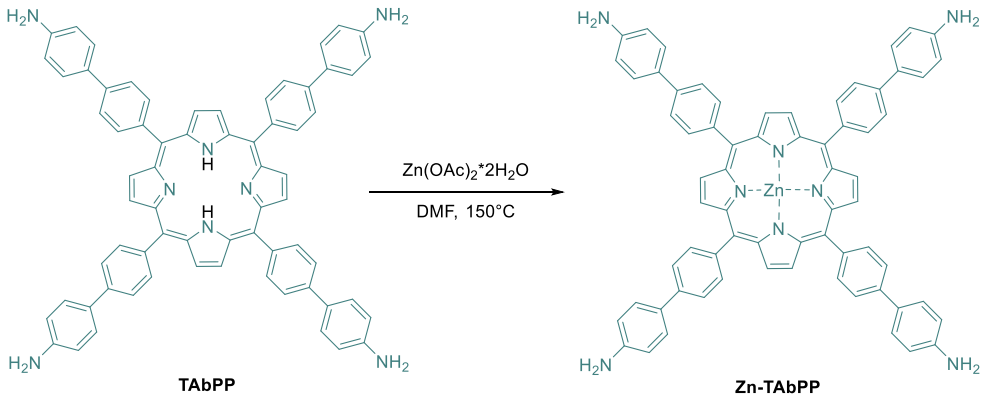

Figure 52: Metalation of **TAbPP** to **Zn-TAbPP**.

This was performed in close analogy to the metalation of **TAPP**, which has been discussed in detail in earlier chapters. In line with established procedures, zinc(II) acetate was added as the

metal source in over-stoichiometric amounts (12.0 equivalents), while DMF was employed as the solvent due to its observed capability to dissolve porphyrins and to facilitate efficient metal insertion, while still ensuring simple purification. The results of systematic studies on the effect of concentration and reaction time are summarised in table 13. In the first set of experiments, the concentration of 0.002 M was applied, identical to the conditions previously optimised for the metalation of **TAPP**.

Under these conditions, the reaction gave a good yield of 82% after only 20 hours, demonstrating the general efficiency of this modified protocol. When the reaction time was extended to 48 hours, the yield increased to almost quantitative 98%. This suggests that the reaction benefits from additional time at low concentrations, allowing near-complete conversion of the porphyrin to its zinc complex.

Table 12: Screening of reaction condition for the metalation of **TAbPP**.

concentration	time	yield
0.002 M	20 h	82%
0.002 M	48 h	98%
0.014 M	20 h	20%
0.014 M	72 h	44%

In analogy to the *Suzuki* cross-coupling reaction, it was investigated whether increasing the concentration accelerates the metalation process. Therefore, the porphyrin concentration was increased from 0.002 M to 0.014 M. However, after 20 hours the yield significantly decreased to 20% compared to the 82% at a lower concentration. Even an elongated reaction time of 72 hours only yielded the product in 44% and thereby remained less effective than the diluted system. These results reveal that the metalation of **TAbPP** is highly sensitive to concentration and proceeds best under relatively dilute conditions. A likely explanation therefore is that higher concentrations benefit aggregation of the porphyrin molecules in solution, which hinders the accessibility of the central cavity for metal coordination. With the building blocks in hand, the complex formation could be addressed.

10. Complex formation of supramolecular catalysts

The formation of porphyrin-based supramolecular cubes has been described on several occasions in the literature, reflecting the considerable attention these systems have received due to their well-defined geometry, host-guest properties and potential applications in catalysis and molecular recognition. Among the various reported examples, one of the most prominent is the supramolecular cubic host reported by *Nitschke* and co-workers in 2011. This system was constructed from six equivalents of **Zn-TAPP**, 24 equivalents of 2-pyridinecarbaldehyde and eight equivalents iron(II)-triflate, yielding a highly ordered and discrete cubic cage structure, shown in figure 53.[107]

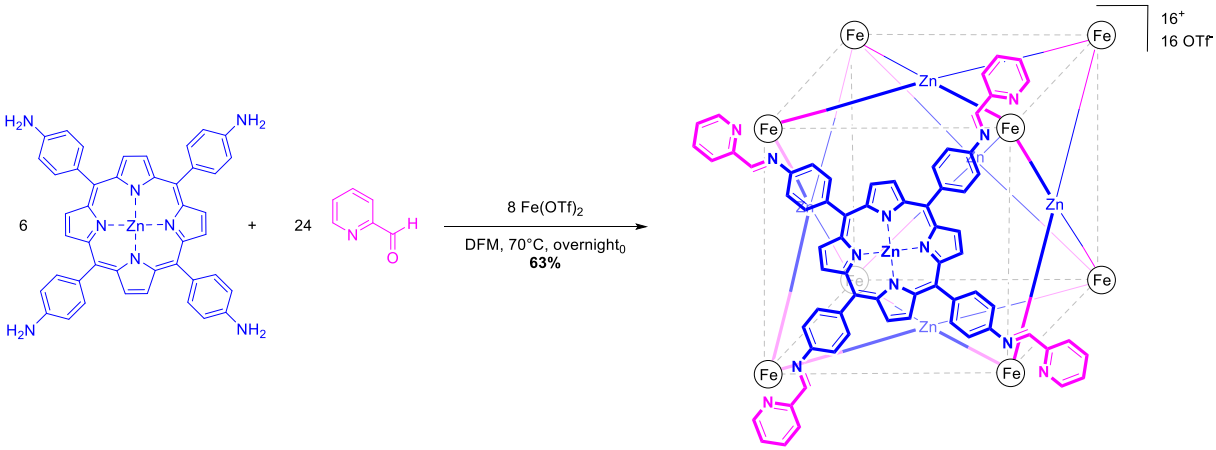

Figure 53: Supramolecular cubic host by *Nitschke* and co-workers.[107]

The self-assembly of this host was achieved by a subcomponent self-assembly process, which required carefully controlled reaction conditions to ensure successful cage formation. The procedure was carried out under an inert gas atmosphere in a *Schlenk* flask in order to exclude air, thereby minimising any potential oxidative side reactions. The three building blocks were used in the precise stoichiometric ratio, required for the cube formation, after which the atmosphere was changed three times to guarantee complete removal of oxygen. Subsequently, DMF was added and the mixture was heated to 70°C overnight. Thereby, the reversible dynamic covalent and coordinative bonds could form, leading to the thermodynamically most stable aggregate. Upon cooling to room temperature, diethyl ether vapours were allowed to slowly diffuse into the solution, which gradually reduced solubility and promoted the stepwise growth of dark, needle-shaped crystals.[107]

Building up on this work, *de Bruin* and co-workers later adopted a closely related strategy to prepare analogous porphyrin-based supramolecular catalysts. While the overall design and stoichiometric principles were comparable, they introduced subtle changes in the synthetic

procedure. In their approach, all components were likewise combined in a *Schlenk* tube, while additionally excluding water from the reaction environment. For this reason, the reaction vessel was flame-dried, ensuring the complete removal of residual moisture that could potentially disrupt the assembly process, by cleaving the imine bonds. Following this, the atmosphere was changed three times and after DMF was added the mixture was heated to 70°C for 16 hours. After cooling to room temperature, the resulting solution was added to diethyl ether directly, which induced precipitation of the cage structure. The solid was collected by filtration, dissolved in DMF and the solvent was removed under reduced pressure, yielding the supramolecular cube in isolated form.[81]

In the underlying studies, different approaches were tested in order to form the desired supramolecular host. A major impact on the formation of three-dimensional supramolecular structures is generated by the interior of these aggregates. On the one hand, templates can be used in order to benefit the formation by already introducing a certain geometry which will be adapted of the other building blocks.

Therefore, the catalytically active cobalt-porphyrin represents a particularly illustrative example to underline how template effects can drive and stabilise the formation of supramolecular architectures. The cobalt-porphyrin scaffold, with its peripheral pyridine substituents, offers well-defined coordination sites that can selectively interact with positively charged or polarised species such as zinc ions. The pyridine moieties provide a fixed orientation in space, due to the planar geometry of the porphyrin macrocycle. Specifically, they provide an angle of 90° between adjacent coordination sites. Upon coordination of zinc ions to the pyridine groups in **Zn-TAPP**, the first level of supramolecular orientation is already achieved, as the metal-ligand interactions benefit a box-like framework around the porphyrin centre. This partially assembled motif functions as a preorganised template, aiding the overall self-assembly in the formation process. In the absence of this template effect, the components would remain in solution, forming a vast number of conformations with significantly lower tendency to form a discrete, ordered architecture. Thus, the zinc coordination directs the system towards the correct spatial arrangement required for cube formation.

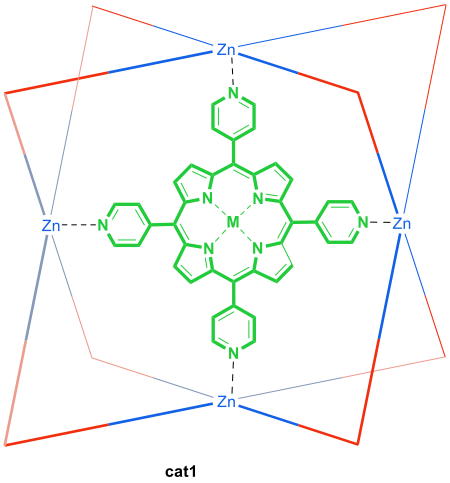

Figure 54: Template effect evoked by **TPyP**.

As illustrated schematically in figure 54, even in the absence of iron ions, this preorganisation could benefit the pseudo-cubic arrangement of porphyrin-units. Once iron(II) ions are introduced, their octahedral coordination geometry provides additional stabilisation by occupying the cube's corners, bridging the individual subunits and "locking in" the final structure. This cooperative action highlights a fundamental principle of supramolecular chemistry: template effects not only reduce the entropic barrier of assembly but also channel the system into the thermodynamically most favourable product by aligning multiple weak interaction in a synergetic manner. However, the order of steps in the assembly remains unclear.

This principle was adapted by *de Bruin* and co-workers.[81] Instead of first assembling the supramolecular host in its "empty" form, with no **TPyP** present inside its cavity, they directly constructed the "filled" supramolecular catalyst additionally through a one-pot synthesis. In this approach, the templating guest is present during the assembly process, guiding the formation of the host framework. This offers several advantages. On the one hand, the beneficial template effect is employed since the **TPyP** stabilises the developing architecture, promotes correct connectivity, and thereby, leads to a more efficient cage formation. On the other hand, the direct synthesis of the host-guest complex in a single step shortens the overall process, requiring only one purification step instead of multiple ones.

In contrast, synthesising the "empty" **cube1** beforehand, while beneficial in certain aspects, comes with additional challenges. The **cube1** is more versatile, as it can be modified post-assembly, allowing the easy and fast exchange of the catalytically active species, and thereby, addressing different catalytic conversions. However, in this pathway two separate purification steps are necessary, one after the initial host assembly and the other after introducing the **TPyP** into the cavity. This not only increases the synthetic effort, but also raises the risk of yield losses during the purification. Consequently, the one-pot formation of the filled supramolecular catalyst provides a more efficient and practical route, especially when the guest, which will be encapsulated, is already known in advance and does not have to be exchanged.

The other important aspect of how the interior of a supramolecular host can influence its formation is the occupation of the volume within its internal cavity. In both supramolecular cubes **cat1** and **cat2**, the templating **Co-TPyP** occupies the central space, but it does not fill the entire void. The remaining volume is not left empty, as depicted for simplicity in previous figures, instead it is occupied by solvent molecules. These play a crucial stabilising role by

balancing the overall thermodynamic of the assembly and prevent the collapse or decomposition of the host structure.

This highlights how the void volume inside supramolecular structures influences their stability and formation process. Empty cavities tend to be destabilising upon creating unfavourable enthalpic and entropic contributions, as unsatisfied interactions or unwanted conformational flexibility. By filling these cavities, solvent molecules can contribute to the overall stability by formation of weak but cumulative interactions, such as *van der Waals* or hydrogen bonding. Thus, the interior environment is no passive structural feature but an active part of maintaining the hosts integrity.[109]

This principle can explain, why *Nitschke* and co-workers chose to isolate their cubic cage by crystallisation instead of using the method applied by *de Bruin* and co-workers, in which the supramolecular structure was dissolved and the solvent was subsequently removed under reduced pressure. Supramolecular complexes, particularly in solution, are vulnerable structures, especially towards the removing of solvent from the cavity, since their stability depends on a balance of non-covalent interaction, that are dynamic and reversible. This reversibility is advantageous during the self-assembly process, as it allows the system to correct “mistakes” and thereby, form the thermodynamically most stable aggregate. However, the same feature can become problematic after the desired structure has been formed.

When the supramolecular cage is redissolved following the synthesis and the solvent is removed under reduced pressure, the dynamic equilibrium is disturbed. Instead of preserving the intact cage, the removal of solvent can shift the equilibrium back towards the dissociated building blocks or incomplete assemblies. As a result, the carefully constructed architecture can be reorganise to an undesired polymeric structure before it can be successfully isolated. Crystallisation, in contrast, provides a gentler and more stabilising route.

For this reason, *Nitschke’s* choice to isolate the product through crystallisation can be considered the safer and more reliable option. This becomes especially important in their case, since the cubic cage was formed without an additionally stabilising template inside. Thereby, the host is more prone to structural collapse under destabilising conditions.

In the underlying studies, attempts to form both supramolecular cubes, **cat1** and **cat2**, initially failed to yield the desired product when the isolation method employed by *de Bruin* and co-workers was applied. The sensitivity of the cage in solution lead to partially or fully disassembling of the already formed cage, preventing successful isolation of the intact product.

To circumvent this issue, an alternative strategy was employed in which the cage structure was precipitated directly from the reaction mixture using diethyl ether, followed by careful filtration. This method allowed the supramolecular cubes to be isolated in a solid form, while preserving their structural integrity.

In addition to the altered isolation procedure, the influence of oxygen and water content during the complexation process were studied. Both factors were presumed to have potential impacts on the efficiency and selectivity of cage formation, likely due to their interaction with metal centres or labile coordination sites. The results for **cat1** and **cat2** are summarised in table 14.

Table 13: Condition screening for the complex formation of **cat1** and **cat2**. Method 1 is precipitation in diethyl ether, followed by filtration, dissolving the solid in DMF and removing the solvent under reduced pressure. Method 2 describes the precipitation in diethyl ether, followed by filtration and collection of the solid from the filter.

cage structure	time	isolation	templating Co-TPyP	oxygen content	water content	product formation
cat1OTf	16 hours	method 1	no	inert gas	dry conditions	no
cat1OTf	72 hours	method 1	no	inert gas	dry conditions	no
cat1OTf	72 hours	method 2	yes	inert gas	dry conditions	yes
cat1OTf	72 hours	method 2	yes	inert gas	no dry conditions	yes
cat1OTf	72 hours	method 2	yes	no inert gas	no dry conditions	yes
cat2OTf	72 hours	method 2	yes	inert gas	dry conditions	yes
cat2OTf	72 hours	method 2	yes	no inert gas	no dry conditions	yes
cat2OTf	7 days	method 2	yes	no inert gas	no dry conditions	yes
cat2NTf_2	72 hours	method 2	yes	no inert gas	no dry conditions	yes
cat2NTf_2	7 days	method 2	yes	no inert gas	no dry conditions	yes
cat2NTf_2	7 days	method 2	no	no inert gas	no dry conditions	yes

These results of the condition screening for the complex formation of **cat1** and **cat2** show several important trends regarding factors that influence successful cage assembly.

For **cat1**, all attempts to isolate the cage using method 1, the procedure introduced by *de Bruin* and co-workers, in which the cage product is filtered, dissolved and subsequently subjected to solvent removal under reduced pressure, failed to yield the desired supramolecular structure.

Even when the reaction time was extended from 16 hours to three days, no improvement was observed. This indicates that method 1 is insufficient to isolate the supramolecular cage. The process of dissolving the assembled structure and evaporating the solvent under vacuum likely destabilises architecture, leading to disassembly of the formed complex or the formation of a polymeric structure.

In contrast, when method 2 was applied, in which the cages were precipitated by the addition of diethyl ether and the resulting solid collected *via* filtration, successful product formation was observed in the presence of **Co-TPyP**. Remarkably, under these conditions, the supramolecular aggregate could be obtained after 72 hours regardless of the presence or absence of oxygen and water. Initially, the formation was carried out under inert and anhydrous conditions following the procedure of *de Bruin* and co-workers. This involved the use of oven-dried glassware, dry solvent and repeated evacuation-refill cycles of the atmosphere in the *Schlenk* tube prior to solvent addition. Subsequently, the reaction was repeated following the procedure of *Nitschke*, where only oxygen was excluded, without the need of dried glassware or solvent. Finally, the reaction was also performed without excluding either oxygen or water and once again the desired cage structure was obtained, demonstrating that the assembly process of **cat1** is robust towards water and oxygen, provided that a template benefits the formation and the isolation method is chosen appropriately.

The results for **cat2** align with this trend. When using method 2 in presence of **Co-TPyP**, **cat2** could be obtained under both strictly controlled exclusion of water and oxygen and under ambient conditions without such precautions. Even when the reaction time was extended to seven days, the outcome remained unchanged, yielding the desired product in all cases. This indicates that both supramolecular catalysts tolerate variations in oxygen and water content during their formation without compromising cage formation.

Analytical methods for structure validation

The formation of both supramolecular assemblies was checked by ESI (electron spray ionisation) mass spectrometry (MS), which is the most suitable method for labile structures as supramolecular aggregates, since it is a mild ionisation method. In the respective spectra, species with charges between +9 and +16 could be observed in a region of *m/z* (mass/charge) between 0 and 1200. These charges correspond to different numbers of counterions. In the formation of the complexes, either triflate or triflimide were used as counterions to the eight iron(II) ions, forming the edges of the cubic system. Both anions provide a charge of -1, so that 16 of them are necessary to cancel out the positive charge of the iron ions. The signal in the

mass spectrum with a charge of z = 16 consequently corresponds to the supramolecular assembly without any counterions present.

An example of such a mass-spectrum is shown in figure 55. In this case, a section of an electron spray ionisation spectrum recorded in positive mode (ESI-(+)) for **cat2**NTf_2 is shown on the left, covering the range of *m/z* value between approximately 760 and 1300. Within this window, several distinct peaks can be observed, each of which can be assigned to a particular charge of the molecular assembly in combination with the appropriate number of counterions. By comparing the experimentally measured values to theoretically calculated ones, the specific composition of the observed species can be assigned.

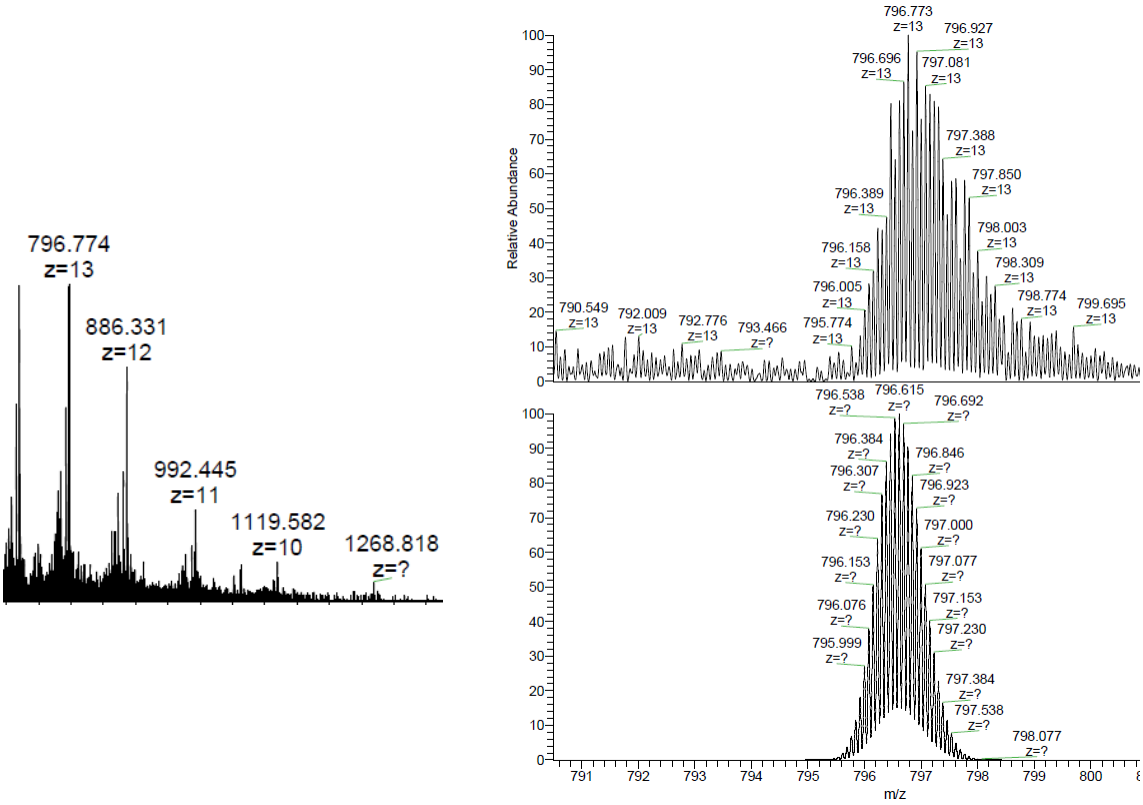

Figure 55: Section of ESI MS-spectrum of **cat2**NTf_2 (left) with the isotopic pattern of the signal at *m/z*=796.774 (top right) and the respective calculated isotopic pattern (bottom right).

For instance, the peak at *m/z* = 796.774 has been assigned to an ion with a charge of z = 13. Given that the overall charge of the assembly is +16, this assignment corresponds to three triflimide counterions. The calculated value for this species is 796.615 *m/z*. The slight deviation between the measured and calculated values can be attributed to the fact, that the labelled value does not always correspond to the most intense peak of the isotopic distribution, which can be seen by zooming in to the isotopic pattern or that multiple signals overlap, shown exemplarily in figure 55 on the right.

As an additional analytical method NMR analysis of supramolecular assemblies is in general a highly valuable and widely used tool to investigate their structural properties. This method provides insight into both the arrangement of the individual building blocks and the dynamic process that govern their interactions. Typically, in such systems, the observed signals tend to adopt a broader shape compared to those of small, well-defined molecules. This broadening arises from factors such as slow molecular tumbling in solution, conformational flexibility, or the presence of multiple equilibrating species. As a result, the spectra become more complex and it is sometimes challenging to assign the signals to specific molecular groups.

In the case of paramagnetic supramolecular assemblies, these difficulties are further increased. Paramagnetic centres introduce additional interactions with nearby nuclei, leading not only to significant peak broadening but also to drastic reductions in signal intensity. In some cases, resonances may become so weak, that they are barely detectable, complicating the analysis even further. Moreover, paramagnetic effects can cause substantial shifts in resonance frequencies, sometimes displacing peaks far away from the shifts observed for their diamagnetic analogues. While these shifts can provide unique information about the spatial proximity of nuclei to the paramagnetic centre, they simultaneously increase the complexity of the spectrum and hinder straightforward interpretation.

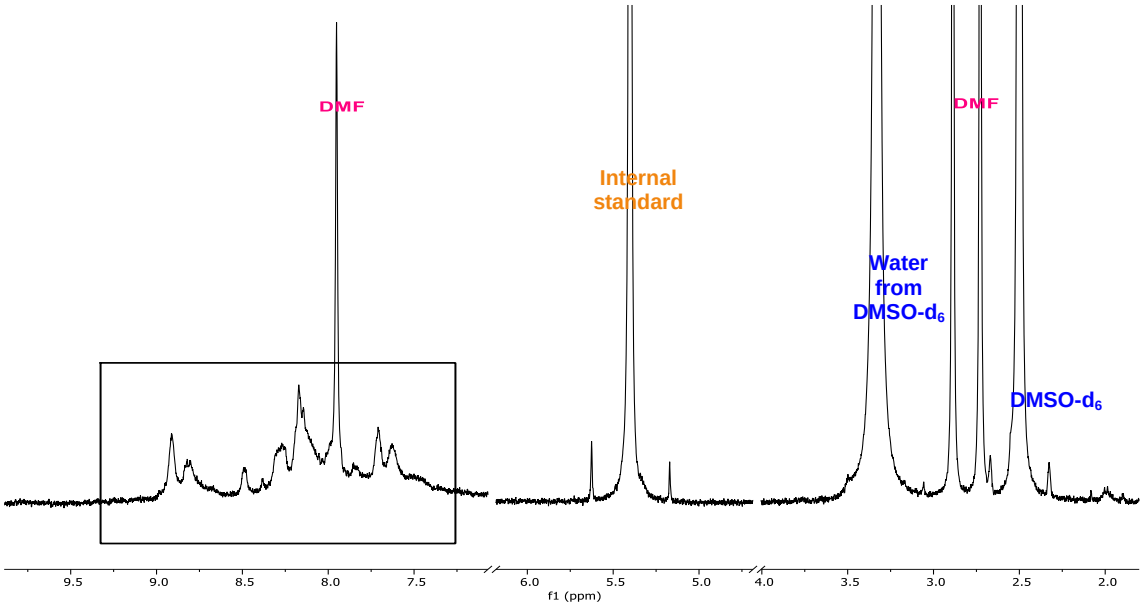

Figure 56: ^{1}H-NMR of **cat2**NTf$_2$ with residual DMF (pink), the internal standard (orange), the deuterated DMSO (blue) and the signals corresponding to the supramolecular assembly (black box).

Even more complicated is the analysis of paramagnetic supramolecular assemblies that additionally suffer from poor solubility. Solubility is a crucial factor in NMR spectroscopy, as insufficient concentrations of the analyte directly translate into weak or even undetectable

signals. Porphyrins, which serve as key building blocks in many supramolecular assemblies, are themselves only poorly soluble in most common organic solvents. As a result, these assemblies dissolve only in a very limited range of solvents, often requiring carefully chosen conditions or specialised solvent mixtures.[81,82,107] However, even in those cases, the concentration of the dissolved species typically remains low, thereby strongly reducing the signal-to-noise ratio in the spectra.

When this poor solubility is combined with the already introduced issues of paramagnetic effects, such as low intensities, peak broadening and extreme chemical shift deviations, the outcome is an even stronger decrease in the visibility of NMR peaks. This cumulative effect makes it difficult to extract reliable structural information and, in many cases, alternative characterisation methods must be considered to complement or substitute NMR analysis. In figure 56, the ^{1}H-NMR spectrum of **cat2**NTf_2 is shown, showcasing the effect of poor solubility and the paramagnetic nature of the system.

Additional to the standard ^{1}H-NMR, a DOSY measurement was performed for **cat1**OTf to determine an estimated diameter of the supramolecular system. To analyse the data from this experiment, the *Stokes-Einstein* equation is used, which is optimised for spherical systems. Even though the cubic supramolecular assembly is not spherical the calculation gives a decent estimation of the size of the assembly. Additionally, the cubic system has pores and a partially hollow inside, which alters its diffusion behaviour, which again can falsify the determined value. This experimental value can then be compared with the predicted diameter from a three-dimensional model. From the model, the diameter of one face (**A**) was determined with 27.164 Å and the diagonal of the complete system (**B**) with 37.622 Å. The experimental value with 29.5 Å lies between both predicted values, indicating a good fit to the theoretically expected value.

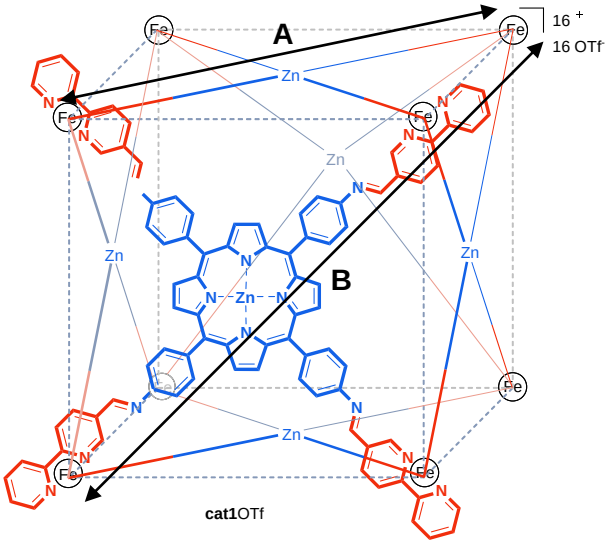

Figure 57: Simplified structure of **cat1** with marked diameters.

DMF content of supramolecular catalysts

In addition to providing structural information, these spectra also allow the detection of residual DMF content, which had been employed as the solvent during the complex formation. By introducing internal standards into the measurement, it was possible to quantitatively determine the amount of DMF present. At some extend DMF has to be present in the spectra since, as described in previous chapters, the solvent stabilises the internal cavity by filling volume, which is not occupied by substrates or the catalytically active **Co-TPyP**. The resulting DMF content, in weight percentage, is summarised and illustrated in figure 58, thereby offering direct insight into the extent of solvent incorporation within the assembly.

This plot clearly shows the gradual decrease of DMF content over time when the supramolecular assembly is subjected to fine vacuum conditions (10^{-2} mbar). Other than evaporation of solvent molecules while the supramolecular assembly is still in solution, which gradually increases the effective molarity, the overall aggregation remains unaffected in the drying process of the solid structure under fine vacuum, since the effective molarity does not change. This stability can be attributed to the fact that the supramolecular structure has already adopted its thermodynamically most stable form and, in the solid state, is significantly less sensitive towards external influences.

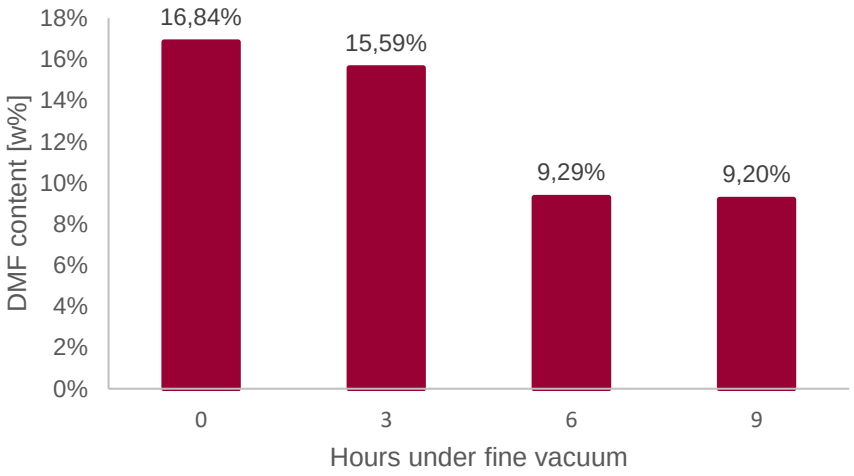

Figure 58: DMF content of **cat2**OTf after different durations under fine vacuum.

The first column, showing a value of 16.84 w% DMF, corresponds to the assembly direct after isolation prior to any drying treatment. After three hours at 10^{-2} mbar, the DMF content shows only a modest reduction to 15.59 w%, but following additional three hours, a larger decrease to 9.29 w% is observed. Beyond this point, the DMF content no longer decreases significantly. This behaviour suggests that the weakly bound DMF molecules, coordinated to the outer surface of the supramolecular host, are rapidly removed during the initial drying period,

whereas the remaining solvent molecules, located within the cavity of the host structure, are retained in the system. These studies on the DMF content are of considerable importance for the performance of the supramolecular catalysts. Since the remaining solvent significantly contributes to the overall weight of the assemblies, variation in DMF content directly affect the effective concentration of catalyst in stock solutions prepared for catalytic experiments, which will be discussed in more detail in chapter 12 in the course of catalytic experiments.

11. Introduction into cyclopropanation reactions

Cyclopropanation reactions are often carried out using transition-metal catalysts that operate *via* a radical mechanism. Thereby, iron(II/III) and cobalt(II) are among the most prominent and widely studied systems. Their success can be explained by a combination of favourable electronic and practical properties.[110]

Both iron and cobalt ions possess open-shell electronic configurations, which enable them to interact effectively with diazo compounds, the most common coupling partners in cyclopropanation chemistry. Upon interaction, these metals can form metal-carbene radical intermediates, which proceed through a stepwise radical addition pathway rather than the concerted carbene transfer which is performed by rhodium- or cupper-based catalysts. This, not only, has a major impact on the systems reactivity, but also offers unique opportunities for stereocontrol in combination with an appropriate ligand-environment.[111]

In addition to their mechanistic advantages, iron and cobalt stand out in terms of sustainability and practicality. Unlike rhodium, which is very expensive due to its low natural abundance, cobalt and iron are among the most abundant transition metals in the earth crust. This makes them significantly cheaper and widely available. Moreover, depending on the ligand-environment, they often exhibit lower toxicity compared to many other transition-metal catalysts. This combination of economic viability, reduced environmental burden and effective catalytic performance makes iron- and cobalt-based systems highly effective catalysts for cyclopropanation reactions.[112]

Porphyrins are widely used ligands in this class of transition-metal-catalysed transformations, due to their unique combination of structural robustness, electronic properties and synthetic versatility. The rigid, planar and highly conjugated macrocycle provides a stable environment that is able to stabilise unusual oxidation- and spin-states of the coordinated metal ion. This is especially useful in catalytic processes that involve open-shell intermediates, such as carbene radicals, which would otherwise be extremely reactive and thereby short-lived.[113]

A further advantage of porphyrins is their synthetic tunability. The macrocycle can be modified at different positions, enabling the introduction of steric bulk, electron-donating or -withdrawing substituents. These modifications allow the adjustment of electronic and steric environment of the central metal. As a result, key parameters of the catalytic system, like intermediate lifetime, redox potentials or transition state geometry can be controlled comparably easy. This degree of versatility makes porphyrin-based catalysts not only robust but also highly efficient tools for challenging reactions.

However, cobalt-porphyrin based catalysts are often performing rather poorly in the catalytic cyclopropanation of styrene derivatives. *De Bruin* and co-workers found an explanation for that, by investigation of the radical mechanism pathway.[111]

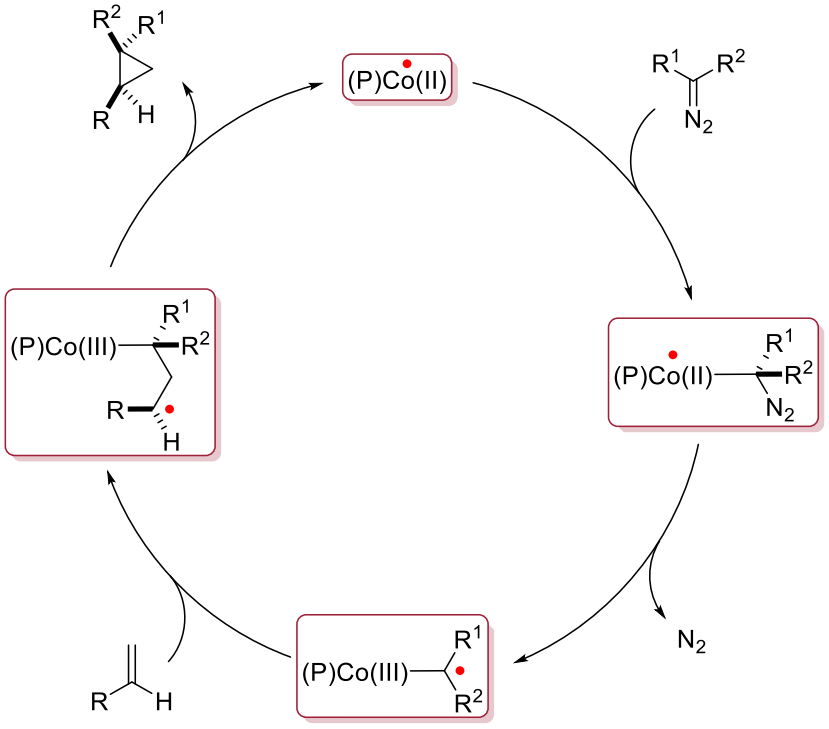

Figure 59: Catalytic cycle for the radical cyclopropanation.[111]

At the beginning of the catalytic cycle the cobalt in the porphyrin cavity has the oxidation state +II and thereby provides an unpaired electron. In the first step, the diazo component is added to the cobalt complex. Afterwards, elemental nitrogen is cleaved as a stable leaving group and a radical carbene intermediate is formed.

Unlike the classical electrophilic *Fischer*-type carbene species often encountered in organometallic chemistry, the intermediate formed in this catalytic cycle does not exhibit the typical carbene character. Instead, it is best described as a carbon-centred radical. This distinction arises from the unique stabilising influence of the cobalt porphyrin scaffold, which enables the radical nature of the carbene to be delocalised. As a result, the intermediate generated in this system does not follow the traditional pathways associated with electrophilic carbenes but instead is able to perform radical chemistry. Thereby, it is well suited for radical additions or radical substitutions, expanding the scope beyond standard carbene chemistry.[111]

In the following third step of the catalytic cycle, the alkene substrate is introduced to the radical carbene intermediate. This results in the formation of a new carbon-carbon bond. This step is

followed by the closure of the three-membered ring of the final cyclopropane product. At the same time, the cobalt catalyst is regenerated in its initial oxidation state, which closes the catalytic cycle and enables further turnover.[111]

A major issue arises when styrene derivatives undergo this transformation. As shown in figure 60, the intermediate formed after the third step is problematic. During the catalysis, the carbene radical, shown on the left, is formed. The delocalisation of the unpaired electron across the metal centre and the porphyrin scaffold plays a crucial role in the formation of this intermediate.[111]

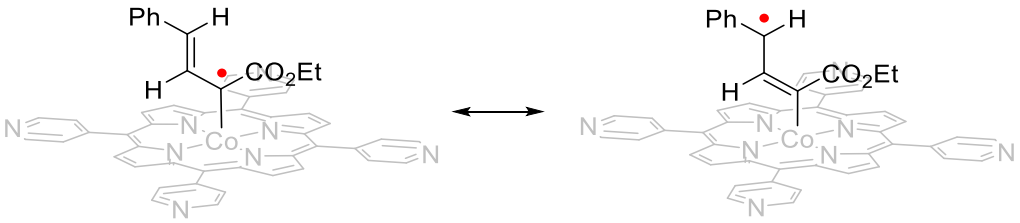

Figure 60: Equilibrium of two possible carbene radical species.[111]

However, when styrene is used the radical can undergo rearrangement to the benzylic position. Instead, the radical can undergo rearrangement, migrating to the benzylic position. This alternative radical species, shown in figure 60 on the right, is particularly favoured because benzylic radicals benefit from the resonance stabilisation in the ring system.

The general coexistence of these two radical forms would not hinder the catalytic process, since both intermediates remain in a dynamic equilibrium with each other. As a result, one might expect the reactivity of the system to be preserved, since either radical could, in principle, proceed along the intended catalytic pathway. However, the high thermodynamic stability of the benzylic radical introduces a competing side reaction. Two benzylic radicals can couple with one another in a C-C bond formation, yielding a dimeric by-product, shown in figure 61.[111]

This undesired radical-radical recombination effectively removes the active intermediates from the catalytic cycle, thereby reducing catalytic efficiency and lifetime. The tendency towards the side reaction represents a significant challenge in the use of styrene derivatives as substrates within this cobalt-porphyrin-catalysed system.

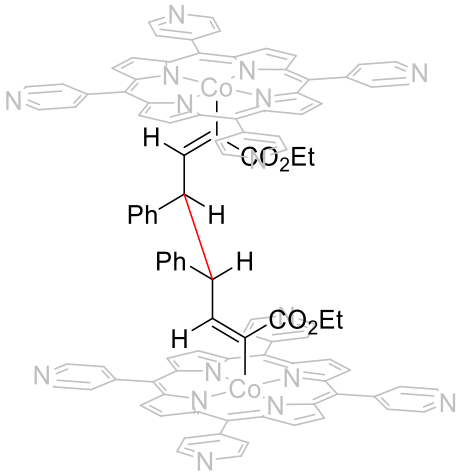

Figure 61: Dimeric species formed upon radical-radical recombination of benzylic radicals.[111]

In order to prevent the undesired radical-radical coupling, the reactive cobalt-porphyrin species can be confined within a well-defined supramolecular host environment, such as **cat1** and **cat2**. By encapsulating the catalytic centre, not only the advantages, commonly associated with supramolecular catalysis, such as preorganisation, enhanced selectivity and controlled microenvironments, are exploited, but the spatial isolation of reactive intermediates is also ensured. This controlled separation plays a crucial role in stabilising highly reactive species, thereby allowing the catalytic cycle to proceed with improved efficiency and reduced likelihood of unproductive side reactions.

In order to prove this principle, a series of catalytic experiments was carried out in which both supramolecular catalysts, **cat1**OTf and **cat2**OTf, were compared to the unencapsulated **Co-TPyP**. The chosen reaction was the cobalt-catalysed cyclopropanation of *para*-trifluoromethyl styrene.

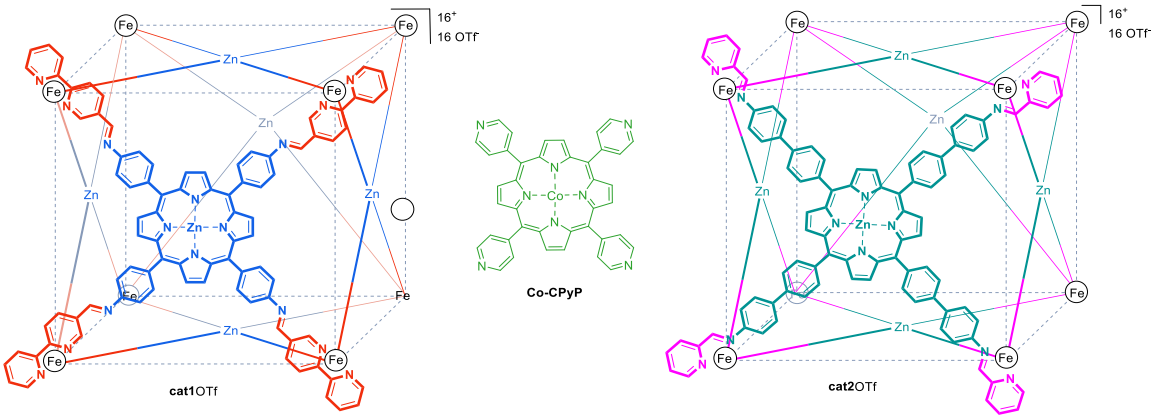

Figure 62: Overview of different applied catalytic systems.

The obtained results are summarised in figure 65, enabling a direct comparison of the catalytic activities under otherwise identical reaction conditions.

For this purpose, the *para*-trifluoromethyl styrene was chosen as alkene component, since it allows dual spectroscopic analysis. In addition to the conventional ^{1}H-NMR, the progress and outcome of the reaction can also be monitored by ^{19}F-NMR, thereby providing complementary insights into product formation, conversion and the presence of possible side products.

The reaction conditions were chosen as employed by *de Bruin et al*.[81] To ensure reproducibility and to avoid catalyst deactivation, all stock solutions of the substrates and the catalysts were prepared and combined under inert conditions inside a glovebox, thereby excluding moisture and oxygen. The catalyst was employed at a loading of 0.8 mol% relative to ethyl diazotate (**EDA**), which served as the carbene precursor. While **EDA** was employed in a stoichiometry of 1.0 equivalents, the *para*-trifluoromethyl styrene **P$_1$** was added in a slight excess of 1.2 equivalents. The solvent of choice was dry and degassed dimethylformamide, in order to ensure a completely dissolved catalyst. After combination of all stock solutions, DMF was added until the overall concentration of 0.3 M with respect to **EDA** was reached. After preparation, the vials were carefully sealed inside the glovebox and subsequently moved to the outside to perform and monitor the reactions, which were heated to 70°C for four hours.

The yield, diastereomeric ratio and **TON** were all determined by quantitative NMR analysis, of which one exemplary ^{1}H-NMR spectrum of **P$_1$** is shown in figure 63. In order to ensure a suitable measurement method, 10 µL of styrene was combined with 2 µL of dibromomethane and 2 µL of nitromethane. Thereby, the micromolar amount of substances could be compared and it is guaranteed that the ^{1}H-NMR analysis is indeed quantitative. In general, two internal standards are used to exclude potential handling errors. Both standards are chosen, since they produce distinct sharp signals in a region of chemical shifts, in which no products signals are expected, so that they don’t interfere with each other. In the following NMR, only one internal standard was used for a better clarity.

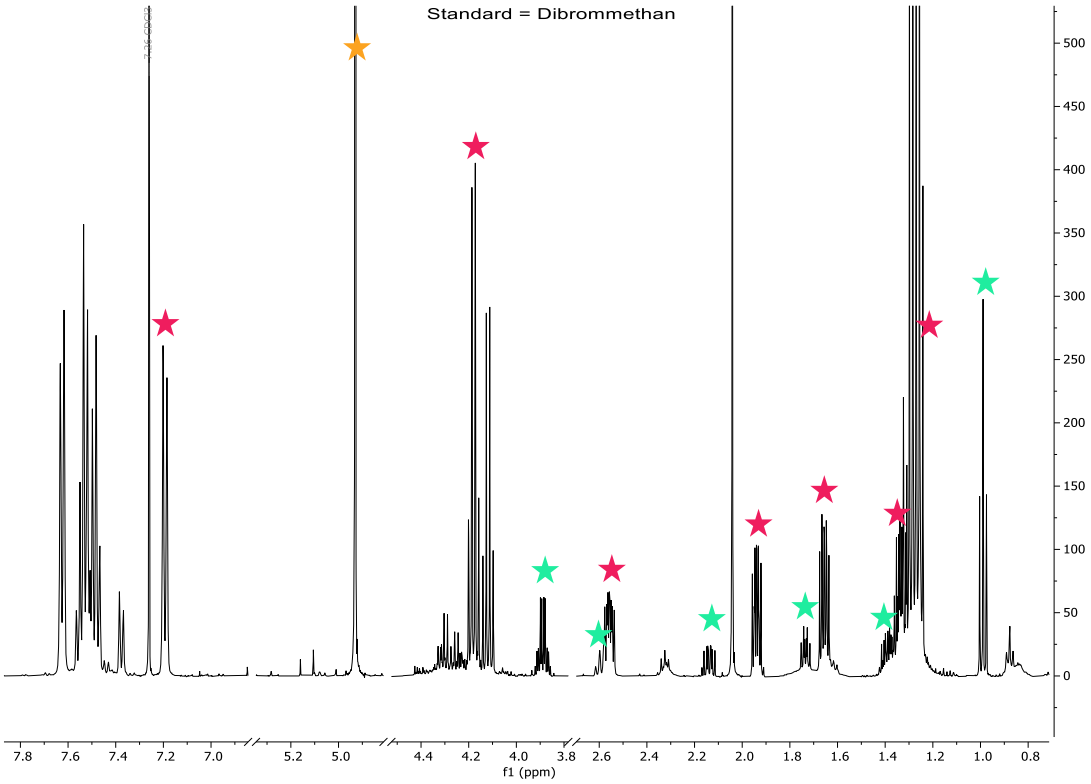

Figure 63. ^{1}H-NMR spectrum of the *cis*- (turquois) and *trans*-isomer (pink) of **P$_1$** in DMSO-d$_6$ with dibromomethane is internal standard (orange).

For analysis, a set of signals in the region between 1.6 and 1.8 ppm was chosen, in which the *cis*- and *trans*-isomer form sharp and distinct signals, which are not overlapped by other product, substrate or solvent signals. By determining the integrals of both signals, with respect to the internal standard, the exact amount of each species could be determined, giving the overall yield, which is combined of both enantiomers, the diastereomeric ratio and the turnover number.

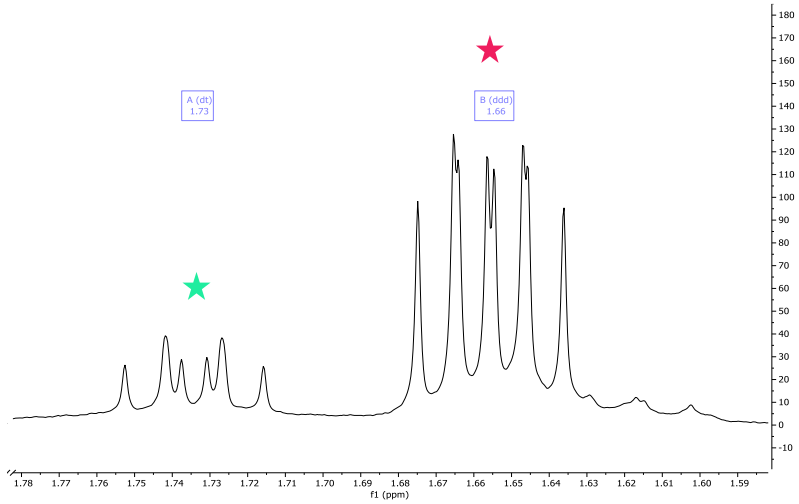

Figure 64: Region of the ^{1}H-NMR of **P$_1$**, used for analysis with the *cis*- (turquois) and *trans*-isomer (pink).

This set of signals remain relatively steady in its position, independent of the substitution of the aromatic ring, which allows its usefulness in the analysis of all following cyclopropanation products. Thereby, small changes can be observed in the chemical shift, with sometimes even the overlapping of both signals, which hinders the determination of diastereomeric ratios, but still allows the identification of yield and **TON**.

The **TON**, which is calculated by dividing the yield by the applied catalyst loading, thereby reflects the average number of catalytic cycles that a single catalyst molecule can perform before deactivation. Notably, the catalyst loading employed in these studies is already rather low by comparison to other well-established catalytic systems. For example, in palladium-catalysed cross-coupling reactions, such as the *Suzuki* reaction, typical catalyst loadings are in the range between 5-10 mol%. Even assuming a yield of 100% this would correspond to turnover numbers of only 10-20, which underscores the efficiency of the supramolecular catalysts in the present study.

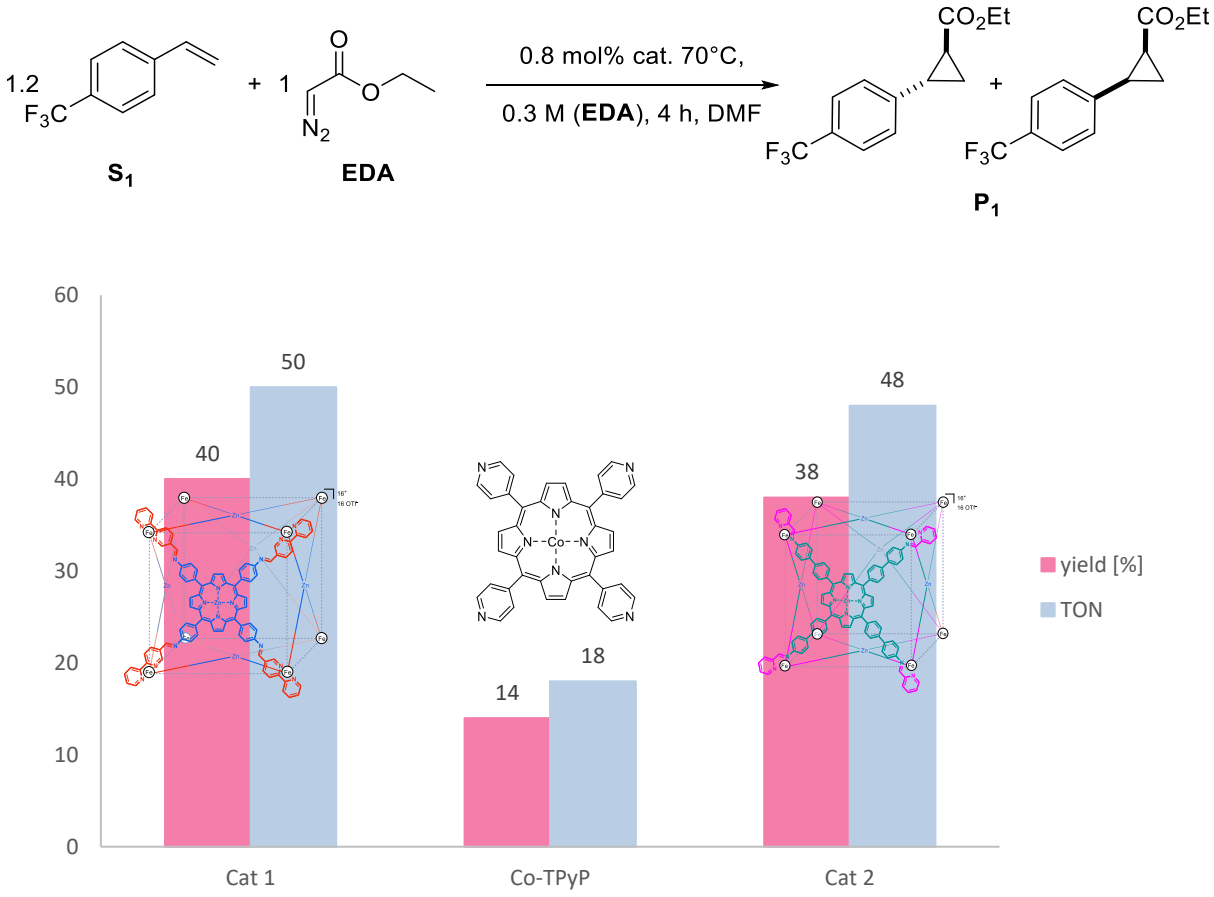

Figure 65: Comparison of **cat1**OTf, **Co-TPyP** and **cat2**OTf in the cyclopropanation of **S1**.

The results presented in figure 65 clearly highlight the significantly higher activity of the supramolecular catalysts compared to the unencapsulated analogue. **Cat1**OTf delivered $\mathbf{P_1}$ in a yield of 40%, while **cat2**OTf provided a comparable yield of 38%. These correspond to turnover numbers (**TON**) of 50 and 48. In contrast, the unencapsulated **Co-TPyP** reference catalyst performed considerably worse under identical conditions. It provided only 14% yield, combined of both diastereomers of the product, corresponding to a **TON** of 18 thus highlighting the beneficial effect of the encapsulation of the reaction inside a supramolecular assembly on catalyst stability and performance.

Following the initial screening, a second set of experiments was performed to investigate the catalysis under even lower catalyst loadings. Therefore, the 0.8 mol% catalyst loading was reduced further to 0.4 mol%. The results of this study are summarised in figure 66, enabling a direct comparison of the catalytic activity, not only between the species at this decreased catalyst loading, but also the performance of each system at two different catalyst loadings.

By comparing the results presented in both graphs, the beneficial effect of catalyst encapsulation becomes even more apparent. For the supramolecular systems, a slight increase in yield was observed upon lowering the catalyst loading.

The increase from 40% to 43% for **cat1**OTf and from 38% to 40% for **cat2**OTf are small but compared to the 14% and 8% yield for **Co-TPyP** they clearly demonstrate the efficiency of the encapsulated catalysts, which not only maintain but even enhance their performance under more challenging conditions with reduced catalyst concentration.

In contrast, the unencapsulated cobalt porphyrin **Co-TPyP** showed an opposite behaviour. Instead of benefiting from the reduced catalyst loading, its catalytic activity further decreased, yielding significantly less product than the supramolecular systems. However, a slight increase in the turnover number for **Co-TPyP** was observed. This provides further support for the mechanistic concept that encapsulation prevents the deactivation of active intermediates. At the lower catalyst loadings, fewer catalytically active species are present in solution and their overall concentration is decreased. Thereby, the probability of radical-radical recombination of the unencapsulated catalyst, leading to the deactivation of the catalyst, is reduced. For the encapsulated systems, the supramolecular host environment provides an additional protective effect, which supresses side reactions and enables higher efficiency.

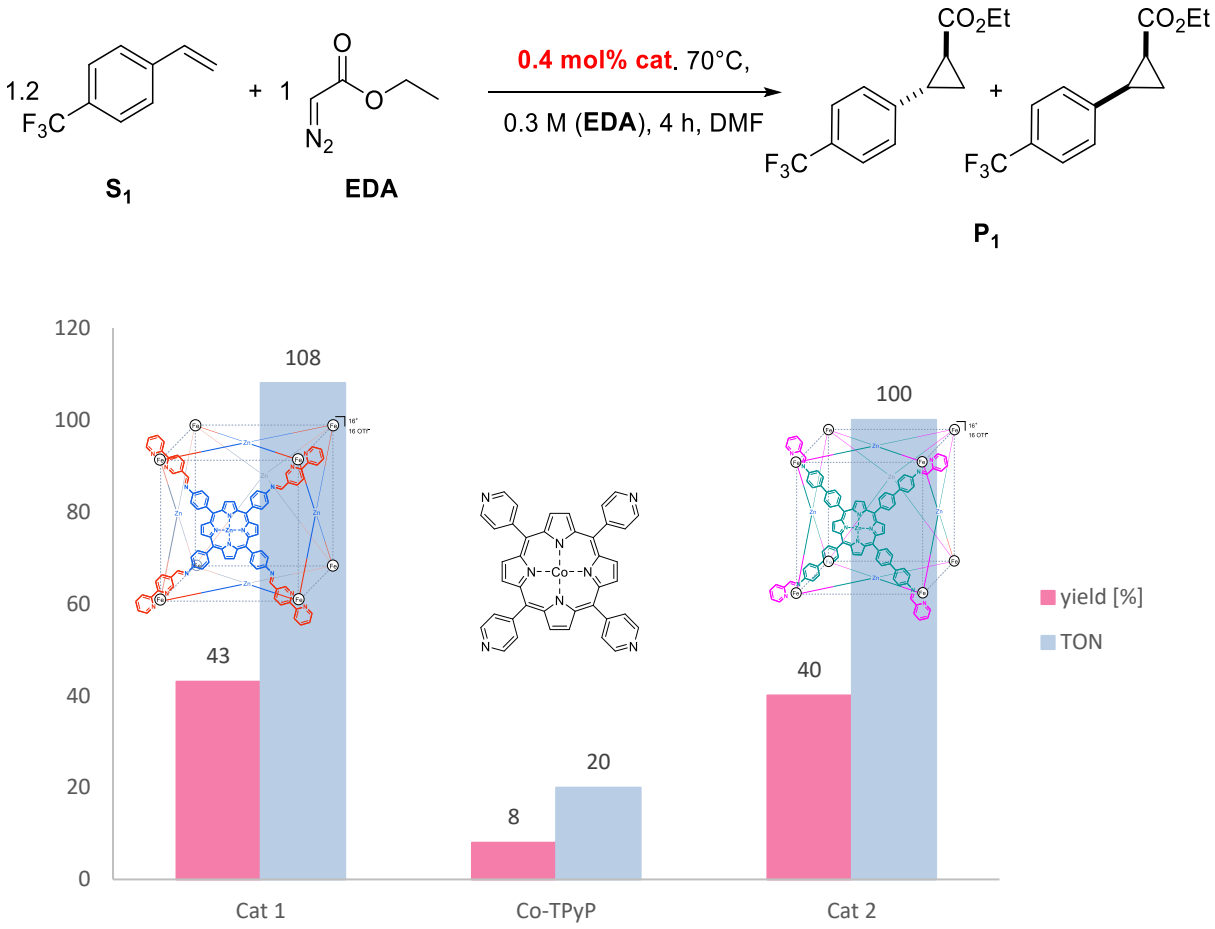

Figure 66: Comparison of **cat1**OTf, **cat2**OTf and **Co-TPyP** with a catalyst loading of 0.4 mol%.

These results not only prove the validity of supramolecular catalysis as a general concept, but also provide insights into the comparison of both supramolecular catalysts **cat1** and **cat2**. While **cat2** has a significantly shorter, and therefore higher yielding, overall synthesis, it is the economically more meaningful supramolecular assembly. The results in figure 65 and 66 show, that both supramolecular catalysts perform similar in the cyclopropanation of styrene derivatives, which favours synthetically more straightforward catalyst **cat2** for further investigations.

12. Condition screening for cat2OTf

Based on the promising catalytic performance observed in the previous experiments, shown in figure 65 and 66, the reaction conditions of the cyclopropanation of *para*-trifluoromethyl styrene were investigated further. Therefore, **cat2**OTf was selected as the supramolecular catalyst, owing to his high activity, while needing significantly fewer synthetic steps to form the supramolecular host structure.

Catalyst loading

First, the catalyst loading of the reaction was investigated further. For these experiments, the same substrates and reaction conditions, as employed in the previous experiments, were applied, with only varying amounts of catalyst. This strategy ensured better comparability between the data sets and allowed to only investigate the desired effect. The respective results are summarised in figure 67.

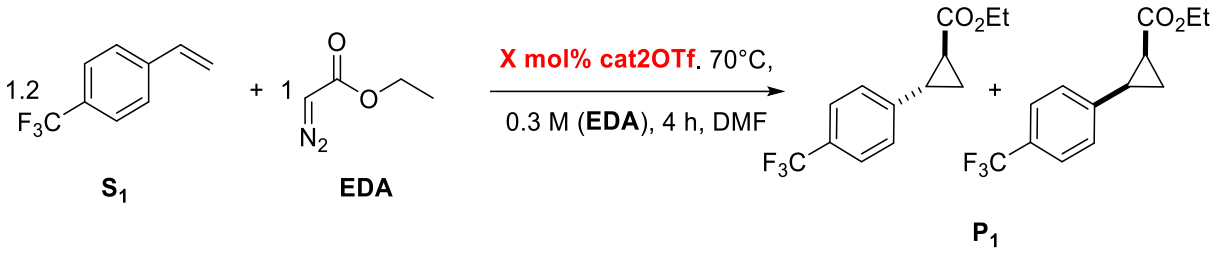

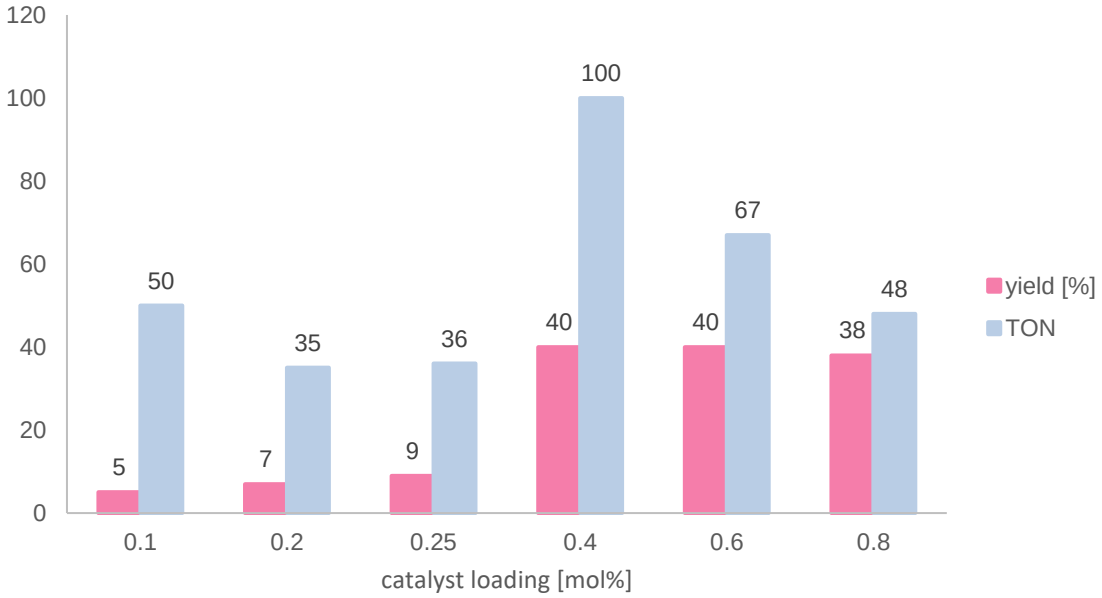

Figure 67: Screening of different catalyst loadings in the cyclopropanation of **S₁** with **EDA** by **cat2**OTf.

The results clearly show that for catalyst loadings of 0.4 mol%, 0.6 mol% and 0.8 mol%, the obtained yield remained nearly constant, falling within the narrow range of 38-40%, or in some cases showing no difference at all. This plateau suggests that under these conditions the catalytic efficiency is not strongly dependent on the amount of catalyst present, indicating that the system is already operating close to its optimal efficiency. However, this interpretation changes when the turnover number is considered additionally. Since the **TON** is defined as the yield divided by the catalyst loading, the turnover number increases significantly as the catalyst loading decreases. As a result, the lowest catalyst loading of these three experiments, 0.4 mol%, achieves the highest turnover number, thereby being the best value for the catalyst loading. The decrease of turnovers at higher catalyst loadings could be explained by catalyst aggregation into colloids, which is hard to determine due to the strong dark red colouration of the solution.

However, if the substrate would bind more strongly than the transition state, the catalyst would preferentially hold onto the substrate, lacking a driving force to convert it. On the other hand, if the product binds most tightly to the catalyst, then product inhibition arises. This occurs because the product, once formed, remains strongly bound, or even rebinds after dissociation, instead of freeing the active site for another reaction cycle. As a result, the catalyst becomes effectively “poisoned”, locked in an inactive state at which it is unable to bind new substrate molecules.[114]

To avoid this scenario, careful consideration of binding affinities is essential. More practically, strategies to minimise product inhibition can include the ensuring that the substrate is a more favourable coordination partner than the product, thereby promoting continual reaction turnover. Alternatively, adjusting the catalyst loading can be beneficial, by lowering the relative concentration of catalyst in the solution, which reduces the probability of the formed product to interact with a catalyst molecule.

However, when the catalyst loading was decreased even further the trend emerged, which is typically attributed to catalytic conversions, in which the yield decreases at lower catalyst loadings. Reducing the catalyst concentration beyond this value, decreased the yield even further, with loadings of 0.2 mol% and 0.1 mol% giving only 7% and 5% yield. These results indicate that below a critical threshold of catalyst concentration, the system becomes unable to efficiently catalyse the respective reaction, most likely due to insufficient availability of active sites to capture and convert the reactive carbene intermediates.

Substrate stoichiometry

The second parameter to be explored, was the stoichiometry of the styrene derivative **S$_1$** and **EDA**. In the preliminary studies, the *para*-trifluoromethyl styrene was used in a slight excess of 1.2 equivalents relative to 1.0 equivalents of **EDA**. This ratio was chosen in accordance to the procedure published by *de Bruin et al*. in 2013.[81]

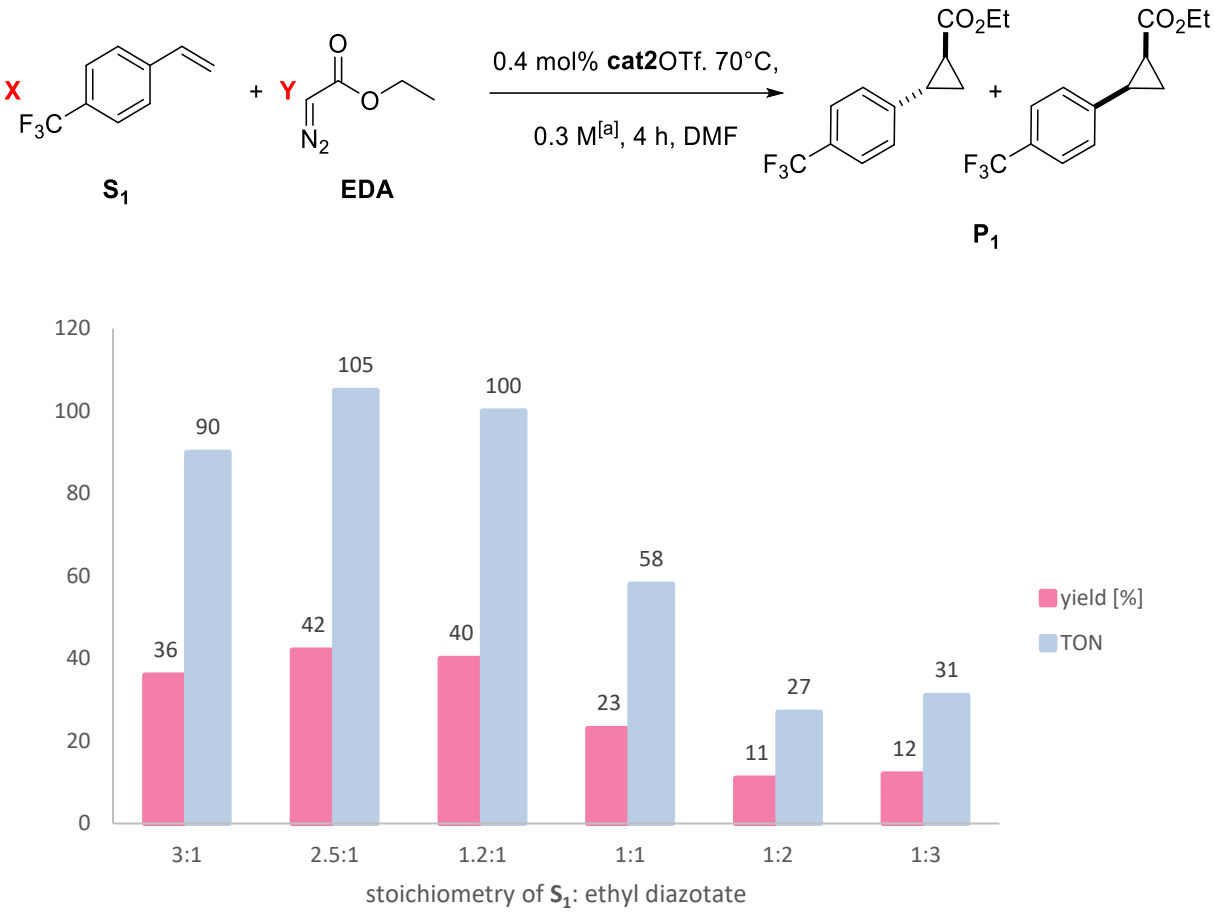

Figure 68: Screening of different substrate ratios of *para*-trifluoromethyl styrene/**EDA,** at a concentration of 0.3 M respective to the 1.0 equivalents of either **S1** or **EDA**[a].

In the present work, this parameter was systematically varied in order to evaluate the effect of substrate stoichiometry on the product formation. By altering the ratio of the styrene derivative and **EDA**, it was possible to investigate whether the reaction is limited by substrate availability, carbene transfer efficiency or side product formation. Beginning with the initial ratio of 1.2:1 (styrene derivative/**EDA**), which in earlier studies afforded **S$_1$** in a yield of 40%, the effect of increasing the styrene excess was investigated. When the ratio was increased to 2.5:1, the yield rose slightly to 42%, corresponding to a **TON** of 105. This indicates that a moderate excess of styrene can promote more efficient carbene transfer to the alkene or the presence

of side reactions in which the styrene is consumed. However, when the styrene excess was increased even further to 3:1, the yield decreased to 36%. This suggests that an excessive amount of alkene may lead to altered catalyst-substrate interactions that limit the overall efficiency or might benefit the formation of polymeric styrene structures. At a ratio of 1:1, the yield decreased significantly to only 23%, corresponding to a **TON** of 58. This indicates that a moderate excess of the styrene derivative prevents the undesired side reaction of carbene-dimerisation, which is a well-known issue for radical cyclopropanations, shown in figure 69.[115]

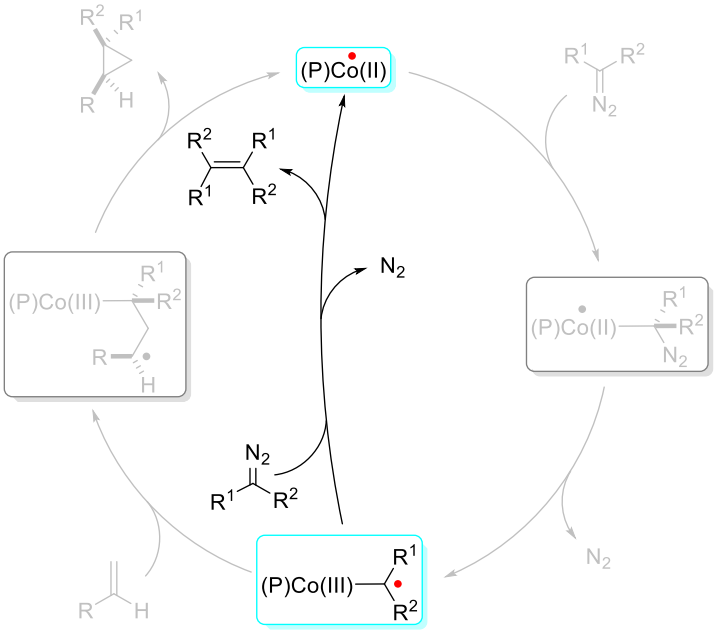

Figure 69: Dimerisation of carbene radical upon an excess of **EDA**.[115]

As shown in the catalytic cycle, the carbene radical, formed after the second step of the original catalytic cycle, can either proceed as desired, or interacts with another **EDA** molecule under cleavage of elemental nitrogen. This forms a stable alkene and regenerates the catalyst, without formation of the desired product. Therefore, an excess of **EDA** hinders the efficient synthesis of the cyclopropane product.

Finally, reactions with an excess of **EDA** were tested. At a ratio of 1:2 (styrene derivative/**EDA**) the yield dropped to 11%, while a 1:3 ratio yielded nearly the same, giving the desired products in 12%. These results showed that increasing the relative amount of **EDA** was strongly hindering the effective proceeding of the catalysis, likely due to the enhanced formation of carbene-derived side products such as dimers, which compete with product formation. An additional by-product can form *via* carbene polymerisation forming a carbon chain with ester substituents, which also decreases the amount of active catalyst.[116]

Temperature

The next factor, that significantly influences the outcome of chemical reactions, is the reaction temperature. Temperature not only dictates the rate at which molecules collide but also determines whether the energy threshold required for a reaction to proceed can be overcome. *De Bruin* and co-workers performed their cyclopropanation reactions in supramolecular complexes at 70°C,[81,82] which was therefore chosen as a starting point for further investigations in this study. To maintain highly comparable and reproducible results, the temperature was the only variable parameter during these experiments. Other conditions, such as the substrate stoichiometry, were kept constant, even though it had already been shown that 2.5:1 would be beneficial compared to the initial ratio of 1.2:1. This strict control allows to observe the isolated effect of varying temperatures on the reaction without the need to repeat previous screenings. The respective results are summarised in figure 70. The outcome at different reaction temperatures shows a clear trend. At 25°C, no product formation could be observed. This absence of reactivity can be explained by the insufficient thermal energy available, whereby the activation energy barrier is not overcome.

Upon increasing the temperature to 50°C, product formation becomes noticeable, with a yield of 17%, corresponding to a turnover number of 42. This marks the threshold at which the reaction begins to overcome the activation barrier, but only partially.

At 70°C, the yield rises significantly to 40%, suggesting that this temperature provides enough energy to overcome the activation barrier effectively. This result validates the conditions originally reported by *de Bruin* and co-workers.[81,82] However, further increasing the temperature to 85°C does not lead to any significant improvement anymore. This plateau indicates that once the activation barrier has been surpassed, additional thermal energy does not translate into enhanced performance. This suggests, that the catalyst already operates at its maximum efficiency at 70°C and the rate-determining step may no longer be directly influenced by the temperature.

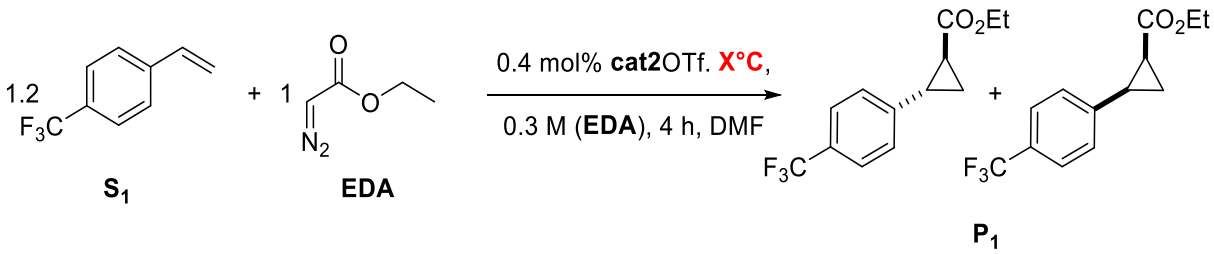

S1 **EDA** **P1**

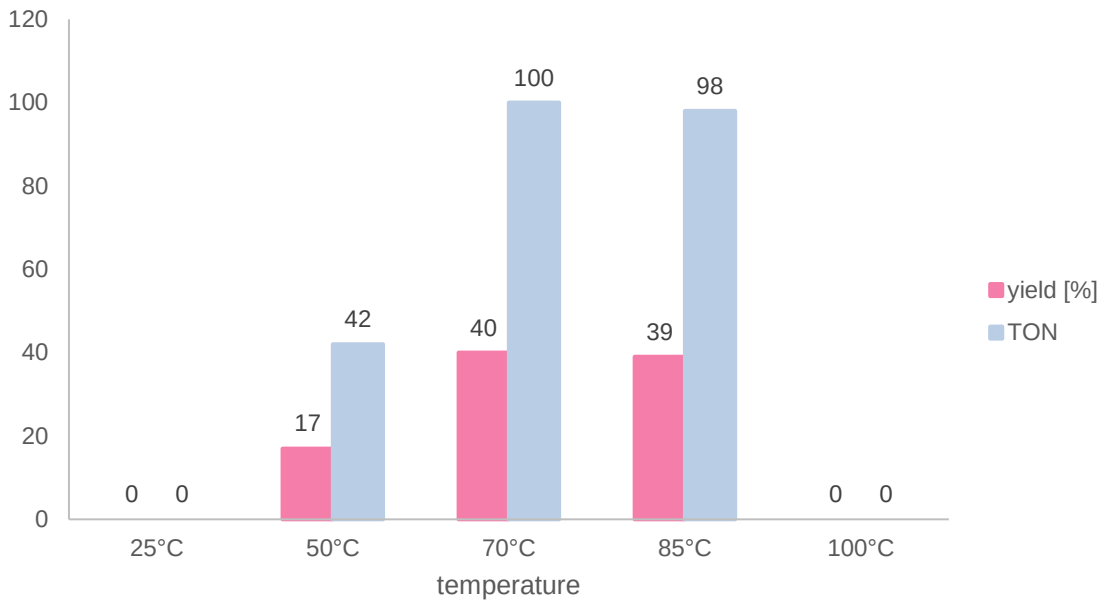

Figure 70: Results for the cyclopropanation of *para*-trifluoromethyl styrene with **EDA** at varying temperatures.

At 100°C the reaction outcome changes drastically, with no product formation observed. This loss of activity is most likely due to the thermal degradation of ethyl diazotate. At elevated temperatures, **EDA** can decompose by cleaving off elemental nitrogen, leading to the formation of dimers, thereby decreasing the supply of the reactive carbene precursor. As a result, the system fails to generate the desired cyclopropane under such harsh conditions.

Concentration

Next, the effect of the overall concentration was studied under the same experimental conditions as reported in the previous experiments. According to the literature, a standard concentration of 0.3 M relative to one equivalent of **EDA** was applied. The results are shown below.

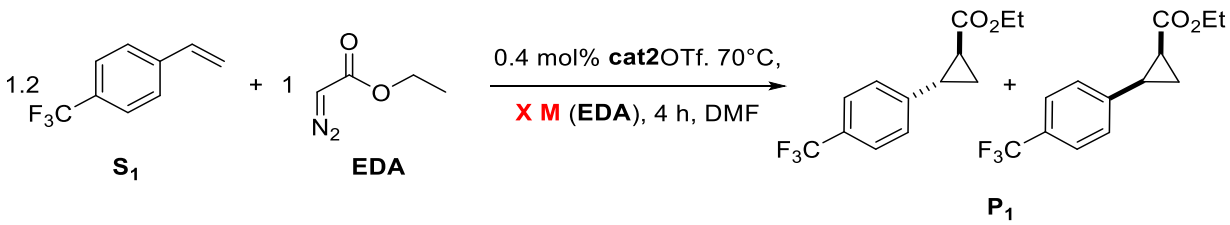

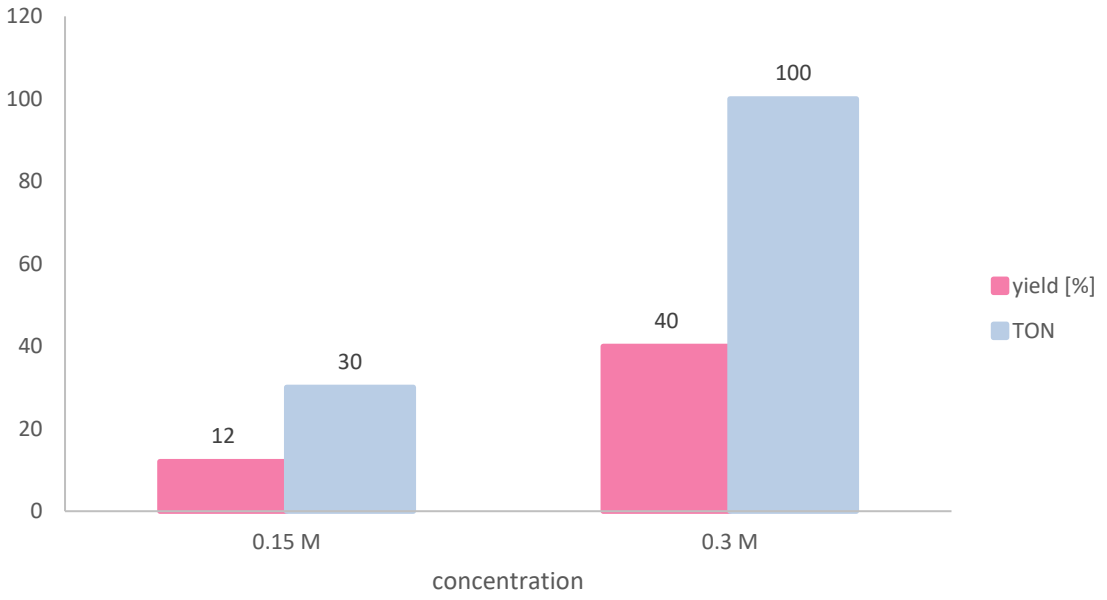

Figure 71: Results for the cobalt-catalysed cyclopropanation at different concentrations.

Monitoring the overall concentration is crucial because it directly influences the collision frequency of substrates with each other and the catalyst, similar to the temperature. At lower concentrations, the probability of productive collision between **EDA** and the styrene derivative is reduced, resulting in a decreased yield or incomplete substrate conversion. However, excessively high concentrations can accelerate side reactions, such as the dimerisation or decomposition of **EDA**, thereby lowering the efficiency of the desired reaction.

Since the stoichiometric studies had already proven that an increased concentration of **EDA** leads to faster formation of undesired side products, such as **EDA** dimers, further testing at concentrations higher than the 0.3 M reported in literature was avoided. To ensure that the focus remained on conditions likely to deliver promising results, attention was therefore restricted to exploring the effects of a lower concentration.

A decreased overall concentration of 0.15 M was therefore tested, under otherwise identical conditions. At this more diluted setting, the observed yield dropped significantly to 12% from initial 40% at 0.3 M. This decline can be explained by the lower effective collision frequency between substrate molecules and the catalyst. With fewer productive encounters per time, the catalytic cycle becomes less effective and a considerable portion of the substrates remain unreacted. These results highlight the existence of a narrow optimal concentration window: while higher concentrations enhance the formation of side products, lower concentrations lead to insufficient conversion, whereby the literature-reported 0.3 M already balance perfectly between productivity and selectivity.

This interpretation is further supported by comparing the substrate conversion achieved at both concentrations. At higher concentration of 0.3 M, 69% of the styrene derivative were converted, whereas at the more diluted 0.15 M setting, only 25% conversion was observed. This difference underlines the central role of concentration in catalytic efficiency. While yield reflects the amount of product, conversion provides additional insight into how much of the starting styrene derivative was consumed during the reaction. The difference therefore confirms that the decreased performance at 0.15 M is not due to side processes, but rather can be explained by the significantly reduced collision of substrates with each other or the catalyst.

Reaction time

Following the optimisation of temperature, catalyst loading, stoichiometry and concentration, the next parameter investigated was the reaction time, to investigate if longer reaction times would drive the reaction to a higher conversion. Studying the time-dependency of the reaction provides valuable insights into the turnover frequency (**TOF**) of the catalyst and the overall efficiency of the process. By systematically testing the reaction over defined intervals, it becomes possible to determine not only how rapidly the catalyst is able to convert substrates into product, but also the minimum time required to reach efficient conversion, which this series of experiments mainly focused on. Such kinetic information is particularly important to determine whether the reaction is limited by catalyst activity, substrate availability of by competing deactivation and side reactions that may occur as the reaction mixture ages.

In this study, the reaction was monitored over different time periods in order to evaluate its efficiency and progression over time. Therefore, the reaction was stopped after 4, 6 and 23 hours and after each of these reactions the yield and turnover number were determined. After four hours, the reaction had already reached a yield of 40% indicating that a substantial portion of the substrate had been converted into the desired product. When the reaction was performed for a longer time span of six hours the yield increased to 48%. This showed that the reaction does not reach completion within the first four hours, but still continues to proceed, however, with an already reduced rate. This lowered rate at only 40% yield suggests the presence of side processes as partial substrate depletion, as for dimers of **EDA**, or the establishment of an equilibrium state.

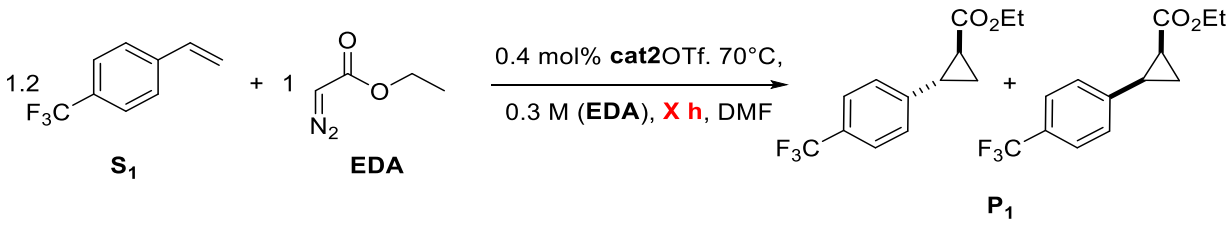

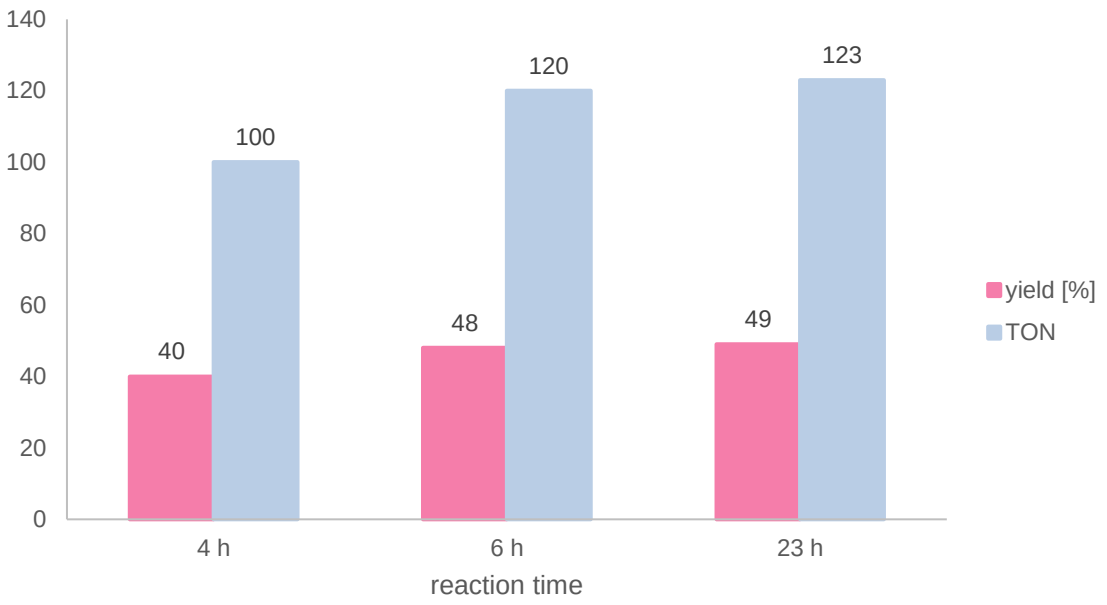

Figure 72: Results of the cobalt-catalysed cyclopropanation after different reaction times.

Extending the reaction time even further, from six hours up to 23 hours, did not result in a significant improvement in yield. This shows that after six hours, the reaction reaches a plateau without further conversion of substrate into product taking place. Therefore, the data suggest that six hours are the effective endpoint of the reaction, after which further reaction time does not lead to measurable benefits.

Sensitivity

The final property of the reaction mechanism left to be investigated is the sensitivity towards the water and air content. This is of particular importance because both oxygen and water interact differently with radical-based catalytic systems and supramolecular assemblies. Since the catalytic process proceeds *via* a radical pathway, oxygen is expected to cause severe issues. The presence of molecular oxygen in the reaction mixture can lead to the formation of oxo-radical species, competing with product formation, or the oxidation of the catalytic system.[117] Such side reactions not only consume reactive species, but can also drive the reaction to unproductive or even inhibitory pathways. Thereby, oxygen contamination is expected to severely hinder the efficiency of the catalytic system, making inert conditions highly preferable.

Condition screening for **cat2**OTf

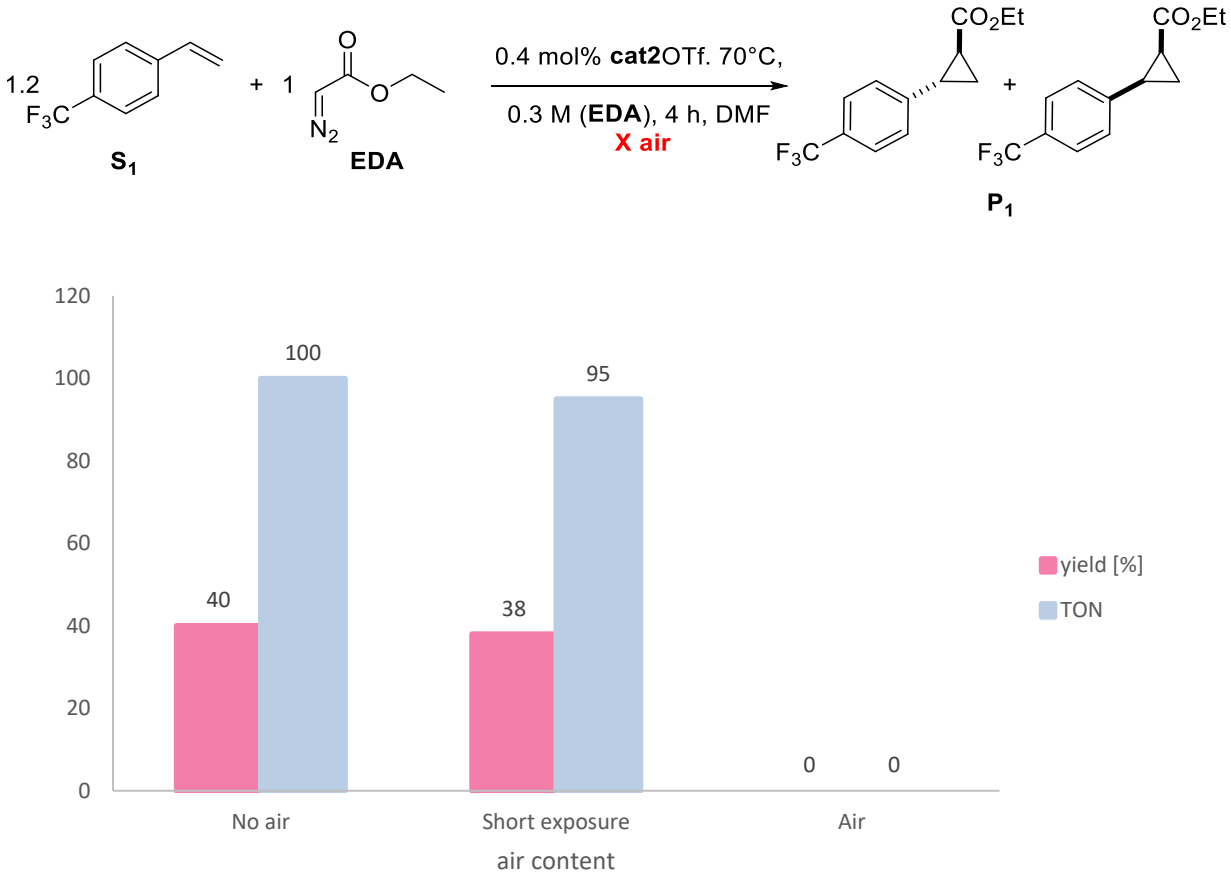

Figure 73: Cyclopropanation of *para*-trifluoromethyl styrene with varying air content.

For the first two experiments, the set-up was kept consistent with the previously described procedure. Therefore, stock solutions of the substrates and the catalyst were prepared inside a glovebox using dry and degassed DMF as solvent. These solutions were combined and the reaction vials were tightly sealed while still inside the glovebox, to prevent exposure to air or moisture. The sealed vials were then removed from the glovebox and heated to 70°C for four hours.

In the modified version of the experiment, corresponding to the second column, the procedure was altered slightly, by briefly opening the lid of the vial for approximately 10 seconds before resealing it and heating under otherwise identical conditions. This exposure was expected to introduce small amounts of oxygen into the system, serving as a way to test the reaction's sensitivity towards only slight contamination. Interestingly, comparison of the yields obtained from these two experiments revealed no significant difference. This indicated that the catalytic process tolerates small amounts of oxygen and such brief exposure does not substantially interfere with the radical mechanism.

In contrast, the outcome of the third experiment, shown in the third column of figure 73, was significantly different. Here, the entire reaction was started under ambient conditions outside of the glovebox, including the preparation of stock solutions. Under these conditions, no product formation was observed. This demonstrates that, while traces of oxygen introduced by short exposure are tolerated, the presence of oxygen in larger amounts is determining the reaction progress.

Since this process not only introduced air into the system, but also moisture, the influence of water on the catalysis needs further investigation. Water itself is not expected to directly interfere with the radical catalytic cycle, nor have beneficial effects. However, its presence may still play an important role in altering the host structure, surrounding the encapsulated catalyst and substrates. The supramolecular host consists of dynamic and reversible imine bonds, which are formed by condensation of amines and aldehydes, releasing water. The reverse reactions, the hydrolysis of the formed imine, can be promoted in the presence of water. Thereby, some imine linkages might be partially cleaved or at least weakened, resulting in a more flexible or partially opened framework.

Such partial opening of the host structure might benefit the diffusion of substrates, especially for large or sterically demanding compounds, into the supramolecular cavity or enhance the release of products after conversion. However, the opening of the supramolecular host, could also have a negative effect on the catalytic conversion since the active site is less shielded from the surrounding bulk, reversing the main advantage of supramolecular catalysis as a general concept. The investigations on the effect, that different water contents have on the catalytic process, are summarised in figure 74. For these experiments, the same set-up as under dry and degassed reaction conditions was used. After the closed vials were removed from the glovebox, the desired amount of degassed water was added into the reaction mixture through a septum in the vial lid. This prevents direct exposure of the reaction mixture to air and avoid any undesired addition of oxygen or moisture.

The results show a distinct trend in the influence of water content on the catalytic performance. For the first four data points, corresponding to water contents of 0, 1, 10 and 20 equivalents, respective to **EDA**, the yields remained relatively constant between 38% and 42%. This indicates that small amounts of water do not significantly interfere with the catalytic cycle or alter the supramolecular structure drastically. However, when 30 equivalents of water were added, the yield increased to 47%, corresponding to a **TON** of 118. This is the highest value observed in this series, suggesting that water can, to some extent, promote the reaction. A

possible explanation might be the enhanced dynamic behaviour of the supramolecular host, and thereby, improved diffusion of substrates into and products out of the host environment.

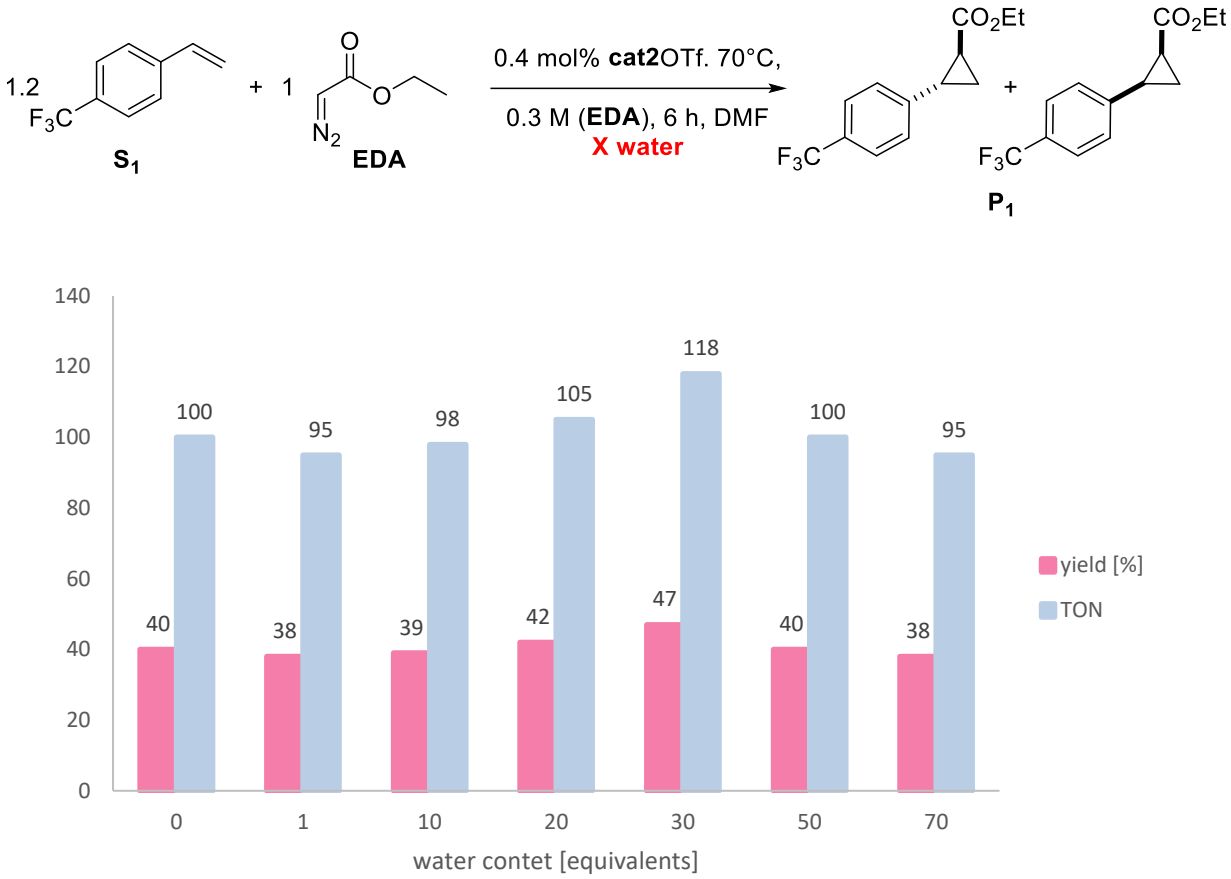

Figure 74: Results of the cobalt-catalysed cyclopropanation with different water content.

At higher water contents the beneficial effect decreased. With 50 equivalents of water, the yield dropped back to 40% and with 70 equivalents it further decreased to 38%. This suggests that excessive water contents might disrupt the balanced supramolecular system. In such cases, the host structure might open too widely, which decreases structural integrity of the supramolecular reaction vessel. Instead of selectively shielding the reactive intermediates from the surrounding bulk, the host cavity might become overly accessible, leading to reduced control over the environment and thereby a decline in performance.

Summarising the most efficient reaction conditions

In summary, the influence of several key reaction parameters, namely substrate stoichiometry, temperature, overall concentration, reaction time and sensitivity towards water and air content, were investigated for the cyclopropanation of *para*-trifluoromethyl styrene with **EDA**, using a constant catalyst loading of 0.4 mol%. The baseline conditions introduced by *de Bruin et al.*

already provided high performance in many aspects.[81,82] Nevertheless, the investigations revealed that modifications of certain parameters, such as reaction time and water content, can lead to significant improvements in yield.

From these experiments, the optimal reaction conditions were identified. A substrate stoichiometry of 2.5:1 (styrene derivative/**EDA**) was most effective, as it minimises the undesired dimerisation of **EDA** while maintaining availability of the carbene precursor. The reaction temperature of 70°C was confirmed to provide the best balance between catalytic activity and thermal stability of the used compounds. In line with literature, an overall concentration of 0.3 M of **EDA** remained optimal, while an elongated reaction time of six hours, instead of four, resulted in increased yields, after which further extension of reaction duration did not improve the product formation.

Regarding the system sensitivity, the experiments revealed clear trends. While minor oxygen contaminations were tolerated, full ambient conditions effectively suppressed catalytic turnover. This confirms the necessity of performing the catalytic reactions under inert atmosphere, which is consistent with the radical-based mechanism. Finally, the role of water was especially interesting. At low to moderate water contents only a small effect was observed, however, the addition of 30 equivalents resulted in the highest yield. This could possibly be explained by the dynamic equilibrium between a partially opened and closed supramolecular host allowing a good product release and coordination of the substrate.

In conclusion, these results define the optimised conditions for this supramolecular cyclopropanation reaction, while also highlighting the interplay between reaction environment, host dynamics and catalytic performance.

DMF content

In figure 58 the DMF content of **cat2**OTf was depicted directly after isolation and again after three and six hours of exposure to fine vacuum. These experiments revealed a gradual decrease in DMF content, indicating that residual solvent molecules are removed from the catalyst material during drying. Since the presence of DMF effectively dilutes the reaction and decreases the actual catalyst loading, its removal is essential for an effective conversion. To investigate the practical consequences of this effect, the cyclopropanation of $\mathbf{S_1}$ was performed using catalyst samples at different drying stages.

Condition screening for **cat2**OTf

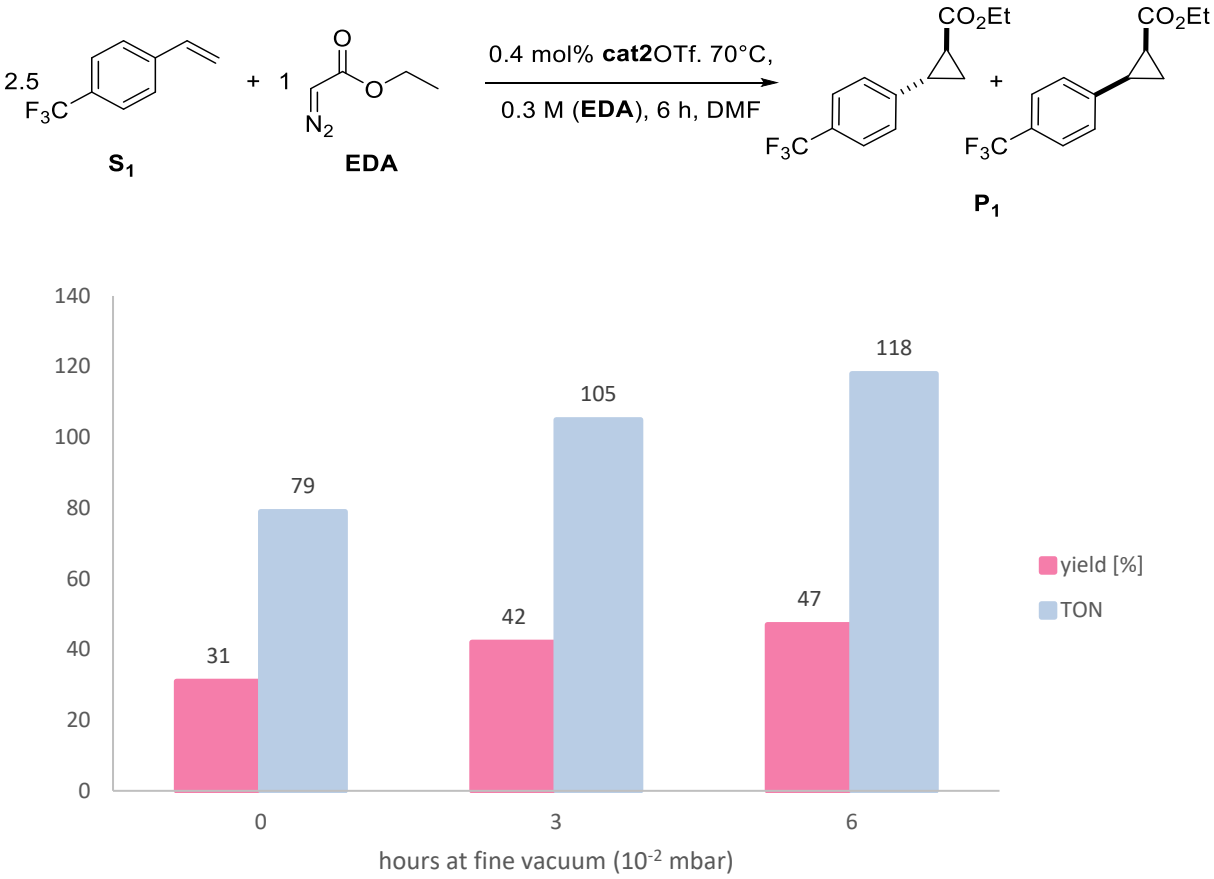

Figure 75: Results of cyclopropanation reaction with **cat2**OTf with different DMF contents.

When the non-dried catalyst was used directly, the reaction gave only 31% yield, corresponding to a turnover number of 79. After three hours of drying under fine vacuum (10^{-2} mbar), the yield improved to 42%, showing that even partial removal of DMF leads to an enhanced performance. Extending the drying period to six hours increased the yield further to 47%, which corresponds to a **TON** of 118.

This highlights the importance of the drying process, which is more a technical detail, than a real reaction condition but it directly impacts the effective catalyst loading. This means that the actual catalytic performance cannot be reliably compared unless the DMF content is controlled. Alternatively, when weighing catalyst samples for stock solution preparation, the residual DMF must be carefully accounted to ensure an accurate determination of the actual catalyst loading. The effective catalyst loadings and the respective reaction outcomes are summarised in figure 76. Therefore, the amount of catalyst was added which would correspond to a catalyst loading of 0.4 mol%. Subsequently, the molar amount of DMF was subtracted, which gave the effective catalyst loading of 0.33 mol%, 0.34 mol% and 0.37 mol%.

Condition screening for **cat2**OTf

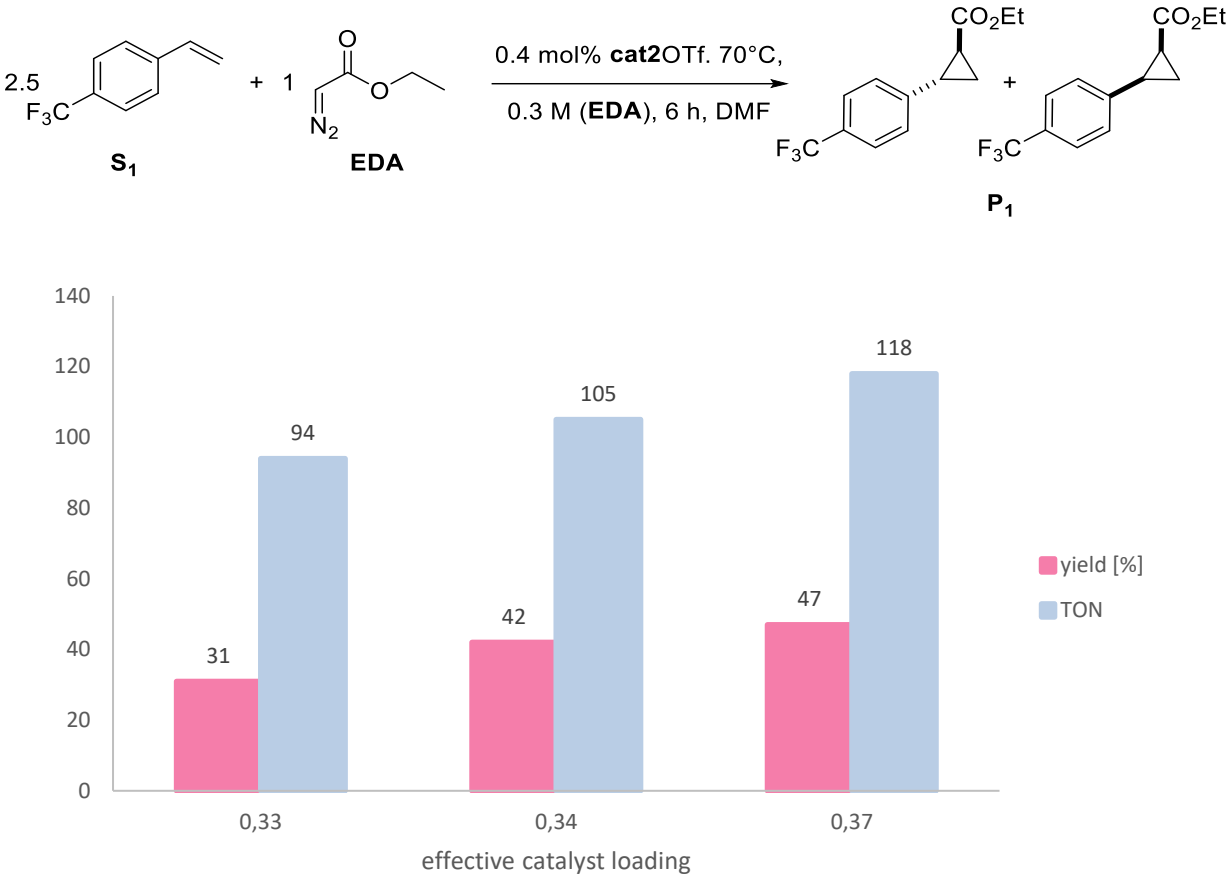

Figure 76: Results of the cyclopropanation of *para*-trifluoromethyl styrene with effective catalyst loadings.

Here, it becomes clear that even small changes in the DMF content of the catalyst can already have a noticeable impact on the reaction outcome. After three hours under fine vacuum, the DMF content decreased only slightly form 16.84 w% to 15.59 w%. Despite this rather small reduction, the yield increased significantly from 31% to 42%. In terms of effective catalyst loading, this corresponds to only a slight increase from 0.33 mol% to 0.34 mol%, yet the catalytic performance improved disproportionally.

In contrast, drying the catalyst for six hours, under the same conditions, reduced the DMF content more noticeably and increased the effective catalyst loading to 0.37 mol%. However, this additional improvement only had a minor effect on the reaction outcome. The yield increased only slightly, from 42% to 47%. This indicates that the system reaches a plateau where additional drying and the resulting increase in effective catalyst loading no longer leads to significantly increased yields anymore. This means that already 0.37 mol% effective catalyst loading are sufficient to reach this level of activity with no substantial improvements beyond this value.

13. Substrate scope for cat2OTf

With the optimised reaction conditions in hand, the next step was to investigate the range of possible substrates that can undergo the cyclopropanation within this supramolecular catalytic system. Previous studies by *de Bruin* and co-workers have already provided valuable insights into the size-selectivity of a closely related supramolecular catalyst, by investigating differently sized styrene derivatives, bearing either aromatic or aliphatic substituents.[82] Their results highlighted the importance of steric bulk and size of the substrates, determining whether a substrate can access the cavity and undergo transformation.

On this basis, the present work aims to extend the investigation beyond steric effects. Therefore, functional group tolerance of the system has to be studied, since electronically diverse substituents can influence the systems reactivity drastically. Additionally, non-terminal double bonds represent a crucial step towards a broader substrate scope of this transformation. Such substrates may introduce additional steric and electronic challenges, for encapsulation, as well as the catalysis itself, but if tolerated, would greatly expand the synthetic scope of application of the supramolecular system.

Functional group tolerance

To determine the tolerance towards different functionalities while simultaneously investigating the influence of different electronical effects, a variety of substituents were chosen. First, a spectrum of electron-withdrawing groups, ranging from relatively weak halogens to strongly withdrawing nitro groups, thus ensuring a representable scope of effects, were tested. For these experiments, the modified reaction conditions, introduced previously were applied, shown in figure 77. The reaction proceeds *via* a radical mechanism, which leads to the formation of a mixture of diastereomers. In the absence of catalyst encapsulation, the reaction environment is not confined and the thermodynamically more stable *trans*-product is strongly favoured over the *cis*-isomer.

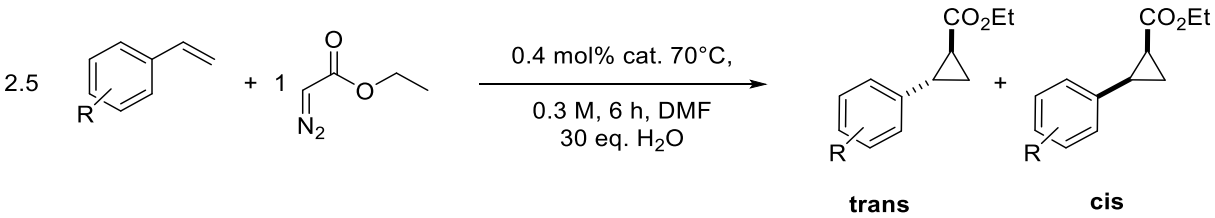

Figure 77: Optimised reaction conditions used to screen potential substrates.

This is reflected in the observed diastereomeric ratio of 6.5:1 (*trans*/*cis*) when free **Co-TPyP** is used as catalyst. In contrast, encapsulation of the cobalt catalyst inside a supramolecular host

introduces a restricted reaction volume and additional non-covalent interactions with the cavity walls. These spatial and electronic constraints can stabilise certain transition states, leading to an increased formation of the *cis*-isomer. Although this effect does not completely compensate the natural preference for the *trans*-product, a noticeable increase in *cis*-product formation can be observed upon encapsulation.

Electron-withdrawing groups

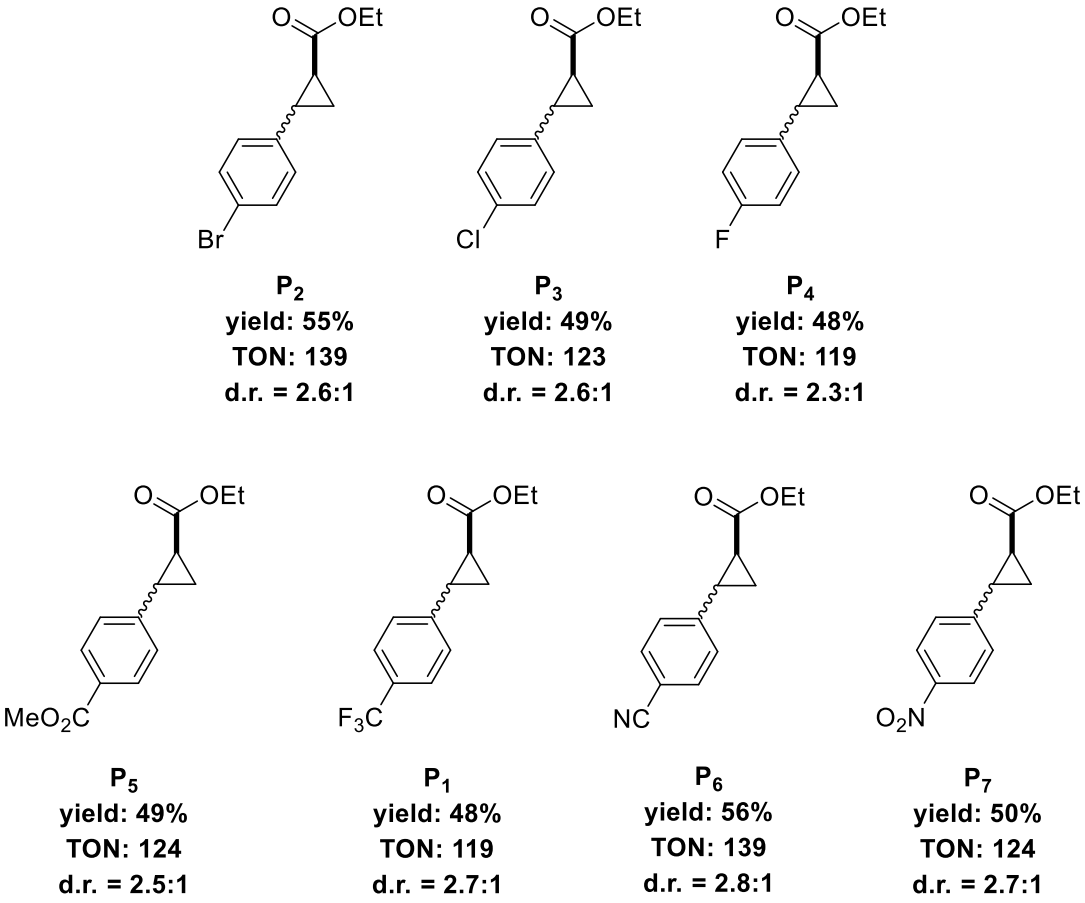

Figure 78: Substrate scope including results of electron-withdrawing substituents in *para*-position.

The first investigations focused on substituents with different electron-withdrawing strength. Weakly withdrawing groups, such as halogens, were compared to stronger withdrawing groups like nitriles or even the nitro group, which provides one of the strongest -M effects.[118] To ensure comparability, all substituents are in *para*-positions of the aromatic system, thereby minimising steric hindrance at the active site and allowing the electronic influence to be the dominant factor.

Substrate scope for **cat2**OTf

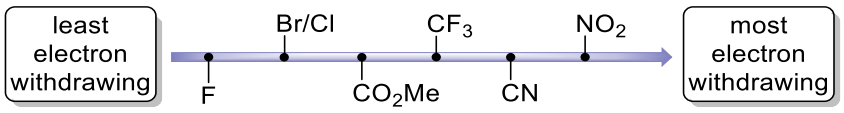

Figure 79: Order of substituents from the least to most electron-withdrawing nature.[118]

This series proved the reaction to be tolerant towards a variety of functional groups with the products yield ranging from 48%, overserved for **P$_1$** and **P$_4$**, to 56% for the **P$_6$**. This suggests, that the catalytic system is not sensitive to variations in electron-withdrawing effect in the *para*-position.

The diastereomeric ratios were found to remain relatively stable, ranging between 2.6:1 and 2.8:1 (*trans*/*cis*). The only significant deviation showed **P$_4$**, where the ratio decreased slightly to 2.3:1 (*trans*/*cis*). This can be explained by the small steric bulk of fluorine, compared to bulkier substituents, which introduces less steric hindrance at the supramolecular hosts wall, thereby facilitating the formation of the *cis*-isomer.

To further investigate steric and electronic contributions, the influence of substituent position was studied using bromine. Therefore, substrates with bromine in *ortho*-, *meta*- and *para*-position were employed. This positional analysis allows further insights, since *ortho*-substitution introduces steric constraints in close proximity to the reactive site, *meta*-substitution provides the least electronic effect and *para*-substitution might interfere sterically with the surrounding supramolecular host.

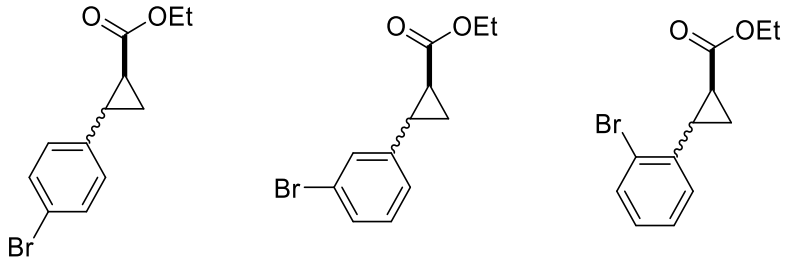

P$_2$
yield: 55%
TON: 139
d.r. = 2.6:1

P$_8$
yield: 58%
TON: 144
d.r. = 2.3:1

P$_9$
yield: 51%
TON: 127
d.r. = 3.5:1

Figure 80: Influence of substitution pattern of the cobalt catalysed cyclopropanation.

The results showed only small differences in the observed yield, with values ranging from 51% for *ortho*-substitution in **P$_9$** to 58% for *meta*-substitution in **P$_8$**. This indicates that either steric hindrance at the *ortho*- and *para*-positions limits access to the reactive site, or that the

presence of electron-withdrawing substituents leads to a general electronic suppression of the reaction. This cannot be fully distinguished on the basis of the yields alone, but with a *Hammett*-plot, which will be discussed in a later section.

Interestingly, selectivity was more affected than the yield. The *ortho*-substitution showed a significantly increased preference for the *trans*-isomer of 3.5:1 (*trans*/*cis*), compared to both *meta*- and *para*-substitution. This can be explained by steric effects, since the proximity of the bromine atom to the reaction centre makes it sterically demanding for the reactive intermediate to approach along the trajectory leading to the *cis*-product. As a result, the formation of *cis*-isomer becomes disfavoured and the *trans*-species is more dominant. In contrast, *meta*- and *para*-substitution showed diastereomeric ratios comparable to those, observed with other electron-withdrawing substituents.

Electron-donating groups

Along the electron-withdrawing groups introduced previously, the influence of electron-donating groups was investigated in order to obtain a more complete picture of how electronic effect influence the reactivity and selectivity of the transformation. The inclusion of electron-donating groups such as alkyl and methoxy substituents enables a direct comparison with the results for electron-withdrawing groups, thereby allowing the identification of contrasting trends. Especially interesting is the investigation of electron-donating substituents since the reaction conditions were optimised for the electron-withdrawing CF_3-group, which allows to test the universal validity of the reaction conditions. Furthermore, steric effects were also tested in this series, in order to compare whether they provide similar results than for electron-withdrawing groups.

First, the influence of different substitution patterns for alkyl chains was investigated, by comparing substrates bearing methyl groups on either the *meta*- or *ortho*-position. These results showed only small differences in yield, with 43% for the *ortho*-substituted styrene and 46% for *meta*-substituted analogue. However, the diastereomeric ratios (**d.r.**) followed the trend, which was already observed for electron-withdrawing groups, that substituents in the *ortho*-position introduce steric bulk close to the active site, which hinders the formation of the *cis*-isomer and thereby, shift the **d.r.** to 3.0:1 (*trans*/*cis*) towards the *trans*-isomer. The introduction of even more steric bulk, with methyl-groups occupying both *ortho*-positions as well as the *para*-position, led to a significant decrease in yield to 25%. Thereby, the ^{1}H-NMR signals of the two diastereoisomers overlapped to such an extent that the diastereomeric ratio could not be determined reliably.

Substrate scope for **cat2**OTf

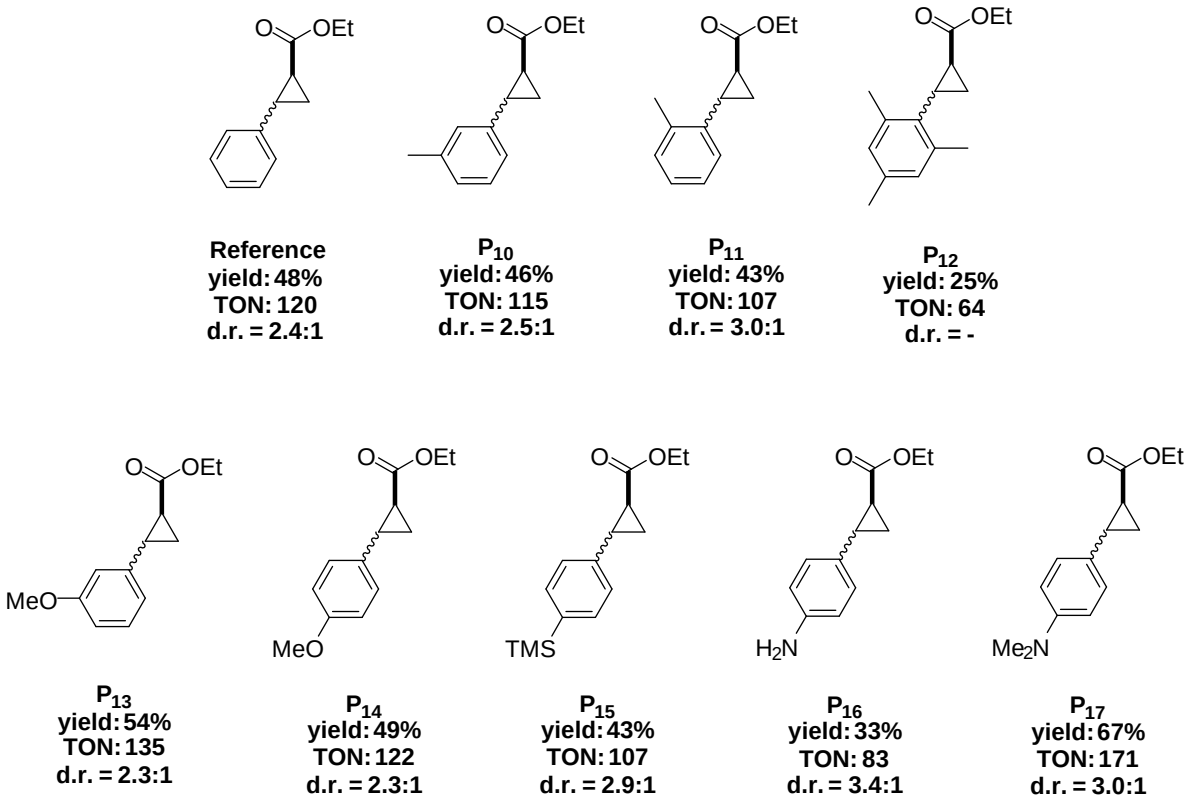

Figure 81: Results for testing of electron-donating groups.

This positional effect was investigated next for a methoxy substituent, introduced either at the *para*- **P$_{14}$** or *meta*-position **P$_{13}$**. In line with earlier observations, *meta*-substitution gave a slightly higher yield of 54% compared to 49% for the *para*-position. This difference can, most likely, be explained by steric effects. The *meta*-substituent does not interfere directly with the reactive site or the confinement of the supramolecular host, whereas *para*-substitution can introduce steric clash with the cavity walls, thereby reducing efficiency.

Comparing of different *para*-substituted styrene derivatives the results further proved the trends, which were found previously. The trimethylsilyl (TMS) group **P$_{15}$** performed similarly to methoxy in terms of yield, but showed a slightly higher ratio of *trans*-isomer formation. This can be explained by the significant steric bulk of the TMS group, which again disfavours *cis*-product formation. The amine-substituted substrate gave **P$_{16}$** in a significantly lower yield of 33%, which is most likely due to competing side reactions involving the free amine functionality, such as catalyst deactivation by the amine coordinating to the catalytically active metal, which is a well-known issue in catalytic conversions. The trans-heavy diastereomeric ratio of **P$_{16}$** still needs to be investigated.[119]

To test this hypothesis, a protected amine derivative, bearing two additional methyl groups **S$_{17}$**, was employed. This substrate performed extraordinarily well, giving the highest yield observed in the entire study with 67%, corresponding to a turnover number of 171. This supports the theory, that free amine groups interfere with the catalysis, whereas sterically protected amines do not suffer from this issue. Again, a reliable explanation for the diastereomeric ratio could not be found on the basis of the present results.

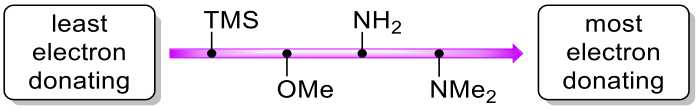

Figure 82: Electron-donating substituents ordered from weakest to strongest.[118]

Additionally, the yields are increasing with stronger electron-donating groups in *para*-position, but to validify this, a *Hammett*-plot will be introduced in a later chapter.

With these promising results in hand, further optimisations were approached by addressing one of the major limitations of the system, namely its poor solubility. The restricted solubility limited the choice of potential solvents to pure DMF, a solvent which is well known to be less suitable for these types of conversions. Although DMF provides sufficient polarity to solubilise both catalyst and substrates, it is not always compatible with high catalytic performance and its coordinating nature can even interfere with the efficiency of radical pathways or the supramolecular system.[82]

To address this issue, the supramolecular host was modified by exchanging the counterion from triflate to triflimide. The bulkier and more weakly coordinating triflimide anion is known to significantly improve solubility in a broader range of organic solvents due its delocalised charge distribution. This modification should enable the exploration of alternative solvents beyond pure DMF and the evaluation of their impact on both yield and selectivity.[82]

14. Condition screening for cat2NTf$_2$

To investigate the influence of the exchanged counterion, the solvent mixture, introduced by *de Bruin et al*. in 2014, was employed. Thereby, also different mixing ratios of acetone and water were investigated further, than just the 1:2 ratio, stated in literature.[82] In order to provide the best comparability, *para*-trifluoromethyl styrene was used and the optimised reaction conditions, introduced in previous chapters, were employed.

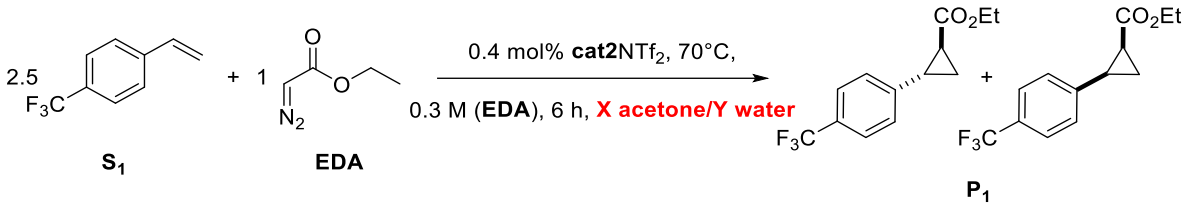

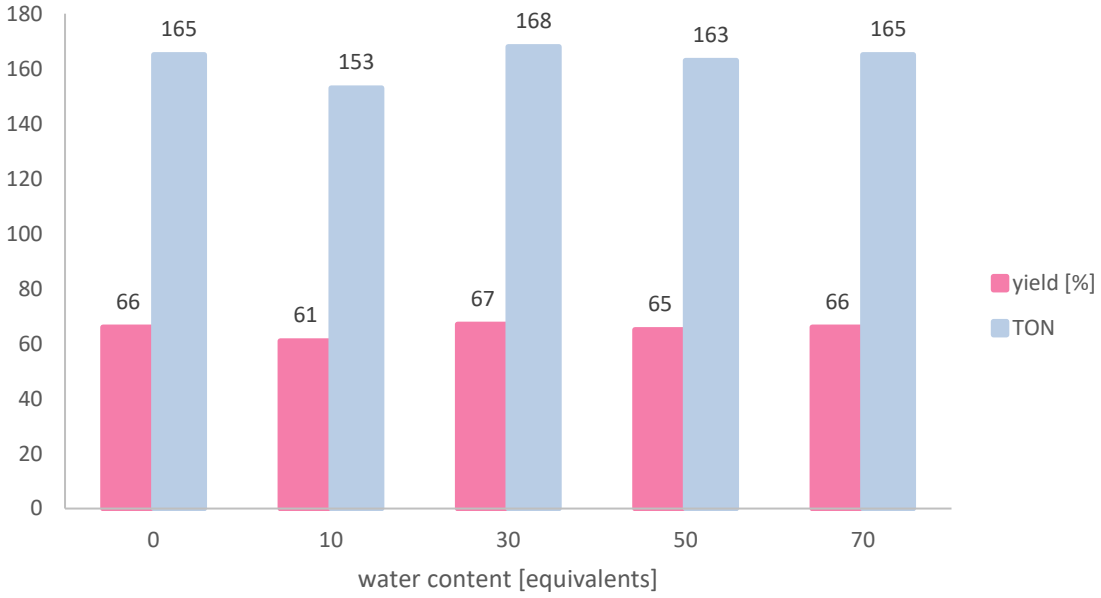

Figure 83: Screening of different water contents in the cobalt catalysed cyclopropanation with **cat2**NTf$_2$.

This set of experiments was prepared following the previously introduced procedure. Stock solutions of both substrates and the catalyst were prepared in acetone inside the glovebox and subsequently combined. After sealing the vials, they were removed from the glovebox and degassed water was added, *via* a septum in the lid, so that the overall concentration was 0.3 M in respect to **EDA**. The mixtures were then heated to 70°C for six hours.

The results, showed a remarkably high tolerance of this system towards water, as the yields remained relatively constant in the range of 61-67%. This can be explained by two factors. First, triflate is significantly less bulky than triflimide which allows the water molecules to get

into close proximity with the imine bonds, which are then potentially hydrolysed, and thereby, potentially cleaved. With the bulkier triflimide, these bonds are shielded from water and the assembly is less prone towards “re-opening” of the imine condensations.[120]

Secondly, triflimide has a rather hydrophobic character, as triflate is relatively polar and can thereby interact well with water. Thereby, the triflimide anions could surround the imine bonds with a hydrophobic barrier, which potentially blocks water from approaching and thereby, protects the structural integrity of the system additionally.[120]

Comparing these results with the earlier obtained data for **cat2**OTf in DMF highlights the importance of this modification. Under the previously optimised conditions, the conversion of *para*-trifluoromethyl styrene **S_1** with **cat2**OTf in pure DMF resulted in a yield of 48% of **P_1**, corresponding to a **TON** of 119. In contrast, upon exchanging the counterion from triflate to triflimide and thereby enabling the use of acetone as solvent, the yield increased to 66%, corresponding to a **TON** of 165. Thus, a seemingly minor modification resulted in a 39% increase in catalytic turnover, clearly showing the influence of solvent effects and the choice of a suitable counterion on the overall efficiency of this reaction.

Despite this improvement, acetone was not the ideal solvent. The new catalyst **cat2**NTf_2 provided a better solubility but this was still insufficient, leading to minor precipitates in the stock solution. This prevented the precise determination of the effective catalyst loading and reproducibility of the reaction. Therefore, further optimisation focused on the identification of alternative solvents, which could combine the beneficial influence of enhanced solubility with the high activity and selectivity, showed in acetone.

To compare both supramolecular systems properly, the conversion of *para*-trifluoromethyl styrene was repeated under identical conditions in DMF. In these experiments, the only modification was the replacement of the catalyst **cat2**OTf with **cat2**NTf_2. The reaction with **cat2**NTf_2 gave a yield of 49%, corresponding to a **TON** of 123. This result does not significantly differ from the outcome obtained with **cat2**OTf, which gave a yield of 48% and a **TON** of 118 under the same conditions. Thereby, it is clearly shown that the counterion itself provides no major influence on the catalytic performance. Consequently, both catalysts can be regarded as functionally equivalent under the examined conditions.

With these results in hand, different solvent mixtures were investigated. The experimental setting was similar to the previously introduced one, but for the solvent mixtures, the stock solution of the catalyst was prepared in DMF, except for the pure solvents, while everything else was prepared in the respective other solvent. This ensured that the catalyst, which is only

reliably soluble in DMF, could be added in a reproducible manner, while the effect of the co-solvent was studied. The results of the respective solvent screening are summarised in figure 84.

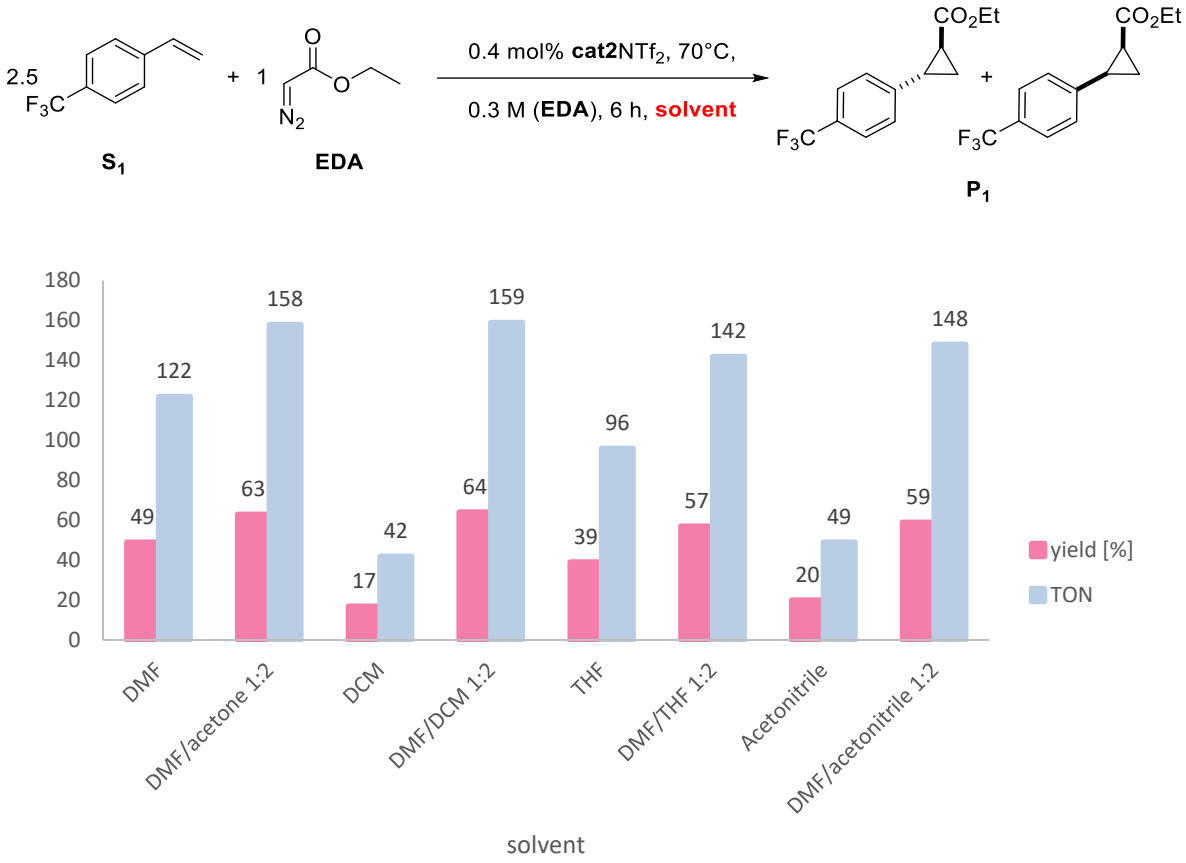

Figure 84: Results for the solvent screening of the cyclopropanation of *para*-trifluoromethyl styrene.

In general, the addition of a second solvent to DMF improved the catalytic performance compared to reactions in pure DMF. Among these experiments, the highest yields were obtained with DMF/acetone (63%) and DMF/DCM (64%), followed by moderate yields for DMF/THF (57%) and DMF/acetonitrile (59%). This suggests that the beneficial effect on yield is achieved rather independent of the specific second solvent.

In contrast, reactions carried out in the pure solvents performed significantly worse. This can be explained by the poor solubility of the catalyst. In acetone and THF, the catalyst stock solution showed partial solubility, indicated by the characteristic red colour of the solution, which is commonly attributed to porphyrin-based systems. However, large amounts of undissolved catalyst remained, limiting catalytic efficiency and reproducibility. In DCM and acetonitrile, the solubility was even worse and no colour change was observed, implying no

solubility of the catalyst at room temperature. This was directly reflected by the low yields of 17% for DCM, 39% for THF and 20% for acetonitrile.

For following experiments, the DMF/acetone mixture was selected. Although the yield obtained with DMF/DCM was essentially identical, acetone offered practical advantages. Deuterated acetone is commercially available in dry form, making it suitable as an NMR solvent in post-reaction analysis, whereby dryness of the NMR-solvent is a crucial property. The work-up followed the protocol published by *de Bruin et al*. in 2013.[81] After completion, the reaction mixture was allowed to cool to room temperature and diethyl ether was added. This step precipitates the catalyst, while both substrates and products remain in solution. The solvents were removed under reduced pressure, yielding a residue which was dissolved in one millilitre of deuterated acetone.

For quantitative ^{1}H-NMR analysis, two microlitres of two internal standards, dibromomethane and nitromethane, were added. The use of two standards, instead of one, provides an additional level of control by reducing the risk of errors stemming from slightly inaccurate pipetting or volume loss upon evaporation. This dual-standard approach enhances the precision of yield determination.

The choice of dry deuterated acetone was crucial in order to analyse the measured ^{1}H-NMR spectra. The signal region around 1.6 ppm is especially valuable for analysis of the yield and diastereomeric ratio, as it shows distinct signals of both isomer without any other overlapping species or solvent. However, in this region the contamination with water would hinder the analysis by forming an additional signal, which overlaps the product signals. Thus, ensuring the dryness of the NMR solvent is essential for reliable interpretation of the results.

With these promising results in hand, further investigation of the reaction conditions, which were already optimised for **cat2**OTf, were considered. Since the supramolecular host structure of **cat2**NTf_2 is very similar to **cat2**OTf, the hypothesis was proposed that the optimised reaction parameters of previous experiments would also be applicable here. In particular, factors as the stoichiometry of the substrates, the reaction temperature, overall concentration of the system and the reaction time are expected to remain relatively unaffected by the change of the solvent mixture.

Catalyst loading

Nevertheless, the higher catalytic activity observed for **cat2**NTf_2 suggested the additional investigation of the catalyst loading. While a loading of 0.4 mol% had previously been identified as the most efficient balance of activity and economy for **cat2**OTf, it was unclear if this would

remain optimal for the more active system. Therefore, the loading was systematically reduced stepwise to 0.1 mol%. This investigation is especially valuable in the context of sustainable catalysis, as reducing catalyst loading not only improves cost-efficiency but is very beneficial since the catalyst is not commercially available and requires a rather complex and multi-step synthetic process. The results for this investigation are summarised in figure 85.

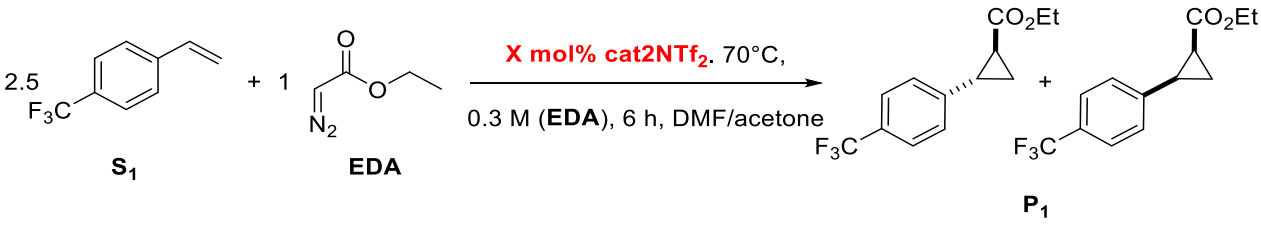

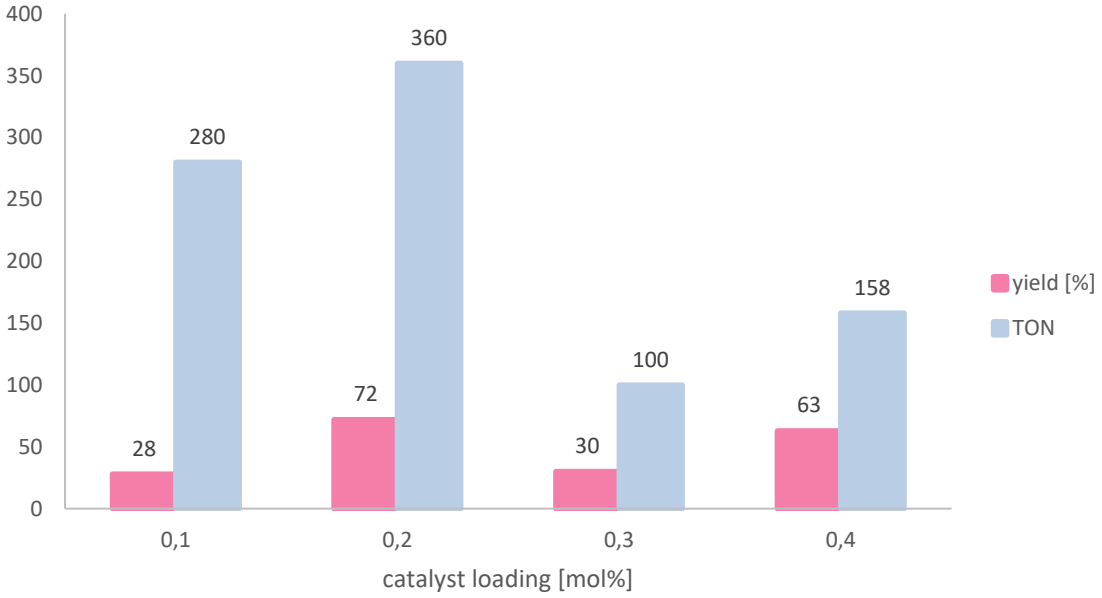

Figure 85: Results for different catalyst loadings of **cat2**NTf$_2$.

The experimental results showed a clear trend with one notable irregularity. When the catalyst loading was reduced from 0.4 mol% to 0.3 mol%, the yield dropped significantly from 63% to 30%. This also means a drastic decrease in the **TON**, suggesting, at first glance, a lower activity of the system at this catalyst loading. In general, such a decrease could be explained by the reduced number of active sites, leading to a slower overall reaction rate. However, setting this result into context with the results at 0.2 mol% and 0.1 mol%, the outcome at 0.3 mol% does not fit to the overall trend, and therefore, is regarded as an experimental outlier. Due to the good results with 0.2 mol% catalyst loading, the outcome with 0.3 mol% was considered less relevant and was not repeated to prove it as an outlier.

At 0.2 mol%, the system preformed significantly better. Not only did the yield increase from 63% (at 0.4 mol%) to 72%, but this also corresponded to a drastic increase in the **TON** from 158 to 360. This indicates that, under these conditions, the catalyst can operate far more efficiently, achieving higher productivity per active site. This shows the importance of screening the catalyst loading since excessive amounts may not only be unnecessary but could even reduce the efficiency of the system.

Even when the catalyst loading was decreased further to 0.1 mol%, the catalyst remained active, resulting in a yield of 28%. Although the yield was lower than at higher loadings, the corresponding **TON** of 280 is still remarkably high, indicating that the catalyst maintains its extraordinarily high activity even at very low concentrations. Compared to **cat2**OTf, for which the best results yielded $\mathbf{P_1}$ in 48%, corresponding to a **TON** of 119, even at 0.1 mol% catalyst loading **cat2**NTf_2 performs more than double the number of catalytic cycles before deactivation.

By analysing these results, new optimal reaction conditions were found. These were built upon parameters that had already been established in previous studies, as the stoichiometric ratio of substrates, temperature, reaction time and overall concentration. These factors were kept constant, which also enables better comparability with previous results. However, in order to improve the efficiency of the process, modifications of the solvent system and the catalyst loading were introduced. The mixed solvent system of DMF and acetone in a 1:2 ratio was employed, which balances solubility and activity of the catalytic system. Additionally, the catalyst loading could be reduced to 0.2 mol%. These optimised conditions, summarised in table 15 were subsequently applied in the following series of experiments.

Table 14: Summary of the optimised conditions for **cat2**NTf_2.

alkene/EDA	temperature	time	concentration	solvent	catalyst loading
2.5:1	70°C	6 hours	0.3 M	DMF/acetone 1:2	0.2 mol%

15. Substrate scope for cat2NTf_2

In order to systematically study the influence of electronic and steric factors, a set of substrates with different substituents and substitution patterns was investigated. For better comparability, the same substrate scope as described previously for **cat2**OTf was used. This allowed to clearly show the effect of the different solvent mixture and catalyst loading.

Electron-withdrawing groups

First, substrates with electron-withdrawing substituents in the *para*-position of the aromatic ring were studied. The corresponding results in figure 86 show an increase in yield for every substrate compared to the one which was achieved with **cat2**OTf, even though only 0.2 mol% of **cat2**NTf_2 were employed instead of 0.4 mol%. In some cases, the increase in yield is rather small as for the **P_2**, **P_4** and **P_5**, where the yield only increases by 6%. However, due to the lower catalyst loading, even those small changes correspond to an increase in the **TON** from 139 to 303 (**P_2**), 119 to 272 (**P_4**) and from 124 to 276 (**P_5**), doubling the **TON** obtained with **cat2**OTf.

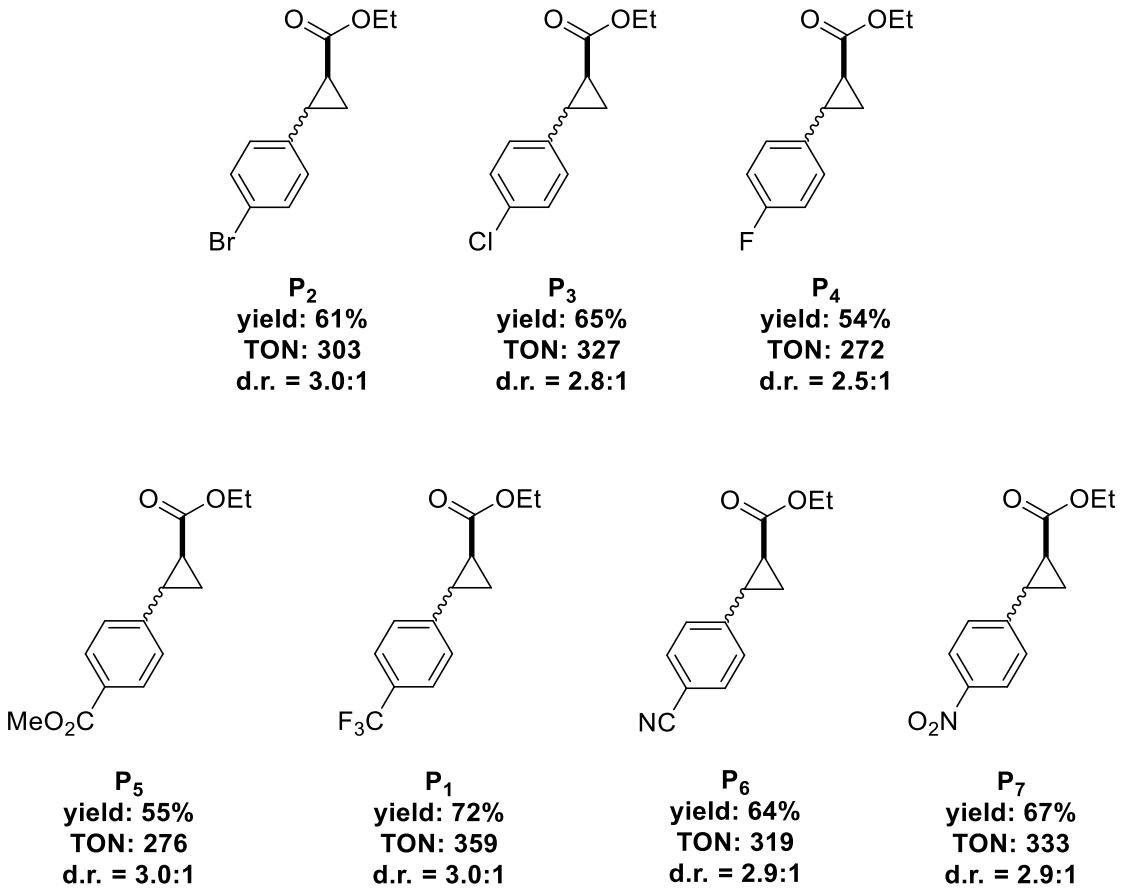

Figure 86: Results for conversion of styrene derivatives with electron-withdrawing groups by **cat2**NTf_2.

The highest increase is observed for $\mathbf{P_1}$, whereby the yield increases from 48% to 72%, which is an increase to the 1.5-fold yield. $\mathbf{P_7}$ and $\mathbf{P_3}$ also benefited strongly by the altered reaction conditions, with increases in yield of 17% ($\mathbf{P_7}$) and 16% ($\mathbf{P_3}$) compared to **cat2**OTf.

The diastereomeric ratios shifted slightly towards the formation of the *trans*-isomer, with average values of 2.6:1 (*trans*/*cis*) with **cat2**OTf and 2.8:1 for **cat2**NTf_2. This could be explained by differences in the stabilisation of the corresponding transition states, which is influenced by the solvent system, or the higher conversion at the iron-centres at the corners of the cube, which are potentially less shielded from the bulk with triflimide than with triflate.

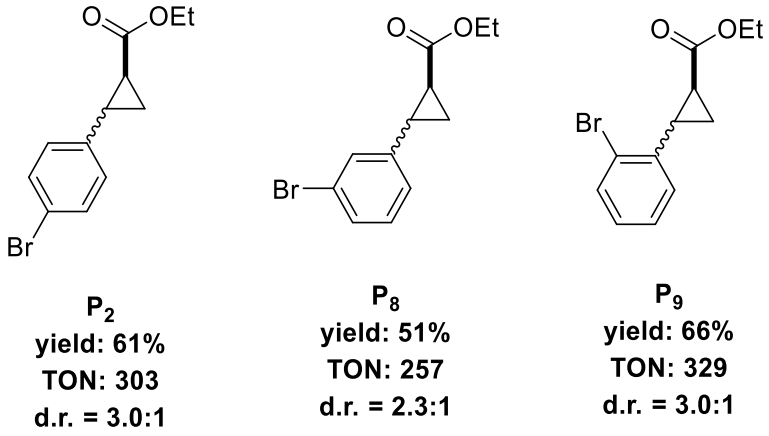

P_2
yield: 61%
TON: 303
d.r. = 3.0:1

P_8
yield: 51%
TON: 257
d.r. = 2.3:1

P_9
yield: 66%
TON: 329
d.r. = 3.0:1

Figure 87: Results for bromo-styrene with different substitution patterns, using **cat2**NTf_2.

The investigation of the different substitution patterns, using bromine substituents, interestingly, showed a trend that was opposite to what had previously been observed with **cat2**OTf. Thereby, *meta*-substitution provided the highest yield, whereas the *ortho*-position gave the lowest yield, also providing the largest share of the *trans*-isomer in the product mixture.

However, in this study, the *ortho*-substituted styrene performed best, giving the highest yield among the employed substitution patterns. In comparison with previous experiments on this substrate, the yield increased significantly from 51% to 66%, suggesting that under the modified conditions, the steric influence of the *ortho*-bromine atom might not interfere as strongly with the formation of the transition state. At the same time, the diastereomeric ratio shifted to a less *trans*-favoured outcome, decreasing from 3.5:1 to 3.0:1 (*trans*/*cis*).

Interestingly, the *meta*-substituted derivative, which had previously provided the highest yield, was the only substrate in this system that showed a decrease in yield, dropping from 58% to 51%. Nevertheless, the lower catalyst loading of the modified reaction conditions, corresponds

to an increase in turnover numbers, rising from 144 to 257. This underlines the importance of considering both yield and catalyst efficiency in evaluating catalytic performance. Although the overall yield decreased, the catalyst itself performed the reaction far more efficiently.

Electron-donating groups

Again, the same substrates bearing electron-donating substituents, which had already been studied for **cat2**OTf, were re-investigated using **cat2**NTf_2 under the modified reaction conditions.

The results showed a clear improvement for the majority of the substrates. The styrene derivatives bearing a single methyl group, positioned either in *meta*- or *ortho*-position, provided significantly increased yields when the catalyst was switched to **cat2**NTf_2. Thereby, the *meta*-substituted derivative showed an increase from 46% to 59%, while the *ortho*-substituted analogue rose from 43% to 62%.

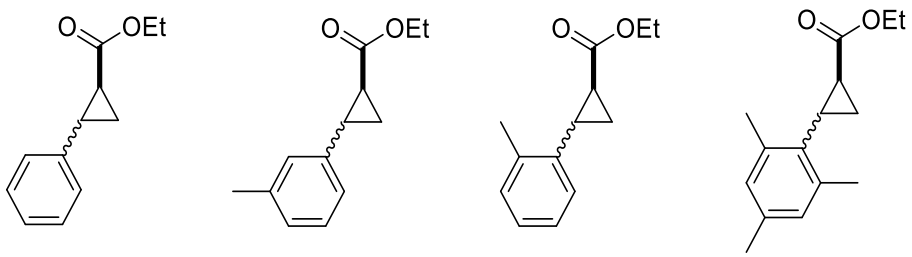

Reference	P_{10}	P_{11}	P_{12}
yield: 64%	yield: 59%	yield: 62%	yield: -
TON: 320	TON: 297	TON: 308	TON: -
d.r. = 2.9:1	d.r. = 2.8:1	d.r. = 3.1:1	d.r. = -

Figure 88: Conversion of alkyl substituted styrene derivatives and styrene with **cat2**NTf_2.

This corresponds not only to a significant increase in yield but also to a more than twofold increase in turnover number, demonstrating that the catalyst is not only producing more product but also operates more efficiently in this system. However, **P_{12}** showed no conversion. This complete lack of reactivity, is highly interesting, especially compared to the performance of the same substrate with **cat2**OTf, where it still yielded modest 25%. This suggests that the limiting factor is steric hindrance or restricted access to the active site. The bulkiness, especially the two methyl substituents in *ortho*-position, could prevent the substrate from adopting the necessary transition state geometry, which explains the low yield for **cat2**OTf. However, this effect would remain rather similar, whereby the complete lack of conversion cannot be explained.

This suggest, that the limited access to the catalytically active cobalt centre is preventing conversion for this substrate. In the case of **cat2**OTf, the supramolecular host is presumably prone towards partially disassembling under the aqueous reaction conditions, as can be assumed by the influence of the water content on its performance. This can be beneficial to some extent, as it temporarily opens the host structure and thereby enables the encapsulation of bulky or sterically demanding substrates that would otherwise struggle to diffuse through the narrow pores of the intact assembly. This potentially explains the low but still considerable conversion of this substrate with **cat2**OTf.

In contrast, **cat2**NTf_2 is potentially better shielded from water due to the hydrophobic character of the rather bulky counterions, as can be assumed by the consistent outcome of the catalysis with changing water content. While this structural integrity improves catalytic efficiency for smaller and moderately substituted substrates, it could become a disadvantage for sterically demanding substrates. This could in theory prevent encapsulation of the bulky **S_{12}** and as a result, no conversion is observed. This result demonstrates how the balance between host-stability and dynamic adaptability of complex supramolecular systems could determine the substrate scope and highlight the interplay of catalyst robustness and flexibility, while also giving insights on the effective pore size of the system. The results for other electron-donating substituents are summarised in figure 89, providing further insights into how different functional groups influence the reactivity of this modified system.

In general, the use of **cat2**NTf_2 improves reaction efficiency compared to **cat2**OTf, with all investigated substrates giving higher yields. The improvement varies depending on the substituents, with the smallest increase observed for **P_{17}**, which showed only a 3% gain, while the largest enhancement showed **P_{15}** with an increase of 14%. The diastereoselectivity remained relatively constant for most substrates, indicating that the altered solvent medium mainly affects the overall catalytic efficiency rather than the stereochemistry. Two exceptions were observed, as the diastereomeric ratio for **P_{14}** shifted from 2.3:1 to 2.9:1 (*trans*/*cis*). For **P_{16}** the ratio decreased from 3.4:1 to 2.6:1.

Comparing the different substitution patterns for methoxy-substituted derivatives, the trend that already been found for **cat2**OTf is observed again. Here, *meta*-substitution provides higher yields than *para*-substitution, indicating either an electronic effect, which is less strong for *meta*-substitution, or steric clashing of the *para*-substituent with the host shell.

Substrate scope for **cat2**NTf_2

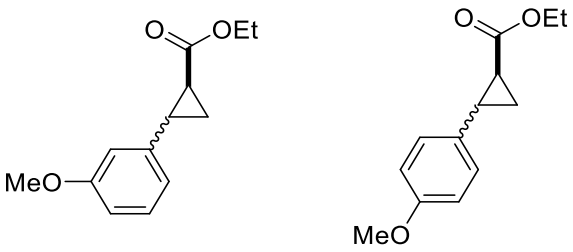

P_{13}
yield: 63%
TON: 316
d.r. = 2.1:1

P_{14}
yield: 58%
TON: 291
d.r. = 2.9:1

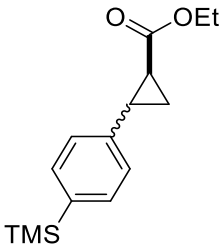

P_{15}
yield: 57%
TON: 286
d.r. = 2.9:1

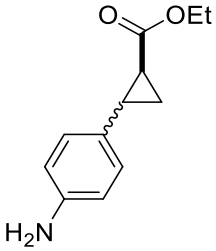

P_{16}
yield: 36%
TON: 178
d.r. = 2.6:1

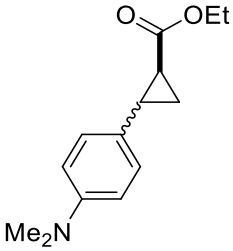

P_{17}
yield: 70%
TON: 351
d.r. = 3.0:1

Figure 89: Conversion of electron-donating systems with **cat2**NTf_2.

For two of the investigated substrates, isolated yields were determined in order to provide a more accurate picture of the catalytic performance beyond the initially obtained NMR yields. Therefore, the work-up was performed following the general procedure described in previous chapters, with an additional purification step to ensure complete removal of the catalyst.

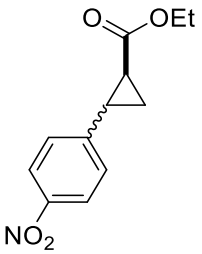

P_7
NMR: 67%
isolated: 44%
d.r. = 2.7:1

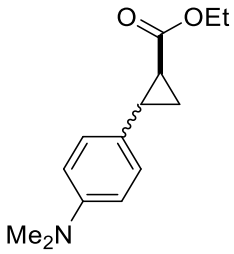

P_{17}
NMR: 70%
isolated: 38%
d.r. = 2.9:1

Figure 90: NMR yield in comparison to isolated yields.

The crude mixture was purified by preparative TLC (SiO_2) using cyclohexane/ethyl acetate (9:1) as the mobile phase. Under these conditions, the cobalt catalyst remained immobile at the baseline, whereas both the substrate and the products migrated with the solvent front, forming separated spots on the TLC plate. This provided a first separation, effectively removing the metal complex, which would cause issues in the following HPLC separation. The collected product was then subjected to HPLC separation, using an acetonitrile/water mixture (1:1). Thereby, both diastereomers could be separated in a diastereomeric ratio of 2.7:1 (*trans*/*cis*) for $\mathbf{P_7}$ and 2.9:1 for $\mathbf{P_{17}}$, which is close to the values in the ^{1}H-NMR analysis, allowing precise quantification of the stereoisomeric distribution and the yield. However, it should be noted that the additional separation steps, particularly the preparative TLC, cause the loss of material, resulting in significantly lower isolated yields compared to the initial NMR yields. Thereby, a similar loss in yield was observed for both substrates, from 67% to 44% ($\mathbf{P_7}$) and from 70% to 38% ($\mathbf{P_{17}}$), independent of their electronic effect.

Non-terminal double bonds

The cobalt-catalysed cyclopropanation of styrene derivatives has been extensively studied and a wide range of different catalysts were investigated. However, the application of the same conditions to styrene derivatives bearing non-terminal double bonds has remained rather underexplored, with only limited number of examples reported in literature.[121] This can be explained by the steric hindrance and electronic environment of these compound which make them considerably less reactive in radical carbene transfer processes.

In order to study the compatibility of the introduced catalytic system with these sterically more demanding substrates, the compounds shown in figure 91 and 92 were investigated first. These substrates, bearing either a methyl or aryl substituent at the double bond, were chose to test the fundamental steric and electronic effects without the complication of additional functional groups. Thereby, the experiments allow the investigation of how cobalt-carbene intermediates interact with non-terminal double bonds.

The experimental results showed a significant decrease in yield for $\mathbf{P_{18}}$ and $\mathbf{P_{19}}$ compared to the terminal derivatives. This suggests, that steric hindrance around the olefinic bond drastically hampers the formation of the cobalt-carbene radical intermediate, which lowers the overall catalytic efficiency. The results showed essentially no difference in yield for the (*E*)- or (*Z*)-configuration of the double bond, which gave a yield of 2% ($\mathbf{P_{18}}$) and 3% ($\mathbf{P_{19}}$). However, the diastereoselectivity of the reaction was strongly influenced by the applied isomer of the starting material. For the (*E*)-configurated double bond, $\mathbf{P_{18}}$ was obtained in a ratio of 1.5:1:0:0,

whereas **S_{19}** yielded a **d.r.** of 2.6:1:0:0. Due to the presence of only two signals in the ^{1}H-NMR, the diastereomers could not reliably be assigned.

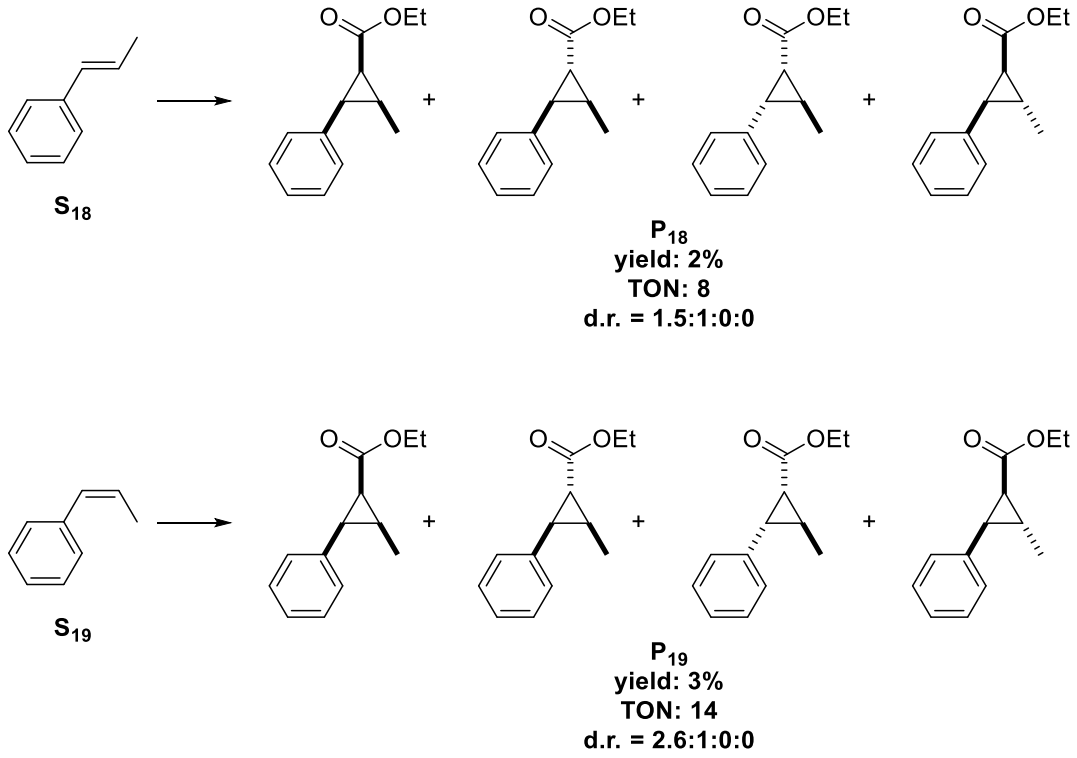

Figure 91: Cyclopropanation of **S_{18}** and **S_{19}** with all possible diastereomers.

In the (*Z*)-configurated double bond, the aromatic ring and the methyl group already point towards the same side of the system, which favours the transition state in which the newly introduces ester group orientates on the other side, leading to the *trans*-product. In contrast, in the (*E*)-isomer the aromatic ring and the methyl group are positioned on opposite sides of the double bound, which favours the newly introduced ester function to be on the same side as the aromatic system.

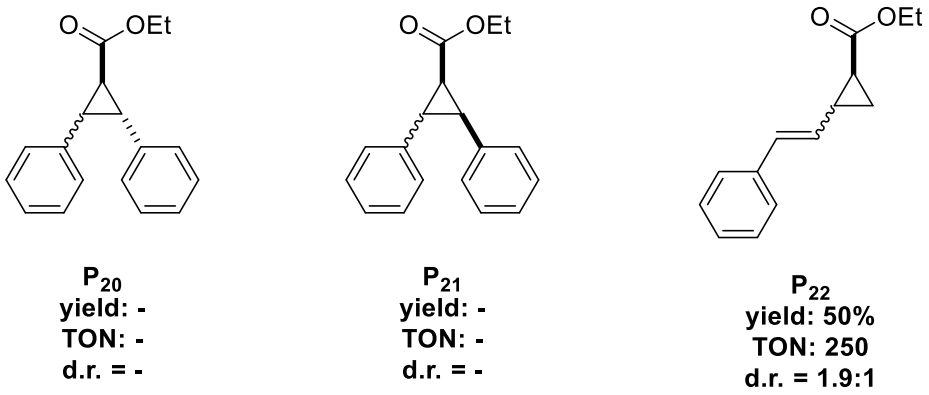

Figure 92: Results for the cyclopropanation of non-terminal double bonds bearing methyl or aryl groups.

Next, the influence of the double bond isomerisation of the substrate was investigated further. **P_{20}** and **P_{21}** did not show any conversion under the applied conditions. As discussed in previous chapters, the stilbene framework introduces too much steric bulk to enter the confined supramolecular cavity of the catalytic system. Consequently, these substrates could not be converted, regardless whether the double bond adopts an (*E*)- or (*Z*)-configuration. This potentially highlights the limitations of the catalysis inside supramolecular confinement, which can provide a distinct control over the reaction's outcome, but simultaneously restrict the size and shape of potential substrates.

Lastly, the selectivity of this conversion was tested by applying **S_{22}** with one internal double bond in benzylic position and a terminal double bond. Interestingly, the only detectable conversion was of the terminal double bond, where **P_{22}** was obtained in 50%. For the other double bond, not even traces of product formation were observed, showing a remarkable selectivity of this system, which might be explained by the completely conjugated system, and thus, the stabilisation of charges and electrons in conjugation with the aromatic system. For **P_{18}** to **P_{29}** it remains unclear, if the conversion is achieved inside the supramolecular complex or whether the low conversion was obtained *via* background reactions. This has to be evaluated in future, by performing these conversions without any catalyst.

The next step was to investigate the tolerance of these systems towards functional groups. Therefore, both previously studied substrate classes were combined by introducing functional groups to the aromatic ring, in the presence of non-terminal double bonds. The respective results are summarised in figure 93.

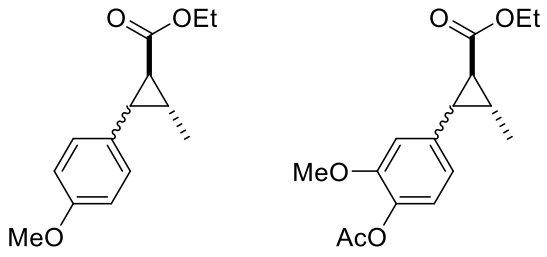

P_{23}
yield: 1%
TON: 6
d.r. = 2.8:1

P_{24}
yield: -
TON: -
d.r. = -

Figure 93: Results for the conversion of methyl styrene with different functionalities on the aromatic system.

The introduction of a methoxy substituent in the *para*-position provided only 1% yield, which, nonetheless, corresponds to a turnover number of 6. Compared to the corresponding terminal

analogue, where a yield of 58% was observed, this highlights the drastic loss in efficiency upon moving to non-terminal bonds, while retaining the functional group tolerance, proved in previous chapters. Interestingly, the diastereomeric ratio of the product remained the same, what suggests that while the steric environment of the non-terminal double bond hampers productive catalysts, the transition state geometry in not strongly influenced by this.

The second substrate in this series was chosen to introduce additional steric bulk, which lead to no detectable conversion. This can be explained by the spatial constraints of the supramolecular cavity. The sterically more demanding substituents may prevent the substrate from being efficiently encapsulated, thereby excluding it from the catalytic pocket. Alternatively, partial encapsulation of the substrate might still occur, but the substituents could interact with the surrounding sphere of the host in an unfavourable manner. This brings the double bond into the wrong position in respect to the catalytically active cobalt centre, which prevents efficient conversion.

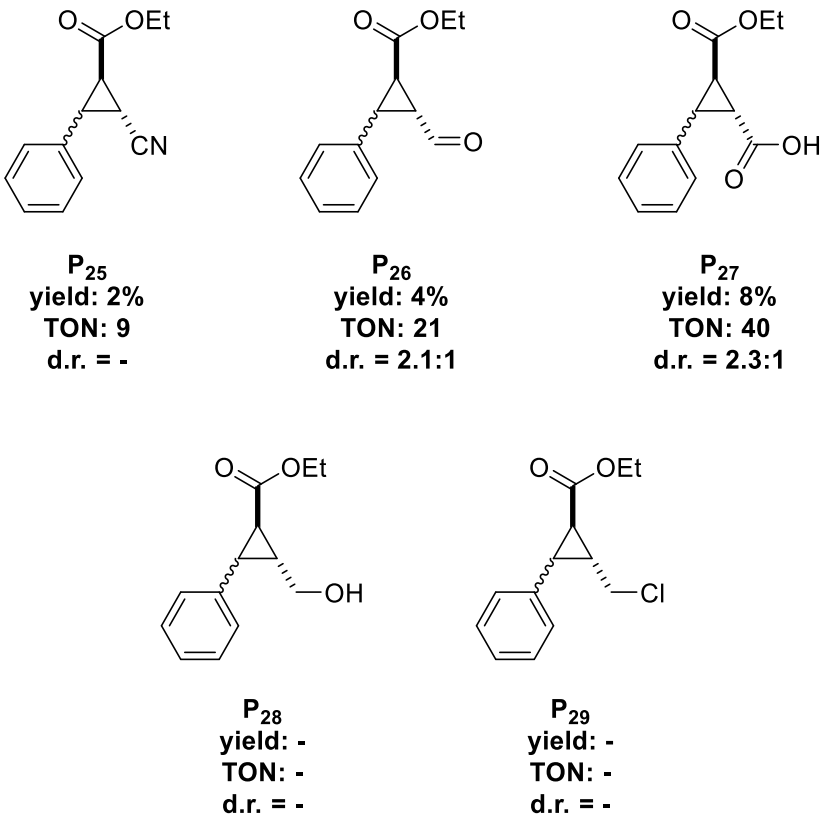

Figure 94: Results for the conversion of styrene derivatives.

In the final group of substrates, functional groups were introduced in the aliphatic region. Thereby, the effect of immediate substitution at the reactive site was investigated. Unlike the previous series, where substituents were located on the aromatic ring and influenced the

reaction mainly through steric or electronic effects at a distance, this set of substrates could provide additional insights of how functionalisation influences the catalytic behaviour. The results are summarised in figure 94. First, the functionalisation of the double bond was studied using cinnamyl alcohol **S_{28}**, cinnamaldehyde **S_{26}** and cinnamic acid **S_{27}**. These three examples allowed the direct comparison of how increasingly oxidised substituents influence the reaction.

For **S_{28}**, no conversion was observed. The higher oxidised cinnamaldehyde gave **P_{26}** in 4% yield, while the cinnamic acid **S_{27}** showed a slightly increased yield of 8%, corresponding to a **TON** of 40. Beyond these oxygenated species, the introduction of a nitrile group resulted in a low yield of 2%, suggesting that the deactivating character is non-beneficial for this conversion. The cinnamyl chloride showed no conversion to the desired product. In general, the trend is becoming evident, that substrates with a higher mesomeric stabilisation, as **S_{25}**, **S_{26}** and **S_{27}**, provide the respective products, while with a lower mesomeric stabilisation (**S_{28}** and **S_{29}**) no product formation was observed.

However, these experiments have to be further investigated by mechanistical studies as presented in the following chapter for the conversion of terminal-double bonds. Without these additional studies, the observed yields and diastereomeric ratios are only a hint on the limitations of the performance of the supramolecular catalysts, but it has to be investigated whether the conversion takes place inside the host environment to provide reliable informations.

16. Further mechanistical studies

In order to gain deeper insight into the cobalt-catalysed cyclopropanation reactions, additional studies were performed with the aim of clarifying distinct catalytic activity of the supramolecular systems and investigating the influence of the electronic effects of different substituents. This build directly on the mechanistic work established by *de Bruin* and co-workers as well as *Zhang* and co-workers, who showed that cobalt(II) complexes often operate *via* carbene radical intermediates.[81–83,115]

Thereby, two aspects are particularly relevant for the supramolecular system. First, the spatial confinement of the catalytic pocket, which can lead to specific orientations of the carbene radical and the alkene, thereby altering both activity and stereoselectivity. The increased catalytic activity of the supramolecular systems was already discussed in chapter 11, where both supramolecular catalysts **cat1**OTf and **cat2**OTf were compared directly to the bare **Co-TPyP**. While these earlier results clearly showed the beneficial effect of encapsulation, the reason for this enhancement remains to be fully clarified. To address this, it is necessary to evaluate not only the complete catalytic assembly but also the individual components of the supramolecular aggregate.

Catalytic activity of the components of cat2

Therefore, the supramolecular catalyst **cat2**NTf_2 was studied in the absence of the cobalt(II) ion (**cat3**NTf_2) and of the whole catalytically active **Co-TPyP** moiety (**cube2**NTf_2), shown in a simplified manner in figure 95.

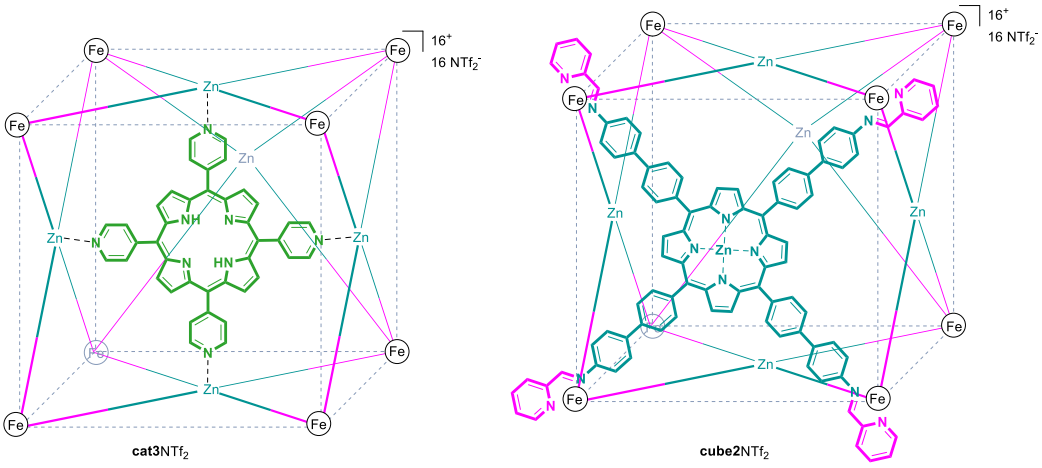

Figure 95: **Cat3**NTf_2 and **cube2**NTf_2 as schematic structures.

Thereby, it can be investigated whether the supramolecular cage itself is able to catalyse cyclopropanation reaction by spatial confinement and the resulting local increase in effective substrate concentration.

To ensure optimal comparability with earlier experiments, the catalyst loading for both **cat3**NTf_2 and **cube2**NTf_2 remained at 0.2 mol%, with the respective results summarised below.

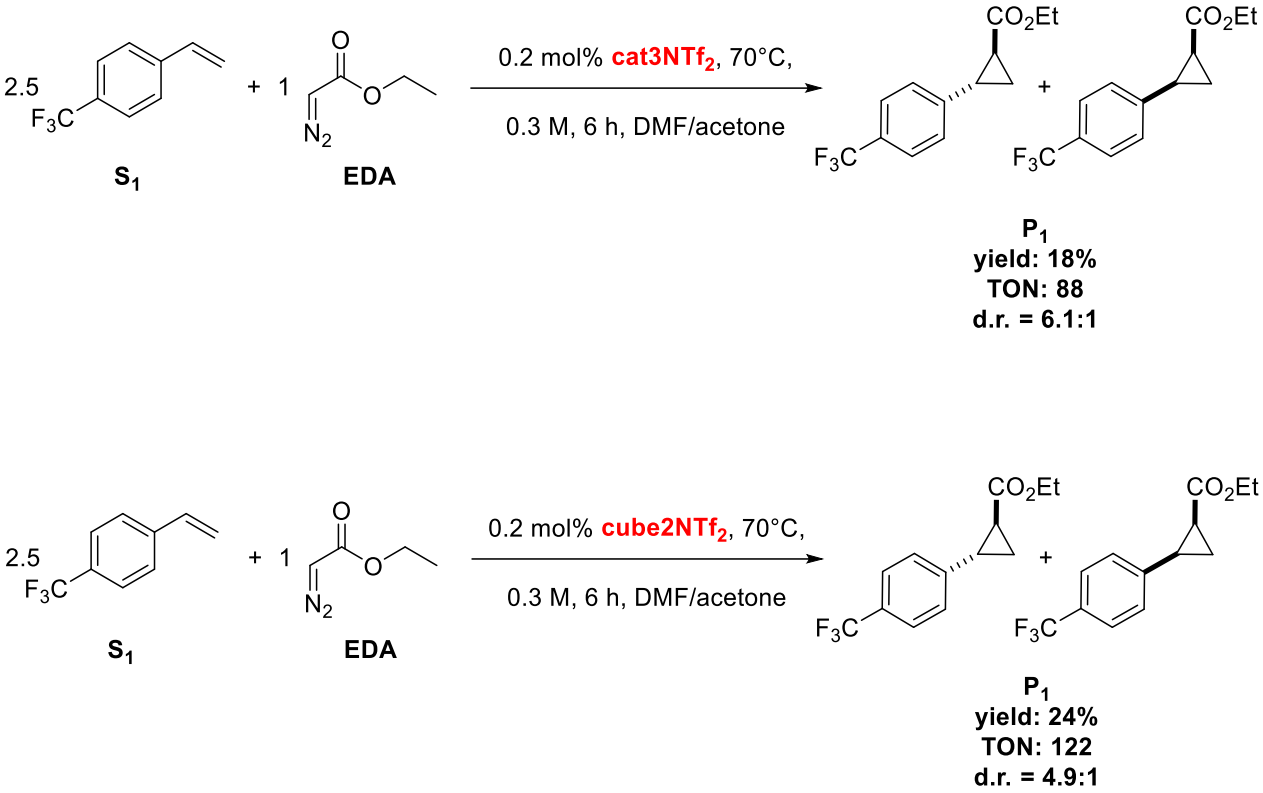

Figure 96: Control experiments with **S₁** and **cat3**NTf_2 and **cube2**NTf_2.

With both catalysts the standard substrate, *para*-trifluoromethyl styrene, was converted to the respective products. In the case of **cat3**NTf_2 18% yield was observed, which corresponds to a turnover number of 88. With **cube2**NTf_2 a yield of 24% was obtained, corresponding to a turnover number of 122. Although these values are significantly lower than the previously observed 72% yield with the complete cobalt-containing catalyst (**cat2**NTf_2), it nonetheless highlights the catalytic influence of confinement. This effect on its own contributes significantly to the reactivity by increasing the local effective concentration of substrates. Thereby, the host could act as a molecular flask, which already introduces shielding effects and increases the reactivity of the conversion.

The diastereomeric ratios in these cases were 4.9:1 (*trans*/*cis*) for **cube2**NTf_2 and even 6.1:1 for **cat3**NTf_2, which is higher than in comparable cobalt catalysed supramolecular catalysis. This needs to be investigated further to provide reliable informations.

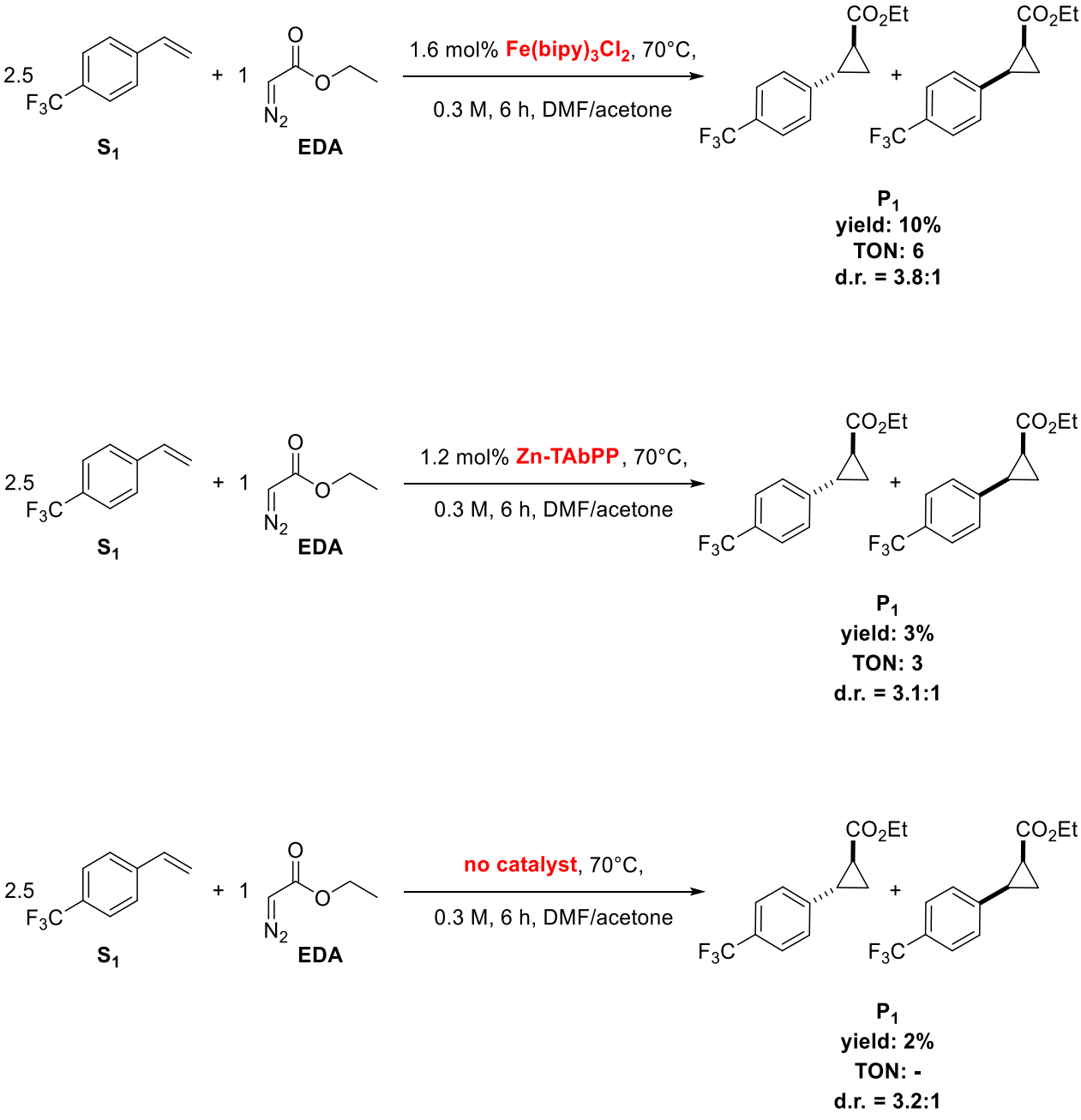

Figure 97: Results for the catalytic conversion with $Fe(bipy)_3$ and no catalyst.

In order to investigate the unexpected results, iron(II) bipyridine was studied as an example system. Iron(II) complexes are well-known catalysts for carbene transfer and cyclopropanation reactions, often operating *via* similar mechanisms to those of cobalt porphyrins. This also provides a direct comparison of the activity and selectivity of cobalt in comparison to iron

catalysts. For iron(II) bipyridine, a higher catalyst loading of 1.6 mol% was chosen. This corresponds to the fact that each supramolecular catalyst contains eight iron(II) corner units, and thus, the molar amount of iron introduced matches the total number of potential catalytic sites present in the supramolecular assembly. Bipyridine was chosen as the ligand, since it provides a coordination environment that mimics the local ligand sphere surrounding each iron centre in the supramolecular assembly best. This structural analogy makes the $Fe(bipy)_3$ complex a good reference for investigations of the catalytic effects form the metal identity in combination with the ligand sphere. The iron(II) bipyridine complex gave a relatively low yield of 10%, corresponding to a **TON** of 6. This limited catalytic performance suggests that the iron centres positioned at the corners of the supramolecular assembly contribute only marginally to the overall activity. Although iron(II) complexes are well-known to act as a catalyst in cyclopropanation reactions, in this low catalyst loading the effect is only small compared to the confinement driven and the overall reactivity of the supramolecular system. This highlights the effect confinement of a reaction in a small distinct reaction chamber can have. Even without a catalytic species in the conventional sense the supramolecular system provides a reduced but still measurable activity.

Additionally, **Zn-TAbPP** was applied in the conversion of $\mathbf{S_1}$ with a catalyst loading of 1.2 mol%, corresponding to 6 * 0.2 mol% since 6 molecules of **Zn-TAbPP** are present in one cubic host. This yielded $\mathbf{P_1}$ in 3% with a diastereomeric ratio of 3.1:1 (*trans*/*cis*), which supports the theory that the surprisingly high yield with **cat3**NTf_2 and **cube2**NTf_2 is evoked by the confinement effect inside a molecular flask and not by any of the components on their own.

To test potential background reactions, a control experiment was performed under identical reaction conditions but in the absence of any catalyst. This yielded only 2%, confirming that spontaneous or thermal reactivity of these substrates is minimal. Since no catalyst was present, a turnover number could not be determined. Interestingly, the *trans*-fraction in the diastereomeric ratio of the resulting cyclopropane products decreased even further to 3.2:1 (*trans*/*cis*). This ratio becomes comparable to that observed for reactions inside the supramolecular catalyst **cat2**NTf_2, wherefore the reason also has to be investigated by additional studies.

Consequently, the observed reactivity of **cat2**NTf_2 seems to be evoked primarily by the catalytic effect of cobalt(II) in combination with the surrounding confinement rather than by catalytic activity of one distinct part of the assembly.

The second effect, mentioned earlier in this chapter, is the electronic influence of the alkene substate, tuned by substituents on the aromatic ring. To get systematic insights into electronic effects, a *Hammett*-plot is often the remedy of choice.[118] Therefore, half of the amount of the respective alkene substrate is combined in the cobalt catalysed cyclopropanation with equimolar amounts of styrene to investigate the effect of the substituents independent of any possible error source. By combining both potential substrates in one reaction vial, it is possible to determine precisely which of the two substrates is preferentially converted in the presence of a possible alternative. For the graph, shown in figure 98, the *Hammett*-parameters[118] were plotted against the decimal logarithm of the yield of the respective derivative divided by the yield for unsubstituted styrene. In order to exclusively study the influence of the electronic effect, which is strongest in *ortho*- and *para*-position, only *para*-substituted derivatives were chosen, since *ortho*-substitution often introduces hindering steric bulk close to the catalytically active site.

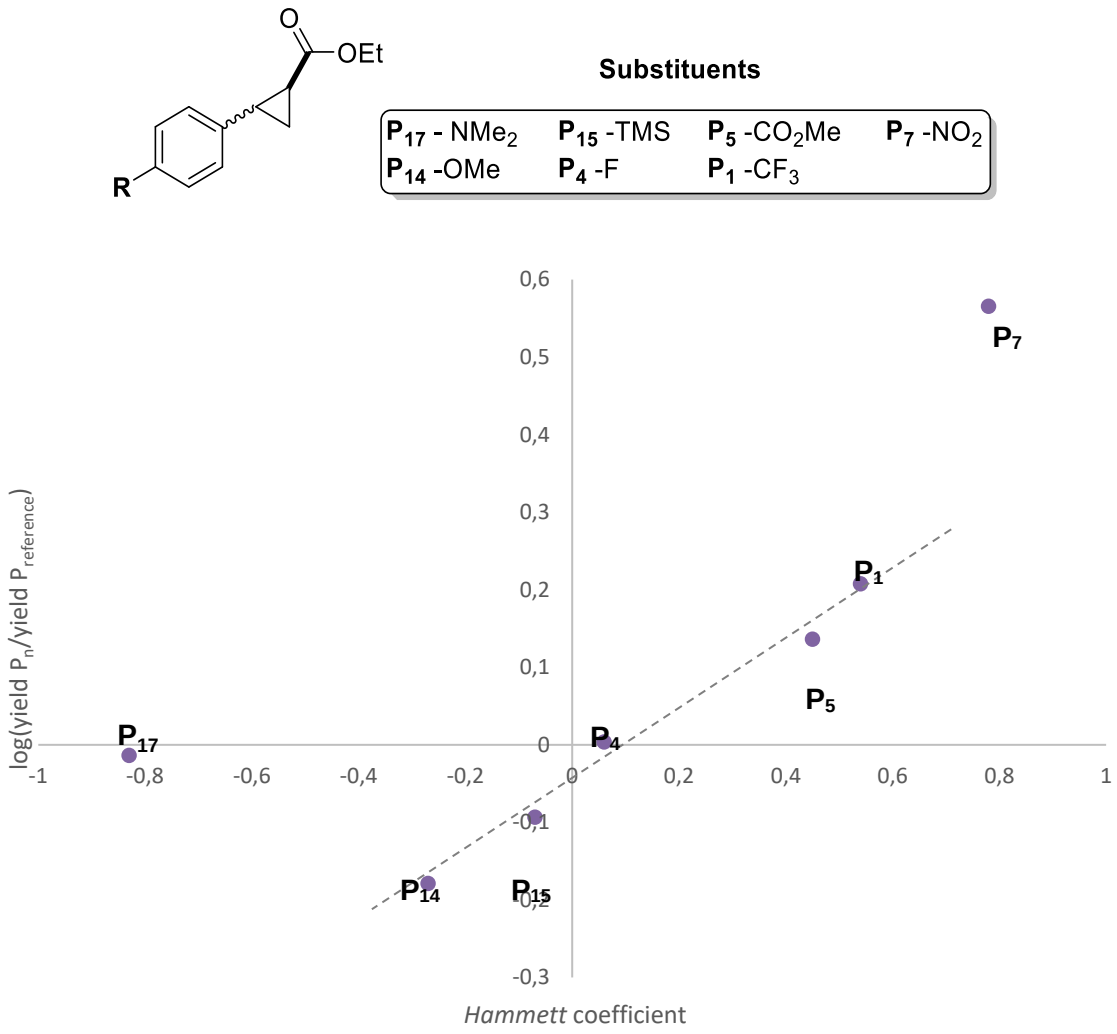

Figure 98: *Hammet*-plot of seven *para*-substituted styrene derivatives.[118]

The *Hammett*-plot shows for **P$_1$**, **P$_4$**, **P$_5$**, **P$_{14}$** and **P$_{15}$** a straight, linear trend, which is expected when the electronic effects of substituents strongly influence the reactions outcome. This linear correlation shows that the substituents on the aromatic ring alter the electron density of the styrene double bond, thereby affecting its reactivity. The positive slope of the line indicates that electron-withdrawing substituents, which correspond to positive *Hammett* coefficients, are converted more efficiently than the unsubstituted styrene. This corresponds to the fact that groups who pull electron density away from the aromatic system are beneficial for the transition state of the reaction, and thereby, facilitate the catalytic process. This matches the mechanism introduced by *de Bruin* and co-workers in which the unpaired electron is transferred from the radical carbene intermediate to the alkene, which is more favourable for electron deficient systems.[111]

In contrast, electron-donating groups, which appear on the left side of the plot with negative *Hammett* coefficients, are converted less likely. By increasing the electron density at the double bond, the electron transfer to the double bond is less likely and the reaction becomes hindered.

Interestingly, two outliers can be identified with **P$_{17}$** and **P$_7$**, both bearing highly coordinating substituents. These substrates perform significantly better than predicted by the linear regression. This could suggest the presence of additional effects beyond the simple electronic substitution. The coordinating substituents could potentially interact directly with the surrounding supramolecular host, guiding or anchoring the styrene units in a beneficial orientation relative to the cobalt centre. This preorganisation could bring active sites into close proximity, which would lead to faster and more efficient conversion.

Thus, while the *Hammett*-plot shows the predominant role of electronic substitution effects, the deviations observed with **P$_{17}$** and **P$_7$** highlight the importance of the secondary coordination sphere not only as a passive shield but rather as an active participant in the catalytic conversion. This underlines the complex interplay of electronic and supramolecular factors in determining catalytic performance.

17. Summary

Porphyrin synthesis and purification

The first chapter of this work focused on the synthesis and purification of porphyrins, based on the classical method introduced by *Adler et al*.[86] From there on, possible methods were investigated to enhance the rather low yield, the purity and applicability across a broad range of derivatives. Even though the *Adler* protocol offers simplicity and reliability, incomplete precipitation, variations in solubility and the formation of by-products leads to poor yields around 20%.

The key modifications introduced in this work included controlled dilution and cooling steps after the reaction to ensure complete precipitation, solvent selection tailored to each porphyrin's substituents and the systematic use of fluorescence monitoring to track product recovery. Thereby, additional procedures for specific porphyrins were necessary, as the neutralisation of protonated pyridyl groups prior to the work-up of **TPyP**. While column chromatography remains widely used, it was found to be inefficient and less sustainable for porphyrins due to strong interactions with silica, leading to poor recovery and excessive solvent use. Recrystallisation was found to be a greener and effective alternative, but it is compound-specific and requires extensive solvent screening. Therefore, a novel purification method based on acid-base recrystallisation was established, which can fundamentally advance porphyrin chemistry. Herein, protonation precipitates the porphyrin as a salt, separating it from impurities, while subsequent deprotonation regenerates the neutral macrocycle in high purity. This method was shown to be broadly applicable, efficient and more sustainable. This combination of a modified synthetic procedure with a new technique for the purification yielded porphyrins in remarkably good yields up to 70%, which drastically increase the "standard" yield in porphyrin synthesis of 20%. Additionally, the completely new purification strategy allows the formation of porphyrins in an extraordinary high purity, which is often a severe problem in porphyrin chemistry or is not sufficiently analysed. In order to provide a reliable analytic method elemental analysis was employed as a new gold standard to evaluate the purity of porphyrins.

The modified synthesis and purification were tested in a scope of symmetrical and less symmetrical porphyrins. Most systems were successfully synthesised and purified in high yields, up to 70%, though sterically hindered substitution patterns caused synthetic failure. For less symmetrical porphyrins, efficient condensation was achieved by first preparing suitable precursors and was adaptable for different substituents. An overview of the discussed porphyrin is shown in figure 99.

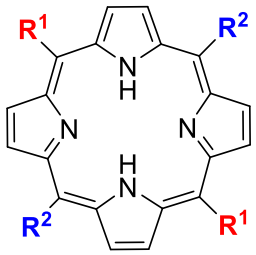

R¹ substituent	R² substituent	yield
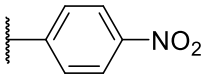	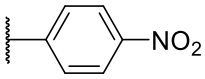	70%
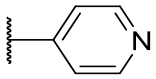	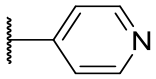	51%
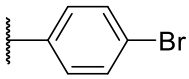	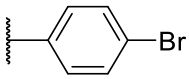	45%
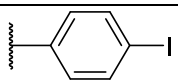	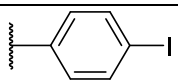	30%
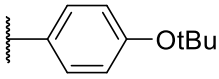	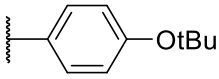	23%
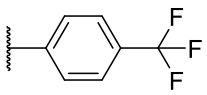	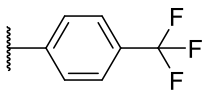	30%
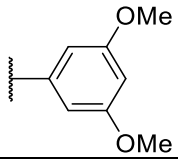	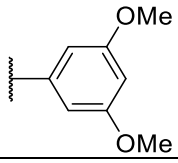	52%
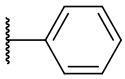	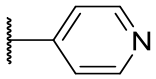	35%
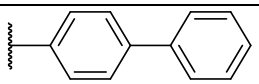	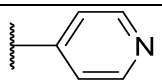	59%
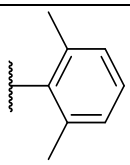	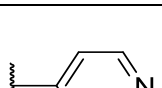	-

Figure 99: Overview of the synthesised porphyrins.

Finally, elemental CHNS analysis was highlighted as a key complementary tool to NMR, overcoming limitations of NMR spectroscopy due to the generally poor solubility of porphyrins. Unfortunately, elemental analysis, an only rarely used analytical tool these days is indispensable to verify both identity and purity. This high standard for the purity of porphyrins enables the efficient use of porphyrins in the first place.

Overall, the first part of this thesis established a versatile synthesis and purification route to access non-metalated porphyrins. Thereby, not only the previously known methods were systematically optimised but also a broadly applicable purification method was introduced, overcoming the previously limiting factors in porphyrin chemistry. This allows for the first time to form porphyrins in higher efficiency and excellent purity while improving sustainability, which allows them to be now regarded as attractive and efficient building blocks for a variety of applications.

Formation and characterisation of porphyrin-based supramolecular cubes

In the second chapter, the formation of porphyrin-based supramolecular cubes was investigated, using the porphyrins from the first part. These studies focused on how assembly conditions, isolation technique and cavity occupancy determine the stability and successful isolation of the cage.

One central aspect is the role of templates during the formation of **cube 1**, **cube 2**, **cat1** and **cat2**, respectively. Incorporating the catalytically active **Co-TPyP** in a template approach into the cavity during the synthesis of **cat1** and **cat2** significantly enhanced cage assembly. This provided directional coordination sites, preorganising the framework and lowering the entropic barrier. Additionally, the formation of the "filled" cube directly in a one-pot process not only led to effective cage formation but also avoided additional purification steps. In order to keep structural integrity of the fragile supramolecular assembly once it is formed, the standard isolation *via* dissolution and solvent removal under reduced pressure was exchanged for direct collection of the cage after filtration. Thereby, the disassembling back into subcomponents was prevented, which yielded the intact architecture without collapse.

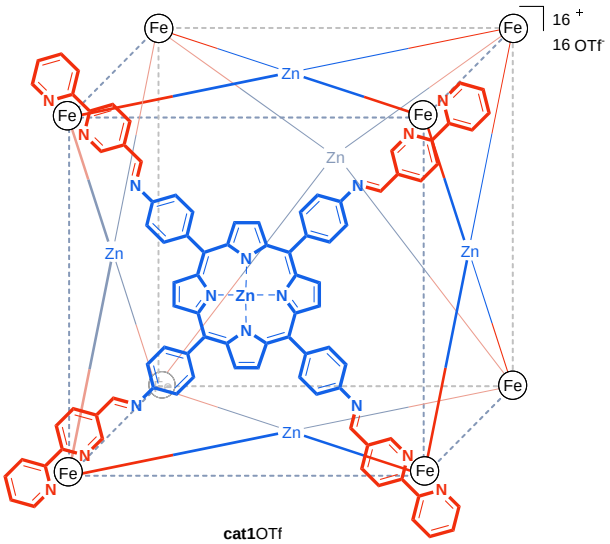

Figure 100: Simplified structure of **cat1**OTf.

Condition screening revealed that in combination with appropriate templates and isolation strategies, the formation of the supramolecular system tolerated the presence of water and air. Thereby, not only the robustness of this assembly was proven but also the synthetic effort was reduced, which made it less prone towards errors. Another key factor was the stabilising contribution of solvent molecules within the internal cavities. DMF, used during the assembly,

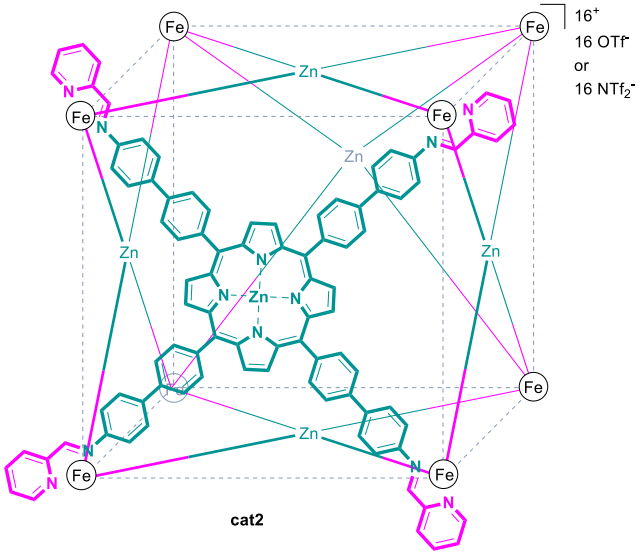

Figure 101: Simplified structure of **cat2**.

remained partially bound inside the cubes even after extended drying under fine vacuum (10^{-2} mbar). Quantitative ^{1}H-NMR showed an initial DMF content of around 17%, which decreased only partially over time. These trapped molecules remain inside the cavity of the supramolecular assembly and benefit its stability by filling otherwise destabilising voids. However, their presence also complicates catalyst handling, since variations in DMF content affect the effective concentration of active species in solution.

Characterisation of these large, paramagnetic and poorly soluble supramolecular cubes remained challenging. ESI-MS proved to be the most reliable technique, detecting intact assemblies with multiple charge states and allowing comparison with calculated isotopic patterns. NMR analysis, however, was hampered by low solubility, broad signals and paramagnetic effects, leading to an overall poor signal-to-noise ratio. While limited structural information could be generated, the DMF content was investigated by this method, giving essential insights which drastically determine the applicability of the system in further catalysis.

Cobalt-catalysed cyclopropanations

The ultimate goal of this thesis was to investigate cyclopropanation reactions using the cobalt-porphyrin supramolecular systems, highlighting their effective performance in these reactions.

Initial condition screening was performed with **cat2**OTf regarding the DMF content inside the supramolecular cavity, the stoichiometry of both substrates, temperature, reaction time, overall concentration, catalyst loading and the sensitivity towards water and air content. Thereby, the reactions showed a distinct improvement in turnover numbers at lower catalyst loadings, confirming the efficiency gains upon encapsulation. Small amounts of water in the solvent mixture were found to increase activity, by potentially facilitating substrate diffusion into the confined cavity by partially disassembling and afterwards reassembling of the host structure.

With those optimised conditions established, the substrate scope of **cat2**OTf was studied. Beyond size selectivity, already introduced by *de Bruin* and co-workers, this work focused on functional group tolerance, whereby styrene derivatives bearing electron-withdrawing as well as electron-donating substituents provided decent yields and turnover numbers which are significantly higher than with the unencapsulated **Co-TPyP**. As expected, the confinement shifted the product distribution towards higher *cis*-selecetivity compared to the free, non-encapsulated cobalt-porphyrin, demonstrating that the supramolecular host not only acts as a shield for the reactive species but also actively influences the reactions outcome.

Building on these results, the counterion of the supramolecular system was exchanged from triflate (OTf) to triflimide (NTf_2), yielding **cat2**NTf_2. This improved solubility and robustness significantly, enabling catalytic conversion not only in pure DMF, as used for **cat2**OTf, but also allows the use of solvent mixtures. With a mixture of DMF and acetone in a ratio of 1:2 under otherwise identical conditions, the yields already increased substantially and turnover number improved by nearly 40%. Further experiments regarding the catalyst loading, which was for **cat2**OTf already remarkably low with 0.4 mol%, could be reduced to 0.2 mol% which showed even slightly higher efficiency than at 0.4 mol%.

Afterwards, the same substrate scope as for **cat2**OTf, was investigated with **cat2**NTf_2. Again, nearly all substrates gave yields between 50% and 72% which corresponded to turnover numbers of 250 to 360, which demonstrate the extraordinary efficiency of the catalytic system.

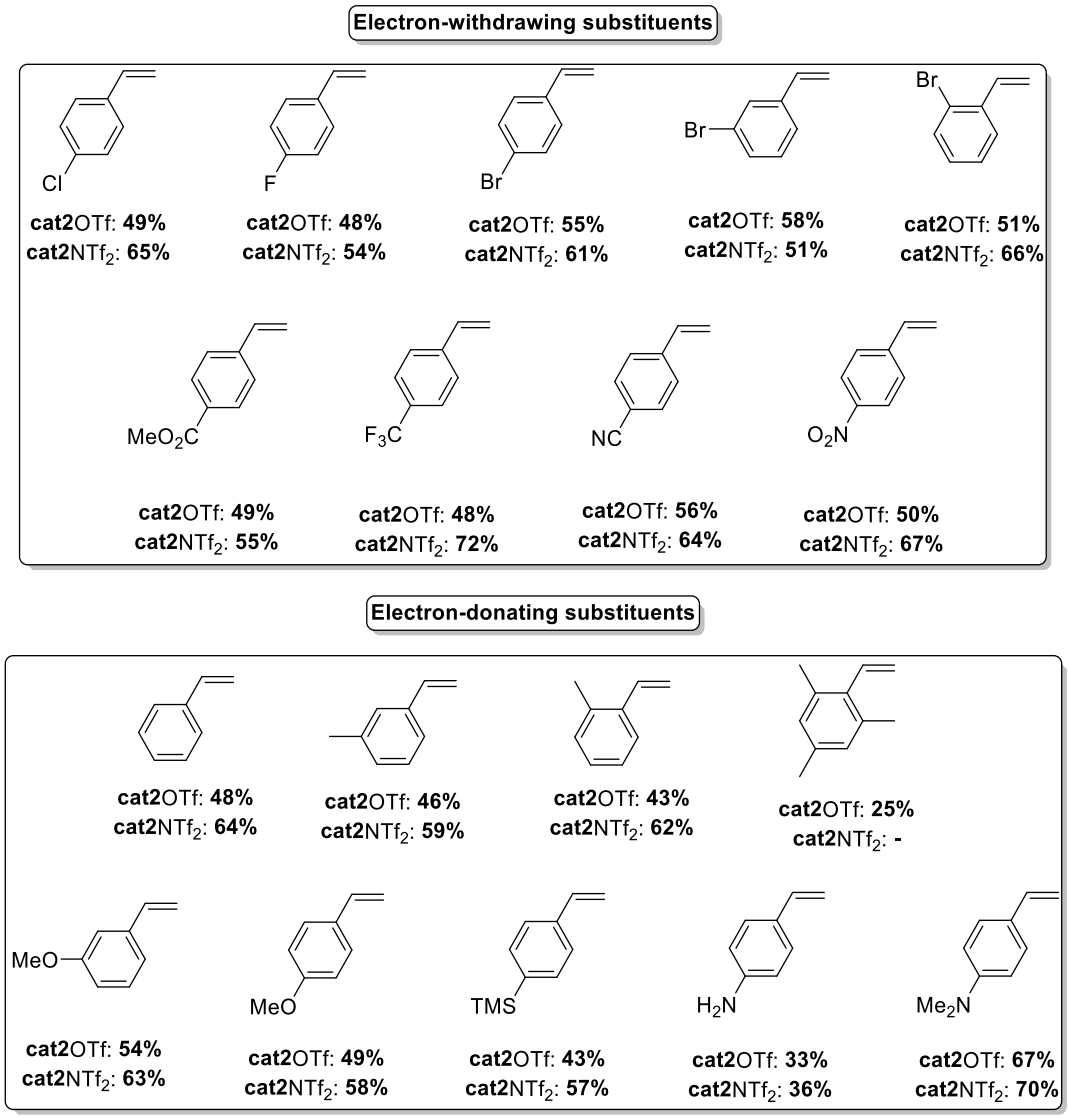

Figure 102: Summary of the substrate scope for both supramolecular catalysts **cat2**OTf and **cat2**NTf_2.

Additionally, styrene derivatives with a non-terminal double bond were tested, which showed only small yields below 10% but are one of the few examples for the cobalt-catalysed cyclopropanation of styrene derivatives that are published. Mechanistic studies further clarified the role of the supramolecular environment. Control reactions showed that the cage without the **Co-TPyP** inside showed some catalytic activity due to the presence of iron(II) ions, which are well known catalysts for cyclopropanations, and the confinement of substrates. To investigate the influence of the iron centres on the corners of the cubic system showed even lower activity, which proves that the high activity of the established system is based on the well-levelled interplay of each component.

A *Hammett*-plot supported the radical-carbene mechanism, published by *de Bruin* and co-workers, with electron-withdrawing substituents accelerating the process.[111] However, deviations from the electronic trend in substrates bearing coordinating groups indicated that secondary interactions with the host framework might lead to a favourable preorganisation of the substrates inside the cavity, directly influencing reactivity and product outcome.

Altogether, these results demonstrate that supramolecular porphyrin-based catalysts can significantly outperform their non-encapsulated analogues, preventing well-known issues of “standard” catalytic systems. Thereby, not only turnover numbers, up to remarkable values of 360 are reached while the stability of intermediates is enhanced but also additional stereocontrol, with significantly higher yield of the *cis*-product with the encapsulated catalysts than with **Co-TPyP**, as well as substrate selectivity are obtained.

18. Experimental section

General information

Working methods

All reactions using air or water sensitive reagents were carried out in oven dried glassware and under inert-gas conditions (argon) using *Schlenk* techniques. Solids were added to the reaction vessel under argon counter-flow or in the *glovebox*. Liquid substances or solvents were added by using plastic syringes flushed with argon multiple times or transfer cannulas through septa. Commercially available chemicals were used without further purification if not stated otherwise from *Sigma Aldrich*, *BLDPharm*, *ChemPur*, *Alfa Aesar*, *Acros Organics*, *abcr*, *TCI Chemicals*, *Fluorochem*, *Fisher scientific* and *Merck*. The removal of solvents was carried out at a rotation evaporator with a temperature of the water bath of 40°C.

Solvents

All solvents were purchased from commercial sources and distilled, if necessary, before usage (cyclohexane, ethyl acetate and dichloromethane). Dry solvents were obtained from the *M. Braun SPS 800* solvent purification system under argon counter stream.

Instruments and analytic

NMR-spectroscopy

^{1}H-, ^{13}C-, ^{19}F-, H-COSY-, HSQC- and HMBC-NMR spectra were measured on *Avance* I 400 ^{1}H-(base frequency 400.13 MHz), *Avance* I 500 (base frequency 499.13 MHz), *Avance* III 500 ^{1}H-(base frequency 500.13 MHz), and *Avance* III 700 ^{1}H-(base frequency 700.41 MHz) from *Bruker*. Chemical shifts (δ) are denoted in ppm and are calibrated using the centre of the residual undeuterated solvent signals as internal reference. These spectra were analysed using the software *MestReNova* from *Mestrelab*.

Coupling constants (*J*) are reported in Hz. Diastereomeric ratios are determined by ^{1}H-NMR, using dibromomethane and nitromethane as internal standards, if possible.

Mass spectrometry

EI-MS measurements were performed with a *MAT 95XL*- and *APCI*-mass spectrometer from *Thermo Finnigan*. ESI-MS measurements were carried out at an *Orbitrap XL*-mass spectrometer from *Thermo Fisher Scientific*. MALDI-MS measurements were performed with an *ultrafleXtreme TOF/TOF* mass spectrometer from *Bruker Daltonic*.

Elemental Analysis

EA measurements were carried out with a *varioMICRO V1.6.1* from *Elementar Analyensysteme GmbH* in CHNS-mode.

Chromatography

Column chromatography was performed on silica gel from *Merck* (particle size 0,04 - 0,06 nm).

Thin-layer chromatography (TLC)

TLC was performed using *Merck* silica gel 60 F254 TLC aluminium sheets and analysed by using UV-light (wavelength of 254 nm or 366 nm).

Porphyrin synthesis

5,10,15,20-tetrakis(4-nitrophenyl)porphyrin (TNPP)

The synthesis of **TNPP** was performed in a modified version of the procedure described by *Adler*.[37]

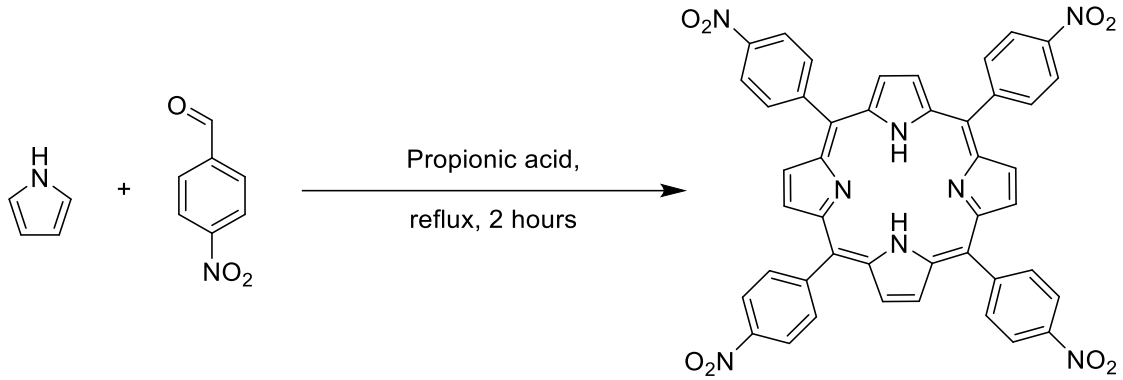

Figure 103: Synthesis of **TNPP**.

Pyrrole (4.15 mL, 60.00 mmol, 1.0 eq.) was dissolved in propionic acid (300 mL) and the solution was heated to 100°C. 4-nitrobenzaldehyde (9.07 g, 60.00 mmol, 1.0 eq.) was added, the solution was refluxed for 30 minutes at 150°C and afterwards cooled to room temperature. The mixture was added dropwise to an excess of water (500 mL) and stored in the fridge overnight. Following, the suspension was filtered and the remaining solid washed with water and methanol until the filtrate exhibited no colour. The solid was extracted with dichloromethane until the extract was colourless and showed no more fluorescence. The solvent was removed under reduced pressure and the black solid was recrystallised from pyridine (150 mL). Afterwards, the mixture was again added dropwise to an excess of water (250 mL) and stored in the fridge overnight. After the formed solid was filtered it was washed with water and methanol until the filtrate exhibited no more colour or fluorescence. The solid was extracted with acetone until the extract was colourless and showed no more fluorescence. The solvent was removed under reduced pressure and the remaining solid was recrystallised in acetone (150 mL). The mixture was cooled to room temperature, added an additional time dropwise into an excess of water (250 mL) and was stored in the fridge overnight. The

suspension was filtered one last time, washed thoroughly with water and methanol until the filtrate showed no more colour or fluorescence and the product was extracted with chloroform. The solvent was removed under reduced pressure and the product was obtained, after drying *in vacuo* overnight, as a dark purple solid (8.28 g, 10.43 mmol, 70%).

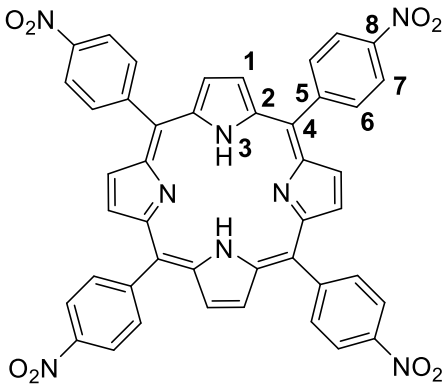

^{1}H-NMR (400 MHz, TFA-d_1, 298 K): δ[ppm] = 9.02 (d, $^{3}J_{7,6}$ = 8.7 Hz, 8 H, H-7), 8.97 (s, 8 H, H-1), 8.87 (d, $^{3}J_{6,7}$ = 8.7 Hz, 8 H, H-6).

^{13}C-NMR (176 MHz, TFA-d_1, 298 K): δ[ppm] = 151.4 (C-4), 147.8 (C-2), 146.6 (C-8), 140.7 (C-6), 132.1 (C-1), 125.9 (C-7), 124.3 (C-5).

HRMS-MALDI ($C_{44}H_{26}N_8O_8$) *m/z*: calculated [M^+] = 794.1868, experimental [M^+] = 794.1836.

Elemental Analysis: ($C_{44}H_{26}N_8O_8$): calculated = 66.50% (C), 3.30% (H), 14.10% (N), experimental = 67.11% (C), 3.87% (H), 13.97% (N).

This data agrees with the results reported in literature.[122]

5,10,15,20-tetrakis(4-pyridin-4-yl)porphyrin (TPyP)

The synthesis of **TPyP** was performed in a modified version of the procedure described by *Adler*.[37]

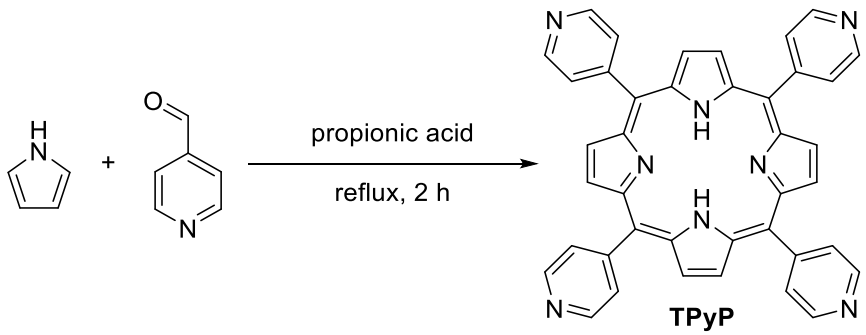

Figure 104: Synthesis of **TPyP**.

Pyrrole (0.35 mL, 5.00 mmol, 1.0 eq.) was dissolved in propionic acid (25 mL) and the solution was heated to 100 °C. Next, isonicotinaldehyde (0.47 mL, 5.00 mmol, 1.0 eq.) was added dropwise and the solution was heated at 150°C for 2 hours, followed by cooling to room temperature. The mixture was neutralised with saturated $NaHCO_3$ solution and stored in the

fridge overnight. The formed precipitate was filtered off, washed with water until the filtrate became colorless and the remaining solid was dissolved in chloroform. Then the solvent was removed under reduced pressure.

Afterwards the solid was dissolved in dimethylformamide and concentrated hydrochloric acid was added dropwise (8 drops) until the color changed from red to a dark green/blue. The suspension was stored in the fridge overnight, then filtered and the remaining solid was dissolved in water. The dark solution was mixed with potassium hydroxide pallets in order to provide a basic pH-level of the solution and the formed dark precipitate was filtered. The solid was washed with water until the filtrate became colorless. Next the solid was dissolved in chloroform, the solvent was removed under reduced pressure and the solid was dried *in vacuo* overnight. The product was obtained as a bright purple solid (396.2 mg, 0.64 mmol, 51%).

Table 15: Overview of tested reaction conditions.

time	concentration	yield
30 minutes	0.2 M	32%
2 hours	0.2 M	51%
3 hours	0.2 M	49%
1 hour	0.07 M	3%
2 hours	0.07 M	10%
3 hours	0.07 M	21%
1 hour	0.002 M	-
2 hours	0.002 M	5%
3 hours	0.002 M	17%

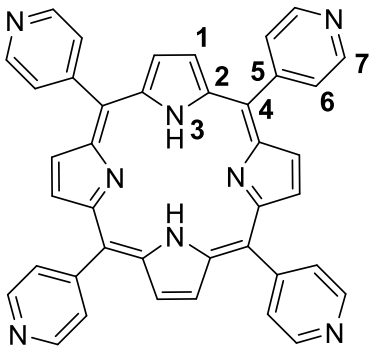

^{1}H-NMR (500 MHz, $CDCl_3$, 298 K): δ[ppm] = 9.07 (d, $^{3}J_{7,6}$ = 5.9 Hz, 8 H, H-7), 8.87 (s, 8 H, H-1), 8.17 (d, $^{3}J_{6,7}$ = 5.9 Hz, 8 H, H-6), -2.92 (s, 2 H, H-3).

^{13}C-NMR (126 MHz, $CDCl_3$, 298 K): δ[ppm] = 149.9 (C-5), 148.6 (C-7), 129.5 (C-6), 118.0 (C-4).

HRMS-MALDI ($C_{40}H_{26}N_8$) *m/z*: calculated [M^+] = 618.2275, experimental [M^+] = 618.2275.

Elemental Analysis: ($C_{40}H_{26}N_8$): calculated = 77.65% (C), 4.24% (H), 18.11% (N), experimental = 77.17% (C), 4.62% (H), 17.84% (N).

The ^{1}H-NMR spectrum of **TPyP** shows traces of propionic acid. Taken this into account, the expected values were recalculated with **TPyP** * 1/7 propionic acid to be 77.16% (C), 4.30% (H) and 17.81 (N). This reduces the deviation to 0.01% (C), 0.32% (H) and 0.03% (N).

This data agrees with the results reported in literature.[123]

5,10,15,20-tetrakis(4-bromophenyl)porphyrin (TBrPP)

The synthesis of **TBrPP** was performed in a modified version of the procedure described by *Adler*.[37]

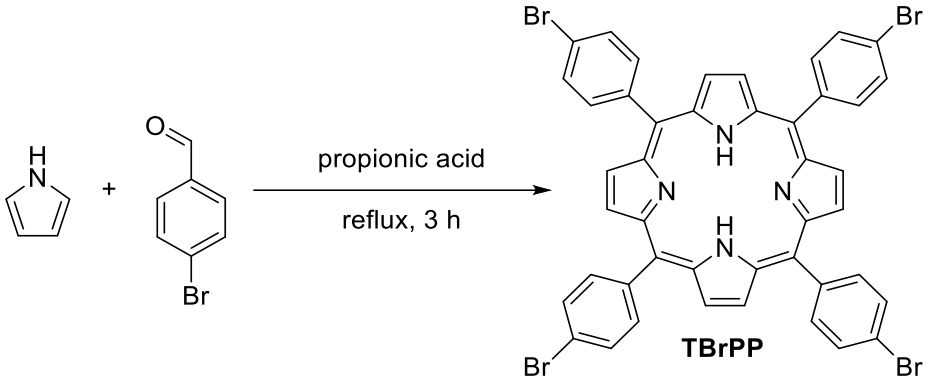

Figure 105: Synthesis of **TBrPP**.

Pyrrole (1.40 mL, 20.00 mmol, 1.0 eq.) was dissolved in propionic acid (100 mL) and the solution was heated to 100 °C. Next, 4-bromobenzaldehyde (3.68 g, 20.00 mmol, 1.0 eq.) was added and the solution was heated at 150°C for 3 hours, followed by cooling to room temperature. The mixture was added dropwise to an excess of water (500 mL) and the suspension was stored in the fridge overnight. The formed precipitate was filtered off, washed with water, methanol and ethyl acetate until the filtrate became colorless and the remaining solid was dissolved in dichloromethane. Then the solvent was removed under reduced pressure.

Afterwards the solid was dissolved in acetone and concentrated hydrochloric acid was added dropwise (25 drops) until the color changed from red to a dark green. The suspension was stored in the fridge overnight, then filtered and the remaining solid was dissolved in water. The dark solution was mixed with potassium hydroxide pallets in order to provide a basic pH-level of the solution and the formed dark precipitate was filtered. The solid was washed with water until the filtrate became colorless. Next the solid was dissolved in chloroform, the solvent was removed under reduced pressure and the solid was dried *in vacuo* overnight. The product was obtained as a bright purple solid (2.09 g, 2.26 mmol, 45%).

Table 16: Overview of tested reaction conditions.

time	concentration	yield
1 hour	0.2 M	11%
2 hours	0.2 M	26%
3 hours	0.2 M	45%

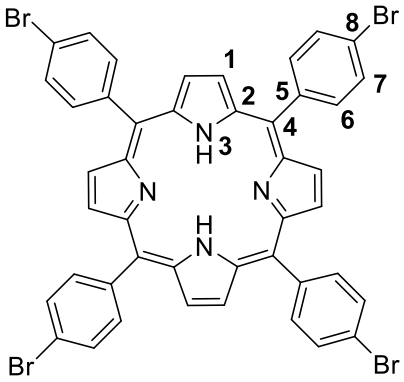

^{1}H-NMR (400 MHz, $CDCl_3$, 298 K): δ[ppm] = 8.84 (s, 8 H, H-1), 8.07 (d, $^{3}J_{6,7}$ = 8.3 Hz, 8 H, H-6), 7.90 (d, $^{3}J_{7,6}$ = 8.3 Hz, 8 H, H-7), -2.86 (s, 2 H, H-3).

^{13}C-NMR (176 MHz, $CDCl_3$, 298 K): δ[ppm] = 141.0 (C-5), 136.0 (C-6), 130.1 (C-7), 122.8 (C-8), 119.1 (C-4).

HRMS-APCI ($C_{44}H_{26}Br_4N_4$) *m/z*: calculated: $[M+H^+]$ = 930.8928, experimental: $[M+H^+]$ = 930.8932, $[M+2ACN+2H^{2+}]$ = 547.980, $[M+NH_4+H^+]$ = 482.953.

Elemental Analysis: ($C_{44}H_{26}Br_4N_4$): calculated = 56.81% (C), 2.82% (H), 6.02% (N), experimental = 56.12% (C), 2.72% (H), 5.80% (N).

The ^{1}H-NMR spectrum of **TBrPP** shows traces of water. Taken this into account, the expected values were recalculated with **TBrPP** * ½ H_2O to be 56.26% (C), 2.90% (H) and 5.96% (N). This reduces the deviation to 0.14% (C), 0.18% (H) and 0.16% (N).

This data agrees with the results reported in literature.[124]

5,10,15,20-tetrakis(4-iodophenyl) porphyrin (TIPP)

The synthesis of **TIPP** was performed in a modified version of the procedure described by *Adler*.[86]

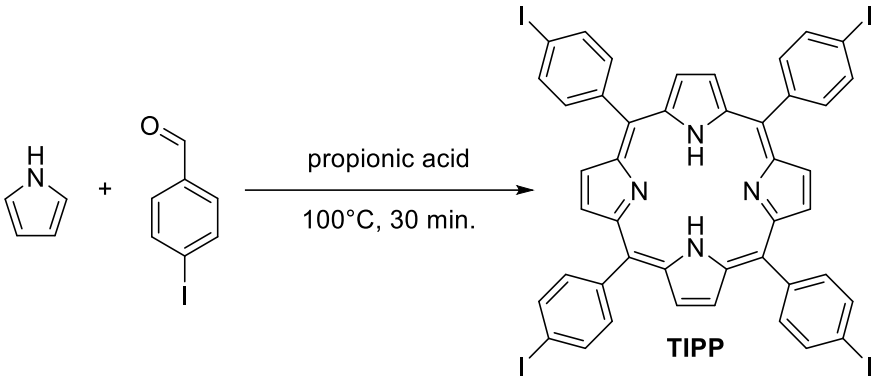

Figure 106: Synthesis of **TIPP**.

Pyrrole (0.69 mL, 10.00 mmol, 1.0 eq.) and 4-iodobenzaldehyde (2.32 g, 10.00 mmol, 1.0 eq.) were dissolved in propionic acid (50 mL) and the solution was heated to 100 °C for 30 minutes in the dark. After the mixture had cooled to room temperature, it was added dropwise to an excess of water (200 mL) and stored in the fridge overnight. The formed precipitate was filtered off and washed with water until the filtrate was colourless and showed no more fluorescence. The remaining solid was dissolved in acetone. Then the solvent was removed under reduced pressure.

Afterwards the solid was dissolved in acetone and concentrated hydrochloric acid was added dropwise (19 drops) until the color changed from red to a dark green/blue. The suspension was stored in the fridge overnight, then filtered and the remaining solid was dissolved in water. The dark solution was mixed with potassium hydroxide pallets in order to provide a basic pH-level of the solution and the formed dark precipitate was filtered. The solid was washed with water until the filtrate became colorless. Next the solid was dissolved in chloroform, the solvent was removed under reduced pressure and the solid was dried *in vacuo* overnight. The product was obtained as a purple solid (832.8 mg, 0.74 mmol, 30%).

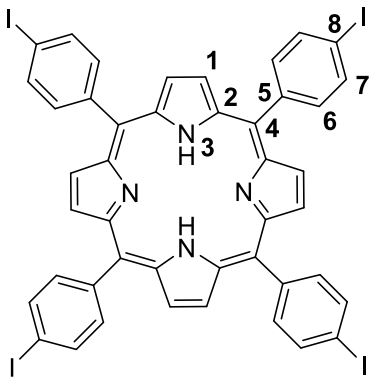

^{1}H-NMR (500 MHz, CD_2Cl_2, 298 K): δ[ppm] = 8.88 (s, 8 H, H-1), 8.15-8.11 (m, 8 H, H-7), 7.98-7.94 (m, 8 H, H-6), -2.92 (s, 2 H, H-3).

Due to the poor solubility of **TIPP**, no meaningful ^{13}C-NMR spectrum could be recorded.

HRMS-ESI-(+) ($C_{44}H_{26}I_4N_4$) *m/z*: calculated: $[M+H^+]$ = 1118.8415, experimental: $[M+H^+]$ = 1118.8410, $[M+2H^{2+}]$ = 558.924.

Elemental Analysis: ($C_{44}H_{26}I_4N_4$): calculated = 47.17% (C), 2.52% (H), 5.00% (N), experimental = 47.33% (C), 2.31% (H), 5.27% (N).

This data agrees with the results reported in literature.[125]

5,10,15,20-tetrakis(3,5-dimethoxyphenyl)porphyrin (T(OMe)$_2$PP)

The synthesis of **T(OMe)$_2$PP** was performed in a modified version of the procedure described by *Adler*.[86]

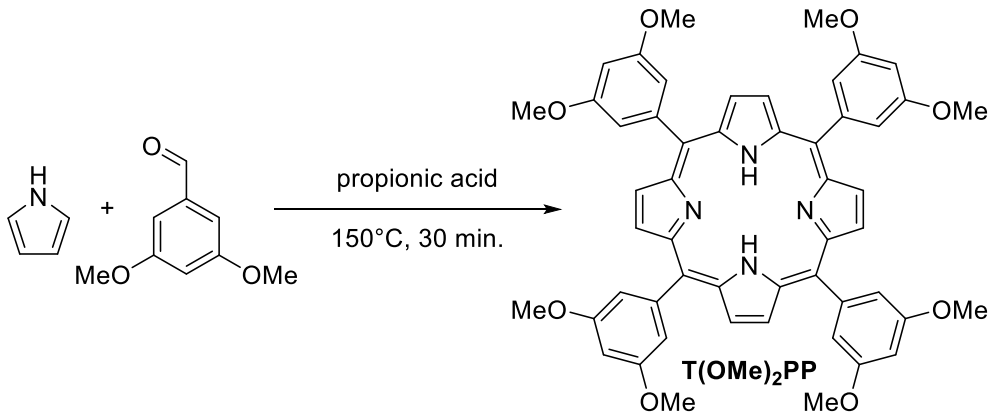

Figure 107: Synthesis of **T(OMe)$_2$PP**.

Pyrrole (0.69 mL, 10.00 mmol, 1.0 eq.) and 3,5-dimethoxybenzaldehyde (1.66 g, 10.00 mmol, 1.0 eq.) were dissolved in propionic acid (50 mL) and the solution was heated to 150 °C for 30 minutes, followed by cooling to room temperature. The mixture was added dropwise to an excess of water (150 mL) and the suspension was stored in the fridge overnight. The formed precipitate was filtered off, washed with water until the filtrate became colorless and the remaining solid was dissolved in chloroform. Then the solvent was removed under reduced pressure.

Afterwards the solid was dissolved in acetone and concentrated hydrochloric acid was added dropwise (17 drops) until the color changed from red to a dark green. The suspension was stored in the fridge overnight, then filtered and the remaining solid was dissolved in water. The dark solution was mixed with potassium hydroxide pallets in order to provide a basic pH-level of the solution and the formed dark precipitate was filtered. The solid was washed with water until the filtrate became colorless. Next the solid was dissolved in chloroform, the solvent was removed under reduced pressure and the solid was dried *in vacuo* overnight. The product was obtained as a bright purple solid (1.12 g, 1.31 mmol, 52%).

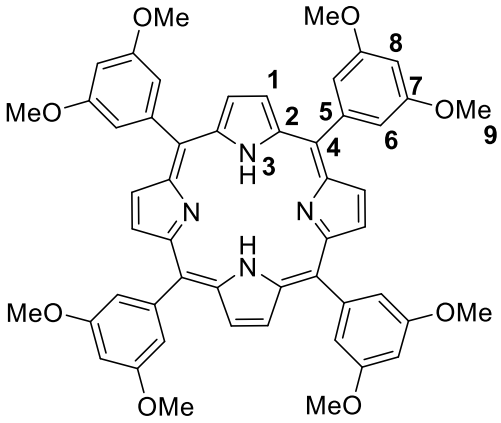

^{1}H-NMR (400 MHz, CD_2Cl_2, 298 K): δ[ppm] = 8.96 (s, 8 H, H-1), 7.39 (d, $^{4}J_{6,8}$ = 2.3 Hz, 8 H, H-6), 6.91 (t, $^{4}J_{8,6}$ = 2.3 Hz, 4 H, H-8), 3.96 (s, 24 H, H-9), -2.89 (s, 2 H, H-3).

^{13}C NMR (126 MHz, CD_2Cl_2, 298 K) δ [ppm]: 159.4 (C-7), 144.3 (C-5), 120.3 (C-4), 114.2 (C-6), 100.4 (C-8), 56.0 (-OMe).

HRMS-ESI-(+) ($C_{52}H_{46}O_8N_4$) *m/z*: calculated: [M+H$^+$] = 855.3394, experimental: [M+H$^+$] =855.3380.

Elemental Analysis: ($C_{52}H_{46}O_8N_4$): calculated = 73.05% (C), 5.42% (H), 6.55% (N), experimental = 72.78% (C), 5.42% (H), 6.23% (N).

This data agrees with the results reported in literature.[126]

5,10,15,20-tetrakis(4-methoxyphenyl)porphyrin (TOMePP)

The synthesis of **TOMePP** was performed in a modified version of the procedure described by *Adler*.[86]

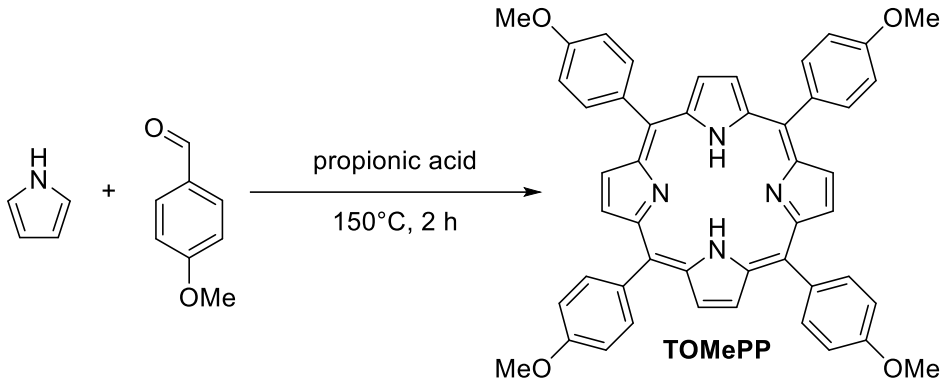

Figure 108: Synthesis of **TOMePP**.

Pyrrole (0.55 mL, 8.00 mmol, 1.0 eq.) and 4-iodobenzaldehyde (1.09 g, 8.00 mmol, 1.0 eq.) were dissolved in propionic acid (30 mL) and the solution was heated to 150 °C for 2 hours. After the mixture had cooled to room temperature, it was added dropwise to an excess of water (100 mL) and stored in the fridge overnight. The formed precipitate was filtered off and washed with water until the filtrate was colourless and showed no more fluorescence. The remaining solid was dissolved in acetone. Then the solvent was removed under reduced pressure.

Afterwards the solid was dissolved in acetone and concentrated hydrochloric acid was added dropwise (13 drops) until the color changed from red to a dark green/blue. The suspension was stored in the fridge overnight, then filtered and the remaining solid was dissolved in water. The dark solution was mixed with potassium hydroxide pallets in order to provide a basic pH-level of the solution and the formed dark precipitate was filtered. The solid was washed with water until the filtrate became colorless. Next the solid was dissolved in chloroform, the solvent was removed under reduced pressure and the solid was dried *in vacuo* overnight. The product was obtained as a purple solid (543.81 mg, 0.74 mmol, 37%).

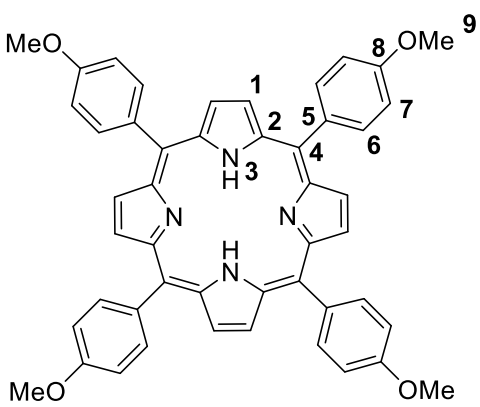

^{1}H-NMR (400 MHz, CD_2Cl_2, 298 K): δ[ppm] = 8.88 (s, 8 H, H-1), 8.13 (d, $^{3}J_{7,6}$ = 8.6 Hz, 8 H, H-7), 7.31 (d, $^{3}J_{6,7}$ = 8.6 Hz, 8 H, H-6), 4.09 (s, 12 H, H-9), -2.81 (s, 2 H, H-3).

^{13}C-NMR (126 MHz, CD_2Cl_2, 298 K): δ[ppm] = 160.0 (C-8), 136.0 (C-6), 134.9 (C-5), 120.2 (C-4), 112.6 (C-7), 56.0 (C-9).

HRMS-ESI-(+) ($C_{48}H_{38}O_4N_4$) *m/z*: calculated: [M+H$^+$] = 735.2971, experimental: [M+H$^+$] = 735.2961.

Elemental Analysis: ($C_{48}H_{38}O_4N_4$): calculated = 78.45% (C), 5.12% (H), 7.62% (N), experimental = 78.62% (C), 5.07% (H), 7.44% (N).

This data agrees with the results reported in literature.[127]

5,10,15,20-tetrakis(4-hydroxyphenyl)porphyrin (TOHPP)

The synthesis of **TOHPP** was performed in a modified version of the procedure described by *Jamaat*.[128]

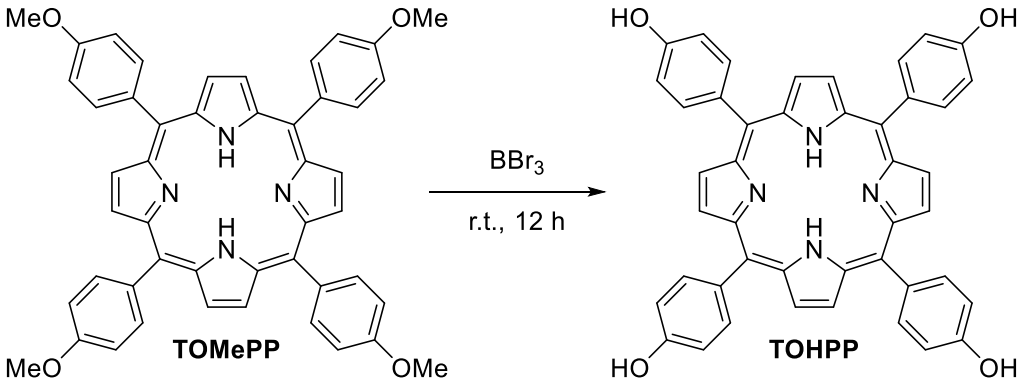

Figure 109: Synthesis of **TOHPP**.

The reaction was performed under argon gas atmosphere.

An oven dried *Schlenk* tube was equipped with **TOMePP** (100.04 mg, 0.14 mmol, 1.0 eq.) at -75°C and dry DCM (7 mL) was added. Afterwards BBr_3 (0.13 mL, 1.36 mmol, 10.0 eq.) was added dropwise and the resulting green solution was allowed to reach room temperature with subsequent stirring for 12 hours. Next, the mixture was neutralised with a saturated aqueous solution of $NaHCO_3$ (40 mL) and the resulting phases were separated. The organic phase was washed with water (3x20 mL) and the combined organic layers were dried with $MgSO_4$. After

filtration, the solvent was removed under reduced pressure giving the product as a bright purple shiny solid (53.96 mg, 0.08 mmol, 88%).

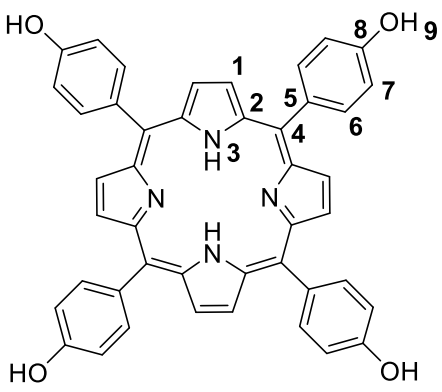

^{1}H-NMR (400 MHz, Acetone-d_6, 298 K): δ[ppm] = 8.84 (s, 8 H, H-1), 8.00 (d, $^{3}J_{7,6}$ = 8.4 Hz, 8 H, H-7), 7.31 (d, $^{3}J_{6,7}$ = 8.4 Hz, 8 H, H-6), -2.74 (s, 2 H, H-3).

Due to the poor solubility of **TOHPP**, no meaningful ^{13}C-NMR spectrum could be recorded.

HRMS-ESI-(+) ($C_{44}H_{30}O_4N_4$) *m/z*: calculated: [M+H$^+$] = 679.2345, experimental: [M+H$^+$] = 679.23413.

Elemental Analysis: ($C_{44}H_{30}O_4N_4$): calculated = 77.86% (C), 4.46% (H), 8.25% (N), experimental = 77.59% (C), 4.71% (H), 8.10% (N).

This data agrees with the results reported in literature.[129]

5,15-diphenyl-10,20-di(pyridin-4-yl)porphyrin (DPhDPyP)

The synthesis of **DPhDPyP** was performed in a modified version of the procedure described by *Adler*.[37]

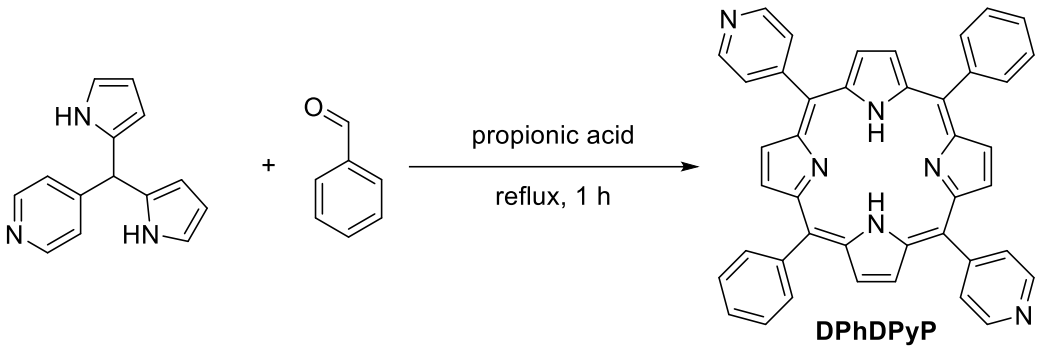

Figure 110: Synthesis of **DPhDPyP**.

4-(Di(1H-pyrrol-2-yl)methyl)pyridine (214.93 mg, 0.90 mmol, 1.0 eq.) and benzaldehyde (90.0 mL, 0.90 mmol, 1.0 eq.) were dissolved in propionic acid (4.5 mL) and the solution was heated to 150 °C for 1 hour. After the mixture had cooled to room temperature, it was added dropwise to an excess of a saturated aqueous solution of potassium hydroxide (50 mL) and stored in the fridge for 72 hours. The formed precipitate was filtered off and washed with water until the filtrate was colourless and showed no more fluorescence. The remaining solid was dissolved in chloroform. Then the solvent was removed under reduced pressure.

Afterwards the solid was dissolved in acetone and concentrated hydrochloric acid was added dropwise (10 drops) until the color changed from red to a dark green/blue. The suspension was stored in the fridge overnight, then filtered and the remaining solid was dissolved in water. The dark solution was mixed with potassium hydroxide pallets in order to provide a basic pH-level of the solution and the formed dark precipitate was filtered. The solid was washed with water until the filtrate became colorless. Next the solid was dissolved in chloroform, the solvent was removed under reduced pressure and the solid was dried *in vacuo* for 48 hours. The product was obtained as a purple solid (95.7 mg, 0.16 mmol, 35%).

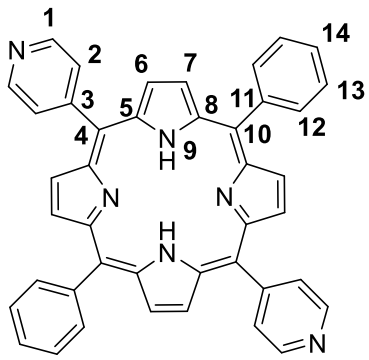

^{1}H-NMR (500 MHz, $CDCl_3$, 298 K): δ[ppm] = 9.06-9.01 (m, 4 H, H-2), 8.91 (d, $^{3}J_{6,7}$ = 4.8 Hz, 4 H, H-6), 8.81 (d, $^{3}J_{7,6}$ = 4.8 Hz, 4 H, H-7), 8.23-8.20 (m, 4 H, H-12), 8.18-8.15 (m, 4 H, H-1), 7.85-7.72 (m, 6 H, H-13, H-14), -2.82 (s, 2 H, H-9).

^{13}C-NMR (126 MHz, $CDCl_3$, 298 K): δ[ppm] = 150.4 (C-5), 148.5 (C-1), 142.1 (C-8), 141.9 (C-3), 134.7 (C-6, C-7), 129.6 (C-12), 128.2 (C-11), 128.0(C-4), 127.0 (C-13), 126.9 (C-14), 121.1 (C-10), 117.2 (C-2).

HRMS-ESI-(+) ($C_{42}H_{28}N_6$) *m/z*: calculated: $[M+H^+]$ = 617.2454, experimental: $[M+H^+]$ = 617.2427.

Elemental Analysis: ($C_{42}H_{28}N_6$): calculated = 81.80% (C), 4.58% (H), 13.63% (N), experimental = 81.55% (C), 4.42% (H), 13.70% (N).

This data agrees with the results reported in literature.[130]

Synthesis of the building blocks for cube 1, cube 2, cat1 and cat2

6-phenyl-2-(pyridin-2-yl)-1,3,6,2-dioxazaborocane

The synthesis was performed as described by *Hodgson*.[105]

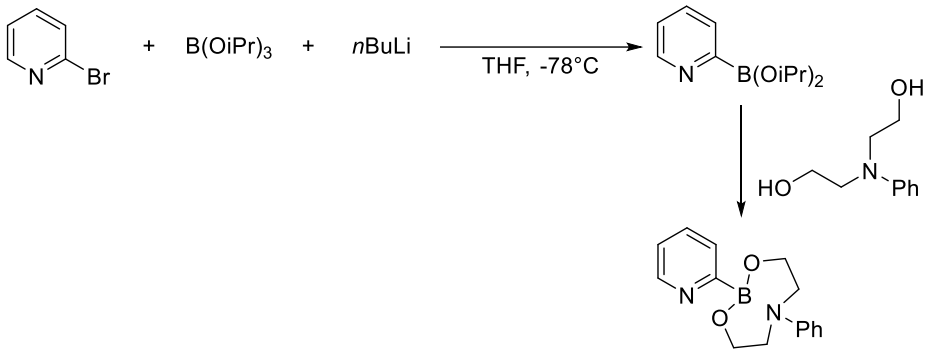

Figure 111: Reaction scheme of the synthesis of 6-phenyl-2-(pyridin-2-yl)-1,3,6,2-dioxazaborocane.

The reaction was performed under argon-gas atmosphere. 2-Bromopyridine (0.40 mL, 4.00 mmol, 1.0 eq.) and triisopropylborate (1.20 mL, 4.80 mmol, 1.2 eq.) were dissolved in dry and degassed THF (5 mL) and the solution was cooled to -78°C using a cooling-bath of acetone and liquid nitrogen. A 2.5 molar solution of *n*BuLi in hexanes (3.00 mL, 7.60 mmol, 1.9 eq.) was added dropwise while the temperature did not exceed -70°C. Afterwards, the reaction mixture was allowed to slowly reach room temperature (over 2.5 hours) and *N*-phenyl-diethanolamine (863.84 mg, 4.80 mmol, 1.2 eq.) was added. The solution was refluxed overnight and subsequently added to isopropanol (100 mL), whereby a white precipitate formed. THF was removed under reduced pressure and the mixture was stirred for additional 4 hours at room temperature. Afterwards the formed precipitate is filtered through a celite-pad and the remaining solid was washed with isopropanol (3x20 mL) and extracted with chloroform. The solvent was removed under reduced pressure yielding the product as a white solid (629.19 mg, 2.35 mmol, 59%).

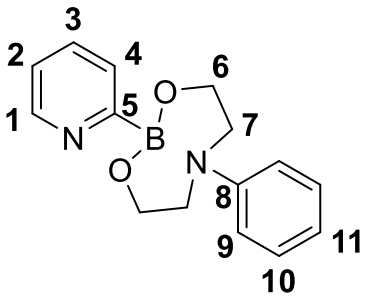

^{1}H-NMR (500 MHz, CD_3OD, 296 K): δ[ppm] = 8.52 (dt, $^3J_{1,2}$ = 4.4 Hz, $^4J_{1,3}$ = 1.7 Hz, 1 H, H-1), 7.88-7.81 (m, 1 H, H-3), 7.43 (ddd, $^3J_{2,3}$ = 4.8 Hz, $^3J_{2,1}$ = 4.4 Hz, $^4J_{2,4}$ = 1.3 Hz, 1 H, H-2), 7.19-7.10 (m, 3 H, H-4, H-10), 6.76-6.70 (m, 2 H, H-9), 6.61 (tt, $^3J_{11,10}$ = 7.3 Hz, $^4J_{11,9}$ = 1.0 Hz, 1 H, H-11), 3.71 (t, $^3J_{6,7}$ = 6.1 Hz, 4 H, H-6), 3.52 (t, $^3J_{7,6}$ = 6.1 Hz, 4 H, H-7).

^{13}C-NMR (126 MHz, CD_3OD, 296 K): δ[ppm] = 150.0 (C-1), 149.3 (C-5, C-8), 138.4 (C-3), 130.1 (C-10), 125.6 (C-2), 117.3 (C-11), 113.2 (C-9), 60.4 (C-6), 55.0 (C-7).

HRMS-ESI-(+) ($C_{15}H_{17}BN_2O_2$) *m/z*: calculated: $[M+H^+]$ = 269.1461, experimental: $[M+H^+]$ = 269.1452.

This data agrees with the results reported in literature.[105]

(2,2'-bipyridine)-5-carbaldehyde

The synthesis was performed as described by our group.[85]

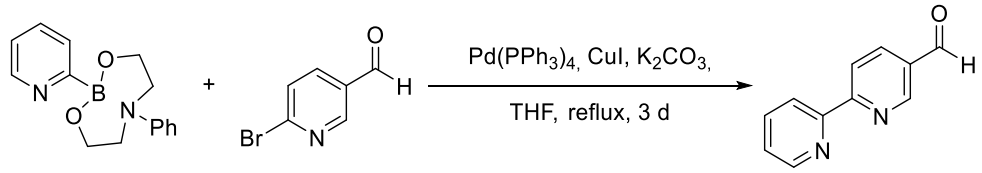

Figure 112: Synthesis of (2,2'-bipyridine)-5-carbaldehyde.

The reaction was performed under argon gas atmosphere.

The previously synthesised boronic acid ester (597.04 mg, 2.23 mmol, 3.0 eq.), 6-bromonicotinaldehyde (138.93 mg, 0.75 mmol, 1.0 eq.), $Pd(PPh_3)_4$ (90.00 mg, 0.075 mmol, 0.1 eq.), K_2CO_3 (207.56 mg, 1.5 mmol, 2.0 eq.) and CuI (57.25 mg, 0.3 mmol, 0.4 eq.) were added to an oven dried *Schlenk* flask and the atmosphere was changed three times. Afterwards, the solids were dissolved in dry and degassed THF (10 mL) and the mixture was heated to reflux for three days. After allowing the mixture to cool to room temperature it was quenched with a saturated aqueous solution of EDTA (100 mL) and the product was extracted with DCM (4x50 mL). The combined organic phases were dried with $MgSO_4$, filtered and the solvent was removed under reduced pressure. The product was separated *via* column chromatography using cyclohexane and ethyl acetate (9:1+5% TEA) as mobile phase. The product was obtained as a white solid (72.75 mg, 0.39 mmol, 53%).

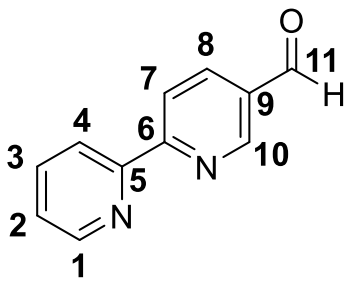

^{1}H-NMR (500 MHz, $CDCl_3$, 298 K): δ[ppm] = 10.18 (s, 1 H, H-11), 9.13 (dd, $^4J_{10,8}$ = 2.1 Hz, $^5J_{10,7}$ = 0.9 Hz, 1 H, H-10), 8.74 (ddd, $^3J_{1,2}$ = 4.8 Hz, $^4J_{1,3}$ = 1.8 Hz, $^5J_{1,4}$ = 1.0 Hz, 1 H, H-1), 8.64 (d, $^3J_{7,8}$ = 8.3 Hz, 1 H, H-7), 8.53 (dt, $^3J_{4,3}$ = 8.0 Hz, $^5J_{4,1}$ = 1.0 Hz, 1 H, H-4), 8.30 (dd, $^3J_{8,7}$ = 8.3 Hz, $^4J_{8,10}$ = 2.1 Hz, 1 H, H-8), 7.89 (td, $^3J_{3,2}$ = 7.6 Hz, $^4J_{3,1}$ = 1.8 Hz, 1 H, H-3), 7.41 (dd, $^3J_{2,3}$ = 7.6 Hz, $^3J_{2,1}$ = 4.8 Hz, 1 H, H-2).

^{13}C-NMR (126 MHz, $CDCl_3$, 298 K): δ[ppm] = 190.7 (C-11), 151.8(C-10), 149.5 (C-1), 137.5 (C-3), 137.2 (C-8), 131.3 (C-9), 125.0 (C-2), 122.5 (C-4), 121.6 (C-7).

MS-EI ($C_{11}H_8N_2O$) *m/z*: calculated: $[M^+]$ = 184.0637, experimental: $[M^{\cdot+}]$ = 184.1.

This data agrees with the results reported in literature.[81]

5, 10, 15, 20-tetrakis(4-aminophenyl)porphyrin (TAPP)

The synthesis was performed as described by *Struch*.[106]

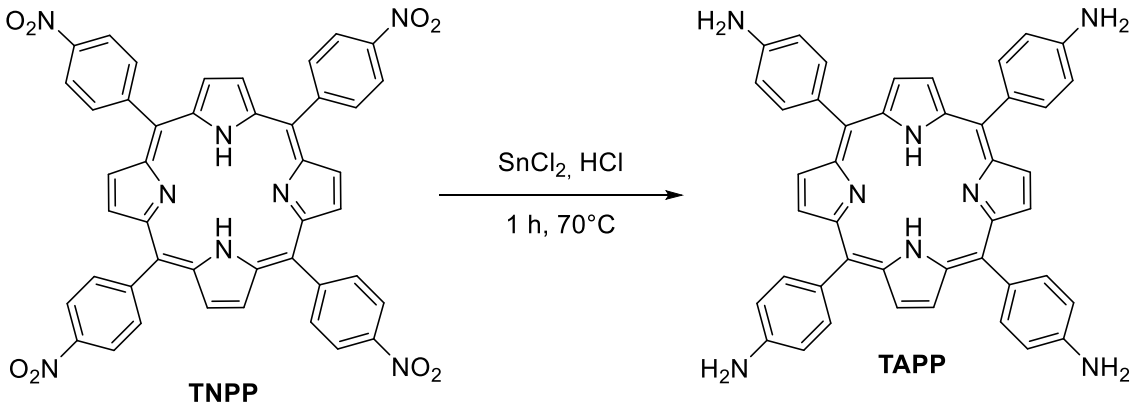

Figure 113: Synthesis of **TAPP**.

TNPP (1.00 g, 1.26 mmol, 1.0 eq.) and $SnCl_2$ (7.95 g, 41.83 mmol, 33.3 eq.) were dissolved in concentrated hydrochloric acid (300 mL) and heated to 70°C for one hour. After allowing the mixture to cool to room temperature, it was added dropwise to an excess of an aqueous saturated solution of Na_2CO_3 (100 mL) and stored in the fridge overnight. The formed precipitate was collected by filtration, washed with water until the filtrate showed no more colour and fluorescence and the remaining solid was dissolved in acetone. The solvent was removed under reduced pressure and the product was obtained as a bright purple solid (466.1 mg, 0.69 mmol, 55%).

Table 17: Overview of tested reaction conditions.

time	temperature	concentration	Yield
1 hour	70°C	0.005 M	50%
1 hour	70°C	0.008 M	22%
1 hour	70°C	0.004 M	55%
2 hours	70°C	0.004 M	26%
1 hour	110°C	0.004 M	32%
2 hours	110°C	0.004 M	42%

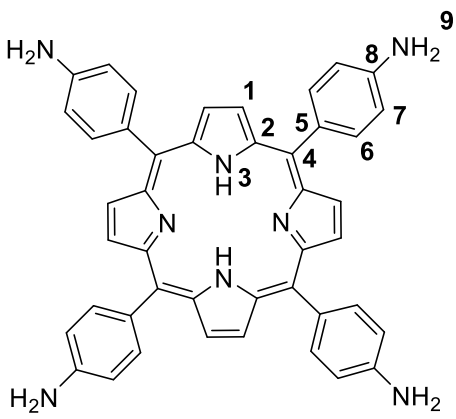

^{1}H-NMR (400 MHz, DMSO-d_6, 298 K): δ[ppm] = 8.96 (s, 8 H, H-1), 7.94 (d, $^{3}J_{6,7}$ = 8.3 Hz, 8 H, H-6), 7.13 (d, $^{3}J_{7,6}$ = 8.3 Hz, 8 H, H-7), 5.13 (s, 8 H, H-9), -2.57 (2, 2 H, H-3).

^{13}C-NMR (126 MHz, DMSO-d_6, 298 K): δ[ppm] = 148.4 (C-5), 135.4 (C-7), 128.7 (C-8), 120.5 (C-4), 112.5 (C-6).

HRMS-ESI-(+) ($C_{44}H_{34}N_8$) *m/z*: calculated: [M+H$^+$] = 675.2985, experimental: [M+H$^+$] = 675.2980.

Elemental Analysis: ($C_{44}H_{34}N_8$): calculated = 78.32% (C), 5.08% (H), 16.61% (N), experimental = 77.99% (C), 5.02% (H), 16.24% (N).

This data agrees with the results reported in literature.[122]

Zinc(II)-5, 10, 15, 20-tetrakis(4-aminophenyl)porphyrin (Zn-TAPP)

The synthesis of **Zn-TAPP** was performed in a modified version of the procedure described by *Meng*.[107]

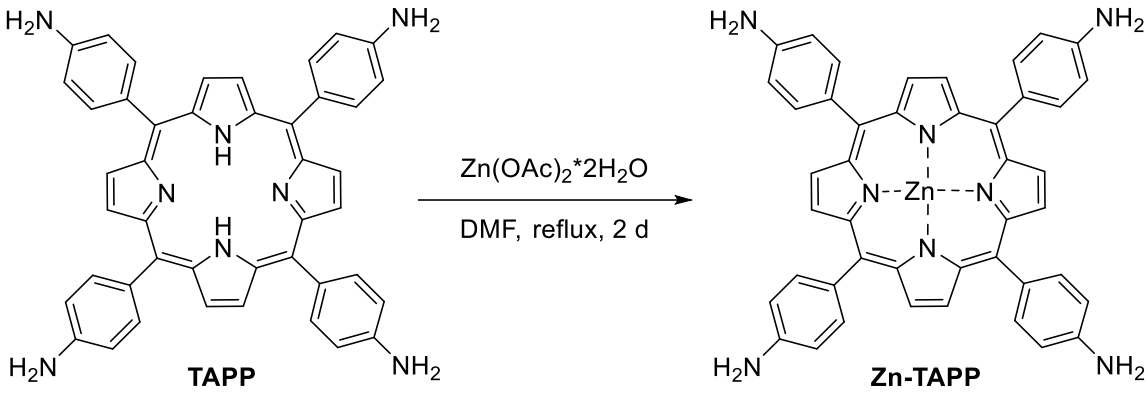

Figure 114: Synthesis of **Zn-TAPP**.

TAPP (200.26 mg, 0.30 mmol, 1.0 eq.) and $Zn(OAc)_2$*2 H_2O (782.68 mg, 3.56 mmol, 12.0 eq.) were dissolved in DMF (120 mL). Afterwards the mixture was heated to refluxed for 48 hours. After cooling to room temperature, the mixture was added dropwise to an excess of water (250 mL) and the mixture was stored in the fridge overnight. Following, the formed precipitate was collected by filtration and washed with water until the filtrate showed no more colour and fluorescence. The product was dissolved in chloroform and the solvent was removed under reduced pressure yielding a bright purple solid (205.93 mg, 0.28 mmol, 94%).

Table 18: Overview of tested reaction conditions.

zinc(II) acetate	time	solvent	yield
4 equivalents	1 day	DMF/$CHCl_3$/MeOH	12%
4 equivalents	1 day	DMF	17%
12 equivalents	1 day	DMF	86%
12 equivalents	2 days	DMF	94%
12 equivalents	3 days	DMF	94%

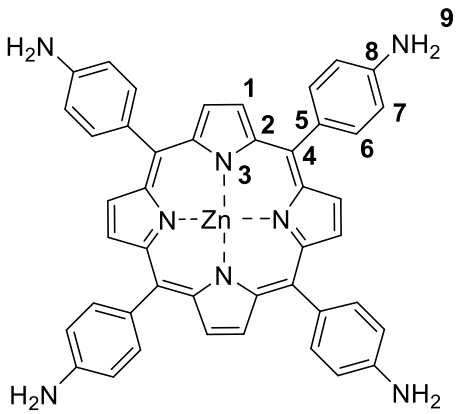

^{1}H-NMR (500 MHz, DMSO-d_6, 298 K): δ[ppm] = 8.84 (s, 8 H- H-1), 7.81 (m, 8 H, H-6), 6.97 (m, 8 H, H-7), 5.42 (s, 8 H, H-9).

^{13}C-NMR (126 MHz, DMSO-d_6, 298 K): δ[ppm] = 149.6 (C-2), 147.9 (C-5), 135.1 (C-6), 131.1 (C-1), 130.4 (C-8), 120.7 (C-4), 112.2 (C-7).

HRMS-MALDI ($C_{44}H_{32}N_8Zn$) *m/z*: calculated: [M+H$^+$] = 737.2120, experimental: [M+H$^+$] = 737.2110, [M+2H^{2+}] = 369.1092, [M+3H^{3+}] = 246.4091, [4M+2H^{2+}] = 1477.4134.

Elemental Analysis: ($C_{44}H_{32}N_8Zn$): calculated = 71.59% (C), 4.37% (H), 15.18% (N), experimental = 71.74% (C), 4.22% (H), 15.11% (N).

This data agrees with the results reported in literature.[107]

(Porphyrin-5,10,15,20-tetrayl)tetrakis(([1,1'-biphenyl]-4-amine)) (TAbPP)

The synthesis of **TAbPP** was performed in a modified version of the procedure described by *de Bruin*.[131]

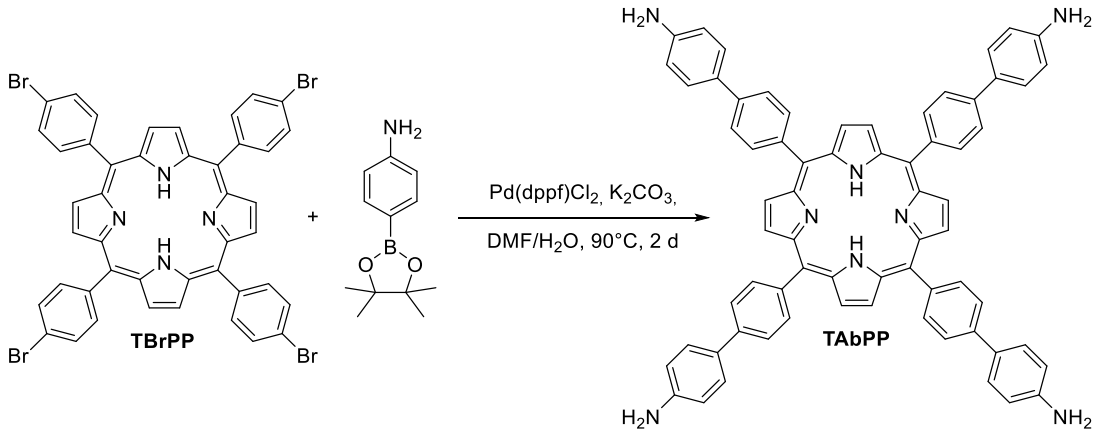

Figure 115: Synthesis of **TAbPP**.

The reaction was performed under argon gas atmosphere.

A *Schlenk* flask was equipped with **TBrPP** (1.48 g, 1.60 mmol, 1.0 eq.), K_2CO_3 (5.09 g, 36.80 mmol, 23.0 eq.), $Pd(dppf)Cl_2$ (117.07 mg, 0.16 mmol, 0.1 eq.) and 4-aminophenylboronic acid pinacol ester (2.98 g, 13.60 mmol, 8.5 eq.). Afterwards, the atmosphere was exchanged three times and a degassed 15:1 mixture of DMF/water (267 mL in total) was added. The mixture was heated to 90°C for 48 hours and after it was allowed to cool to room temperature it was added to an excess of water (400 mL). The resulting suspension was stored in the fridge overnight and the formed solid collected by filtration through a celite pad. This filtration process was repeated multiple times, until the filtrate showed no further precipitate and the remaining solid was washed with water and methanol until the filtrate showed no more colour and fluorescence. The solid was dissolved in chloroform and the solvent was removed under reduced pressure.

Afterwards the solid was dissolved in acetone and concentrated hydrochloric acid was added dropwise (31 drops) until the color changed from red to a dark green/blue. The suspension was stored in the fridge overnight, then filtered and the remaining solid was dissolved in water. The dark solution was mixed with potassium hydroxide pallets in order to provide a basic pH-level of the solution and the formed dark precipitate was filtered. The solid was washed with water until the filtrate became colorless. Next the solid was dissolved in chloroform, the solvent was removed under reduced pressure and the solid was dried *in vacuo* for 48 hours. The product was obtained as a purple solid (1.27 g, 1.30 mmol, 81%).

Table 19: Overview of tested reaction conditions.

substrate	time	concentration	yield
TBrPP	2 days	0.003 M[131]	64%
TBrPP	2 days	0.006 M	81%
TIPP	2 days	0.006 M	48%

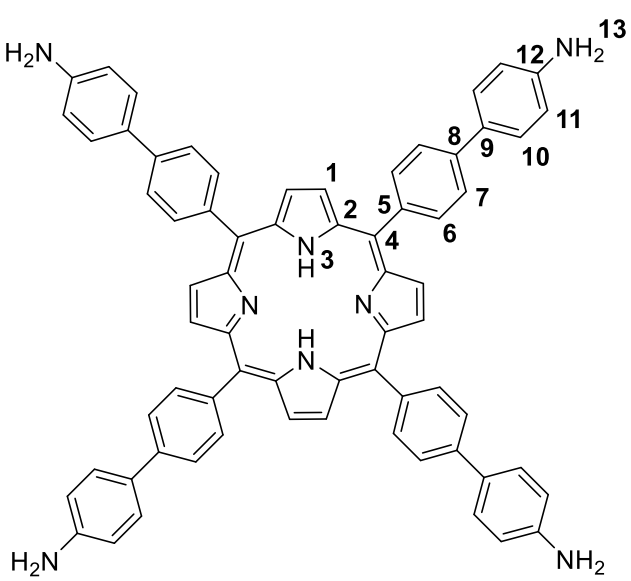

^{1}H-NMR (400 MHz, DMSO-d_6, 298 K): δ[ppm] = 8.94 (s, 8 H, H-1), 8.22 (d, $^{3}J_{7,6}$ = 8.0 Hz, 8 H, H-7), 8.01 (d, $^{3}J_{6,7}$ = 8.0 Hz, 8 H, H-6), 7.72 (d, $^{3}J_{10,11}$ = 8.4 Hz, 8 H, H-10), 6.79 (d, $^{3}J_{11,10}$ = 8.4 Hz, 8 H, H-11), 5.36 (s, 8 H, H-13), -2.81 (s, 2 H, H-3).

^{13}C-NMR (126 MHz, DMSO-d_6, 298 K): δ[ppm] = 148.8 (C-12), 140.0 (C-9), 138.4 (C-4), 134.8 (C-7), 127.5 (C-10), 126.6 (C-9), 123.6 (C-6), 119.9 (C-5), 114.5 (C-11).

HRMS-ESI-(+) ($C_{68}H_{50}N_8$) *m/z*: calculated: [M+H$^+$] = 979.4237, experimental: [M+H$^+$] = 979.4231, [M+2H^{2+}] = 490.2149.

Elemental Analysis: ($C_{68}H_{50}N_8$): calculated = 83.41% (C), 5.15% (H), 11.44% (N), experimental = 82.99% (C), 4.82% (H), 11.27% (N).

This data agrees with the results reported in literature.[131]

Zinc(II)-(Porphyrin-5,10,15,20-tetrayl)tetrakis(([1,1'-biphenyl]-4-amine)) (Zn-TAbPP)

The synthesis of **Zn-TAbPP** was performed in a modified version of the procedure described by *de Bruin*.[131]

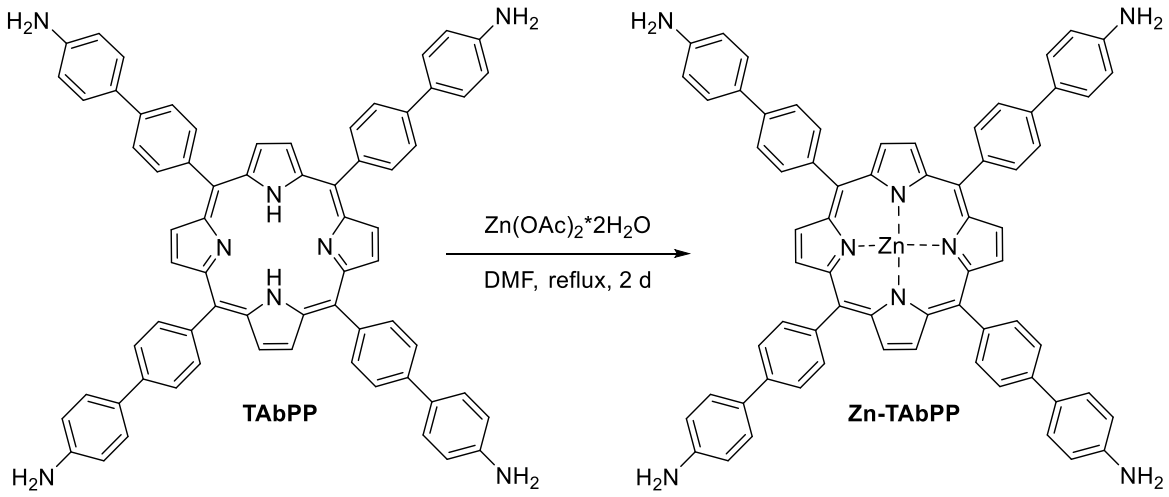

Figure 116: Synthesis of **Zn-TAbPP**.

TAbPP (587.74 mg, 0.46 mmol, 1.0 eq.) and $Zn(OAc)_2$*2 H_2O (1.36 g, 6.24 mmol, 12.0 eq.) were dissolved in DMF (110 mL). Afterwards the mixture was heated to refluxed for 48 hours. After cooling to room temperature, the mixture was added dropwise to an excess of water (250 mL) and the mixture was stored in the fridge overnight. Following, the formed precipitate was collected by filtration and washed with water until the filtrate showed no more colour and fluorescence. The product was dissolved in chloroform and the solvent was removed under reduced pressure yielding a bright purple solid (467.25 mg, 0.45 mmol, 98%).

Table 20: Overview of tested reaction conditions.

concentration	time	yield
0.002 M	20 h	82%
0.002 M	48 h	98%
0.014 M	20 h	20%
0.014 M	72 h	44%

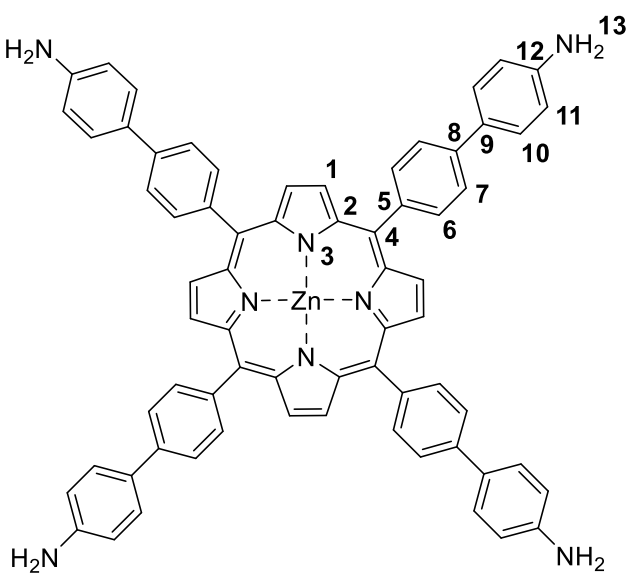

^{1}H-NMR (500 MHz, DMSO-d_6, 298 K): δ[ppm] = 8.89 (s, 8 H, H-1), 8.18 (d, $^{3}J_{6,7}$ = 8.1 Hz, 8 H, H-6), 7.97 (d, $^{3}J_{7,6}$ = 8.1 Hz, 8 H, H-7), 7.71 (d, $^{3}J_{10,11}$ = 8.5 Hz, 8 H, H-10), 6.79 (d, $^{3}J_{11,10}$ = 8.5 Hz, 8 H, H-11), 5.36 (s, 8 H, H-13).

^{13}C-NMR (126 MHz, DMSO-d_6, 298 K): δ[ppm] = 149.4 (C-2), 148.7 (C-12), 140.1 (C-5), 139.6 (C-8), 134.8 (C-7), 131.7 (C-1), 127.5 (C-10), 126.9 (C-9), 123.5 (C-6), 120.3 (C-4), 114.5 (C-11).

HRMS-ESI-(+) ($C_{68}H_{48}N_8Zn$) *m/z*: calculated: $[M+H^+]$ = 1041.3372, experimental: $[M+H^+]$ = 1041.3390.

Elemental Analysis: ($C_{68}H_{48}N_8Zn$): calculated = 78.34% (C), 4.64% (H), 10.75% (N), experimental = 78.11% (C), 4.53% (H), 10.59% (N).

This data agrees with the results reported in literature.[131]

(Porphyrin-5,10,15,20-tetrayl)tetrakis(3,5-dimethyl-[1,1'-biphenyl]-4-amine)

The synthesis was performed in a modified version of the procedure described by *de Bruin*.[131]

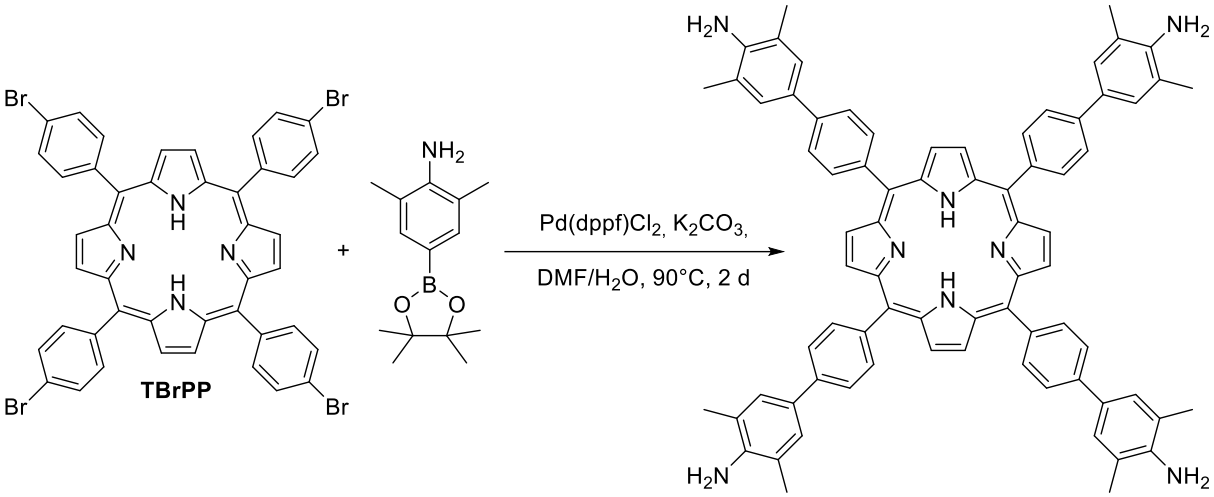

Figure 117: Synthesis of (porphyrin-5,10,15,20-tetrayl)tetrakis(3,5-dimethyl-[1,1'-biphenyl]-4-amine).

The reaction was performed under argon gas atmosphere.

A *Schlenk* flask was equipped with **TBrPP** (670.20 mg, 0.72 mmol, 1.0 eq.), K_2CO_3 (2.31 g, 16.70 mmol, 23.0 eq.), $Pd(dppf)Cl_2$ (52.71 mg, 0.07 mmol, 0.1 eq.) and 2,6-dimethyl-4-(4,4,5,5-tetramethyl-1,3,2-dioxaborolan-2-yl)aniline (1.51 g, 6.12 mmol, 8.5 eq.). Afterwards, the atmosphere was exchanged three times and a degassed 15:1 mixture of DMF/water (120 mL in total) was added. The mixture was heated to 90°C for 48 hours and after it was allowed to cool to room temperature it was added to an excess of water (250 mL). The resulting suspension was stored in the fridge overnight and the formed solid collected by filtration through a celite pad. This filtration process was repeated multiple times, until the filtrate showed no further precipitate and the remaining solid was washed with water and methanol until the filtrate showed no more colour and fluorescence. The solid was dissolved in chloroform and the solvent was removed under reduced pressure.

Afterwards the solid was dissolved in acetone and concentrated hydrochloric acid was added dropwise (16 drops) until the color changed from red to a dark green/blue. The suspension was stored in the fridge overnight, then filtered and the remaining solid was dissolved in water. The dark solution was mixed with potassium hydroxide pallets in order to provide a basic pH-level of the solution and the formed dark precipitate was filtered. The solid was washed with water until the filtrate became colorless. Next the solid was dissolved in chloroform, the

solvent was removed under reduced pressure and the solid was dried *in vacuo* for 48 hours. The product was obtained as a purple solid (422.71 mg, 0.39 mmol, 54%).

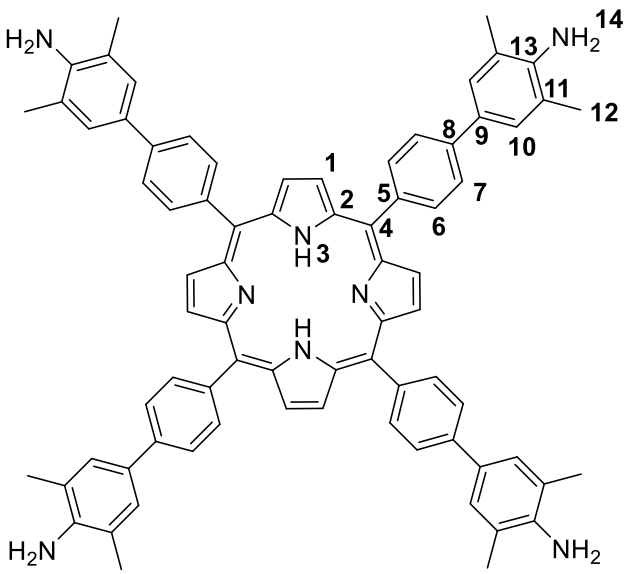

^{1}H-NMR (400 MHz, DMSO-d_6, 298 K): δ[ppm] = 8.94 (s, 8 H, H-1), 8.20 (d, $^{3}J_{7,6}$ = 7.8 Hz, 8 H, H-7), 8.00 (d, $^{3}J_{6,7}$ = 7.8 Hz, 8 H, H-6), 7.52 (s, 8 H, H-10), 4.80 (s, 8 H, H-14), 2.28 (s, 24 H, H-12), -2.77 - -2.87 (m, 2 H, H-3).

^{13}C-NMR (126 MHz, DMSO-d_6, 298 K): δ[ppm] = 144.5 (C-1, C-13), 140.4 (C-5), 138.4 (C-8), 134.8 (C-4), 134.2 (C-2), 127.0 (C-9), 126.8 (C-11), 126.4 (C-10), 123.9 (C-7), 121.2 (C-6), 18.1 (C-12).

Elemental Analysis: ($C_{76}H_{66}N_8$): calculated = 83.64% (C), 6.10% (H), 10.27% (N), experimental = 83.33% (C), 5.94% (H), 10.41% (N).

Zinc-(Porphyrin-5,10,15,20-tetrayl)tetrakis(3,5-dimethyl-[1,1'-biphenyl]-4-amine)

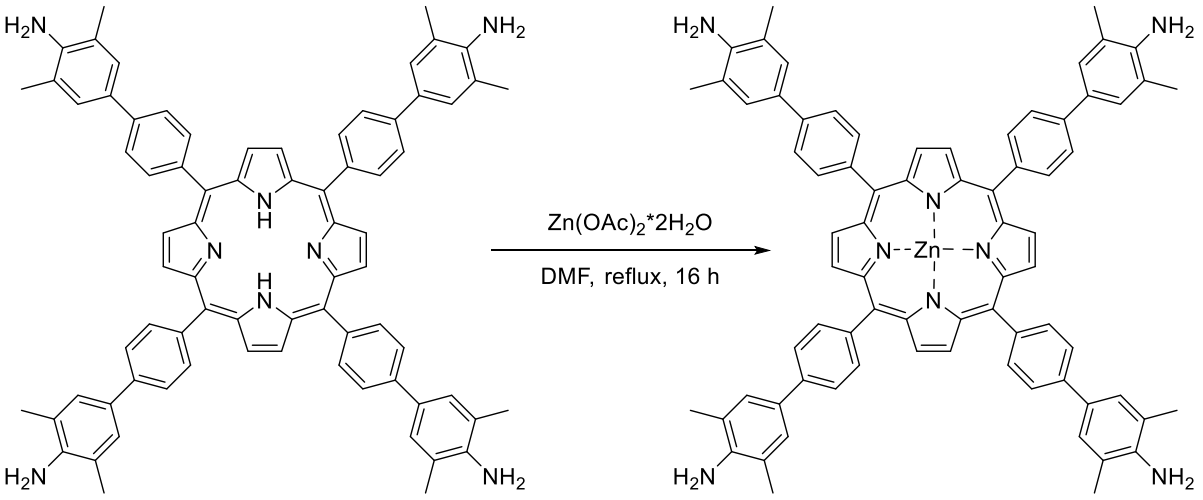

Figure 118: Synthesis of Zinc-(Porphyrin-5,10,15,20-tetrayl)tetrakis(3,5-dimethyl-[1,1'-biphenyl]-4-amine)

The previously synthesised porphyrin (218.41 mg, 0.20 mmol, 1.0 eq.) and $Zn(OAc)_2$*2 H_2O (878.60 mg, 4.04 mmol, 20.0 eq.) were dissolved in DMF (100 mL). Afterwards the mixture was heated to refluxed for 16 hours. After cooling to room temperature, the mixture was added dropwise to an excess of water (200 mL) and the mixture was stored in the fridge overnight. Following, the formed precipitate was collected by filtration and washed with water until the

filtrate showed no more colour and fluorescence. The product was dissolved in chloroform and the solvent was removed under reduced pressure yielding a bright purple solid (216.73 mg, 0.19 mmol, 94%).

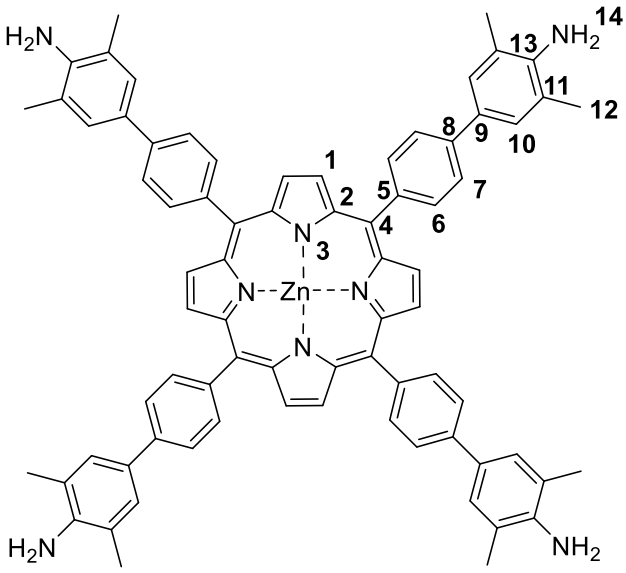

^{1}H-NMR (400 MHz, DMSO-d_6, 298 K): δ[ppm] = 8.89 (s, 8 H, H-1), 8.18 (d, $^{3}J_{7,6}$ = 8.0 Hz, 8 H, H-7), 7.97 (d, $^{3}J_{6,7}$ = 8.0 Hz, 8 H, H-6), 7.46 (s, 8 H, H-10), 4.72 (s, 8 H, H-14), 2.22 (s, 24 H, H-12).

^{13}C-NMR (126 MHz, DMSO-d_6, 298 K): δ[ppm] = 149.3 (C-1, C-13), 144.3 (C-5), 140.0 (C-8), 139.8 (C-4), 134.7 (C-2), 131.6 (C-9), 127.1 (C-11), 126.4 (C-10), 123.6 (C-7), 121.2 (C-6), 18.1 (C-12).

Elemental Analysis: ($C_{76}H_{64}N_8Zn$): calculated = 79.05% (C), 5.59% (H), 9.70% (N), experimental = 78.80% (C), 5.39% (H), 9.96% (N).

(Porphyrin-5,10,15,20-tetrayl)tetrakis(3-methyl-[1,1'-biphenyl]-4-amine)

The synthesis was performed in a modified version of the procedure described by *de Bruin*.[131]

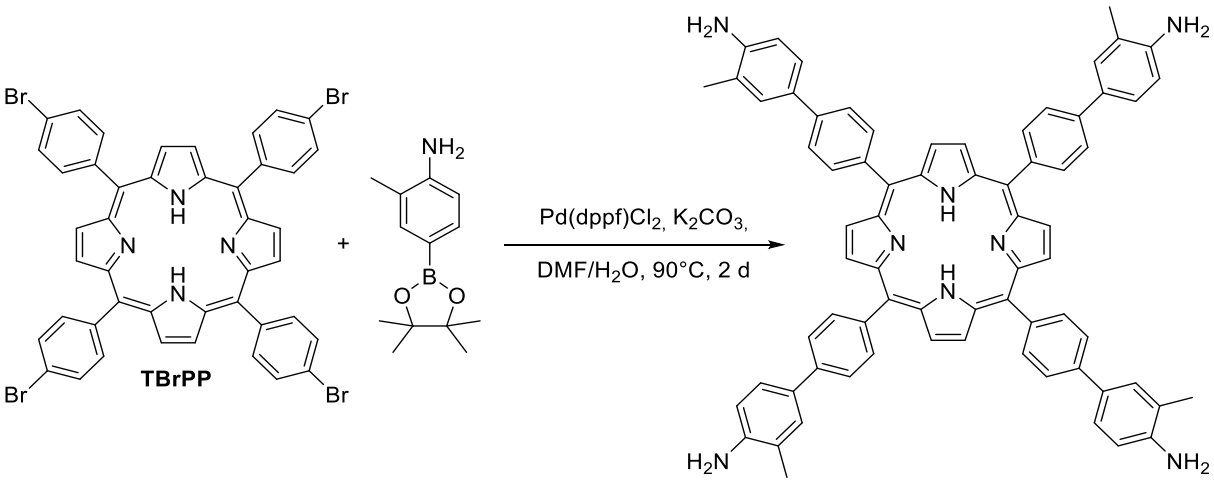

Figure 119: Synthesis of (porphyrin-5,10,15,20-tetrayl)tetrakis(3,5-dimethyl-[1,1'-biphenyl]-4-amine).

The reaction was performed under argon gas atmosphere.

A *Schlenk* flask was equipped with **TBrPP** (670.11 mg, 0.72 mmol, 1.0 eq.), K_2CO_3 (2.29 g, 16.56 mmol, 23.0 eq.), Pd(dppf)Cl_2 (52.68 mg, 0.07 mmol, 0.1 eq.) and 2-methyl-4-(4,4,5,5-tetramethyl-1,3,2-dioxaborolan-2-yl)aniline (1.43 g, 6.12 mmol, 8.5 eq.). Afterwards, the atmosphere was exchanged three times and a degassed 15:1 mixture of DMF/water (220 mL in total) was added. The mixture was heated to 90°C for 48 hours and after it was allowed to cool to room temperature it was added to an excess of water (350 mL). The resulting suspension was stored in the fridge overnight and the formed solid collected by filtration through a celite pad. This filtration process was repeated multiple times, until the filtrate showed no further precipitate and the remaining solid was washed with water and methanol until the filtrate showed no more colour and fluorescence. The solid was dissolved in chloroform and the solvent was removed under reduced pressure.

Afterwards the solid was dissolved in acetone and concentrated hydrochloric acid was added dropwise (22 drops) until the color changed from red to a dark green/blue. The suspension was stored in the fridge overnight, then filtered and the remaining solid was dissolved in water. The dark solution was mixed with potassium hydroxide pallets in order to provide a basic pH-level of the solution and the formed dark precipitate was filtered. The solid was washed with water until the filtrate became colorless. Next the solid was dissolved in chloroform, the solvent was removed under reduced pressure and the solid was dried *in vacuo* for 48 hours. The product was obtained as a purple solid (455.71 mg, 0.44 mmol, 61%).

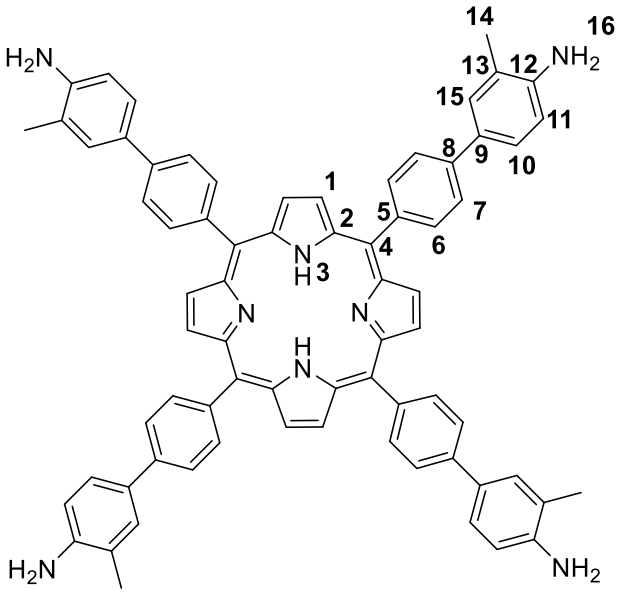

^{1}H-NMR (500 MHz, DMSO-d_6, 298 K): δ[ppm] = 8.92 (s, 8 H, H-1), 8.19 (d, $^3J_{7,6}$ = 7.8 Hz, 8 H, H-7), 7.98 (d, $^3J_{6,7}$ = 7.8 Hz, 8 H, H-6), 7.62 (s, 4 H, H-15), 7.57 (d, $^3J_{10,11}$ = 8.1 Hz, 4 H, H-10), 6.83 (d, $^3J_{11,10}$ = 8.1 Hz, 4 H, H-11), 5.11 (s, 8 H, H-16), 2.24 (s, 12 H, H-14), 2.79 - -2.86 (m, 2 H, H-3).

^{13}C-NMR (126 MHz, DMSO-d_6, 298 K): δ[ppm] = 146.7 (C-1, C-12), 140.2 (C-5), 138.4 (C-8), 135.9 (C-2), 134.8 (C-15), 134.2 (C-4), 129.9 (C-9), 128.5 (C-7), 127.1 (C-13), 125.0 (C-6), 123.8 (C-10), 114.5 (C-11), 17.6 (C-14).

Elemental Analysis: ($C_{72}H_{58}N_8$): calculated = 83.53% (C), 5.65% (H), 10.82% (N), experimental = 83.20% (C), 5.81% (H), 10.67% (N).

Zinc-(Porphyrin-5,10,15,20-tetrayl)tetrakis(3-methyl-[1,1'-biphenyl]-4-amine)

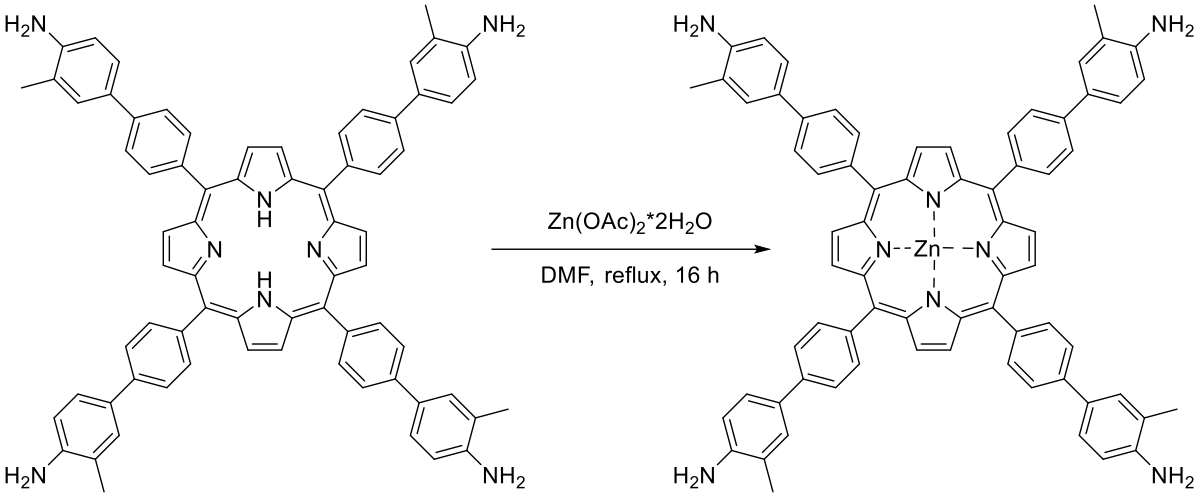

Figure 120: Synthesis of Zinc-(Porphyrin-5,10,15,20-tetrayl)tetrakis(3,5-dimethyl-[1,1'-biphenyl]-4-amine)

The previously synthesised porphyrin (170.84 mg, 0.17 mmol, 1.0 eq.) and $Zn(OAc)_2$*2 H_2O (724.26 mg, 3.30 mmol, 20.0 eq.) were dissolved in DMF (82.5 mL). Afterwards the mixture was heated to refluxed for 16 hours. After cooling to room temperature, the mixture was added dropwise to an excess of water (150 mL) and the mixture was stored in the fridge overnight. Following, the formed precipitate was collected by filtration and washed with water until the filtrate showed no more colour and fluorescence. The product was dissolved in chloroform and the solvent was removed under reduced pressure yielding a bright purple solid (184.22 mg, 0.17 mmol, 99%).

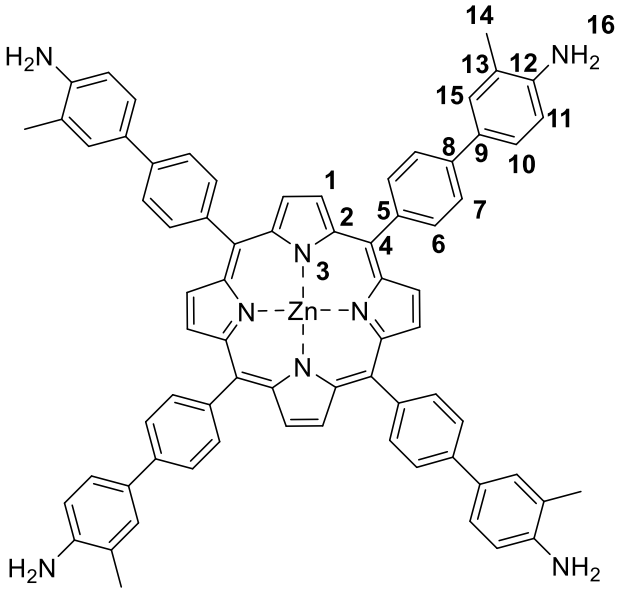

^{1}H- NMR (500 MHz, DMSO-d_6, 298 K): δ[ppm] = 8.90 (s, 8 H, H-1), 8.18 (d, $^{3}J_{7,6}$ = 8.0 Hz, 8 H, H-7), 7.94 (d, $^{3}J_{6,7}$ = 8.0 Hz, 8 H, H-6), 7.63 (s, 4 H, H-15), 7.57 (d, $^{3}J_{10,11}$ = 7.9 Hz, 4 H, H-10), 6.84 (d, $^{3}J_{11,10}$ = 7.9 Hz, 4 H, H-11), 5.09 (s, 8 H, H-16), 2.25 (s, 12 H, H-14).

^{13}C-NMR (126 MHz, DMSO-d_6, 298 K): δ[ppm] = 146.6 (C-1, C-12), 140.1 (C-5), 139.7 (C-8), 135.9 (C-2), 134.7 (C-15), 134.1 (C-4), 129.9 (C-9), 128.5 (C-7), 127.4 (C-13), 125.0 (C-6), 123.5 (C-10), 114.5 (C-11), 17.6 (C-14).

Elemental Analysis: ($C_{72}H_{56}N_8Zn$): calculated = 78.71% (C), 5.14% (H), 10.20% (N), experimental = 78.49% (C), 5.44% (H), 10.03% (N).

Cobalt(II)-5,10,15,20-tetrakis(4-pyridin-4-yl)porphyrin (Co-TPyP)

The synthesis of **Co-TPyP** was performed in a modified version of the procedure described by *Meng*.[107]

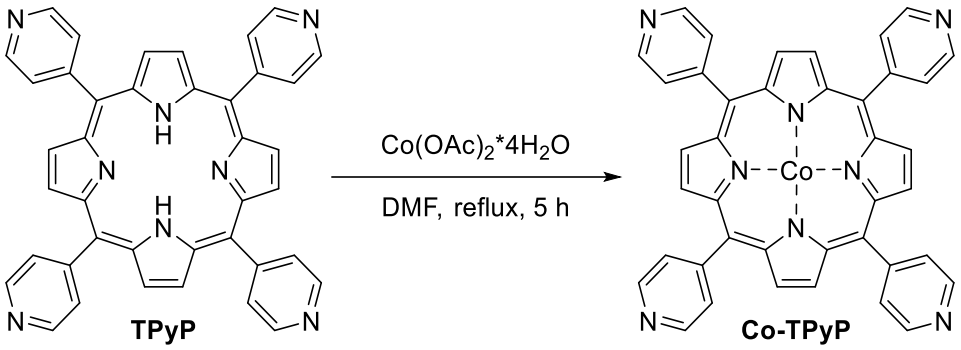

Figure 121: Synthesis of **Co-TPyP**.

TPyP (1.17 g, 1.89 mmol, 1.0 eq.) and $Co(OAc)_2$*4 H_2O (5.66 g, 22.68 mmol, 12.0 eq.) were dissolved in DMF (57 mL). Afterwards the mixture was heated to refluxed for 5 hours. After cooling to room temperature, the mixture was added dropwise to an excess of water (150 mL) and the mixture was stored in the fridge overnight. Following, the formed precipitate was collected by filtration and washed with water, methanol, ethyl acetate, acetone and chloroform until the filtrate showed no more colour and fluorescence. The solid was taken up in methanol

(250 mL) and heated to reflux for 3 hours. Afterwards the mixture was allowed to cool to room temperature and the formed precipitate was collected by filtration. After repeating the washing process, the remaining solid was taken up in chloroform (300 mL) and heated to reflux for 3 hours. After cooling to room temperature, the mixture was filtered and the remaining solid was collected and dried in vacuo for 48 hours. The product was obtained as a red/purple solid (1.15 g, 1.70 mmol, 90%).

Table 21: Overview of tested reaction conditions.

cobalt(II) acetate	time	yield
4 equivalents	5 hours	90%
4 equivalents	3 days	92%

Due to the poor solubility and the paramagnetic character of **Co-TPyP** no meaningful NMR spectrum could be obtained. Only the absence of starting material was observed in the ^{1}H-NMR spectrum.

HRMS-MALDI ($C_{40}H_{24}N_8Co$) *m/z*: calculated: $[M^+]$ = 675.1456, experimental: $[M^+]$ = 675.1462

Elemental Analysis: ($C_{40}H_{24}N_8Co$): calculated = 71.11% (C), 3.58% (H), 16.59% (N), experimental = 70.74% (C), 3.36% (H), 16.40% (N).

This data agrees with the results reported in literature.[132]

Manganese(II)-5,10,15,20-tetrakis(4-pyridin-4-yl)porphyrin (Mn-TPyP)

The synthesis of **Mn-TPyP** was performed in a modified version of the procedure described by *Meng*.[107]

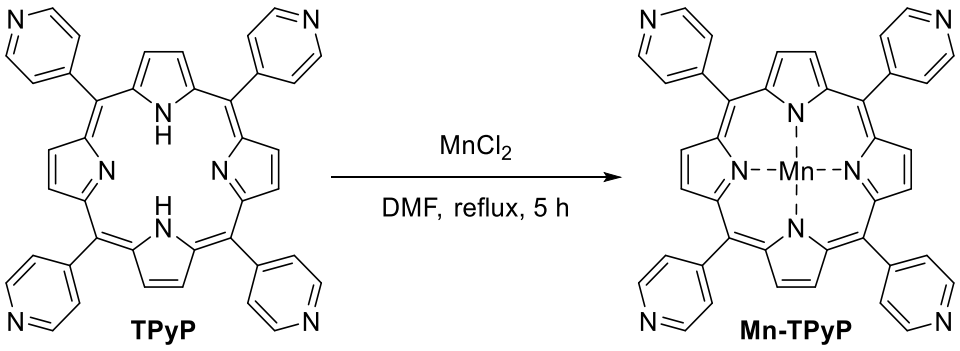

Figure 122: Synthesis of **Mn-TPyP**.

TPyP (105.8 mg, 0.17 mmol, 1.0 eq.) and $MnCl_2$ (207.2 mg, 1.65 mmol, 10.0 eq.) were dissolved in DMF (10 mL). Afterwards the mixture was heated to refluxed for 5 hours. After

cooling to room temperature, the mixture was added dropwise to an excess of water (50 mL) and the mixture was stored in the fridge overnight. Following, the formed precipitate was collected by filtration and washed with water, methanol, ethyl acetate, acetone and chloroform until the filtrate showed no more colour and fluorescence. The solid was taken up in methanol (50 mL) and heated to reflux for 3 hours. Afterwards the mixture was allowed to cool to room temperature and the formed precipitate was collected by filtration. After repeating the washing process, the remaining solid was taken up in chloroform (100 mL) and heated to reflux for 3 hours. After cooling to room temperature, the mixture was filtered and the remaining solid was collected and dried in vacuo for 48 hours. The product was obtained as a red/purple solid (82.21 g, 0.12 mmol, 72%).

Due to the poor solubility and the paramagnetic character of **Mn-TPyP** no meaningful NMR spectrum could be obtained. Only the absence of starting material was observed in the ^{1}H-NMR spectrum.

HRMS-MALDI ($C_{40}H_{24}N_8Mn$) *m/z*: calculated: $[M^+]$ = 671.1504, experimental: $[M^+]$ = 671.1491.

Elemental Analysis: ($C_{40}H_{24}N_8Mn$): calculated = 71.53% (C), 3.60% (H), 16.68% (N), experimental = 71.22% (C), 3.83% (H), 16.47% (N).

Attempts to synthesise cube1OTf

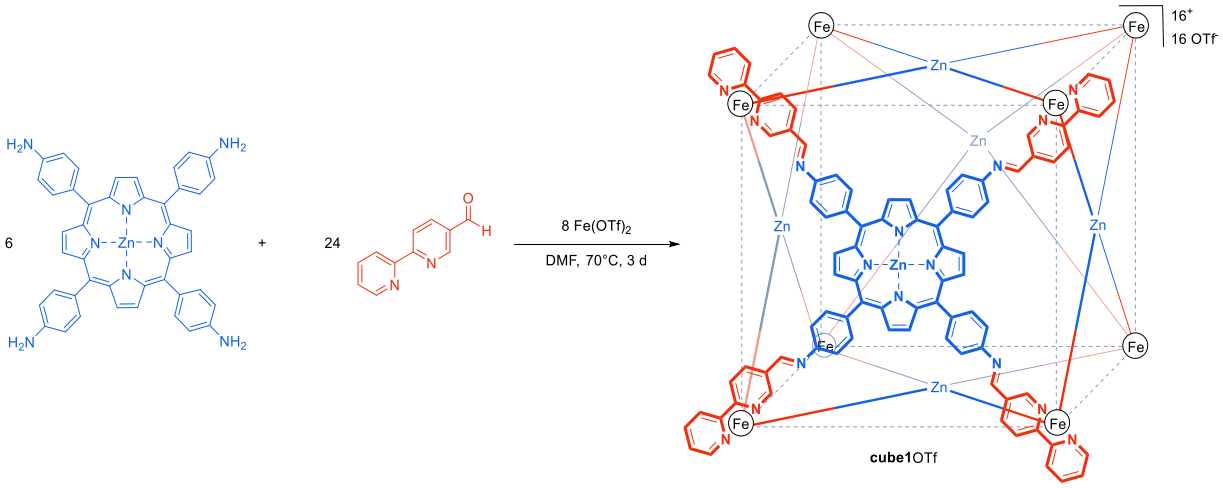

Figure 123: Synthesis of the empty **cube1**OTf.

Method A

The reaction was performed under argon gas atmosphere.

An oven dried *Schlenk* tube was charged with **Zn-TAPP** (51.86 mg, 70.3 µmol, 6.0 eq.), $Fe(OTf)_2$ (34.89 mg, 93.57 µmol, 8.0 eq.) and 2,2'-bipyridine-5-carbaldehyde (51.65 mg,

282.1 µmol, 24.0 eq.). The atmosphere was exchanged three times and dry and degassed DMF was added (5.0 mL). The solution was heated to 70°C overnight and, after allowing it to cool to room temperature, it was added dropwise to diethyl ether (60 mL). The mixture was stored in the fridge overnight and the formed precipitate was collected by filtration. The solid was washed with diethyl ether (3x10 mL) and the remaining solid was dissolved in DMF. The solvent was removed under reduced pressure. This method did not yield the desired product and only the individual building blocks were detected.

Method B

The reaction was performed under argon gas atmosphere.

An oven dried *Schlenk* tube was charged with **Zn-TAPP** (51.86 mg, 70.3 µmol, 6.0 eq.), $Fe(OTf)_2$ (34.89 mg, 93.57 µmol, 8.0 eq.) and 2,2'-bipyridine-5-carbaldehyde (51.65 mg, 282.1 µmol, 24.0 eq.). The atmosphere was exchanged three times and dry and degassed DMF was added (5.0 mL). The solution was heated to 70°C for three days and, after allowing it to cool to room temperature, it was added dropwise to diethyl ether (60 mL). The mixture was stored in the fridge overnight and the formed precipitate was collected by filtration. The solid was washed with diethyl ether (3x10 mL) and the remaining solid was dissolved in DMF. The solvent was removed under reduced pressure. This method did not yield the desired product and only the individual building blocks were detected.

Synthesis of cat1OTf

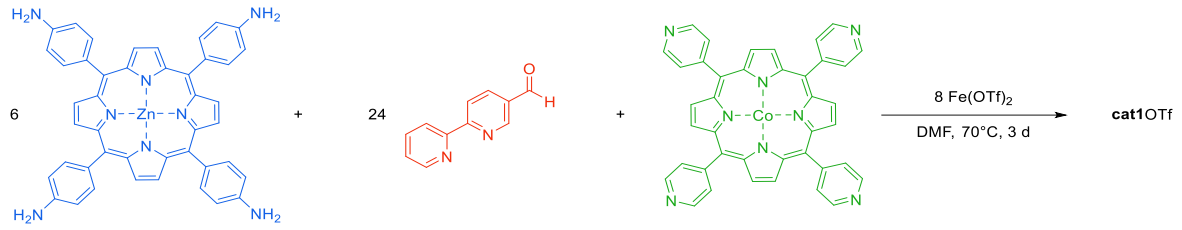

Figure 124: Synthesis of the filled **cat1**OTf.

Method A

The reaction was performed under argon gas atmosphere.

An oven dried *Schlenk* tube was charged with **Zn-TAPP** (51.86 mg, 70.3 µmol, 6.0 eq.), $Fe(OTf)_2$ (34.89 mg, 93.57 µmol, 8.0 eq.), 2,2'-bipyridine-5-carbaldehyde (51.65 mg, 282.12 µmol, 24.0 eq.) and **Co-TPyP** (7.86 mg, 11.98 µmol, 1.0 eq.). The atmosphere was exchanged three times and dry and degassed DMF was added (5.0 mL). The solution was heated to 70°C for three days and, after allowing it to cool to room temperature, it was added

dropwise to diethyl ether (60 mL). The mixture was stored in the fridge overnight and the formed precipitate was collected by filtration. The solid was washed with diethyl ether (3x10 mL) and the remaining solid was collected from the filter. The solid was dried in vacuo for 6 hours and the product was obtained as a micro-crystalline purple solid (128.91 mg, 10.77 µmol, 90%).

Due to the poor solubility and the paramagnetic character of **cat1**OTf no meaningful NMR spectrum could be obtained, but the absence of starting material could be confirmed, since neither the aldehyde nor the amine signal is present, shown in figure 112.

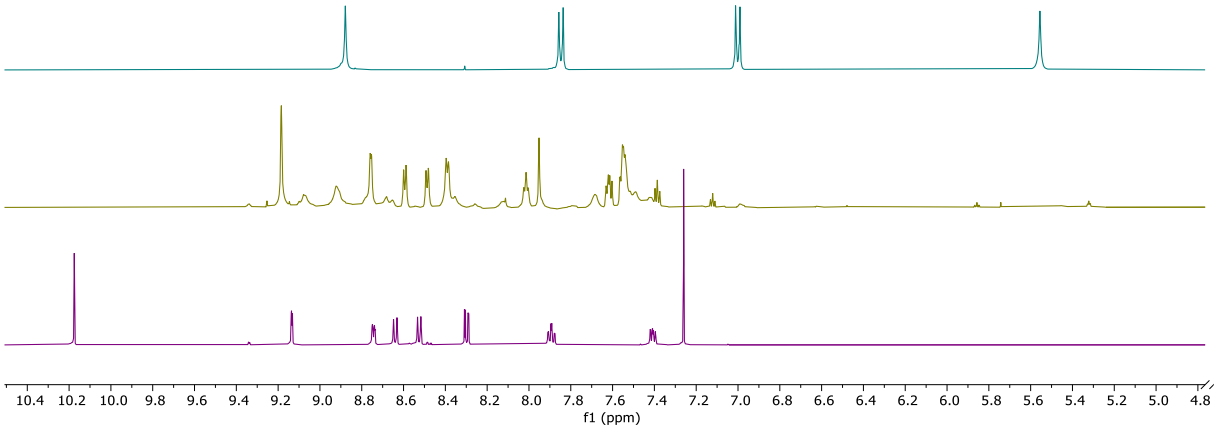

Figure 125: ^{1}H-NMR of Zn-TAPP (blue) in DMSO-d_6, 2,2'-bipyridine-5-carbaldehyde (purple) in $CDCl_3$ and **cat1**OTf in DMSO-d_6 (yellow).

From DOSY-measurements, the experimental diameter of **cat1**OTf could be determined to be 29.5 Å. The calculated from the model differ between 27.2 Å for the diagonal of one face and 37.6 Å for the complete diagonal of the system. Since for the calculations a spherical shape is assumed, the values are only an estimation, but they still match the overall prediction for this system.

HRMS-ESI-(+) ($C_{584}H_{360}N_{104}CoF_{48}Fe_8O_{48}S_{16}Zn_6$)

Table 22: Overview of the result of ESI-MS characterisation of **cat1**OTf.

***m/z* calculated**	***m/z* experimental**	**assignment**
844.5777	844.5860	M^{+12} + 4 OTf^-
847.5795	847.8376	M^{+12} + 4 OTf^- + 2 H_2O
850.7487	850.8385	M^{+12} + 4 OTf^- + DMF
857.0747	857.0005	M^{+12} + 4 OTf^- + H_2O + 2 DMF
860.0886	860.1672	M^{+12} + 4 OTf^- + 3 H_2O + 2 DMF

934.8007	934.802	M^{+11} + 5 OTf^-
935.2626	935.004	M^{+11} + 5 OTf^- + H_2O
948.5463	948.633	M^{+11} + 5 OTf^- + H_2O + 2 DMF

This data agrees with the results reported in literature.[81]

The isotopic patterns in most of the complex-signals are either overlapping each other or suffer from poor resolution. One distinct isotopic pattern of **cat1**OTf is shown in figure 126.

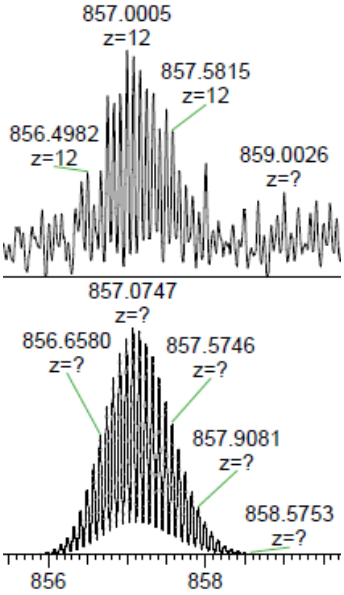

Figure 126: Example of an isotopic pattern of **cat1**OTf (top) to the calculated pattern (bottom).

Method B

The reaction was performed under argon gas atmosphere.

A *Schlenk* tube was charged with **Zn-TAPP** (51.86 mg, 70.3 µmol, 6.0 eq.), $Fe(OTf)_2$ (34.89 mg, 93.57 µmol, 8.0 eq.), 2,2'-bipyridine-5-carbaldehyde (51.65 mg, 282.12 µmol, 24.0 eq.) and **Co-TPyP** (7.86 mg, 11.98 µmol, 1.0 eq.). The atmosphere was exchanged three times and degassed DMF was added (5.0 mL). The solution was heated to 70°C for three days and, after allowing it to cool to room temperature, it was added dropwise to diethyl ether (60 mL). The mixture was stored in the fridge overnight and the formed precipitate was collected by filtration. The solid was washed with diethyl ether (3x10 mL) and the remaining solid was collected from the filter. The solid was dried in vacuo for 6 hours and the product was obtained as a crystalline purple solid (119.28 mg, 9.94 µmol, 83%).

Method C

A screw lid vial was charged with **Zn-TAPP** (51.86 mg, 70.3 µmol, 6.0 eq.), $Fe(OTf)_2$ (34.89 mg, 93.57 µmol, 8.0 eq.), 2,2'-bipyridine-5-carbaldehyde (51.65 mg, 282.12 µmol, 24.0 eq.) and **Co-TPyP** (7.86 mg, 11.98 µmol, 1.0 eq.). The atmosphere was exchanged three times and DMF was added (5.0 mL). The solution was heated to 70°C for three days and, after allowing it to cool to room temperature, it was added dropwise to diethyl ether (60 mL). The mixture was stored in the fridge overnight and the formed precipitate was collected by filtration. The solid was washed with diethyl ether (3x10 mL) and the remaining solid was collected from the filter. The solid was dried in vacuo for 6 hours and the product was obtained as a crystalline purple solid (125.72 mg, 10.54 µmol, 88%).

Method D

A screw lid vial was charged with **Zn-TAPP** (51.86 mg, 70.3 µmol, 6.0 eq.), $Fe(OTf)_2$ (34.89 mg, 93.57 µmol, 8.0 eq.), 2,2'-bipyridine-5-carbaldehyde (51.65 mg, 282.12 µmol, 24.0 eq.) and **Co-TPyP** (7.86 mg, 11.98 µmol, 1.0 eq.). The atmosphere was exchanged three times and DMF was added (5.0 mL). The solution was heated to 70°C for seven days and, after allowing it to cool to room temperature, it was added dropwise to diethyl ether (60 mL). The mixture was stored in the fridge overnight and the formed precipitate was collected by filtration. The solid was washed with diethyl ether (3x10 mL) and the remaining solid was collected from the filter. The solid was dried in vacuo for 6 hours and the product was obtained as a crystalline purple solid (124.18 mg, 10.41 µmol, 87% including 9.27 w% DMF).

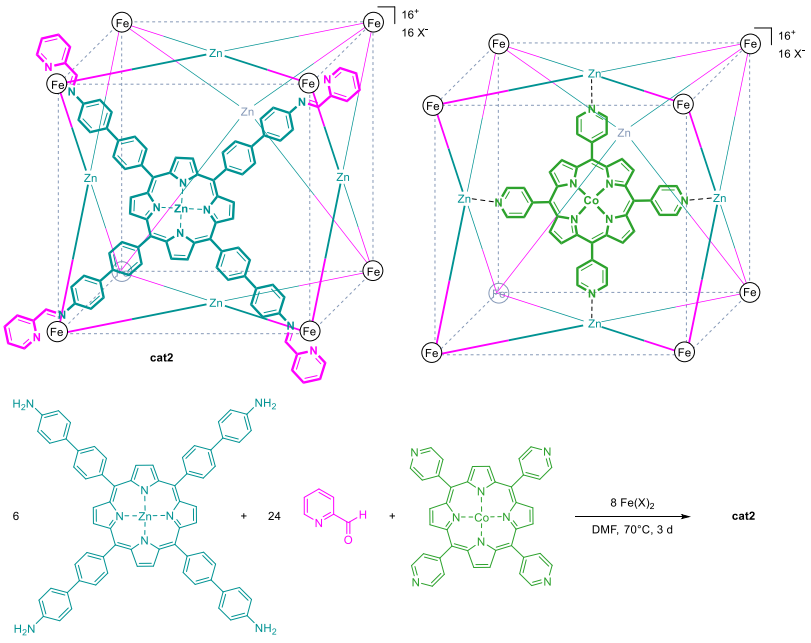

Figure 127: Synthesis of **cat2**.

Synthesis of cat2OTf

A screw lid vial was charged with **Zn-TAbPP** (100.01 mg, 95.92 µmol, 6.0 eq.), $Fe(OTf)_2$ (86.41 mg, 127.89 µmol, 8.0 eq.), picolinaldehyde (36.50 µL, 383.67 µmol, 24.0 eq.) and **Co-TPyP** (10.80 mg, 15.99 µmol, 1.0 eq.). The atmosphere was exchanged three times and DMF was added (7.0 mL). The solution was heated to 70°C for three days and, after allowing it to cool to room temperature, it was added dropwise to diethyl ether (60 mL). The mixture was stored in the fridge overnight and the formed precipitate was collected by filtration. The solid was washed with diethyl ether (3x10 mL) and the remaining solid was collected from the filter. The solid was dried in vacuo for 6 hours and the product was obtained as a crystalline purple solid (170.32 mg, 14.55 µmol, 91% including 9.29 w% DMF).

Due to the poor solubility and the paramagnetic character of **cat2**OTf no meaningful NMR spectrum could be obtained. Only the DMF content could be determined by adding an internal standard (2 µL of dibromomethane) to the NMR solution.

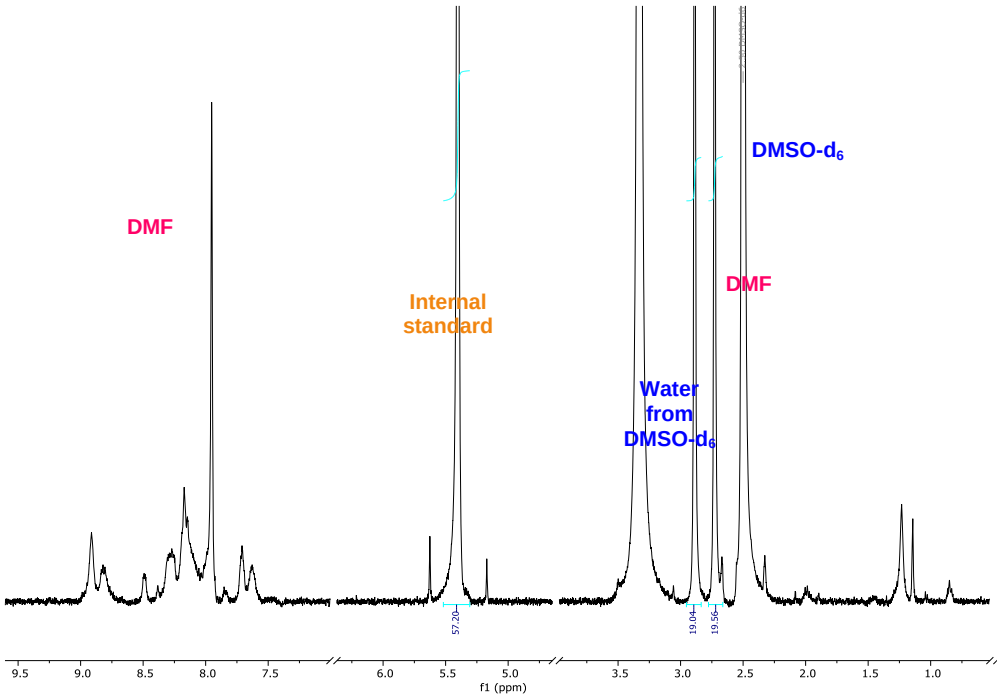

Figure 128: ^{1}H-NMR of **cat2**OTf with internal standard.

To determine the DMF content from these quantitative NMR experiments, the integral of the internal standard at 5.40 ppm was set to 57.20 which corresponds to the chemical amount in µmol. Afterwards, the integrals of both DMF signals at 2.89 ppm and 2.73 ppm were measured and the average was calculated. Since these signals are formed by three hydrogen atoms, the

average of both integrals is divided by 3, giving a value of 6.43 µmol, from which the weight percentage DMF content can be determined.

Table 23: Overview of different DMF contents at different drying stages.

hours under fine vacuum	DMF content
0	16.84w%
3	15.59w%
6	9.29w%
9	9.20w%

HRMS-ESI-(+) ($C_{593}H_{369}CoF_{48}N_{80}O_{48}S_{16}Fe_8Zn_6$)

Table 24: Overview of the result of ESI-MS characterisation of **cat2**OTf.

m/z calculated	*m/z* experimental	assignment
594.7025	594.771	M^{+16} + 0 OTf^-
644.3461	644.487	M^{+15} + 1 OTf^-
700.9389	700.877	M^{+14} + 2 OTf^-
701.2247	701.228	M^{+14} + 2 OTf^- + H_2O
703.0847	703.084	M^{+14} + 2 OTf^- + 2 H_2O
774.1161	774.174	M^{+14} + 2 OTf^- + 2 H_2O + 10 DMF
766.6996	766.706	M^{+13} + 3 OTf^-
767.8543	767.857	M^{+13} + 3 OTf^- + H_2O
771.7038	771.728	M^{+13} + 3 OTf^- + DMF
783.1734	783.174	M^{+13} + 3 OTf^- + 3 DMF
842.6706	842.674	M^{+12} + 4 OTf^-
848.6750	848.677	M^{+12} + 4 OTf^- + DMF
933.0908	933.095	M^{+11} + 5 OTf^-

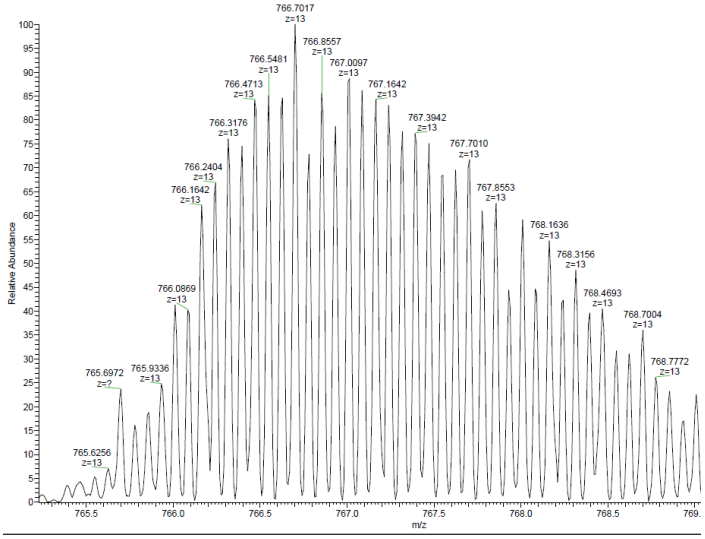

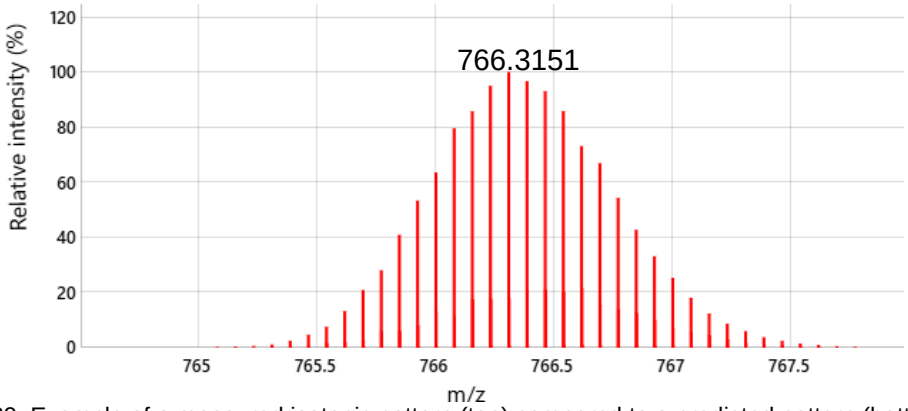

Figure 129: Example of a measured isotopic pattern (top) compared to a predicted pattern (bottom). The isotopic pattern was predicted with chemcalc.org.

Synthesis of cat2NTf$_2$

A screw lid vial was charged with **Zn-TAbPP** (100.01 mg, 95.92 µmol, 6.0 eq.), Fe(NTf$_2$)$_2$ (78.81 mg, 127.89 µmol, 8.0 eq.), picolinaldehyde (36.50 µL, 383.67 µmol, 24.0 eq.) and **Co-TPyP** (10.80 mg, 15.99 µmol, 1.0 eq.). The atmosphere was exchanged three times and DMF was added (7.0 mL). The solution was heated to 70°C for three days and, after allowing it to cool to room temperature, it was added dropwise to diethyl ether (60 mL). The mixture was stored in the fridge overnight and the formed precipitate was collected by filtration. The solid was washed with diethyl ether (3x10 mL) and the remaining solid was collected from the filter. The solid was dried in vacuo for 6 hours and the product was obtained as a crystalline purple solid (194.18 mg, 14.07 µmol, 88%, including DMF content = 9.27w%).

Due to the poor solubility and the paramagnetic character of **cat2**NTf$_2$ no meaningful NMR spectrum could be obtained. Only the DMF content could be determined by adding an internal standard (2 µL of dibromomethane) to the NMR solution.

Table 25: Overview of the result of ESI-MS characterisation of **cat2**NTf$_2$.

***m/z* calculated**	***m/z* experimental**	**assignment**
594.7025	594.956	M^{+16} + 0 OTf^-
595.0794	595.019	M^{+16} + 0 OTf^- + H_2O
653.0771	653.015	M^{+15} + 1 OTf^-
719.6482	719.795	M^{+14} + 2 OTf^-
720.5776	720.581	M^{+14} + 2 OTf^- + H_2O
721.7926	721.797	M^{+14} + 2 OTf^- + 2 H_2O
796.7684	796.773	M^{+13} + 3 OTf^-
798.0770	798.003	M^{+13} + 3 OTf^- + H_2O
886.3256	886.330	M^{+12} + 4 OTf^-
887.5766	887.580	M^{+12} + 4 OTf^- + H_2O
892.8299	892.829	M^{+12} + 4 OTf^- + DMF
992.6203	992.625	M^{+11} + 5 OTf^-
993.6215	993.624	M^{+11} + 5 OTf^- + H_2O
1119.5741	1119.477	M^{+10} + 6 OTf^-

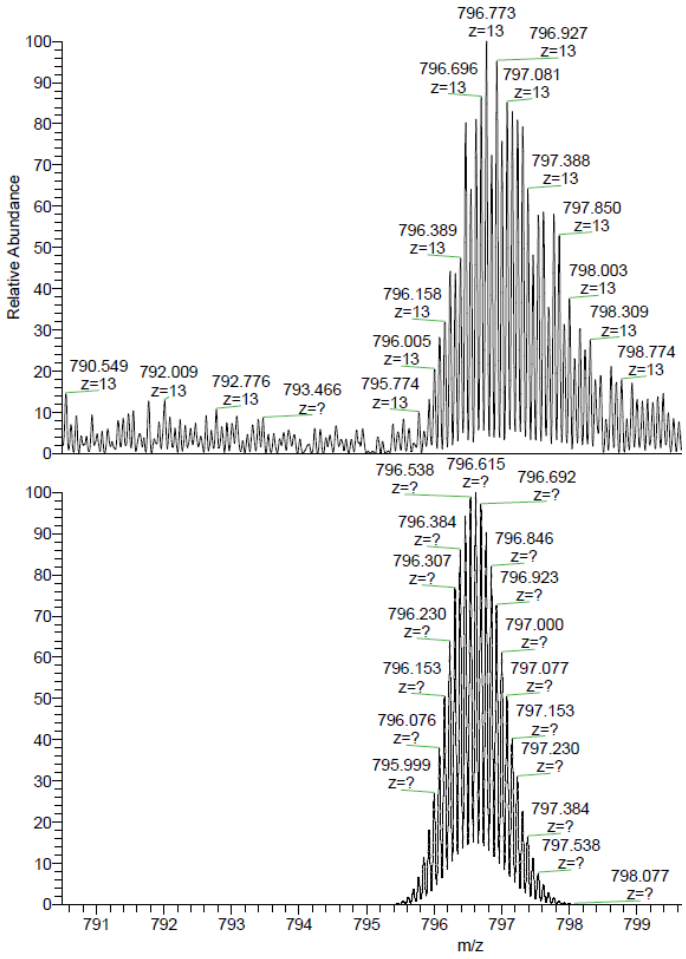

Figure 130: Example of a measured isotopic pattern (top) compared to a predicted pattern (bottom).

Catalytic experiments

General procedure 1

Stock solutions of the catalyst (0.008 M in dry and degassed DMF) and the respective styrene derivative (1.2 M in dry and degassed DMF) were prepared in the glovebox. Under exclusion of water and air, they were combined with ethyl diazotate (5.26 µL, 50.00 µmol, 1.0 eq.) in the respective amounts in a 4 mL screw top vial, equipped with a stirring bar. Afterwards dry and degassed DMF was added until the desired overall concentration was reached and the vial was sealed inside the glovebox. After removing it from the glovebox, the mixture was heated for the specified amount of time, followed by cooling to room temperature. Afterwards ethyl acetate (3.83 mL) was added and the mixture was rested for 2 minutes, to allow the catalyst to precipitate properly. Next, the solid was removed by filtration through a celite plug and the solvent was removed under reduced pressure. Thereby, it was monitored that the pressure would not fall below 130 mbar, in order to not evaporate residues of ethyl diazotate. Afterwards, the remaining mixture was dissolved in dry deuterated chloroform (1 mL) and dibromomethane

(2 µL) as well as nitromethane (2 µL) were added as internal standard. After thorough mixing of the components, 0.5 mL of the mixture were transferred into an NMR tube and a quantitative ^{1}H-NMR spectrum was measured to determine yield, conversion and the diastereomeric ratio. Therefore, two distinct signals were used, since they provide a similar shift for all tested compounds, while not being overlapped by solvent- or remaining substrate-signals. For the standard compound *para*-trifluoromethyl styrene, these signals were observed at 1.73 ppm, corresponding to the *cis*-product and at 1.66 ppm, corresponding to the *trans*-product, as shown exemplary in figure 129 and 130.

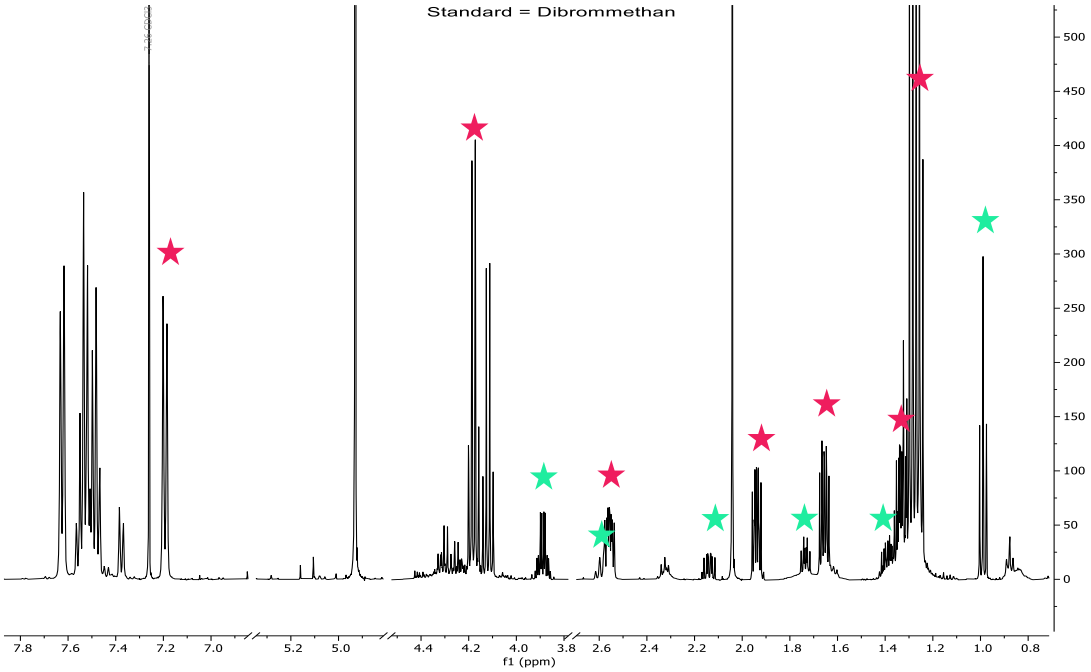

Figure 131: Example ^{1}H-NMR spectrum of the conversion of *para*-trifluoromethyl styrene with *cis*- (turquois star) and *trans*-product (pink star).

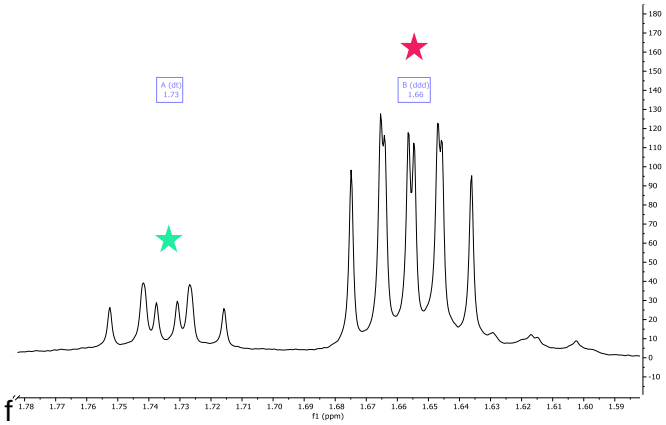

Figure 132: Enlarged section of the two distinct signals which were used to analyse the spectra with *cis*- (turquois star) and *trans*-product (pink star).

General procedure 2

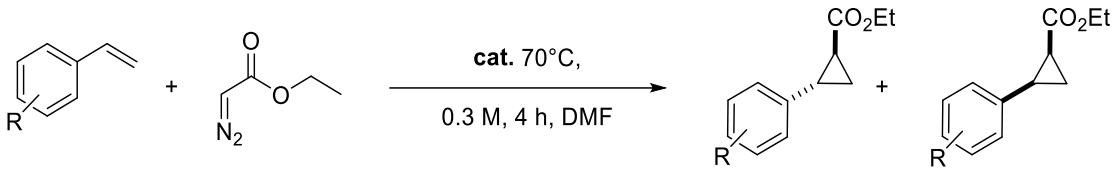

Stock solutions of the catalyst (0.008 M in dry and degassed DMF) and the respective styrene derivative (1.2 M in dry and degassed DMF) were prepared in the glovebox. Under exclusion of water and air, they were combined with ethyl diazotate (5.26 µL, 50.00 µmol, 1.0 eq.) in the respective amounts in a 4 mL screw top vial, equipped with a stirring bar. Afterwards dry and degassed DMF was added until the overall concentration, with respect to the following addition of water, was reached. After removing the vial from the glovebox, degassed water (30 eq.) was added through a septum in the lid and the mixture was heated for the specified amount of time, followed by cooling to room temperature. Afterwards ethyl acetate (3.83 mL) was added and the mixture was rested for 2 minutes, to allow the catalyst to precipitate properly. Next, the solid was removed by filtration through a celite plug and the solvent was removed under reduced pressure. Thereby, it was monitored that the pressure would not fall below 130 mbar, in order to not evaporate residues of ethyl diazotate. Afterwards, the remaining mixture was dissolved in deuterated acetone (1 mL) and dibromomethane (2 µL) as well as nitromethane (2 µL) were added as internal standard. After thorough mixing of the components, 0.5 mL of the mixture were transferred into an NMR tube and a quantitative ^{1}H-NMR spectrum was measured to determine yield, conversion and the diastereomeric ratio.

General procedure 3

Stock solutions of the catalyst (0.004 M in dry and degassed DMF) and the respective styrene derivative (2.5 M in dry and degassed DMF) were prepared in the glovebox. Under exclusion of water and air, they were combined with ethyl diazotate (5.26 µL, 50.00 µmol, 1.0 eq.) in the respective amounts in a 4 mL screw top vial, equipped with a stirring bar. Afterwards dry and degassed DMF (34.01 µL) was added until the desired overall concentration was reached and the vial was sealed inside the glovebox. After removing it, degassed water (27.4 µL, 1.50 mmol, 30.0 eq.) was added through a septum in the lid and the mixture was heated for the specified amount of time, followed by cooling to room temperature. Afterwards ethyl acetate (3.83 mL) was added and the mixture was rested for 2 minutes, to allow the catalyst to precipitate properly. Next, the solid was removed by filtration through a celite plug and the solvent was removed under reduced pressure. Thereby, it was monitored that the pressure would not fall below 130 mbar, in order to not evaporate residues of ethyl diazotate. Afterwards,

the remaining mixture was dissolved in deuterated acetone (1 mL) and dibromomethane (2 µL) as well as nitromethane (2 µL) were added as internal standard. After thorough mixing of the components, 0.5 mL of the mixture were transferred into an NMR tube and a quantitative ^{1}H-NMR spectrum was measured to determine yield, conversion and the diastereomeric ratio.

General procedure 4

Stock solutions of the catalyst (0.004 M in dry and degassed DMF) and the respective styrene derivative (2.5 M in dry and degassed acetone) were prepared in the glovebox. Under exclusion of water and air, they were combined with ethyl diazotate (5.26 µL, 50.00 µmol, 1.0 eq.) in the respective amounts in a 4 mL screw top vial, equipped with a stirring bar. Afterwards dry and degassed acetone was added until the desired overall concentration was reached and the vial was sealed inside the glovebox. After removing it, the mixture was heated for the specified amount of time, followed by cooling to room temperature. Afterwards ethyl acetate (3.83 mL) was added and the mixture was rested for 2 minutes, to allow the catalyst to precipitate properly. Next, the solid was removed by filtration through a celite plug and the solvent was removed under reduced pressure. Thereby, it was monitored that the pressure would not fall below 130 mbar, in order to not evaporate residues of ethyl diazotate. Afterwards, the remaining mixture was dissolved in deuterated acetone (1 mL) and dibromomethane (2 µL) as well as nitromethane (2 µL) were added as internal standard. After thorough mixing of the components, 0.5 mL of the mixture were transferred into an NMR tube and a quantitative ^{1}H-NMR spectrum was measured to determine yield, conversion and the diastereomeric ratio.

Comparison of catalysts

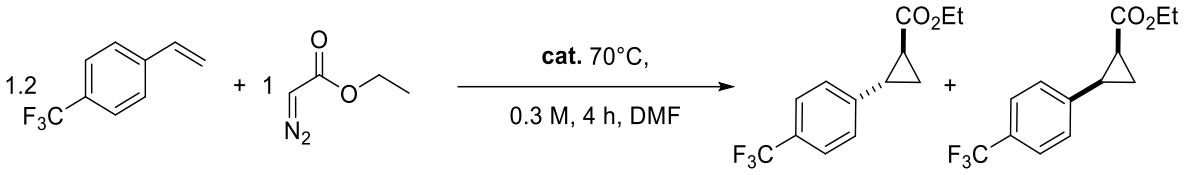

The experiments were performed as described in general procedure 1 by combining the stock solutions of the respective catalyst (50 µL, 0.4 µmol, 0.008 eq.) and *para*-trifluoromethyl styrene (50 µL, 60 µmol, 1.2 eq.) with EDA (5.26 µL, 50 µmol, 1.0 eq.) and 61.41 µL of dry and degassed DMF. The mixture was stirred for 4 hours at 70°C and the results are listed in table 27.

Table 26: Results of comparison of different catalysts.

catalyst	mol% **cat2**OTf	trans/cis	conversion (styrene)	yield	TON
cat1OTf	0.8	3.6:1	100%	40%	50
Co-TPyP	0.8	6.5:1	77%	14%	18
cat2OTf	0.8	3.6:1	64%	38%	48
cat1OTf	0.4	3.6:1	85%	43%	108
Co-TPyP	0.4	6.0:1	76%	8%	20
cat2OTf	0.4	3.6:1	62%	40%	100

Catalyst loading of cat2OTf

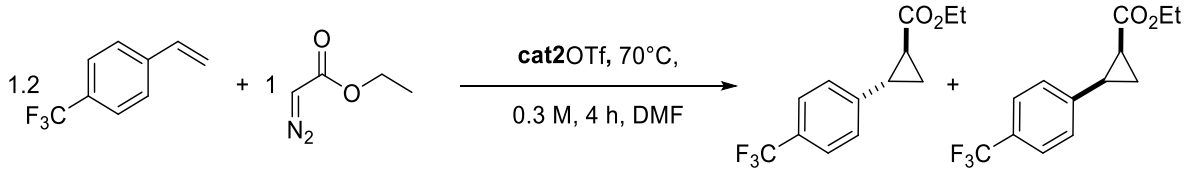

The experiments were performed as described in general procedure 1 by combining the stock solutions of **cat2**OTf (listed in the column “catalyst volume” in table 28) and *para*-trifluoromethyl styrene (50 µL, 60 µmol, 1.2 eq.) with EDA (5.26 µL, 50 µmol, 1.0 eq.) and the respective amount of dry and degassed DMF (listed in the column “DMF volume” in table 28). The mixture was stirred for 4 hours at 70°C and the results are listed in table 28.

Table 27: Results of comparison of different catalyst loadings of **cat2**OTf.

mol% **cat2**OTf	catalyst volume	DMF volume	trans/cis	conversion (styrene)	yield	TON
0.1	6.25 µL	105.16 µL	3.6:1	28%	5%	50
0.2	12.5 µL	98.91 µL	3.4:1	34%	7%	35
0.25	15.63 µL	95.78 µL	3.6:1	38%	9%	36
0.4	25.0 µL	86.41 µL	3.6:1	62%	40%	100
0.6	37.5 µL	73.91 µL	3.6:1	59%	40%	67
0.8	50.0 µL	61.41 µL	3.6:1	92%	38%	48

Substrate stoichiometry with cat2OTf

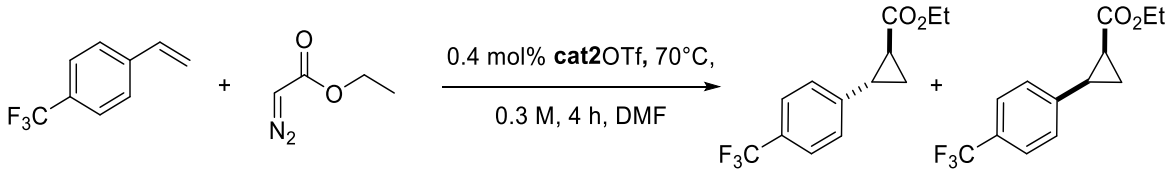

The experiments were performed as described in general procedure 1 by combining the stock solutions of **cat2**OTf (25 µL, 0.2 µmol, 0.004 eq.) with the one of *para*-trifluoromethyl styrene and the respective amount of EDA (listed in the column "EDA volume" of table 29. Therefore, different stock solutions of *para*-trifluoromethyl styrene were prepared. The previously used stock solution with a concentration of 1.0 µmol/µL [a] was used, as well as a higher concentrated stock solution with a concentration of 3.0 µmol/µL [b]. Of these stock solutions, the respective amounts were added (listed in the column "alkene volume" in table 29) to the vial and dry and degassed DMF (listed in the column "DMF volume" in table 29) was added afterwards. The mixture was stirred for 4 hours at 70°C and the results are listed in table 29.

Table 28: Results of comparison of different stoichiometries for **cat2**OTf.

CF_3-styrene	alkene volume	EDA	EDA volume	DMF volume	trans/cis	conversion (styrene)	yield	TON
3.0 eq.	50 µL[b]	1.0 eq.	5.26 µL	86.41 µL	4.0:1	55%	36%	90
2.5 eq.	41.7 µL[b]	1.0 eq.	5.26 µL	94.74 µL	3.3:1	66%	42%	105
1.2 eq.	20 µL[b]	1.0 eq.	5.26 µL	116.41 µL	3.6:1	62%	40%	100
1.0 eq.	50 µL[a]	1.0 eq.	5.26 µL	86.41 µL	3.3:1	47%	23%	58
1.0 eq.	50 µL[a]	2.0 eq.	10.52 µL	81.15 µL	4.0:1	43%	11%	27
1.0 eq.	50 µL[a]	3.0 eq.	15.78 µL	75.89 µL	3.9:1	40%	12%	31

Temperature dependency with cat2OTf

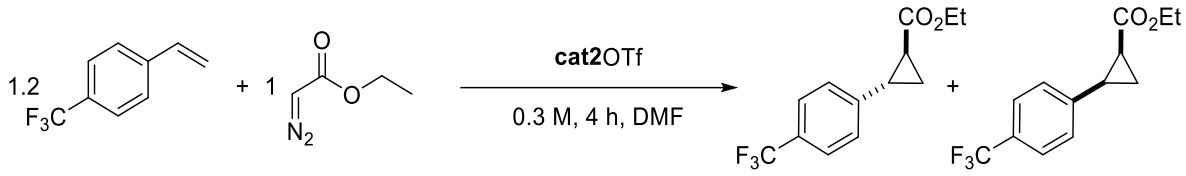

The experiments were performed as described in general procedure 1 by combining the stock solutions of **cat2**OTf (25 µL, 0.2 µmol, 0.004 eq.) and *para*-trifluoromethyl styrene (50 µL, 60 µmol, 1.2 eq.) with EDA (5.26 µL, 50 µmol, 1.0 eq.) and dry and degassed DMF (86.41 µL). The mixture was stirred for 4 hours at the respective temperature (listed in the column "temperature in table 30) and the results are listed in table 30.

Table 29: Results of comparison of different temperatures for **cat2**OTf.

temperature	mol% **cat2**OTf	trans/cis	conversion (styrene)	yield	TON
25°C	0.4	-	2%	0%	0
50°C	0.4	4.1:1	38%	17%	42
70°C	0.4	3.6:1	62%	40%	100
85°C	0.4	3.6:1	60%	39%	98
100°C	0.4	-	1%	0%	0

Concentration dependency of cat2OTf

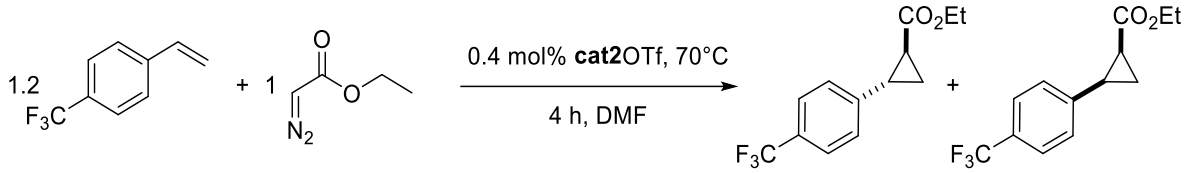

The experiments were performed as described in general procedure 1 by combining the stock solutions of **cat2**OTf (listed in the column "**cat2**OTf volume" in table 31) and *para*-trifluoromethyl styrene (listed in the column "CF_3-styrene volume" in table 31) with EDA (listed in the column "EDA volume" in table 31) and dry and degassed DMF (listed in the column "DMF volume" in table 31). The mixture was stirred for 4 hours at 70°C and the results are listed in table 31.

Table 30: Results of comparison of different concentration for **cat2**OTf.

concentration	cat2OTf volume	EDA volume	CF_3-Styrene volume	DMF volume	trans/cis	conversion (styrene)	yield	TON
0.15 M	12.5 µL	2.63 µL	25 µL	126.54 µL	3.2:1	33%	12%	30
0.30 M	25 µL	5.26 µL	50 µL	86.41 µL	3.6:1	62%	40%	100

Time dependency with cat2OTf

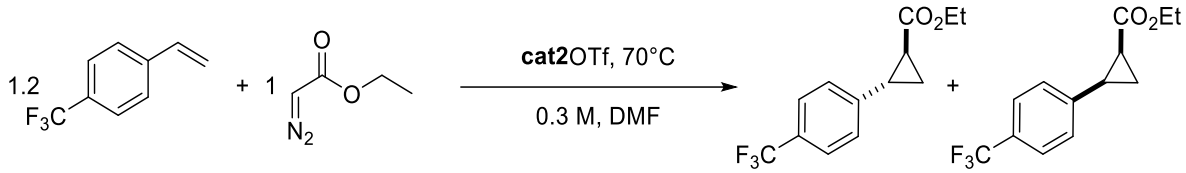

The experiments were performed as described in general procedure 1 by combining the stock solutions of **cat2**OTf (25 µL, 0.2 µmol, 0.004 eq.) and *para*-trifluoromethyl styrene (50 µL, 60 µmol, 1.2 eq.) with EDA (5.26 µL, 50 µmol, 1.0 eq.) and dry and degassed DMF (86.41 µL). The mixture was stirred for the respective time (listed in the column "time" in table 32) at 70°C and the results are listed in table 32.

Table 31: Results of comparison of different reaction times for **cat2**OTf.

time	mol% cat2OTf	trans/cis	conversion (styrene)	yield	TON
4 hours	0.4	3.6:1	62%	40%	100
6 hours	0.4	3.4:1	68%	48%	120
23 hours	0.4	3.3:1	70%	49%	123

Sensitivity of cat2OTf towards ambient air and water

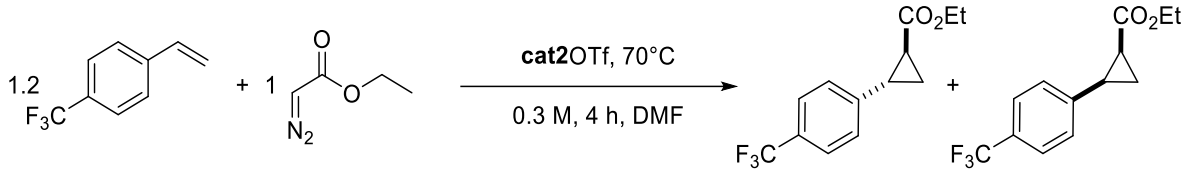

The experiments were performed as described in general procedure 1 by combining the stock solutions of **cat2**OTf (25 µL, 0.2 µmol, 0.004 eq.) and *para*-trifluoromethyl styrene (50 µL, 60 µmol, 1.2 eq.) with EDA (5.26 µL, 50 µmol, 1.0 eq.) and dry and degassed DMF (86.41 µL). The mixture was stirred for 4 hours at 70°C and the results are listed in table 33.

In the second entry of table 33, the vial was opened for 10 seconds before heating it to 70°C. For the last entry, the stock solutions and the reaction itself were not prepared in the glovebox, but under ambient conditions without the use of dry solvents.

Table 32: Results of comparison of different air contents for **cat2**OTf.

air content	mol% **cat2**OTf	trans/cis	conversion (styrene)	yield	TON
no air	0.4	3.6:1	62%	40%	100
short exposure	0.4	3.6:1	61%	38%	95
air	0.4	-	0%	0%	0

The experiments, regarding the water sensitivity of the system were performed as described in general procedure 2 by combining the stock solutions of **cat2**OTf (25 µL, 0.2 µmol, 0.004 eq.) and *para*-trifluoromethyl styrene (50 µL, 60 µmol, 1.2 eq.) with EDA (5.26 µL, 50 µmol, 1.0 eq.) and dry and degassed DMF (listed in the column “DMF volume” of table 34). After removing the vial from the glovebox degassed water (listed in the column “water volume” in table 34) was added and the mixture was stirred for 4 hours at 70°C and the results are listed in table 34.

Table 33: Results of comparison of different water contents for **cat2**OTf.

water content	water volume	DMF volume	trans/cis	conversion (styrene)	yield	TON
0 eq.	-	86.41 µL	3.6:1	62%	40%	100
1 eq.	0.9 µL	85.51 µL	3.8:1	55%	38%	95
10 eq.	9.1 µL	77.31 µL	3.6:1	55%	39%	98
20 eq.	18.2 µL	68.21 µL	3.4:1	60%	42%	105
30 eq.	27.4 µL	59.01 µL	3.2:1	65%	47%	118
50 eq.	45.6 µL	40.81 µL	3.6:1	60%	40%	100
70 eq.	63.8 µL	22.61 µL	3.9:1	59%	38%	95

DMF content of cat2OTf

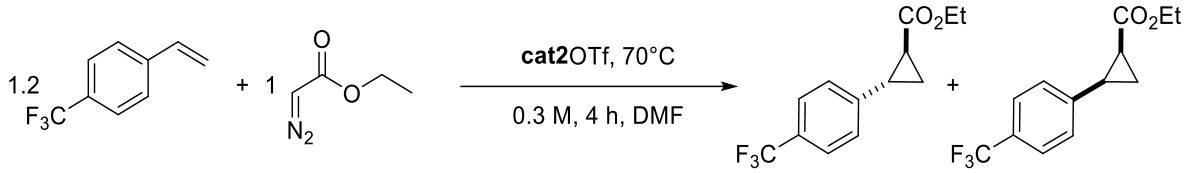

The experiments were performed as described in general procedure 1 by combining the stock solutions of the **cat2**OTf (25 µL, 0.2 µmol, 0.004 eq.) and *para*-trifluoromethyl styrene (50 µL, 60 µmol, 1.2 eq.) with EDA (5.26 µL, 50 µmol, 1.0 eq.) and dry and degassed DMF (86.41 µL). The mixture was stirred for 4 hours at 70°C and the results are listed in table 35. For the stock solutions of these experiments, **cat2**OTf was used after no time, three hours and six hours under fine vacuum.

Table 34: Results of comparison of different effective catalyst loadings of **cat2**OTf.

effective mol% cat2OTf	**trans/cis**	**conversion (styrene)**	**yield**	**TON**
0.33	4.0:1	51%	31%	94
0.34	3.6:1	60%	42%	105
0.37	3.4:1	69%	47%	118

Substrate scope of cat2OTf

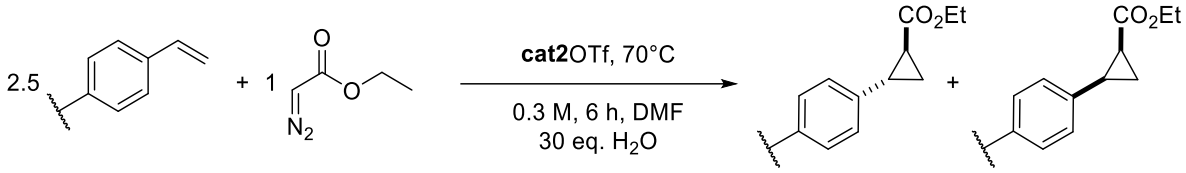

The experiments were performed as described in general procedure 3 by combining the stock solutions of the **cat2**OTf (50 µL, 0.2 µmol, 0.004 eq.) and the respective styrene derivative (50 µL, 125 µmol, 2.5 eq.) with EDA (5.26 µL, 50 µmol, 1.0 eq.) and dry and degassed DMF (34.01 µL). After removing the vial from the glovebox, degassed water (27.4 µL) was added and the mixture was stirred for 6 hours at 70°C. The respective results for *para*-substituted styrene derivatives are listed in table 36 and 37.

Table 35: Results for electron-withdrawing substituents in *para*-position.

R	trans/cis	conversion (styrene)	yield	TON
—Br	2.6:1	60%	55%	139
—Cl	2.6:1	65%	49%	123
—F	2.3:1	73%	48%	119
—CO_2Me	2.5:1	54%	49%	124
—CF_3	2.7:1	64%	48%	119
—CN	2.8:1	66%	56%	139
—NO_2	2.7:1	59%	50%	124

Table 36: Results for electron-donating substituents in *para*-position.

R	trans/cis	conversion (styrene)	yield	TON
—OMe	2.3:1	53%	49%	122
—TMS	2.9:1	64%	43%	107
—NH_2	3.4:1	60%	33%	83
—NMe_2	3.0:1	76%	67%	171
—H	2.4:1	56%	48%	120

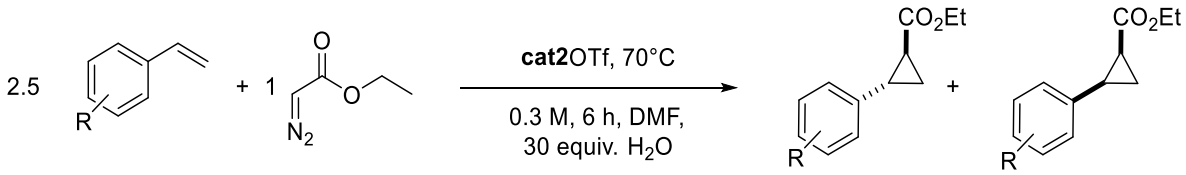

The experiments were performed as described in general procedure 3 by combining the stock solutions of the **cat2**OTf (50 µL, 0.2 µmol, 0.004 eq.) and the respective styrene derivative (50 µL, 125 µmol, 2.5 eq.) with EDA (5.26 µL, 50 µmol, 1.0 eq.) and dry and degassed DMF (34.01 µL). After removing the vial from the glovebox, degassed water (27.4 µL) was added and the mixture was stirred for 6 hours at 70°C. The respective results are listed in table 38.

Table 37: Results for additional substituents.

R	trans/cis	conversion (styrene)	yield	TON
ortho-CH_3	3.0:1	75%	43%	107
meta-CH_3	2.5:1	67%	46%	115
ortho-Br	3.5:1	60%	51%	127
meta-Br	2.3:1	65%	58%	144
meta-OMe	2.3:1	57%	54%	135
2 x *ortho*-CH_3 *para*-CH_3	-	51%	25%	64

Sensitivity of cat2NTf$_2$

The experiments, regarding the water sensitivity of the system were performed as described in general procedure 2 by combining the stock solutions of **cat2**NTf_2 (25 µL, 0.2 µmol, 0.004 eq. in acetone) and *para*-trifluoromethyl styrene (50 µL, 125 µmol, 2.5 eq. in acetone) with EDA (5.26 µL, 50 µmol, 1.0 eq.) and dry and degassed acetone (listed in the column "acetone volume" of table 39). After removing the vial from the glovebox, degassed water (listed in the column "water volume" in table 39) was added and the mixture was stirred for 6 hours at 70°C with the results listed in table 39.

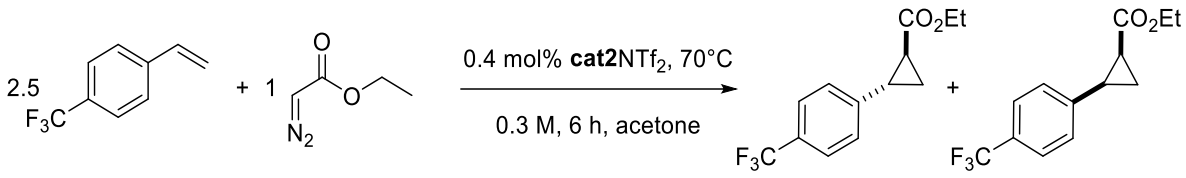

Table 38: Results of comparison of different water contents for **cat2**NTf_2.

water content	water volume	acetone volume	trans/cis	conversion (styrene)	yield	TON
0 eq.	-	86.41	3.2:1	74%	66%	165
10 eq.	9.1 µL	77.31	2.8:1	84%	61%	153
30 eq.	27.4 µL	59.01	2.7:1	78%	67%	168
50 eq.	45.6 µL	40.81	3.1:1	68%	65%	163
70 eq.	63.8 µL	22.61	2.8:1	77%	66%	165

Solvents for cat2NTf$_2$

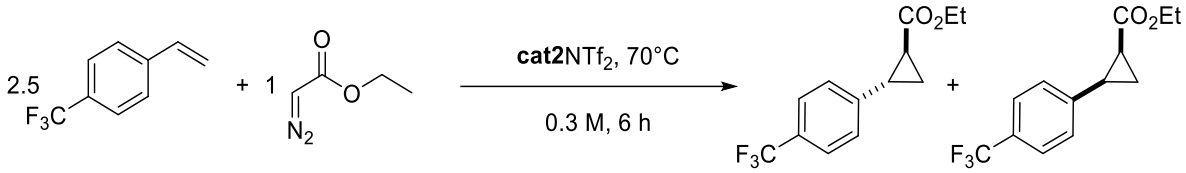

The experiments were performed as described in general procedure 4 by combining the stock solutions of **cat2**NTf$_2$ (50 µL, 0.2 µmol, 0.004 eq.) and *para*-trifluoromethyl styrene (50 µL, 125 µmol, 2.5 eq.) with EDA (5.26 µL, 50 µmol, 1.0 eq.). For the entries 1, 3, 5 and 7 the stock solutions were prepared in the respective solvent (listed in the column "solvent" in table 40) and after combining them the respective solvent was added until the overall concentration of 0.3 M was reached. For the solvent mixtures, the stock solution of the catalyst was prepared in dry and degassed DMF, while the stock solution of *para*-trifluoromethyl styrene was prepared in the respective solvent (listed as the column "solvent" in table 40). After removing the vial from the glovebox, the mixture was stirred for 6 hours at 70°C with the results listed in table 40.

Table 39: Results of comparison of different solvents for **cat2**NTf$_2$.

solvent	mol% **cat2**NTf$_2$	trans/cis	conversion (styrene)	yield	TON
DMF	0.4	3.6:1	67%	49%	122
DMF/acetone 1:2	0.4	3.5:1	69%	63%	158
DCM	0.4	2.7:1	58%	17%	42
DMF/DCM 1:2	0.4	3.1:1	66%	64%	159
THF	0.4	3.0:1	43%	39%	96
DMF/THF 1:2	0.4	3.1:1	64%	57%	142
acetonitrile	0.4	2.6:1	32%	20%	49
DMF/acetonitrile 1:2	0.4	3.1:1	62%	59%	148

Catalyst loading of cat2NTf$_2$

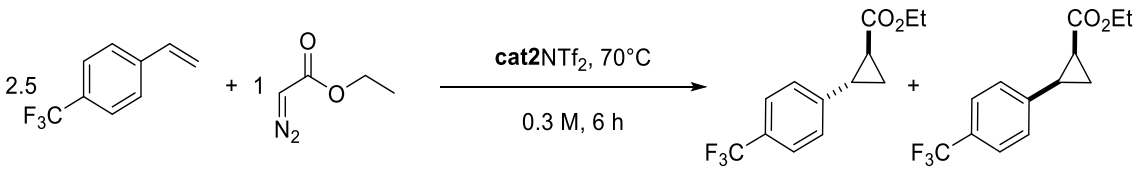

The experiments were performed as described in general procedure 4 by combining the stock solutions of **cat2**NTf$_2$ (listed in the column "**cat2**NTf$_2$ volume" in table 41 in DMF) and

para-trifluoromethyl styrene (50 µL, 125 µmol, 2.5 eq. in acetone) with EDA (5.26 µL, 50 µmol, 1.0 eq.) and the respective amount of dry and degassed acetone (listed in the column “acetone volume” in table 41). The mixture was stirred for 6 hours at 70°C and the results are listed in table 41.

Table 40: Results of comparison of different catalyst loadings of **cat2**NTf_2.

mol%	**cat2**NTf_2 volume	acetone volume	trans/cis	conversion (styrene)	yield	TON
0.1	12.5 µL	98.91 µL	3.4:1	53%	28%	280
0.2	25.0 µL	86.41 µL	3.0:1	77%	72%	360
0.3	37.5 µL	73.91 µL	3.1:1	32%	30%	100
0.4	50.0 µL	61.41 µL	2.6:1	69%	63%	158

Substrate scope of cat2NTf_2

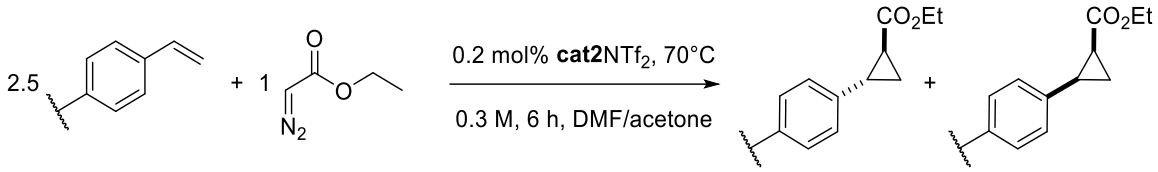

The experiments were performed as described in general procedure 4 by combining the stock solutions of **cat2**NTf_2 (25 µL, 0.1 µmol, 0.002 eq. in DMF) and the respective styrene derivative (50 µL, 125 µmol, 2.5 eq. in acetone) with EDA (5.26 µL, 50 µmol, 1.0 eq.) and dry and degassed acetone (86.41 µL). After removing the vial from the glovebox, the mixture was stirred for 6 hours at 70°C. The respective results for *para*-substituted styrene derivatives are listed in table 42 and 43.

Table 41: Results for electron-withdrawing substituents in *para*-position.

R	trans/cis	conversion (styrene)	yield	TON
—Br	3.0:1	65%	61%	303
—Cl	2.8:1	73%	65%	327
—F	2.5:1	62%	54%	272
—CO_2Me	3.0:1	59%	55%	276
—CF_3	3.0:1	77%	72%	359
—CN	2.9:1	69%	64%	319
—NO_2	2.9:1	75%	67%	333

Table 42: Results for electron-donating substituents in *para*-position.

R	trans/cis	conversion (styrene)	yield	TON
	2.9:1	68%	58%	291
	2.9:1	66%	57%	286
	2.6:1	55%	36%	178
	3.0:1	77%	70%	351
	2.9:1	73%	64%	320

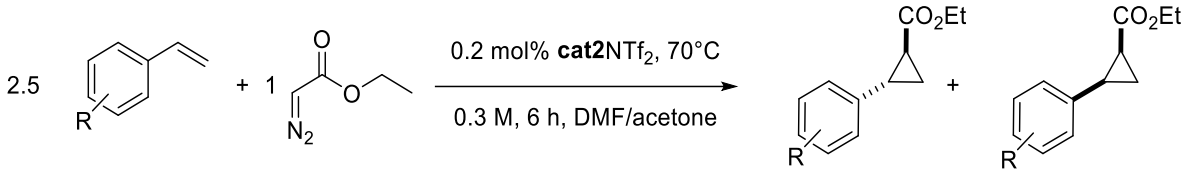

The experiments were performed as described in general procedure 4 by combining the stock solutions of the **cat2**NTf_2 (25 µL, 0.1 µmol, 0.002 eq. in DMF) and the respective styrene derivative (50 µL, 125 µmol, 2.5 eq.) with EDA (5.26 µL, 50 µmol, 1.0 eq.) and dry and degassed acetone (86.41 µL). After removing the vial from the glovebox, the mixture was stirred for 6 hours at 70°C. The respective results are listed in table 44.

Table 43: Results for additional substituents.

R	trans/cis	conversion (styrene)	yield	TON
ortho-CH_3	3.1:1	72%	62%	308
meta-CH_3	2.8:1	66%	59%	297
ortho-Br	3.0:1	68%	66%	329
meta-Br	2.3:1	59%	51%	257
2 x *ortho*-CH_3 *para*-CH_3	-	0%	0%	0

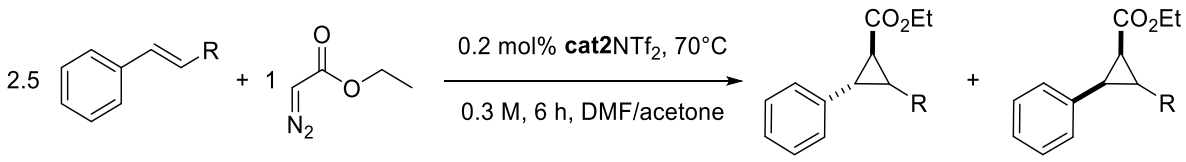

The experiments, regarding the conversion of non-terminal double bonds, were performed as described in general procedure 4 by combining the stock solutions of the **cat2**NTf_2 (25 µL, 0.1 µmol, 0.002 eq. in DMF) and the respective styrene derivative (50 µL, 125 µmol, 2.5 eq.)

with EDA (5.26 µL, 50 µmol, 1.0 eq.) and dry and degassed acetone (86.41 µL). After removing the vial from the glovebox, the mixture was stirred for 6 hours at 70°C. The respective results are listed in table 45.

Table 44: Results for the conversion of non-terminal double bonds.

R	trans/cis	conversion (styrene)	yield	TON
trans-CH_3	1.5:1:0:0	8%	2%	8
cis-CH_3	2.6:1:0:0	7%	3%	14
trans-Ph	-	0%	0%	0
cis-Ph	-	0%	0%	0
	-	0%	0%	0
	2.1:1	10%	4%	21
	2.3:1	15%	8%	40
	-	10%	2%	9
	-	0%	0%	0

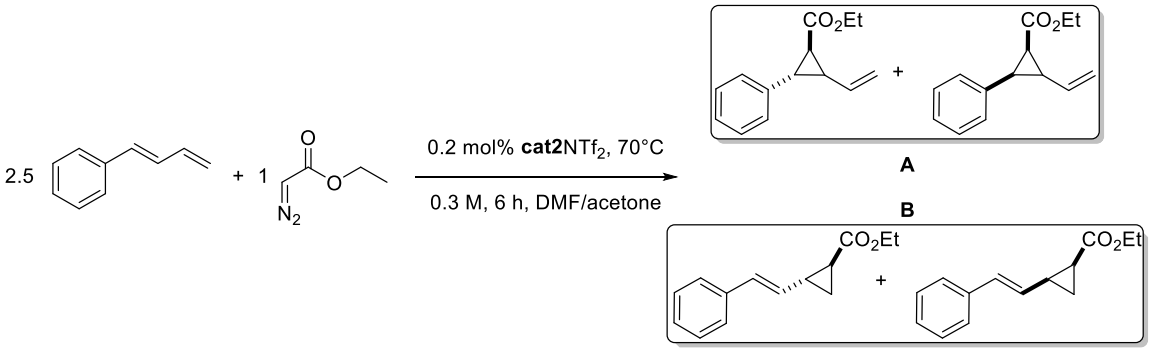

The experiment, regarding the competition of a terminal and a non-terminal double bond was performed as described in general procedure 4 by combining the stock solutions of the **cat2**NTf_2 (25 µL, 0.1 µmol, 0.002 eq. in DMF) and the respective styrene derivative (50 µL, 125 µmol, 2.5 eq.) with EDA (5.26 µL, 50 µmol, 1.0 eq.) and dry and degassed acetone (86.41 µL). After removing the vial from the glovebox, the mixture was stirred for 6 hours at 70°C. From this, only product mixture **B** was observed, without traces of **A** in a yield of 50%, which corresponds to **TON** of 250, with a diastereomeric ratio of 1.9:1 (*trans*/*cis*).

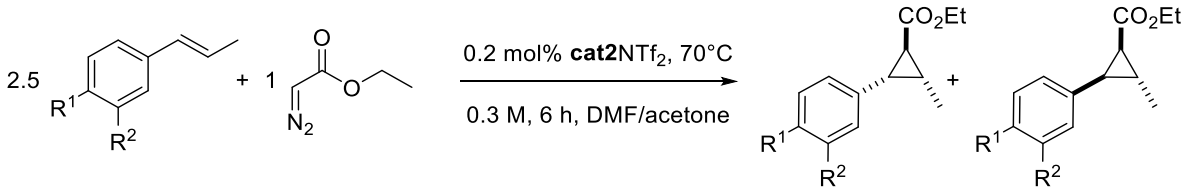

The experiments, regarding the conversion of non-terminal double bonds in the presence of functional groups at the aromatic system, were performed as described in general procedure 4 by combining the stock solutions of the **cat2**NTf_2 (25 µL, 0.1 µmol, 0.002 eq. in DMF) and the respective styrene derivative (50 µL, 125 µmol, 2.5 eq.) with EDA (5.26 µL, 50 µmol, 1.0 eq.) and dry and degassed acetone (86.41 µL). After removing the vial from the glovebox, the mixture was stirred for 6 hours at 70°C. The respective results are listed in table 46.

Table 45: Results for the conversion of non-terminal double bonds.

R^1	R^2	trans/cis	conversion (styrene)	yield	TON
OMe	H	2.8:1	6%	1%	6
OAc	OMe	-	0%	0%	0

Comparison of NMR-yields and isolated yields

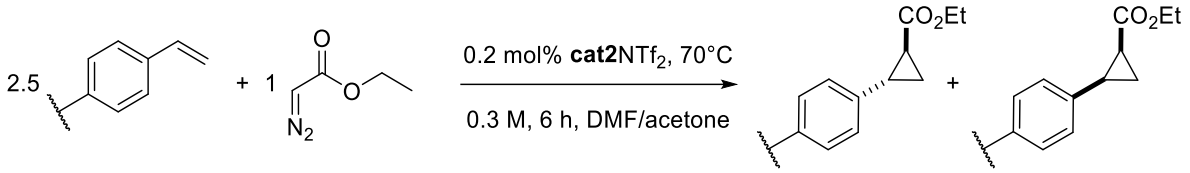

The experiments, regarding isolation of products, were performed as described in general procedure 4 by combining the stock solutions of the **cat2**NTf_2 (25 µL, 0.1 µmol, 0.002 eq. in DMF) and the respective styrene derivative (50 µL, 125 µmol, 2.5 eq.) with EDA (5.26 µL, 50 µmol, 1.0 eq.) and dry and degassed acetone (86.41 µL). After removing the vial from the glovebox, the mixture was stirred for 6 hours at 70°C. Afterwards, the work-up was performed as described in the general procedure 4 with subsequent separation of the compounds on a preparative TLC plate (CH/EA = 9:1). The product was collected from the plate and dissolved in acetone. After filtration, the solvent was removed under reduced pressure and the sample was separated *via* HPLC (ACN/water = 1:1). The respective results are lister in table 47.

Table 46: Results for isolated yields, compared to the respective NMR yields.

R	trans/cis	conversion (styrene)	isolated yield	NMR yield
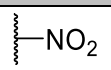	2.7:1	71%	44%	67%
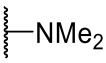	3.1:1	76%	38%	70%

Cis-product

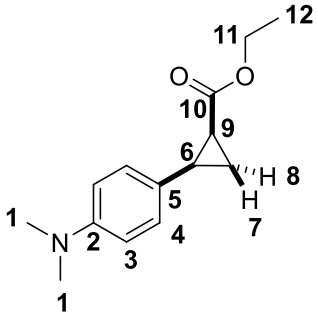

^{1}H-NMR (500 MHz, acetone-d_6, 298 K): δ[ppm] = 7.11-7.04 (m, 2 H, H-4), 6.63 (d, $^{3}J_{3,4}$ = 8.8 Hz, 2 H, H-3), 3.84 (q, $^{3}J_{11,12}$ = 7.6 Hz, 2 H, H-11), 2.88 (s, 6 H, H-1), 2.53-2.44 (m, 1 H, H-6), 2.00 (ddd, $^{3}J_{9,6}$ = 9.02 Hz, $^{3}J_{9,8}$ = 7.7 Hz, $^{3}J_{9,7}$ = 5.6 Hz, 1 H, H-9), 1.53 (ddd, $^{3}J_{7,6}$ = 7.4 Hz, $^{3}J_{7,9}$ = 5.6 Hz, $^{3}J_{7,8}$ = 4.6 Hz, 1 H, H-7), 1.26 (ddd, $^{3}J_{8,6}$ = 8.7 Hz, $^{3}J_{8,9}$ = 7.7 Hz, $^{3}J_{8,7}$ = 4.6 Hz, 1 H, H-8), 0.99 (t, $^{3}J_{12,11}$ = 7.6 Hz, 3 H, H-12).

Due to the small samples size remaining after the separation of both diastereomers, no meaningful ^{13}C-NMR could be measured.

Trans-product

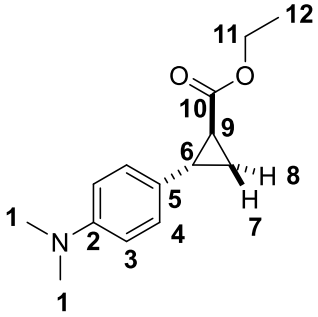

^{1}H-NMR (500 MHz, acetone-d_6, 298 K): δ[ppm] = 6.99 (d, $^{3}J_{4,3}$ = 9.0 Hz, 2 H, H-4), 6.68 (d, $^{3}J_{3,4}$ = 9.0 Hz, 2 H, H-3), 4.16-4.06 (m, 2 H, H-11), 2.94-2.82 (m, 6 H, H-1), 2.83-2.80 (m, 1 H, H-6), 2.38-2.29 (m, 1 H, H-9), 1.79-1.70 (m, 1 H, H-7), 1.45-1.36 (m, 1 H, H-8), 1.26-1.20 (m, 3 H, H-12).

^{13}C-NMR (126 MHz, acetone-d_6, 298 K): δ[ppm] = 173.6 (C-10), 150.6 (C-2), 128.5 (C-5), 127.6 (C-4), 113.6 (C-3), 60.9 (C-11), 40.8 (C-1), 26.2 (C-6), 24.3 (C-9), 16.7(C-7/8), 14.6 (C-12).

This data agrees with the results reported in literature.[133]

***Cis*-product**

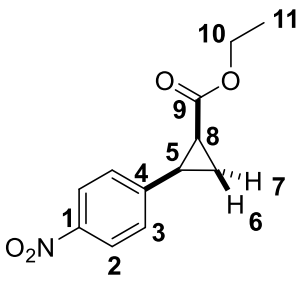

^{1}H-NMR (500 MHz, acetone-d_6, 298 K): δ[ppm] = 8.14 (d, $^{3}J_{2,3}$ = 8.8 Hz, 2 H, H-2), 7.55 (d, $^{3}J_{3,2}$ = 8.8 Hz, 2 H, H-3), 3.87 (q, $^{3}J_{10,11}$ = 7.1 Hz, 2 H, H-10), 2.79-2.77 (m, 1 H, H-6), 2.25 (ddd, $^{3}J_{8,5}$ = 9.4 Hz, $^{3}J_{8,7}$ = 7.8 Hz, $^{3}J_{8,6}$ = 5.7 Hz, 1 H, H-8), 1.73 (ddd, $^{3}J_{6,5}$ = 7.5 Hz, $^{3}J_{6,8}$ = 5.7 Hz, $^{3}J_{6,7}$ = 5.0 Hz, 1 H, H-6), 1.51-1.46 (m, 1 H, H-7), 0.99 (t, $^{3}J_{11,10}$ = 7.1 Hz, 3 H, H-11).

^{13}C-NMR (126 MHz, acetone-d_6, 298 K): δ[ppm] = 170.7 (C-9), 146.2 (C-1), 131.3 (C-3), 130.6 (C-4), 123.6 (C-2), 60.8 (C-10), 25.6 (C-5), 23.2 (C-9), 14.4 (C-7/8), 12.1 (C-12).

This data agrees with the results reported in literature.[134]

***Trans*-product**

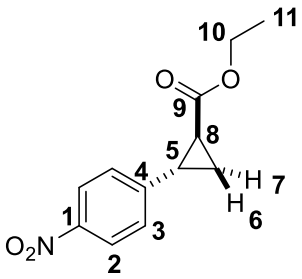

^{1}H-NMR (500 MHz, acetone-d_6, 298 K): δ[ppm] = 8.16 (d, $^{3}J_{2,3}$ = 8.8 Hz, 2 H, H-2), 7.48 (d, $^{3}J_{3,2}$ = 8.8 Hz, 2 H, H-3), 4.19-4.08 (m, 2 H, H-10), 2.66-2.58 (m, 1 H, H-5), 2.10 (ddd, $^{3}J_{8,7}$ = 8.6 Hz, $^{3}J_{8,6}$ = 5.5 Hz, $^{3}J_{8,5}$ = 4.2 Hz, 1 H, H-8), 1.63 (ddd, $^{3}J_{6,5}$ = 9.2 Hz, $^{3}J_{6,8}$ = 5.5 Hz, $^{3}J_{6,7}$ = 4.6 Hz, 1 H, H-6), 1.52 (ddd, $^{3}J_{7,8}$ = 8.6 Hz, $^{3}J_{7,5}$ = 5.6 Hz, $^{3}J_{7,6}$ = 4.6 Hz, 1 H, H-7), 0.99 (t, $^{3}J_{11,10}$ = 7.1 Hz, 3 H, H-11).

^{13}C-NMR (126 MHz, acetone-d_6, 298 K): δ[ppm] = 172.7 (C-9), 149.6 (C-1), 147.5 (C-4), 127.9 (C-3), 124.4 (C-2), 61.3 (C-10), 26.1 (C-5), 25.8 (C-9), 18.2 (C-7/8), 14.5 (C-12).

This data agrees with the results reported in literature.[133]

***Hammett*-plot**

The experiments for the *Hammett*-plot were performed as described in general procedure 4 by combining the stock solutions of the **cat2**NTf_2 (25 µL, 0.1 µmol, 0.002 eq. in DMF), the respective styrene derivative (25 µL, 62.5 µmol, 1.25 eq.) and styrene (25 µL, 62.5 µmol, 1.25 eq.) with EDA (5.26 µL, 50 µmol, 1.0 eq.) and dry and degassed acetone (86.41 µL). After removing the vial from the glovebox, the mixture was stirred for 6 hours at 70°C. The respective results are listed in table 48.

Table 47: Results for the experiments of regarding the *Hammett*-plot.

R	yield derivative	yield styrene	ratio yield (derivative/styrene)	log (ratio)	*Hammett* coefficient
NMe_2	58%	59%	0.9787	-0.0094	-0.83
OMe	45%	68%	0.6624	-0.1789	-0.27
TMS	56%	69%	0.8068	-0.0932	-0.07
F	66%	65%	1.0084	0.0037	0.06
CO_2Me	68%	49%	1.3685	0.1363	0.45
CF_3	65%	40%	1.6135	0.2078	0.54
NO_2	69%	19%	3.6766	0.5654	0.78

Further catalysts

Further control experiments were conducted using **cat3**NTf_2 and **cube2**NTf_2, shown in figure 133, as well as $Fe(bipy)_3Cl_2$.

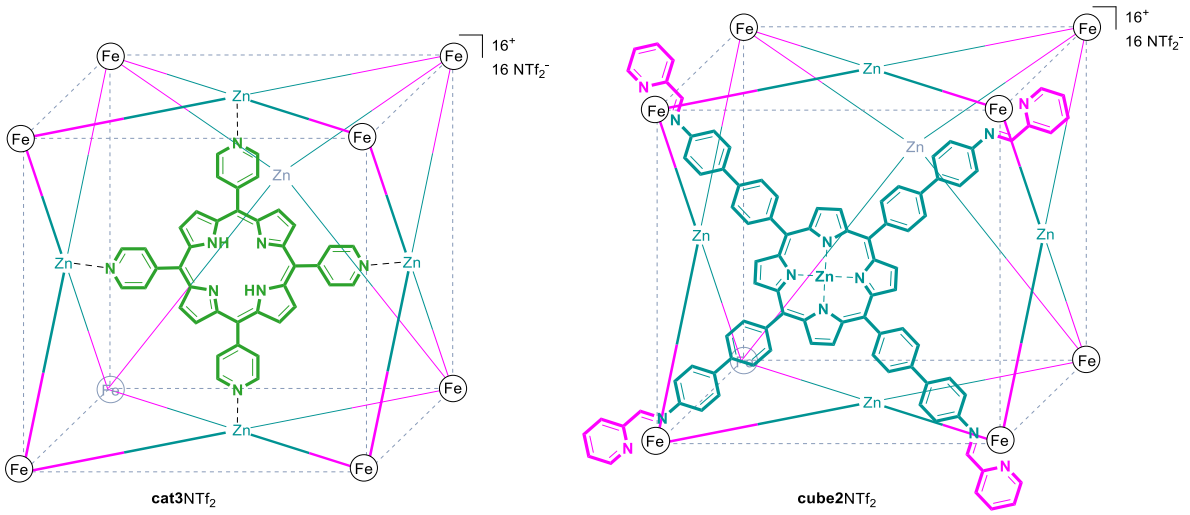

Figure 133: Structure of **cat3**NTf_2 and **cube2**NTf_2.

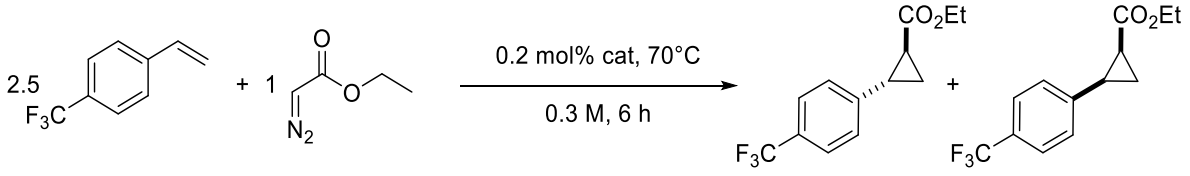

The control experiments were performed as described in general procedure 4 by combining the stock solutions of the respective catalyst (25 µL, 0.1 µmol, 0.002 eq. in DMF) and

para-trifluoromethyl styrene (50 µL, 125 µmol, 2.5 eq.) with EDA (5.26 µL, 50 µmol, 1.0 eq.) and dry and degassed acetone (86.41 µL). After removing the vial from the glovebox, the mixture was stirred for 6 hours at 70°C. The respective results are listed in table 49.

Table 48: Results for control experiments with different catalysts.

catalyst	mol%	trans/cis	conversion (styrene)	yield	TON
cat3NTf_2	0.2	6.1:1	26%	18%	88
cube2NTf_2	0.2	4.9:1	32%	24%	122
$Fe(bipy)_3Cl_2$	1.6	3.8:1	14%	10%	6
Zn-TAbPP	1.2	3.1:1	5%	3%	3
None	-	3.2:1	5%	2%	-

19. List of abbreviations

ALA	Alanine
Ac	Acetyl
Bu	butyl
CH	cyclohexane
CNT	carbon nanotube
cyp	cytochrome P450
d	days
d	doublet
d.r.	diastereomeric ratio
DCM	dichloromethane
DDQ	2,3-dichloro-5,6-dicyano-1,4-benzochinone
DMF	*N,N*-dimethyl formamide
DMSO	*N,N*-dimethyl sulfoxide
DNA	deoxyribonucleic acid
dppf	1,1'-bis(diphenylphosphino)ferrocene
DSSC	*dye-sensitised solar cell*
EA	ethyl acetate
EDTA	ethylenediaminetetraacetic acid
eq.	equivalent
ESI	electron spray ionisation
Et	ethyl
FRET	*Förster* resonance energy transfer
h	hours
HOMO	highest occupied molecular orbital
HPLC	high performance liquid chromatography
HRMS	high resolution mass spectrometry
L	ligand
LUMO	lowest unoccupied molecular orbital
M	molar [mol/L]
M	metal
[M]	molecule
m	multiplet
m	mass
Me	methyl
min.	minutes
MOF	metal organic framework
MS	mass spectrometry
NADP	nicotinamide adenine dinucleotide phosphate
nm	nanometre
NMR	nuclear magnetic resonance
NTf_2	triflimide
OTf	triflate
PBG	porphobilinogen
Ph	phenyl
pH	potential of hydrogen
ppm	parts per million
q	quartet
r.t.	room temperature
s	singlet
sat.	saturated
t	triplet

t	tert
TEA	triethyl amine
TFA	trifluoro acetic acid
THF	tetrahydrofurane
TMS	trimethylsilyl
TOF	turnover frequency
TON	turnover number
UV	ultraviolet
z	charge

20. References

[1] R. R. Naik, S. Singamaneni, *Chem. Rev.* **2017**, *117*, 12581–12583.

[2] B. Bhushan, *Philos. Trans. R. Soc. A.* **2009**, *367*, 1445–1486.

[3] J. F. V. Vincent, O. A. Bogatyreva, N. R. Bogatyrev, A. Bowyer, A.-K. Pahl, *J. R. Soc. Interface* **2006**, *3*, 471–482.

[4] W. Barthlott, C. Neinhuis, *Planta* **1997**, *202*, 1–8.

[5] W. Kim, D. Kim, S. Park, D. Lee, H. Hyun; Kim, Jangho, *J. Ind. Eng. Chem.* **2018**, *61*, 39–52.

[6] A. Solga, Z. Cerman, B. F. Striffler, M. Spaeth, W. Barthlott, *Bioinspir. Biomim.* **2007**, *2*, 126-34.

[7] P. Sudhakar, P. Latha, P. V. Reddy in *Phenotyping Crop Plants for Physiological and Biochemical Traits*, Academic Press, **2016**.

[8] C. R. Carlini, R. Ligabue-Braun, *Plant Toxins*, Springer Netherlands, Dordrecht, **2017**.

[9] F. Abbas, Y. Yu, M. Bendahmane, H.-C. Wang, *Physiol. Plant.* **2023**, *175*, e13947.

[10] L.-L. Li, E. W.-G. Diau, *Chem. Soc. Rev.* **2013**, *42*, 291–304.

[11] M. Ethirajan, Y. Chen, P. Joshi, R. K. Pandey, *Chem. Soc. Rev.* **2011**, *40*, 340–362.

[12] M. J. A. Reis, A. M. V. M. Pereira, N. M. M. Moura, M. G. P. M. S. Neves, *ACS omega* **2024**, *9*, 31196–31219.

[13] S. S. Nurttila, R. Becker, J. Hessels, S. Woutersen, J. N. H. Reek, *Chem. Eur. J.* **2018**, *24*, 16395–16406.

[14] a) A. E. Garrod, *J. Physiol.* **1892**, *13*, 598–620. b) E. Salkowski, *physiol. Chem.* **1893**, *17*, 268–306. c) B. J. Stockvis, *klin. Med.* **1895**, *27*, 1. d) K. Dobriner, C. P. Rhoads, *Physiol. Rev.* **1940**, *20*, 416–468. e) E. Salkowski, *Pflügers Arch.* **1897**, *69*, 268–306.

[15] E. Rabinowitch, *Rev. Mod. Phys.* **1944**, *16*, 226-235.

[16] H. Scheer, J. J. Katz, *Nuclear magnetic resonance spectroscopy of porphyrins and metalloporphyrins*, Elsevier, **1975**.

[17] E. Rabinowitch, Govindjee, *Sci. Am.* **1965**, *213*, 74–83.

[18] G. D. Scholes, T. Mirkovic, D. B. Turner, F. Fassioli, A. Buchleitner, *Energy Environ. Sci.* **2012**, *5*, 9374.

[19] G. H. Krause, E. Weis, *Annu. Rev. Plant Biol.* **1991**, *42*, 313–349.

[20] R. van Grondelle, J. P. Dekker, T. Gillbro, V. Sundstrom, *Biochim. Biophys. Acta* **1994**, 1–65.

[21] D. G. Johnson, M. P. Niemczyk, D. W. Minsek, G. P. Wiederrecht, W. A. Svec; Gaines, George L., III; Wasielewski, Michael R., *J. Am. Chem. Soc.* **1993**, *115*, 5692–5701.

[22] L. Hederstedt, *Biochim. Biophys. Acta* **2012**, *1817*, 920–927.

[23] a) J. M. Baldwin, *Prog. Biophys. Molec. Biol.* **1975**, 225–320. b) T. L. Poulos, *Chem. Rev.* **2014**, *114*, 3919–3962. c) R. M. Winslow, *Respir. Physiol. Neurobiol.* **2007**, *158*, 121–127.

[24] J. A. Hasler, R. Estabrook, M. Murray, I. Pikuleva, M. Waterman; Capdevila, Jorge; Holla, Vijakumar; Helvig, Christina; Falck, J. R.; Farrell, Geoffrey, *Mol. Asp. Med.* **1999**, *20*, 1–137.

[25] I. G. Denisov, T. M. Makris, S. G. Sligar, I. Schlichting, *Chem. Rev.* **2005**, *105*, 2253–2277.

[26] a) C.-M. Che, V. K.-Y. Lo, C.-Y. Zhou, J.-S. Huang, *Chem. Soc. Rev.* **2011**, *40*, 1950–1975. b) C.-C. Guo, X.-Q. Liu, Q. Liu, Y. Liu, M.-F. Chu; Lin, W.-Y., *J. Porphyr. Phthalocyanines* **2009**, *12*, 1250–1254.

[27] J. C. Barona-Castaño, C. C. Carmona-Vargas, T. J. Brocksom, K. T. de Oliveira, *Molecules* **2016**, *21*, 310.

[28] a) E. Rose, B. Andrioletti, S. Zrig, M. Quelquejeu, *Chem. Soc. Rev.* **2005**, *34*, 573–583. b) E. Rose, Q.-Z. Ren, B. Andrioletti, *Chem. Eur. J.* **2004**, *10*, 224–230.

[29] M. Xie, J. Liu, L. Dai, H. Peng, Y. Xie, *RSC advances* **2023**, *13*, 24699–24730.

[30] S. Ramasamy, M. Bhagavathiachari, S. A. Suthanthiraraj, M. Pichai, *Dyes and Pigments* **2022**, *203*, 110380.

[31] ALFA Chemistry, "Porphyrins Catalysts", https://www.alfachemic.com/catalysts/products/porphyrins-catalysts.html, **requested on 2025**.

[32] S. V. Zvezdina, M. B. Berezin, B. D. Berezin, *Russ. J. Coord. Chem.* **2010**, *36*, 711–714.

[33] a) X. Zhou, F. Su, Y. Tian, R. H. Johnson, D. R. Meldrum, *Sens. Actuators B Chem.* **2011**, *159*, 135–141. b) N. Qiu, X. Pan, R. Hu, Z. Hui, *Front. Bioeng. Biotechnol.* **2023**, *11*, 1268458.

[34] F. J. Leeper, *Nat. prod. Rep.* **1989**, 171–203.

[35] H. Tamiaki, P. J. Brothers, M. O. Senge, *Fundamentals of Porphyrin Chemistry: A 21st Century Approach*, Wiley, Weinheim, **2022**.

[36] Paul Rothemund, A. R. Menotti, *J. Am. Chem. Soc.* **1941**, *63*, 267–270.

[37] Alan D. Adler, Frederick R. Longo, William. Shergalis, *J. Am. Chem. Soc.* **1964**, *86*, 3145–3149.

[38] Jonathan S. Lindsey, *The synthesis of meso substituted porphyrins*, Springer Netherlands, Dordrecht, **1994**.

[39] a) P. Asselin, A. Schlachter, D. Fortin, P.-L. Karsenti, P. D. Harvey, *Chem. Mater.* **2022**, *34*, 7242–7255. b) M. Zhao, S. Zhu, X. Yang, Y. Wang, X. Zhou; Xie, X., *Macromol. Rapid Commun.* **18**, *43*, 2200173.

[40] Bi Bi Fatemeh Mirjaili, Abdolhamid Bamoniri, Rasoul Vafazadeh, Leila Zamani, *Bull. Korean Chem. Soc.* **2009**, *10*, 2440–2442.

[41] L. Zamani, B. B. F. Mirjalili, *Chem. Heterocycl. Comp.* **2015**, *51*, 578–581.

[42] C. A. Henriques, S. M. A. Pinto, G. L. B. Aquino, M. Pineiro, M. J. F. Calvete; Pereira, Mariette M., *ChemSusChem* **2014**, *7*, 2821–2824.

[43] S. Singh, A. Aggarwal, C. Farley, B. A. Hageman, J. D. Batteas; Drain, Charles Michael, *Chem. Commun.* **2011**, *47*, 7134–7136.

[44] K. Ariga, T. Kunitake, *Supramolecular chemistry - fundamentals and applications: advanced textbook*, Springer Science & Business Media, Luxemburg, **2006**.

[45] J. D. van der Waals, *Dissertation*, University of Leiden, Leiden, **1873**.

[46] J. M. Berg, J. L. Tymoczko, L. Stryer, *Biochemistry*, W. H. Freeman and Company, New York, **2006**. *6th Editon*.

[47] P. A. Gale, J. W. Steed, Wiley, Weinheim, **2012**.

[48] G. A. Soukup *Encyclopedia of Life Science, John Wiley & Sons*, John Wiley & Sons Ltd, Hoboken, **2001**.

[49] Whitesides, George, M, Kriebel, Jennah, K, Mayers, Brian, T, *Self-Assembly and Nanostructured Materials. In: Huck, W.T.S (eds) Nanoscale Assembly. Nanostructure Science and Technology.*, Springer, Boston, MA, **2005**.

[50] W. T. S. Huck, *Nanoscale assembly*, Springer, New York, **2005**. *Chemical techniques*.

[51] M. Fujita, K. Umemoto, M. Yoshizawa, N. Fujita, T. Kusukawa; Biradha, Kumar, *Chem. Commun.* **2001**, *6*, 509–518.

[52] E. Fischer, *Ber. Dtsch. Chem. Ges.* **1894**, *27*, 2985–2993.

[53] D. E. Koshland, *PNAS* **1958**, *44*, 98–104.

[54] D. E. Koshland, *Angew. Chem. Int. Ed. Engl.* **1995**, *33*, 2375–2378.

[55] H. R. Bosshard, *News Physiol. Sci.* **2001**, *16*, 171–173.

[56] C. J. Pedersen, *J. Am. Chem. Soc.* **1967**, *89*, 7017–7036.

[57] T. Xiao, R. Elmes, Y. Yao, *Front. Chem.* **2023**, *11*, 1162019.

[58] G. Norjmaa, P. Vidossich, J.-D. Maréchal, G. Ujaque, *J. Chem. Inf. Model.* **2021**, *61*, 4370–4381.

[59] J. M. Lehn, *Supramolecular Chemistry*, VCH, Weinheim, **1995**.

[60] M. Raynal, P. Ballester, A. Vidal-Ferran, P. W. N. M. van Leeuwen, *Chem. Soc. Rev.* **2014**, *43*, 1660–1733.

[61] R. Breslow, S. D. Dong, *Chem. Rev* **1998**, *39*, 1997–2011.

[62] R. Breslow, L. Overman, *J. Am. Chem. Soc.* **1970**, *92*, 1075–1077.

[63] J. Dai, H. Zhang, *Small* **2021**, *17*, e2005334.

[64] D. A. Britz, A. N. Khlobystov, K. Porfyrakis, A. Ardavan, G. A. D. Briggs, *Chem. Commun.* **2005**, 37–39.

[65] P. C. M. Laan, E. O. Bobylev, F. J. de Zwart, J. A. Vleer, A. Troglia; Bliem, Roland; Rothenberg, Gadi; Reek, Joost N. H.; Yan, Ning, *Chem. Eur. J.* **2023**, *29*, e202301901.

[66] W. Chen, X. Pan, X. Bao, *J. Am. Chem. Soc.* **2007**, *129*, 7421–7426.

[67] L.-D. Syntrivanis, K. Tiefenbacher, *Angew. Chem. Int. Ed. Engl.* **2024**, *63*, e202412622.

[68] K. Goto, *Comprehensive Supramolecular Chemistry II*, Elsevier, Amsterdam, **2017**. *The concepts of preorgaization*.

[69] R. M. Islam, J. G. Mahdi, I. D. Bowen, *Drug Saf.* **2012**, *17*, 149–165.

[70] R. P. Bonar-Law, L. G. Mackay, C. J. Walter, V. Marvaud, J. K. M. Sanders, *Pure Appl. Chem.* **1994**, *66*, 803–810.

[71] Q. Shi, D. Masseroni, J. Rebek, *J. Am. Chem. Soc.* **2016**, *138*, 10846–10848.

[72] E. Nieland, J. Voss, B. M. Schmidt, *ChemPlusChem* **2023**, *88*, e202300353.

[73] R. Cacciapaglia, S. Di Stefano, L. Mandolini, *J. Am. Chem. Soc.* **2003**, *125*, 2224–2227.

[74] S. M. Jansze, G. Cecot, K. Severin, *Chem. Sci.* **2018**, *9*, 4253–4257.

[75] S. Wang, R. Hübner, H. Karring, V. F. Batista, C. Wu, *Angew. Chem. Int. Ed. Engl.* **2025**, *64*, e202416556.

[76] Y. Ueda, H. Ito, D. Fujita, M. Fujita, *J. Am. Chem. Soc.* **2017**, *139*, 6090–6093.

[77] Y. Zhang, P. E. VanNatta, J. Ren, S. Ma, *CCS Chem.* **2024**, *6*, 1380–1402.

[78] J. P. Collman, R. R. Gagne, C. Reed, T. R. Halbert, G. Lang; Robinson, Ward T., *J. Am. Chem. Soc.* **1975**, *97*, 1427–1439.

[79] J. P. Collman, R. Boulatov, C. J. Sunderland, L. Fu, *Chem. Rev.* **2004**, *104*, 561–588.

[80] K. S. Suslick, P. Bhyrappa, J.-H. Chou, M. E. Kosal, S. Nakagaki; Smithenry, Dennis W.; Wilson, Scott R., *Acc. Chem. Res.* **2005**, *38*, 283–291.

[81] M. Otte, P. F. Kuijpers, O. Troeppner, I. Ivanović-Burmazović, J. N. H. Reek; Bruin, Bas de, *Chem. Eur. J.* **2013**, *19*, 10170–10178.

[82] M. Otte, P. F. Kuijpers, O. Troeppner, I. Ivanović-Burmazović, J. N. H. Reek; Bruin, Bas de, *Chem. Eur. J.* **2014**, *20*, 4880–4884.

[83] V. Mouarrawis, E. O. Bobylev, B. de Bruin, J. N. H. Reek, *Eur. J. Inorg. Chem.* **2021**, *2021*, 2890–2898.

[84] H. Chen, H. Ye, Y. Hai, L. Zhang, L. You, *Chem. Sci.* **2020**, *11*, 2707–2715.

[85] C. Gütz, A. Lützen, *Synthesis* **2010**, *2010*, 85–90.

[86] A. D. Adler, F. R. Longo, J. D. Finarelli, J. Goldmacher, J. Assour; Korsakoff, Leonard, *J. Org. Chem.* **1967**, *32*, 476.

[87] X. Xu, H. Chen, N. Huang, *Macromolecules* **2024**, *57*, 9457–9465.

[88] N. Oppenheimer, H. A. Stone, *Biophys. J.* **2017**, *113*, 440–447.

[89] M. Tobiszewski, M. Marć, A. Gałuszka, J. Namieśnik, *Molecules* **2015**, *20*, 10928–10946.

[90] T. Welton, *Proc. Math. Phys. Eng. Sci.* **2015**, *471*, 20150502.

[91] Z. Safaei, S. Bocian, B. Buszewski, *RSC Adv.* **2014**, *4*, 53915–53920.

[92] J. Płotka, M. Tobiszewski, A. M. Sulej, M. Kupska, T. Górecki; Namieśnik, Jacek, *J. Chromatogr. A.* **2013**, *1307*, 1–20.

[93] T. S. Srivastava, T. Yonetani, *Chromatographia* **1975**, *8*, 124–128.

[94] C. Stella, S. Rudaz, J. L. Veuthey, A. Tchapla, *Chromatographia* **2001**, *53*, 132–140.

[95] S. Mondal, T. Pain, K. Sahu, S. Kar, *ACS omega* **2021**, *6*, 22922–22936.

[96] M. J. Justen, *Bachelorarbeit*, Rheinische Friedrich-Wilhelms-Universität Bonn, Bonn, **2023**.

[97] Q. Lin, X. Bu, A. Kong, C. Mao, F. Bu; Feng, Pingyun, *Adv. Mater.* **2015**, *27*, 3431–3436.

[98] L. F. Schmidt, *Bachelorarbeit*, Rheinische Friedrich-Wilhelms-Universität Bonn, Bonn, **2025**.

[99] G. Magna, D. Monti, C. Di Natale, R. Paolesse, M. Stefanelli, *Molecules* **2019**, *24*, 4307.

[100] J. Bhaumik, G. Gogia, S. Kirar, L. Vijay, N. S. Thakur; Banerjee, Uttam C.; Laha, Joydev K., *New J. Chem.* **2016**, *40*, 724–731.

[101] J. A. Onwudili, M. A. Peters, C. T. Alves, *Molecules* **2024**, *29*, 4346.

[102] R. E. H. Kuveke, L. Barwise, Y. van Ingen, K. Vashisth, N. Roberts; Chitnis, Saurabh S.; Dutton, Jason L.; Martin, Caleb D.; Melen, Rebecca L., *ACS central science* **2022**, *8*, 855–863.

[103] P. Espinet, A. M. Echavarren, *Angew. Chem. Int. Ed. Engl.* **2004**, *43*, 4704–4734.

[104] N. Miyaura, A. Suzuki, *Chem. Rev.* **1995**, *95*, 2457–2483.

[105] P. B. Hodgson, F. H. Salingue, *Tetrahedron Lett.* **2004**, *45*, 685–687.

[106] N. C. Struch, *Masterthesis*, Rheinische Friedrich-Wilhelms-Universität Bonn, Bonn, **2013**.

[107] W. Meng, B. Breiner, K. Rissanen, J. D. Thoburn, J. K. Clegg; Nitschke, Jonathan R., *Angew. Chem. Int. Ed. Engl.* **2011**, *50*, 3479–3483.

[108] T. Nakazono, A. R. Parent, K. Sakai, *Chem. Commun.* **2013**, *49*, 6325–6327.

[109] M. Nolten, K. T. Xia, S. Pezzotti, G. Schwaab, R. G. Bergman; Raymond, Kenneth N.; Dean Toste, F.; Head-Gordon, Teresa; Li, Wan-Lu; Havenith, Martina, *Phys. Chem. Chem. Phys.* **2025**, *27*, 10120–10128.

[110] R. F. J. Epping, D. Vesseur, M. Zhou, B. de Bruin, *ACS catalysis* **2023**, *13*, 5428–5448.

[111] H. Lu, W. I. Dzik, X. Xu, L. Wojtas, B. de Bruin; Zhang, X. Peter, *J. Am. Chem. Soc.* **2011**, *133*, 8518–8521.

[112] S. Gupta, R. Fernandes, R. Patel, M. Spreitzer, N. Patel, *Appl. Catal. A: Gen.* **2023**, *661*, 119254.

[113] R. L. Khade, Y. Zhang, *J. Am. Chem. Soc.* **2015**, *137*, 7560–7563.

[114] J. C. Dorrat, C. G. P. Taylor, R. J. Young, A. B. Solea, D. R. Turner; Dennison, Genevieve H.; Ward, Michael D.; Tuck, Kellie L., *Chem. Eur. J.* **2024**, *30*, e202400501.

[115] Y. Chen, X. P. Zhang, *J. Am. Chem. Soc.* **2007**, *72*, 5931–5934.

[116] A. J. C. Walters, E. Jellema, M. Finger, P. Aarnoutse, J. M. M. Smits; Reek, J. N. H.; Bruin, B. de, *ACS Catal.* **2012**, *2*, 246–260.

[117] R. Simič, J. Mandal, K. Zhang, N. D. Spencer, *Soft matter* **2021**, *17*, 6394–6403.

[118] C. Hansch, A. Leo, R. W. Taft, *Chem. Rev.* **1991**, *91*, 165–195.

[119] H.-U. Blaser, C. Malan, B. Pugin, F. Spindler, H. Steiner; Studer, Martin, *Adv. Synth. Catal.* **2003**, *345*, 103–151.

[120] C. A. Reed, *Chem. Commun.* **2005**, 1669–1677.

[121] a) A. Chirila, B. Gopal Das, N. D. Paul, B. de Bruin, *ChemCatChem* **2017**, *9*, 1413–1421. b) J. Werth, C. Uyeda, *Chem. Sci.* **2018**, *9*, 1604–1609.

[122] S. Bhunia, S. K. Das, R. Jana, S. C. Peter, S. Bhattacharya; Addicoat, Matthew; Bhaumik, Asim; Pradhan, Anirban, *ACS Appl. Mater. Interfaces.* **2017**, *9*, 23843–23851.

[123] Q. Lin, C. Mao, A. Kong, X. Bu, X. Zhao; Feng, Pingyun, *J. Mater. Chem. A.* **2017**, *5*, 21189–21195.

[124] X. Liu, Y. Xu, Z. Guo, A. Nagai, D. Jiang, *Chem. Commun.* **2013**, *49*, 3233–3235.

[125] L. Felix, U. Sezer, M. Arndt, M. Mayor, *Eur. J. Org. Chem.* **2014**, *2014*, 6884–6895.

[126] A. Ellis, L. J. Twyman, *Macromolecules* **2013**, *46*, 7055–7074.

[127] J. Cabrera-González, E. Xochitiotzi-Flores, C. Viñas, F. Teixidor, H. García-Ortega; Farfán, Norberto; Santillan, Rosa; Parella, Teodor; Núñez, Rosario, *Inorg. Chem.* **2015**, *54*, 5021–5031.

[128] P. R. Jamaat, S. S. H. Davarani, N. S. Fumani, L. Masoumi, N. Safari, *J. Porphyr. Phthalocyanines* **2008**, *12*, 85–93.

[129] A. G. Griesbeck, M. Schäfer, J. Uhlig, *Adv. Synth. Catal.* **2008**, *350*, 2104–2108.

[130] M. Boccalon, E. Iengo, P. Tecilla, *Org. Biomol. Chem.* **2013**, *11*, 4056–4067.

[131] V. Mouarrawis, E. O. Bobylev, B. de Bruin, J. N. H. Reek, *Chem. Eur. J.* **2021**, *27*, 8390–8397.

[132] J. M. S. Lopes, R. N. Sampaio, A. S. Ito, A. A. Batista, A. E. H. Machado; Araujo, P. T.; Neto, N. M. Barbosa, *Spectrochim. Acta A Mol. Biomol. Spectrosc.* **2019**, *215*, 327–333.

[133] M. Davi, H. Lebel, *Chem. Commun.* **2008**, 4974–4976.

[134] O. V. Hryschuk, Y. Yurov, A. V. Tymtsunik, V. O. Kovtunenko, I. V. Komarov; Grygorenko, Oleksandr O., *Adv. Synth. Catal.* **2019**, *361*, 5428–5439.